A Song of Ice and Plasma:
The formation and behavior of ice-dusty plasmas, from the laboratory to the edge of the universe

Thesis by
André Nicolov

In Partial Fulfillment of the Requirements for the
Degree of
Doctorate of Philosophy

California Institute of Technology
Pasadena, California

2026
Defended September 30th, 2025

ANDRÉ NICOLOV
ORCID: 0000-0002-1197-4148

ACKNOWLEDGEMENTS

I extend my gratitude to my committee members, Profs. Bill Goddard, Sandra Troian, Geoff Blake, and to my advisor, Paul Bellan.

To Paul, thank you for your endless wisdom, knowledge, and care throughout my graduate studies, and for the many opportunities you have afforded me. While the past six years have been punctuated both with personal challenges and with unprecedented global events, I could always count on your kind support and understanding. From learning laboratory techniques to publishing research and navigating the nuances of academic integrity, I could not ask for a better mentor.

In researching astrophysical ice, I have had the privilege of working with Dr. Murthy Gudipati at JPL. I cannot thank him enough for sharing his time, knowledge, and philosophy with me. I also sincerely thank the whole Ice Spectroscopy Lab for welcoming me, especially Drs. Bryana Henderson, Lora Jovanovic, and Jeehyun Yang.

I extend my heartfelt thanks to Connie Rodriguez, our administrative assistant. I could count on her assistance to simplify any administrative task that came my way, and cherished our frequent and fascinating conversations. I also thank Jennifer Blankenship for being the best Mama Duck an Applied Physics department could ask for, and along with Christy Jenstad, for making our department feel like home.

I thank my senior graduate students: Ryan Marshall, who mentored me in the laboratory when I was but a naive G1; Yi Zhou, my office mate, whose warmth and sage advice always brightened the room; and Yang Zhang, whose physics prowess and lively conversations I've enjoyed at conferences across the continent– even if he gave me the coronavirus in Hawaii.

I'm very grateful to the postdocs who enriched my work: Seth Pree, whose experimental expertise and unique outlook sharpened my thinking; Stratos Kritikos for his energy, guidance, and wit; and Yegeon Lim, whose experience and expertise were inspirational. I also welcome Wentao Yu, and am excited to see in what new terrain his skills and curiosity take our research.

I also thank my junior graduate students. To Josh[1] Morgan, whose integrity, engineering skill, and stream of ambitious ideas shaped a lively and engaging research environment. To Adèle, who kept me sharp with her exacting questions, unique ideas, and passion for plasma astrophysics. To Jules, who joined us for his

[1] Quinn

Master's thesis— his dedication, impressive results, and encyclopedic knowledge of global affairs made our time memorable. And to Jessica, whom I've mentored over the past year– her quick learning, self-motivation, and immaculate vibes give me confidence I am leaving our research in good hands.

I must also acknowledge the undergraduates I've had the privilege to mentor— Geoff, Robert, Zhe, and Muhammad— as well as high school students Daria and Jordan. Their ingenuity and hard work kept me on my toes, and I look forward to hearing of their future accomplishments.

. . .

Throughout my six years at Caltech, I had the privilege of volunteering at Madison Elementary through the Visiting Scientists program. Teaching our 4th graders was the most fulfilling and meaningful work I did; I give my deepest thanks to Kitty Cahalan and Mitch Aiken for running the program, and to Ms. Cambrelen and Mr. Vargas for welcoming me into their classrooms.

I am deeply grateful to Caltech's Performing and Visual Arts programs for offering creative outlets that expanded my skills beyond science. Special thanks to our chamber music coaches, Professors Robert Ward and Maia Jasper White, who sharpened my musicianship, and to Professor Jim Barry, whose art instruction provided a much-needed creative refuge.

I thank all my friends at Caltech and beyond for their support throughout the years. I must especially mention Shruti, Yanky, and Sahangi, for all our adventures and good memories– I could not have made it without their support, and I feel so blessed to have found a family at Caltech.

I also must thank Ana– my UW physics comrade and my first friend at Caltech– and Chandler, for being solid and dependable friends throughout all the uncertainty of grad school from start to finish.

I thank Jen for their constant support, love, and laughs, and for being a voice to turn to through highs and through struggles.

To my family— my parents, Laurent and Deborah, my sister, Anastasia, and all my grandparents— your inspiration, guidance, love, and support led me here, and I am forever grateful for what you inspired me to be.

Finally, I thank my cat Peppercorn for her chaos and affection, both in equal amount, as well as my four pet rats, Soup, Mildew, Bagel, and Penny. They kept me company through ups, downs, successes and true apocalypses, and reminded me to cherish even the briefest moments we have together.

ABSTRACT

Much of the universe is partially ionized by stellar radiation, x-rays, or cosmic rays, forming weakly-ionized plasma. Many of these environments are also extremely cold, from Earth's upper atmosphere to planetary rings, protoplanetary disks, and interstellar clouds. Within these conditions, small grains of ice and dust can form and acquire electric charge by collecting free electrons and ions from the plasma.

This thesis investigates these ice-dusty plasmas in the laboratory, observing the nucleation, growth, and dynamics of water-ice grains within extremely cold plasma. It details the construction and operation of a steady-state radio-frequency plasma in which the electrodes are cryogenically cooled by tandem cryostats; water vapor injected into the plasma spontaneously nucleates into ice grains which grow in dendritic fractal shapes to millimeters in length. Their electric charges confine them to the plasma, where they exhibit complex dynamics such as vortices, lattices, and instabilities.

Notably, ice grains nucleate homogeneously within the plasma: OH^- and H_3O^+ ions, formed by reactions between water vapor and free electrons, attract water molecules via ion-dipole interactions to produce stable, electrically-charged molecule clusters that rapidly grow into ice grains. This process occurs regardless of the ice phase: amorphous ice forms at lower temperatures and transitions irreversibly to crystalline ice at higher temperatures or over time, mirroring processes seen in solar system ices. Further experiments reveal that the complex dynamics of the cloud of ice grains are strongly influenced by their fractal morphology, as the scaling laws of their masses, surface areas, and electric charges are vastly different during fractal growth. This allows them to strongly couple with ambient gas, enhancing momentum transfer between the grains and their surroundings and significantly increasing their charge-to-mass ratio.

This research offers critical insights into the formation and behavior of ice grains in ionized environments, with wide-ranging implications across astrophysics, materials science, and plasma technology. Understanding these processes in a controlled laboratory setting offers a window into complex phenomena across the cosmos.

PUBLISHED CONTENT AND CONTRIBUTIONS

1. Nicolov, A., Kritikos, E. M. & Bellan, P. M. *How anions induce ice nucleation in a cryogenic plasma* (in preparation). 2026.
   A.N. designed and performed laboratory experiments. E.M.K. and P.M.B. both contributed to theoretical modelling and data interpretation.

2. Nicolov, A., Pree, S. & Bellan, P. M. The dynamics of fractal ice grains in cryogenic plasma. *Physical Review Letters*. accepted. http://doi.org/10.1103/rx5l-k7f9 (2025).
   A.N. performed the experiments, analyzed data, developed the analysis techniques, and drafted the manuscript. S.P. assisted in experiments and built the RF modulation system. All authors jointly developed theory, assisted in data interpretation, and contributed to manuscript revisions.

3. Nicolov, A., Gudipati, M. S. & Bellan, P. M. Phase and morphology of water-ice grains formed in a cryogenic laboratory plasma. *The Astrophysical Journal* **966,** 66. http://doi.org/10.3847/1538-4357/ad34b5 (2024).
   A.N. assembled the setup, performed experiments, analyzed data, and developed Mie scattering and phase mixing codes, and drafted the manuscript. M.S.G. and P.M.B. designed the spectrometer setup, contributed to data interpretation, provided technical and scientific guidance, and revised the manuscript.

4. Nicolov, A. & Bellan, P. M. Modeling the energetic tail of a dusty plasma's electron energy distribution and its effect on dust grain charge and behavior. *Physics of Plasmas* **30.** http://doi.org/10.1063/5.0145209 (2023).
   A.N. wrote and performed the numerical simulations, analyzed the results, and wrote the manuscript. Development and interpretation of the analytical model, as well as manuscript revisions, were done jointly by A.N. and P.M.B.

TABLE OF CONTENTS

LIST OF ILLUSTRATIONS

LIST OF TABLES

Part I

THEORY AND METHODS IN DUSTY PLASMAS

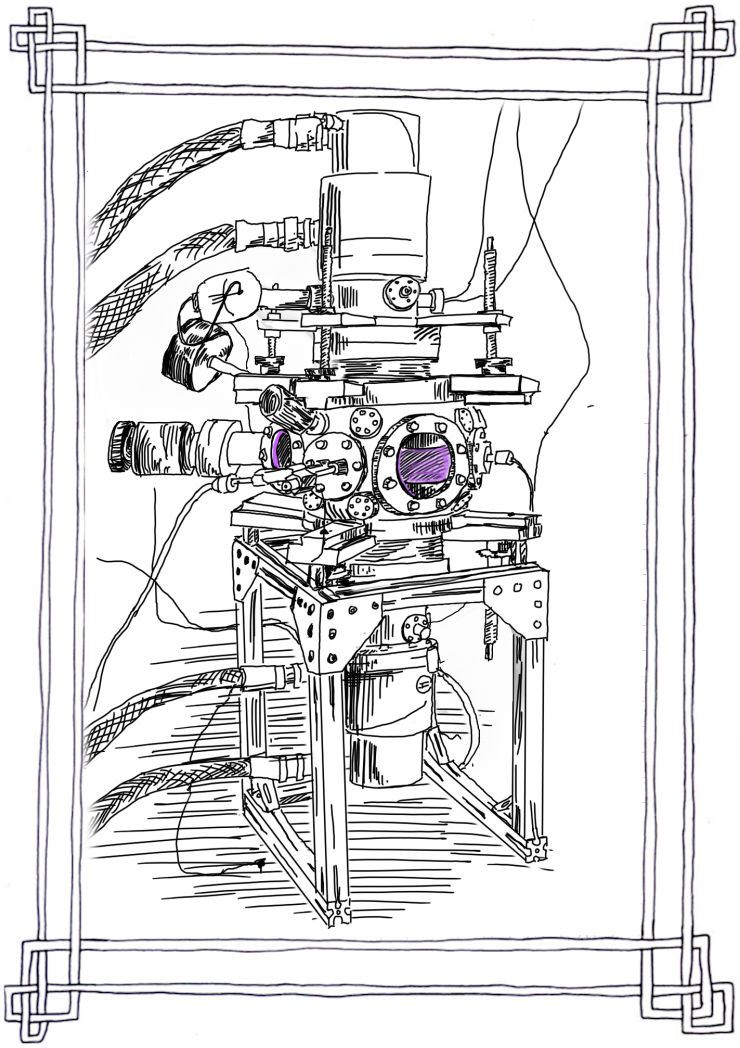

"…for dust thou art, and unto dust thou shalt return." -Genesis 3:19

Chapter 1

AN OVERVIEW OF ICE-DUSTY PLASMAS

Much of the universe is cold, dark, and empty. Diffuse clouds of gas and microscopic grains of dust and ice, formed from the remnants of long-dead stars, are bathed in a background of ionizing radiation, forming a complex system of weakly-ionized plasma and particulate matter. The physical processes within these regions are instrumental to the formation of larger, more energetic, and more complex phenomena, such as stars, nebulae, and galaxies. In this thesis, I use both experimental and theoretical methods to study these icy and dusty plasmas, explore their formation and phase, and examine their intricate dynamics.

1.1 The what, where, and why of plasma physics

Plasma, often called the "fourth state of matter," forms when a gas is energized until electrons are stripped from the constituent molecules. This process, *ionization,* results in a soup of free ions and electrons which is electrically conducting, responds to and produces electromagnetic fields, and exhibits collective behavior due to these long-range forces. This is fundamentally distinct behavior from solids, liquids, and gases, in which atoms interact primarily via collisions.

The transition from gas to plasma does not have a distinct boundary temperature, latent heat, or discontinuity in any specific order parameter. Ionization is thus *not* a thermodynamic first-order phase transition analogous to melting or vaporization, but instead a gradual, statistical process. The cutoff between what constitutes a gas versus a plasma is somewhat arbitrary—indeed, even air at sea level contains a few ions per cubic centimeter, yet it is generally not argued to be plasma, as the weak ionization does not affect its large-scale behavior. The medium in a fluorescent lamp is typically only one part-per-million ionized, yet is undeniably a plasma. Simply,

> *A system is a plasma when it acts like a plasma;*

that is, when its electromagnetic properties influence its collective behavior.

The necessary qualifications to behave like a plasma are generally listed as follows:

1. **Quasineutrality** — electron and ion densities are nearly equal and uniformly dispersed, such that there is no net charge when looking at length scales above an intrinsic length λ_D.
2. **Debye screening** — plasma acts as a conductor, rearranging charges to cancel internal electric fields and screen external ones over the length λ_D.
3. **Collective behavior** — bulk effects due to electromagnetic fields are non-negligible, as important (or more important) than kinetic collisions.

Generally, we can separate plasmas into "weakly-ionized," in which ion densities n_i are much lower than neutral densities, $n_i/n_n << 1$, and "fully-ionized" plasmas, in which ions greatly outnumber neutrals $n_i/n_n >> 1$.

Plasma in nature and technology

About 99% of visible matter in the universe exists in the plasma state, at temperatures spanning several orders of magnitude, and with ion densities spanning several *dozen* orders of magnitude. Energetic phenomena such as stellar winds, the solar corona, and astrophysical jets are hot and fully-ionized. Fusion plasmas within stellar interiors are particularly hot and dense. In contrast, interstellar clouds, planetary ionospheres, and proto-planetary disks are low-temperature, weakly ionized plasmas and often intermixed with cosmic dust and ice.

Plasma is also integral to our technology: Hot dense plasmas undergo nuclear fusion in hot and dense plasma within fusion reactors and thermonuclear bombs. Low-temperature plasmas are ubiquitous, used in neon signs, plasma TVs, fluorescent lighting, as well as a host of manufacturing, medical, and sterilization processes. In Figure 1.1, plasmas in nature and technology are shown on a parameter space of ion density (n_i) versus electron temperature (T_e).

This thesis mainly concerns weakly-ionized, low-temperature plasmas. The physics of these are especially complicated compared to fully-ionized plasmas. Constant ionization and recombination cause these systems to be out

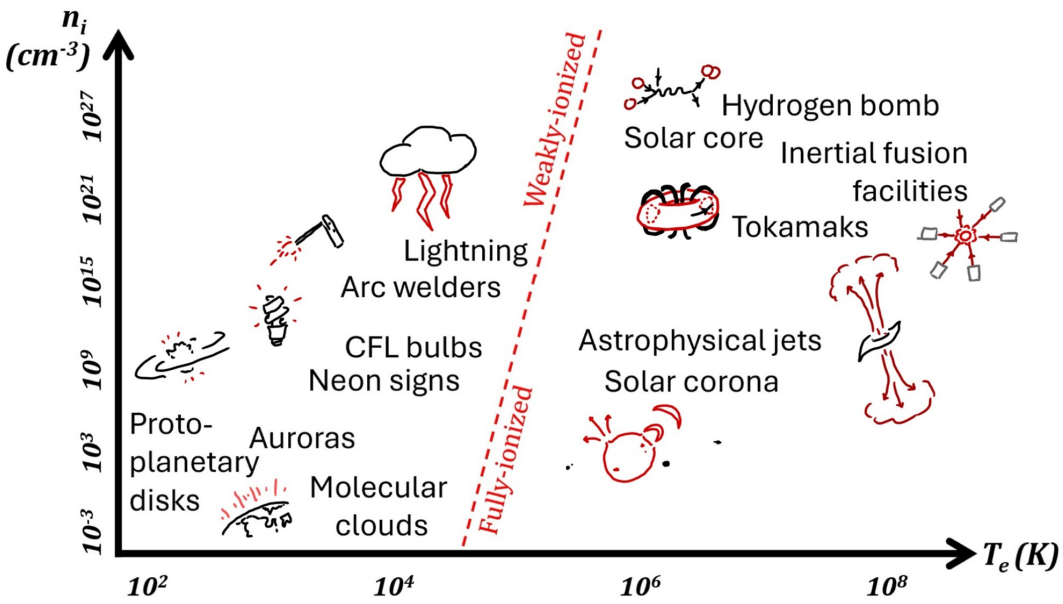

Figure 1.1: Common plasma environments and their electron temperatures and densities.

of thermal equilibrium. Particle transport and energetics are dominated by interactions between charged and neutral particles, such as elastic scattering, charge exchange, and chemical reactions. Surface interactions at plasma boundaries further complicate behavior. Consequently, models such as magnetohydrodynamics, invaluable for fully ionized plasmas, fall short in capturing this complexity.

Radiative properties

Plasmas emit light; this is what allows us to study them through telescopes from across the cosmos, and is one of their most common technological applications. The dominant light emission from plasmas is *spectral line emission*. As plasmas continuously ionize and recombine, energetic electrons decay to lower-energy orbitals,and release photons of corresponding energies. Figure 1.2 shows the dominant lines of hydrogen and their corresponding electron orbital decays.

As each element emits distinct spectral lines, the emission spectra of a plasma function as a fingerprint, revealing their molecular and ionic composition. Because higher-energy electrons produce smaller-wavelength photons, the ratios of various spectral lines change with the electron temperature and

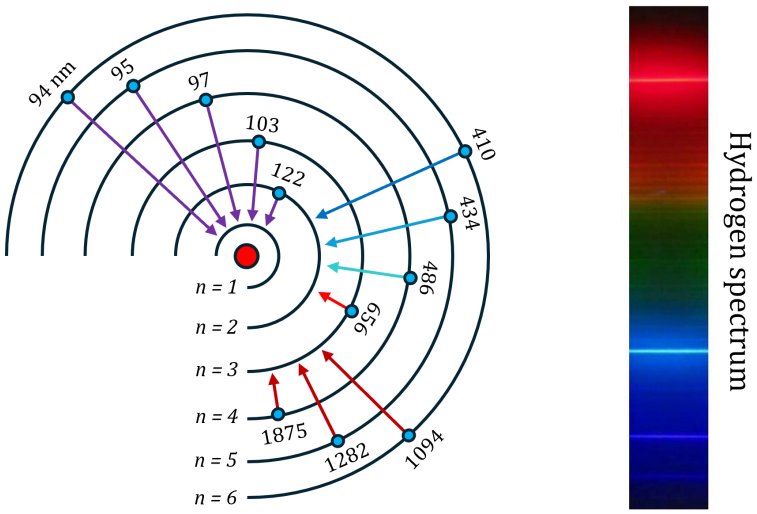

Figure 1.2: Line emission from hydrogen; wavelengths given in nanometers. Three series of emission are shown: the Lyman series (UV), Balmer series (visible), and Paschen series (infrared).

the ionization fraction of the plasma. Lines are also affected by the particle velocity due to the Doppler effect and by strong electromagnetic fields.

Dynamical description

To describe plasma behavior, we can apply a statistical "Vlasov" model, modeling each particle species (ions, electrons, or neutrals) with a distribution function $f_\sigma(\vec{x}, \vec{v}, t)$, which describes the number of particles at any given position x, with velocity v at time t. The index $\sigma \in [e, i, n]$ refers to the particle species.

If the distribution function is known, we can often simplify the model by only considering *moments* of the distribution; this is called a fluid model. Integrating over all possible velocities gives the number density of each particle species:

$$n_\sigma(x,t) = \int_{-\infty}^{\infty} f(\vec{x}, \vec{v}, t) d\vec{v}. \tag{1.1}$$

In a given reference frame, the distribution at any point in space can be approximated using an average velocity of the species,

$$\vec{u}_\sigma(\vec{x}) = \int_{-\infty}^{\infty} \vec{v} f(\vec{x}, \vec{v}, t) d\vec{v}, \tag{1.2}$$

together with a *thermal velocity*

$$v_{T,\sigma}(\vec{x}) \approx \sqrt{\frac{k_B T_\sigma}{m_\sigma}}, \tag{1.3}$$

where k_B is the Boltzmann constant and m_σ is the species mass. This quantifies the spread of velocities about the average value, or equivalently, a *thermal energy* defined by a temperature T_σ. These distributions and their moments are illustrated in Figure 1.3.

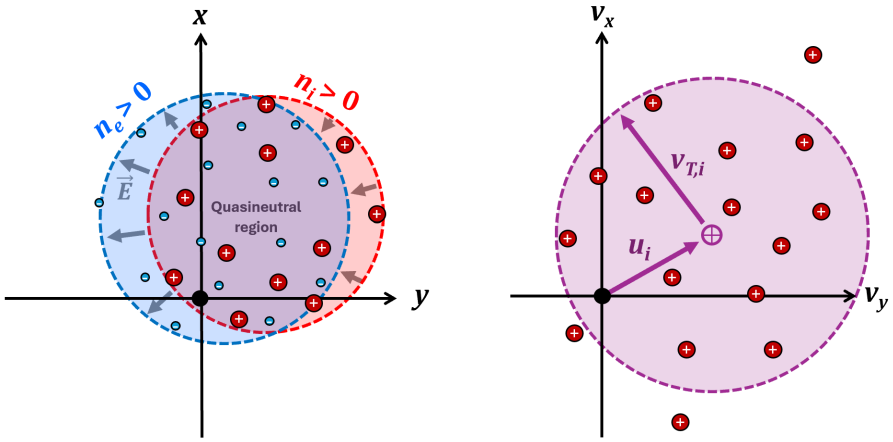

Figure 1.3: Illustrations of position and velocity distributions. Left: spread of e^- and i^+ in (x, y), with regions of nonzero density, the quasineutral region ($n_e = n_i$) and electric fields indicated. Right: ion velocity distribution in (v_x, v_y), with average velocity and thermal velocity indicated (right)

If the system undergoes enough collisions to reach thermal equilibrium, all species' velocity distributions will reach a Maxwell-Boltzmann distribution, with a temperature well-defined by the distribution's standard deviation. However, plasmas are often out-of-equilibrium, as they are relatively collisionless and have energy inputs from external fields, so a single system temperature often does not accurately describe the system. However, it's often sufficient to model *each* particle species as being in equilibrium with itself, treating each particle species as a separate, interacting fluid with its own n_σ, $\vec{u}_\sigma$, and T_σ.

Debye shielding

Plasmas are excellent electric conductors due to the high mobility of their electrons and ions. In general, the ion and electron densities are approx-

imately equal, and become uniformly mixed to minimize their potential energy, leading to quasi-neutrality (see Fig. 1.3). When an electric field is applied across the plasma, the charged particles undergo attraction or repulsion, rearranging to "screen" of the field from the rest of the plasma; this phenomena is called Debye shielding.

In a steady electric field $\vec{E} = -\nabla\phi$. The equation of motion for each fluid (electrons or ions) contains a term for the inertia, the electric field, and the pressure:

$$m_\sigma \frac{D\vec{u}_\sigma}{Dt} = -q_\sigma \nabla\phi - \frac{\nabla p_\sigma}{n_\sigma}, \tag{1.4}$$

where D/Dt signifies a convective derivative. In a static system, all time-dependent terms can be dropped, thermal equilibrium is reached, and pressure can be defined using the ideal gas law. The equation of motion simplifies to:

$$n_\sigma q_\sigma \nabla\phi + k_B T_\sigma \nabla n_\sigma = 0. \tag{1.5}$$

Solving this equation, we see that the density profile is altered by the electric field:

$$n_\sigma = n_{\sigma,0} \exp\left(-\frac{q_\sigma \phi}{k_B T_\sigma}\right). \tag{1.6}$$

Depending on the charge of the particle, therefore, the density is either exponentially enhanced or depleted; this creates a region of net charge, called the "Debye sheath," which screens the applied field from the rest of the plasma. We can find the electric potential using Poisson's equation:

$$\nabla^2\phi = -\frac{1}{\epsilon_0}(q_i n_i - q_e n_e). \tag{1.7}$$

When $\phi << k_B T$, the total electric potential is given by:

$$\phi(r) = \phi_0 \, e^{-r/\lambda_D}, \tag{1.8}$$

where λ_D is the Debye length,

$$\lambda_D = \sqrt{\frac{\epsilon_0 k_B}{\sum_{\sigma=[i,e]} n_{\sigma,0} q_\sigma^2 / T_\sigma}} \approx \sqrt{\frac{\epsilon_0 k_B T_e}{n_{e,0} q_e^2}}. \tag{1.9}$$

This is the scaling length in which the plasma shields electric fields and maintains quasineutrality. When averaging lengths larger than the Debye length, there is no net charge density, and no net electric field.

Plasma oscillations

Debye shielding occurs only when particles have time to respond to the applied fields. The response rate is a characteristic *plasma frequency*— if the field changes more quickly than the plasma frequency, Debye shielding cannot be fully established.

The plasma frequency can be calculated as follows. Imagine a spherical shell of quasi-neutral plasma with a radius r. If you were to expand the electron shell radius by δr, leaving ions behind, the electron shell would have a charge $q = -4\pi e n_e r^2 \delta r$, and the left-behind ion shell would have an equal and opposite charge. An electric field would be produced between them, $\vec{E} = e n_e \delta r / \epsilon_0$. The equation of motion is thus:

$$m_e \frac{d^2 r}{dt} = \frac{e^2 n_e}{\epsilon_0} \delta r. \tag{1.10}$$

Linearizing, such that $r''(t) = r_0 + \delta r''(t)$, yields a 2nd-order differential equation,

$$\delta r''(t) = \frac{n_e e^2}{m_e \epsilon_0} \delta r. \tag{1.11}$$

This gives simple harmonic motion at the *electron plasma frequency,*

$$\omega_{p,e} = \sqrt{\frac{n_e q_e^2}{m_e \epsilon_0}}. \tag{1.12}$$

The plasma frequency of ions takes the same form, considerably smaller due to the inverse dependence on mass. Consequently, electrons are primarily responsible for Debye shielding, as they respond to applied fields more quickly.

As the particles undergo random motion in the plasma, perturbations cause oscillations at the plasma frequency. Sudden perturbations to the plasma by external fields also excite transient oscillations at this frequency; particles are unable to respond to fields changing at faster frequencies, while Debye shielding is established on longer timescales.

1.2 What is a dusty plasma?

In a dusty plasma, "dust grains" ranging in size from nanometers to hundreds of microns are dispersed in the sea of free electrons and ions. They collide

with electrons and ions from the plasma, which stick to them, imparting the grains with large net charges that influences the composition and dynamics of both the grains themselves and the surrounding plasma. The grains can then be treated as a third particle species within the plasma alongside electrons and ions, but one with a vastly different charge-to-mass ratio and a variable charge that depends on the local collision frequency with electrons and ions. This complexity leads to emergent phenomena such as self-organization and phase transitions within the dust-plasma system.

Why study dusty plasmas?

While the study of pristine (i.e., non-dusty) plasma has a 100-year history, dusty plasma research has only gained prominence in the past three to four decades. Initial study of dusty plasmas was mainly theoretical, focused on natural phenomena throughout the solar system and astrophysics. Examples are widespread, as shown in Fig. 1.4, including clouds in the Earth's mesosphere [7], regolith levitating above the lunar surface [8], aerosols in extraterrestrial atmospheres, the tails of comets [9], ring systems [10], interstellar clouds, [11] and accretion disks [12].

Later, the behavior of particulates in laboratory plasmas for industrial applications such as semiconductor processing [13], sanitation [14], and nanoparticle synthesis [15, 16], lead to an explosion in experimental dusty plasma research. This focused on particle formation, especially from reactions of silane gas and ions, controlling the dynamics of the dust particles, and effects of grain nucleation on plasma properties and chemistry.

Now, laboratory dusty plasmas are increasingly used to study the fundamental physics of many-body systems. As first suggested by Ikezi [17], microspheres injected into plasma can form Coulomb crystals which experience lattice waves, melting and re-crystalizing, and a host of dynamic instabilities [15, 18–20]. In bringing many-body physics to the human scale, the dusty plasma serves as a macroscopic model of condensed matter.

Defining characteristics

Because of the large scale separation in mass, cross-section, and charge between the grains, the ions, and the electrons, no singular model can properly

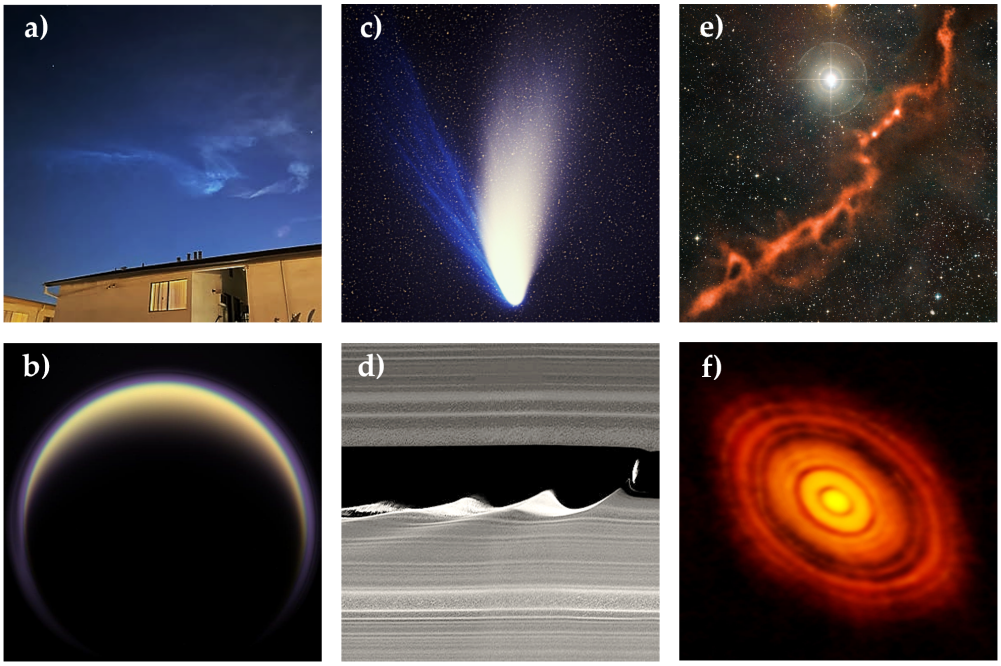

Figure 1.4: Dusty plasmas across the cosmos; (a) a noctilucent cloud formed from rocket exhaust above my apartment; (b) the atmospheric haze of Titan [NASA]; (c) the tails of comet Hale-Bopp [NASA]; (d) Saturn's A ring [NASA Cassini], perturbed by its moon Daphnis; (e) the Taurus Molecular Cloud [NASA]; (f) a protoplanetary disk [ALMA].

describe all aspects of a dusty plasma. Instead, multiple, often-conflicting pictures are required to yield its defining characteristics. Proper description is thus quite ambiguous: the grains must be treated as surfaces that interact with plasma particles, yet also as charged plasma particles themselves; at times grains can be treated as one of many interacting plasma fluids, but at other times as a single-component strongly-coupled plasma. To borrow a phrase from philosopher Simone de Beauvoir, *"[we] must not attempt to dispel the ambiguity of being but, on the contrary, accept the task of realizing it—"* with this in mind, we begin our journey to realize the characteristics of a dusty plasma.

A single dust grain in plasma is bombarded by electrons and ions at a rate,

$$\nu_\sigma = v_\sigma \, \sigma_{\text{grain}} \, n_\sigma, \tag{1.13}$$

where v_σ is the velocity of the impacting particles and σ_{grain} is the collisional cross-section of the grain. We can assume incoming particles stick to the grain. Because of their lower mass, electrons have higher velocities, and so

collide much more frequently with the dust grain; thus, *the grain will charge negatively*.

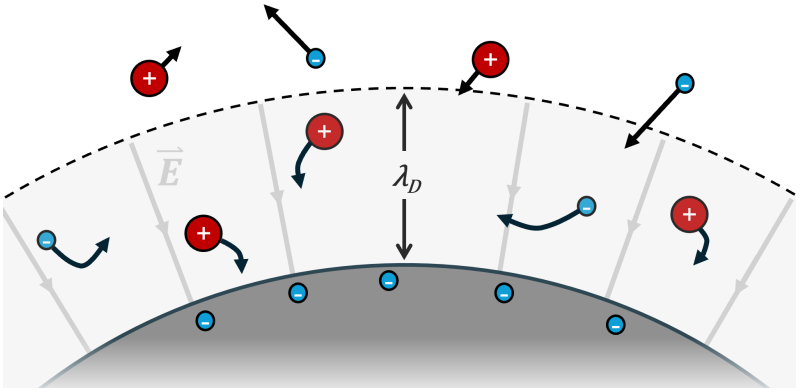

Figure 1.5: The dust grain's Debye sheath deflects electrons and ions.

As the grain charge becomes increasingly negative, it begins repelling incoming electrons while attracting the ions (see Fig. 1.5). The charging continues until the collision frequencies of electrons and ions equate, and the grain reaches an equilibrium charge. To first approximation, this occurs when the potential energy at the grain's surface reaches the electron temperature: $q_{\text{grain}}\phi \approx k_B T_e$. A more detailed treatment of grain charging is presented in Chapter 2.

Many of the infamous instabilities of traditional plasmas stem from the scale separation between electrons and ions, including ion acoustic waves, magnetic instabilities, and sheath effects at the plasma's edge.[1] In a dusty plasma, a third fluid— the collection of grains— introduces yet another scale separation, multiplying the amount of allowable wave modes and instabilities. This causes dusty plasmas to be even more unpredictable than pristine plasmas.

As the grain acquires charge by absorbing free electrons and ions, charge conservation is altered:

$$n_i = Z_d n_d + n_e, \tag{1.14}$$

where Z_d is the charge number on each dust grain and n_d is the dust number density. Thus any charge carried by the dust comes necessarily comes at the expense of electron and/or ion density.

[1] This is why confining plasmas for fusion is inherently difficult.

Depending on the plasma's densities and temperatures, dust may remain weakly-charged, remaining isolated and leaving the plasma mostly unperturbed. Alternatively, they may become strongly negatively charged, depleting electrons and transforming the plasma into a two-component system where dust replaces electrons as the carrier of negative charge. As grains absorb electrons, the Debye length increases, leaving ions as the dominant source of electrostatic shielding. When the dust density becomes high enough for individual Debye spheres to overlap, grains can interact directly via their electric fields and repel. In the presence of a confining force, they can self-organize into Coulomb crystals [17], as shown in Fig. 1.6.

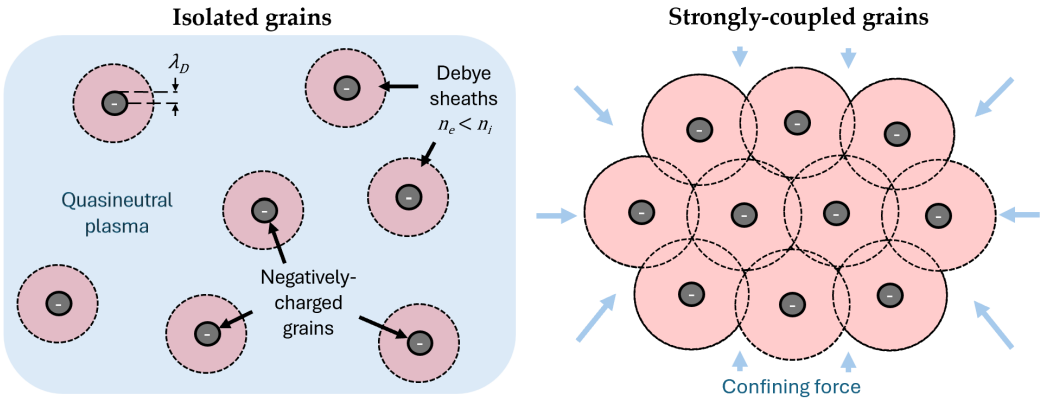

Figure 1.6: A dusty plasma with isolated grains immersed in quasineutral plasma (left), and strongly-coupled grains in an electron-deplete plasma (right).

1.3 Ice in astrophysics

Ices are central to the physical and chemical evolution of planetary systems and the interstellar medium. They promote dust grain coagulation during planet and star formation, catalyze early planetary chemistry, and regulate atmospheric and geological processes [2].

Water ice is the most common in the solar system; CO_2 ice is abundant on Mars; and SO_2, N_2, and CH_4 ices are common in the Jovian and Uranian systems. These materials occur as pure grains, as coatings on silicate or carbonaceous particles, and as surface layers on larger bodies. Examples range from ice mantles on interstellar dust, to Enceladus's plumes that feed Saturn's E ring, to mesospheric ice forming Earth's noctilucent clouds [9, 21]. In

many of these environments, grains of ice acquire electric charge, and many reside in weakly ionized, low-temperature plasmas, making ice–plasma interactions a fundamental process across natural environments.

The phases of water ice

When water solidifies into ice, it can take one of numerous phase structures, depending on the temperature and pressure. Twenty-one or so stable phases, depending on how you count, have been identified, though most of these exist at high pressures that are not relevant to astrophysical conditions. In astrophysical environments, Ice I, which can have a hexagonal (I_h, most common) or cubic (I_c) phase structure, is stable above 75 K. At lower temperatures, ice XI, a proton-ordered variant of ice I_c, becomes dominant. These phases are depicted in the water phase diagram shown in Fig. 1.7.

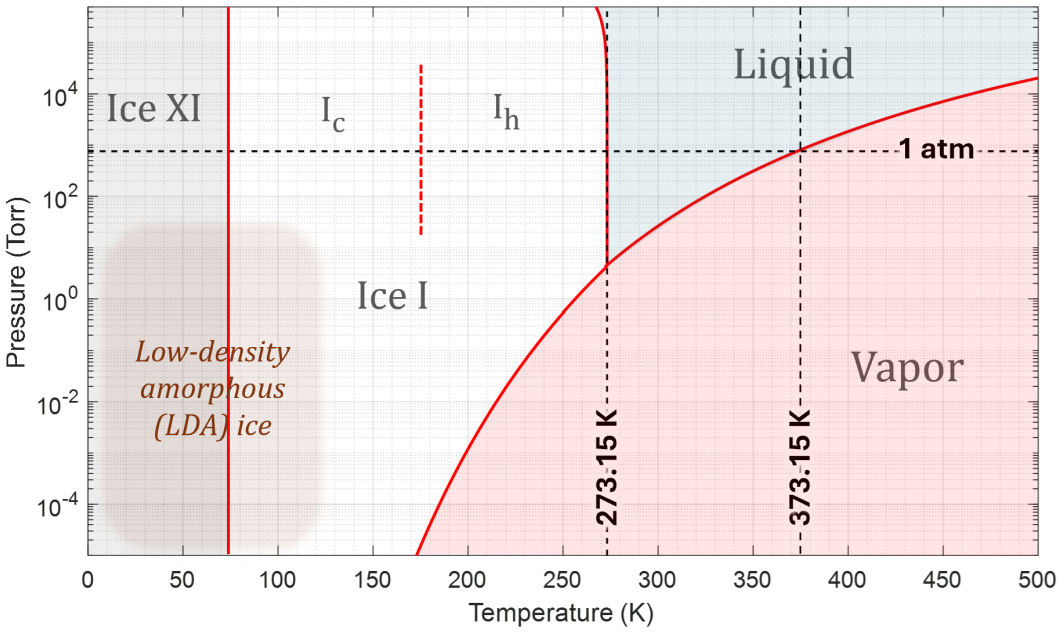

Figure 1.7: A phase diagram of water at low pressures and temperatures.

These stable phases represent minima of potential energy. However, when temperature is low and ice is formed through deposition from the vapor phase, incoming water molecules may not have enough energy to configure into a crystalline structure instantaneously. Ice XI, for example, can take thousands to millions of years to settle to its stable phase structure. In the meantime, ice forms in an amorphous phase, metastable below about 135 K

[2]. This low-density amorphous (LDA) ice has been detected throughout planetary and astrophysical conditions. It has distinct spectral features, such as shorter wavelength absorptions and a weak 1.65-mm absorption peak. It has a significantly lower thermal conductivity due to its irregular lattice structure, enhanced trapping of gas volatiles, and a higher mass-density than crystalline ice, very close to the density of liquid water [22].

LDA ice transitions to crystalline ice over timescales ranging from tens of minutes at 130 K to millions of years at 30 K [2]. This exothermic transformation releases sufficient energy to heat surrounding ice, triggering further crystallization [23] of LDA ice. When any amorphous ice within some sample crystallizes, the crystalline domain propagates rapidly through the amorphous solid, leading to a runaway process reminiscent of Kurt Vonnegut's *ice-nine* in his novel *The Cat's Cradle*; rather than Vonnegut's doomsday scenario, however, this irreversible phase transition simply triggers the rapid release of trapped volatile gases, alters the energy balance within the system, and imprints the ice's thermal and structural history on the remaining grains. Studying the phase, morphology, and chemical composition of icy grains and surfaces thus provides insight into the thermal history and surface processes of icy bodies throughout the cosmos [22].

Characteristics of Ice-Dusty Plasmas

Ices grains immersed in ionized gas occur in diverse natural settings; Figure 1.8 shows some of these *ice-dusty plasmas*.

Unlike silicate or carbonaceous grains, ice is volatile: its size and morphology can change rapidly via sublimation and vapor deposition [24]. Growth rates are enhanced by the interaction between the strong dipole moment of H_2O and the grain's charge, while ambient electric fields can drive anisotropic crystal growth and unusual morphologies [25, 26] . The high surface free energy of ice arising from hydrogen bonding, the presence of a quasi-liquid surface layer, and solvated electrons captured from the plasma, causes the surface to be highly chemically active [27, 28].

The surrounding gas in ice–dusty plasmas contains some water vapor, which is readily ionized and dissociated into H, O, OH, and H_3O [29]. Because water is electronegative, anions such as H^-, OH^-, and O^- can form in addition to cations H_2O^+ and H_3O^+. These undergo ion–molecule reactions

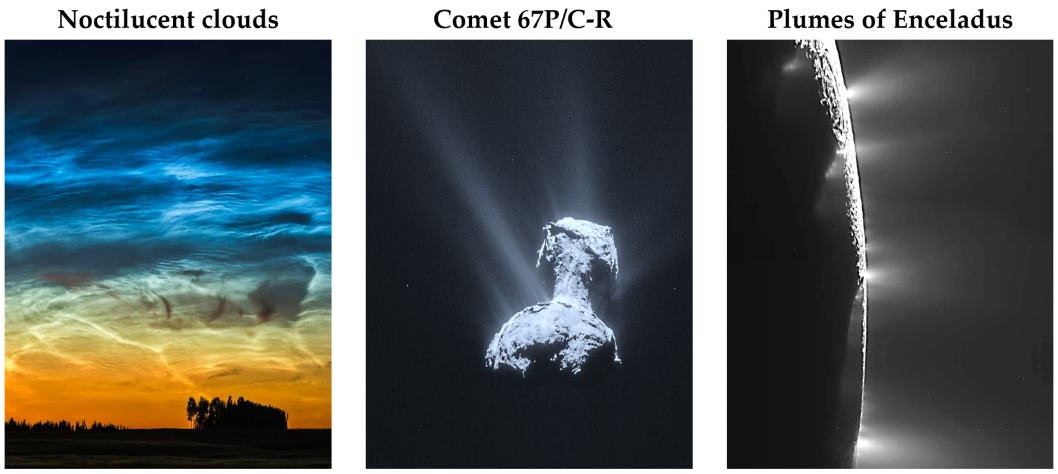

Figure 1.8: Examples of ice grains in the naturally-occurring plasmas: noctilucent clouds [not sure], Comet 67P [Rosetta, ESA], and the plumes of Enceledus [Cassini, NASA].

with other background gases, producing more complex species and seeding nucleation of new grains [30, 31].

Plasma is a hostile environment. Icy surfaces exposed to it are bombarded by electrons, ions, and photons that heat, work, and reshape the ice. As ions are accelerated across the grain's Debye sheath, they bombard the surface, which can reshape or etch the grain [26], drive phase transitions in the ice [22], and release trapped volatiles [28]. Some of these processes are shown in Fig. 1.9.

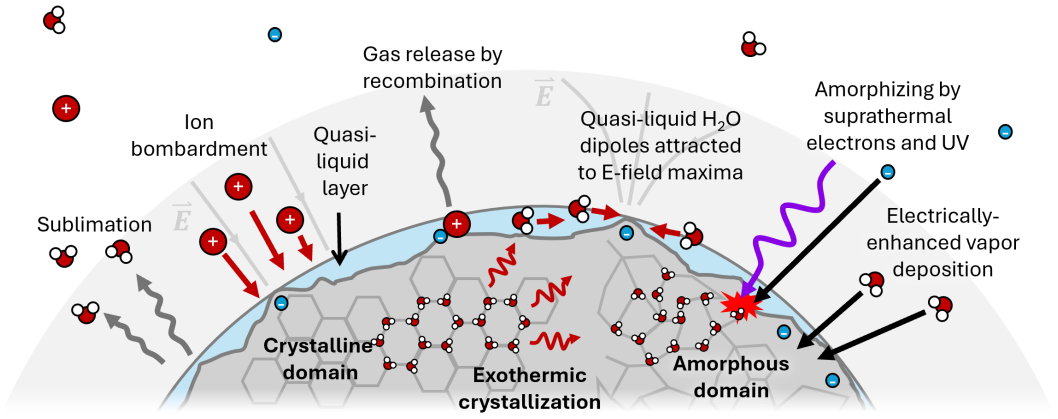

Figure 1.9: Energetic processing of ice in plasma.

The foundations of ice-dusty plasma research were laid mainly by Prof. Ove Havnes at the University of Tromsø throughout the late 20th century.

His research showed how ice formation causes coherent cloud structures that absorb ambient electrons, induce dynamic instabilities, and reflect radio waves [7, 32, 33]. Based on these findings, Shimizu *et al.* [29] created ice-dusty plasmas in the laboratory, studying the formation mechanisms, grain shape, and the chemical composition of the plasma; this work was later picked up by Caltech [24, 34]. My present work described in this thesis builds on these foundations, studying the ice formation mechanisms, grain shape, chemical composition, and effects of ice grains on the ambient plasma.

1.4 Laboratory astrophysics

Nearly all astrophysical data are optical— we observe light emission, transmission, and spectra from faraway plasma and dust in our telescopes, but cannot directly probe their microstructure or dynamics. It is thus difficult to infer the physical behavior of these system from remote observations alone. Addressing this gap is the goal of laboratory astrophysics, in which key physical and chemical processes from space are simulated in controlled experimental conditions. This allows us to directly link optical properties to their underlying mechanisms, which can be applied to better interpret astronomical data.

Most laboratory astrophysics work has focused on ice or on dust, but not both. Most commonly, ice is studied by depositing thin films of ice on a transparent substrate that is mounted to a cryostat. The films are observed through spectroscopy while varying temperature, gas composition, or exposure to radiation or electron beams [2, 22, 28]. Such experiments provide spectral signatures as functions of temperature history, ice composition, and radiative conditions, enabling direct comparison to astrophysical spectra.

On the other hand, low-temperature plasma experiments often focus on dust synthesis and their morphology. Plasma environments enhance dust formation by lowering activation barriers for gas-phase nucleation [31], and plasma reactors have produced aerosol analogues to interstellar grains and planetary hazes that closely match telescope observations [35–37].

Laboratory astrophysics also probes large-scale dust dynamics, including grain alignment, light polarization by dust clouds, and coagulation into larger aggregates [38]. Such experiments isolate specific dynamical mechanisms relevant to astrophysical systems; for example, dusty plasma wave

phenomena observed in the laboratory have been used to explain the formation of transient spokes in Saturn's rings [10].

Ice–dusty plasma research at Caltech integrates these approaches, combining ice spectroscopy, plasma chemistry, and dusty plasma dynamics to investigate nucleation, phase composition, system evolution, and emergent behavior of ice clouds in cold, ionized environments.

1.5 Thesis relevance and overview

Recent advancements in space exploration and astronomy make research on ice-dusty plasmas especially timely. As the James Webb Space Telescope (JWST) enters its so-called "ice age," capturing spectral and photographic data of icy clouds deep into the universe, and obtaining a solid understanding of the interplay between ice and plasma in extraterrestrial environments has never been more critical to advancing astrophysical research. Furthermore, as the recently-launched SPHEREx mission begins mapping galactic ices and organics with unprecedented precision, and the Europa Clipper will soon deliver high-resolution insights into Europa's icy surface and subsurface, understanding the formation, optical behavior, and dynamical impact of irregularly-shaped dust and ice continue to be fundamental to interpreting the new influx of data.

The formation and behavior of ice-dusty plasmas also have important technological implications, as plasma processing in semiconductor manufacturing, plasma-based vapor deposition, and nanoparticle synthesis demand precise particulate control to ensure high-yields and efficiency. Our findings may thus find applications in medical technology, energy storage, and advanced materials.

This thesis is organized into three parts. Part I introduces the theoretical and experimental foundations: in Chapter 2, I develop a model for grain charging due to non-thermal electrons in photoionized plasmas, and in Chapter 3, I describe the operation and design of our Ice–Dusty Plasma Experiment. Part II examines ice formation and growth: Chapter 4 surveys grain growth from nanometers to millimeters, Chapter 5 characterizes the transition from amorphous to crystalline at low temperature, and Chapter 6 investigates the processes of ice nucleation. Part III analyzes grain dynamics: Chapter 7 shows how fractal grain mass and cross-section influence the dynamics

in experiment, Chapter 8 explores how this scales to astrophysical systems, and Chapter 9 summarizes our findings and provides outlooks for future research.

Chapter 2

CHARGING IN A DUSTY PLASMA

Parts of this chapter have been published in:

> Nicolov, A. & Bellan, P. M. Modeling the energetic tail of a dusty plasma's electron energy distribution and its effect on dust grain charge and behavior. *Physics of Plasmas* **30.** `http://doi.org/10.1063/5.0145209` (2023).

...

This chapter traces the physics of grain charging. I start with the commonly-accepted charge model for isolated grains, expand this to more realistic photo-ionized plasmas, and finally explore the effects in plasmas out of thermal equilibrium, as common in atmospheric and space environments.

Dust grains acquire charge in several ways; of these, the dominant mechanisms are:

1. photoemission, which charges grains positively
2. collection of plasma particles, which typically charge grains negatively.

Photoemission is the release of an electron when a high-energy photon impacts the dust grain. It depends on the incident flux of ionizing electromagnetic radiation and the quantum yield, a function of material property and photon wavelength. Photoemission is typically small compared to plasma collection unless there is a particularly high flux of high-energy photons–even when the surrounding gas is photoionized, and is mostly ignored in this study.

We can generally assume that plasma particles stick to the surface of the dust grains with which they collide. The collision frequency is given by:

$$\nu_{s,d} \sim n_s \sigma \sqrt{\frac{kT_s}{m_s}} \tag{2.1}$$

where s is the particle species (ions or electrons), n_s is the particle density, and σ is the grain's cross-section. As electrons are a couple thousand times

less massive than ions, their collision frequency is higher; therefore, dust grains immersed in a plasma typically gain a net negative charge unless electron density is extremely low compared to ion density.

As grains build up charge, they will begin to repel electrons and attract positive ions. Eventually they come to an equilibrium in which electron and ion fluxes to the grain are equal, and charge is approximately constant. While a precise calculation of electron and ion impacts would require solving an N-body problem for the dust cloud, an average *equilibrium* charge on each grain can be approximated by assuming that dust grains are isolated– that is, they have Debye lengths smaller than the inter-particle spacing, such that incoming electrons and ions only feel one grain's potential at a time; simultaneously, we assume the mean free path is larger than the Debye length, such that the trajectories of incoming electrons and ions in the dust grain's Debye sheath are not impeded by collisions with the background gas. This is called Orbital Motion-Limited (OML) theory[1], and has been successfully applied throughout literature on dusty plasmas. [18, 32, 40]

In this chapter, I describe the traditional method of calculating grain charge in a plasma from the fundamental collisions between dust, ions, and electrons. I then apply it to the case of a photoionized plasma typical of the upper atmosphere and space to calculate the effect of dust grains on the plasma behavior. Crucially, this analysis assumes electrons and ions are in thermal equilibrium; I show that this is necessarily *not* the case in weakly-ionized plasmas, presenting a model that describes the emergence of a "hot tail" in the electron energy distribution– a small population of unusually-energetic electrons. Finally, I compute the size of this tail distribution and explore its effect on dust grain charge through both analytical and numerical methods.

2.1 OML theory and the Havnes effect

Suppose a population of charged particles, each with charge q, have some energy distribution $f(w)$, where w is the particle kinetic energy. The current carried by the charged particles to a dust grain with a surface potential of ϕ_d and a cross-section σ_{geo} depends on whether the particles are attracted or repelled by the dust charge.

[1] As opposed to a Diffusion-Limited theory, when the mean free path is very small.

The grain cross-section $\sigma(w)$ is enhanced by the Coulomb interaction between the charged particles and the dust. Applying conservation of angular momentum and energy to a Rutherford scattering model [41], it can be shown:

$$\sigma(w) = \sigma_{geo}\left(1 - \frac{q_s\phi_d}{w}\right). \tag{2.2}$$

If the charged particles are attracted to the grain, the entire energy distribution can intercept the dust's surface; if repelled, however, charged particles with energies $w < q\phi_d$ cannot approach the dust grain. Thus, when dust is negatively-charged, low-energy electrons are unable to intercept the grain. Current of each species is therefore described as follows:

$$I_i = +e\sqrt{\frac{2}{m_i}}\int_0^\infty \sigma_{geo}\left(1 - \frac{e\phi_d}{w}\right)\sqrt{w}f_i(w)dw \tag{2.3}$$

$$I_e = -e\sqrt{\frac{2}{m_e}}\int_{-e\phi}^\infty \sigma_{geo}\left(1 + \frac{e\phi_d}{w}\right)\sqrt{w}f_e(w)dw. \tag{2.4}$$

While often not strictly true, it is typically assumed that electrons and ions have Maxwellian energy distributions, that is:

$$f_s(w) = 2n_s\sqrt{\frac{w}{\pi(kT_s)^3}}\exp\left(-\frac{w}{kT_s}\right). \tag{2.5}$$

Inserting equation 2.5 into equations 2.3 and 2.4 and evaluating the integrals, we can equate them to solve for the charge equilibrium conditions:

$$\frac{n_e}{n_i}\sqrt{\frac{T_e m_i}{T_i m_e}} = \left(1 - \frac{e\phi_d}{kT_i}\right)\exp\left(-\frac{e\phi_d}{kT_e}\right). \tag{2.6}$$

This transcendental equation relates the dust surface potential to the electron and ion densities *while dust is present*. Charge conservation states:

$$n_i = n_e + Z_d n_d, \tag{2.7}$$

where Z_d is the number of negative charges on the dust grain. This charge can be obtained from the surface potential using the capacitance of the grain,

$$q_d = -eZ_d = C(\sigma_{geo})\phi_d. \tag{2.8}$$

For spherical grains, the capacitance $C = 4\pi\epsilon_0 r_d$, from Coulomb's law.

For charge conservation to be fulfilled, dust charge must come at the expense of electrons and ions in the plasma. Generally, the presence of dust causes the density of electrons to decrease; this is called the Havnes effect, and is measured by the Havnes parameter:

$$H = \frac{Z_d n_d}{n_i} = 1 - \frac{n_e}{n_i}. \tag{2.9}$$

When H = 0, dust is uncharged; when H = 1, all electrons are absorbed, and dust becomes the main carrier of negative charge. Equation 2.6 can be rewritten in terms of H and a non-dimensionalized potential $\psi = -e\phi/kT_i$:

$$H = 1 - \sqrt{\frac{T_i m_e}{T_e m_i}}\,(1+\psi)\exp\left(\psi\frac{T_i}{T_e}\right). \tag{2.10}$$

This relationship is plotted in Figure 2.1.

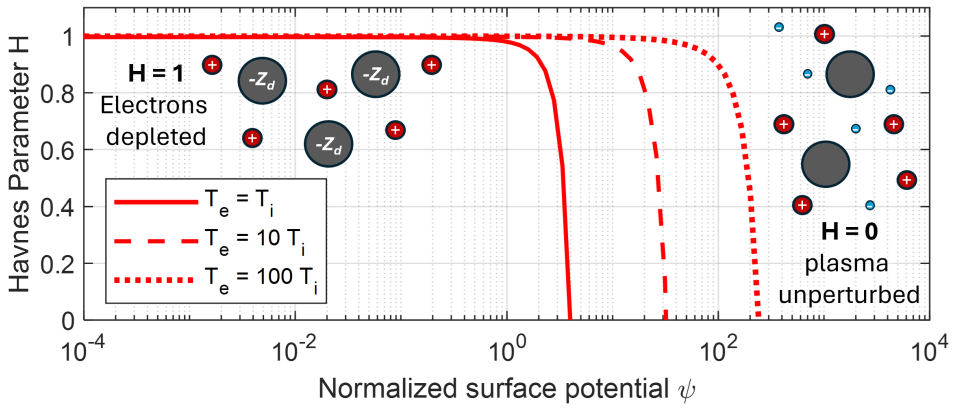

Figure 2.1: Plot of Equation 2.10 for various T_e/T_i; $m_i = 40\ m_p$

.

The Havnes parameter H remains near 1 over a large range of ψ values, and then drops quickly to zero. Therefore, in many cases, it is sufficient to assume either $H = 1$ or $H = 0$.

When $H = 1$, it is not necessary to apply OML theory: from Equation 2.9, we see that $Z_d = n_i/n_d$. Conversely, when $H = 0$, Equation 2.10 can be re-arranged:

$$\begin{aligned} Z_d &= -\frac{r_d k T_e}{e^2}\left[\frac{1}{2}\ln\left(\frac{m_e T_i}{m_i T_e}\right) + \ln(1+\psi)\right] \\ &\approx -\frac{r_d k T_e}{2e^2}\ln\left(\frac{m_e T_i}{m_i T_e}\right). \end{aligned} \tag{2.11}$$

Here it is assumed that dust is spherical with radius r_d, and its charge Z_d relates to ϕ using Coulomb's law. The approximation in Eq. 2.11 gives the *floating potential* of an isolated object in a plasma.

To uniquely-define the system, we require an assumption about grain geometry. Inputting the capacitance of a spherical grain into Eq. 2.8, we find that both ψ and H depend on the charge number Z_d: ψ through the capacitance equation (Eq. 2.8), and H by its definition (Eq. 2.9). Solving both these equations for Z_d, equating them, we rearranging the result gives a second relationship between H and ψ:

$$H = \left(\frac{kT_i 4\pi\epsilon_0 r_d}{e^2} \frac{n_d}{n_i} \right) \psi \equiv P\psi. \tag{2.12}$$

Note that this parameter P is also often referred to in literature as the Havnes parameter, and differs from H by a factor of ψ.

The intercept between Eq. 2.10, which depends on the plasma energetics, and Eq. 2.12, which depends on the grain geometry, fully-defines H and ψ *in charge equilibrium*: in a plasma with given temperatures T_e and T_i, dust density n_d, and grain radius r_d, the plasma densities and grain charges will evolve to this equilibrium.

While use of OML is widespread, it has several pitfalls in practice. Firstly, it assumes dust grains are isolated and do not interact electrostatically; in dense dusty plasmas, however, grains can interact through electrostatic repulsion, deviating from OML predictions. OML thus does not capture important effects such as Coulomb crystallization, dust lattice waves, and ion wake interactions [40]. Secondly, when the dust density approaches the electron density, charge discretization become significant. OML treats charge as a continuous variable, but in reality, dust grains acquire discrete charge values due to individual electron and ion collection. This assumption is reasonable when $Z_d >> 1$, but detrimental when Z_d is of order unity, as is common in many astrophysical situations [39, 42].

2.2 Charging in a photoionized plasma

Dusty plasmas in upper atmosphere and outer space are typically ionized by high-energy radiation, such as stellar UV emissions, X-rays, or cosmic rays. Electrons are sourced both through photoionization of neutrals and through

photoemission from dust particulates; ions, meanwhile, are predominantly produced by photoionization. Free electrons and ions eventually meet their demise, either recombining with one another or collecting on a dust grain. The densities of electrons and ions thus change dynamically, determined by the flux of ionizing radiation and dust densities, sizes, and equilibrium charges.

I here develop a self-consistent model of charge density between dust and plasma for a given photon flux, neutral density, temperature, and dust grain distribution. This calculation is inspired by the methods of Rapp & Lübken [42] and Parthasarathy [43] in calculating mesosphere conditions, which I have adapted to follow OML theory.

Let Q_e be the production rate of electrons, which depends on both photoionization and photoemission rates, and Q_i be the production rate of ions, which depends only on photoionization. For an incoming photon flux Φ_p, the production rates are given by:

$$Q_e = (n_n \sigma_n + n_d \pi r_d^2 Y)\Phi_p \tag{2.13}$$

$$Q_i = n_n \sigma_n \Phi_p, \tag{2.14}$$

where Y is the photoelectric yield. The rate of change of electron and ion densities can be written as follows:

$$\frac{dn_e}{dt} = Q_e - \alpha n_e n_i - D_e n_e n_d \tag{2.15}$$

$$\frac{dn_i}{dt} = Q_i - \alpha n_e n_i - D_i n_i n_d. \tag{2.16}$$

The constant α is the recombination rate of electrons and ions, while D_i and D_e represent the fluxes of ions and electrons to the dust grain. They can be obtained with OML theory: $D_i = I_i/n_i e$, where I_i is the ion current of Eq. 2.3.

Charge equilibrium calculation

As grains will reach an equilibrium charge, ion and electron collection rates equate. Simultaneously, electron and ion densities will come to steady state, such that the ionization and recombination rates equate. We solve both these equilibria at once by setting the left-hand side of Eqs. 2.15 and 2.16 to zero.

Note that in the absence of dust, the third term on the right-hand side vanishes, $n_e = n_i$, and electrons and ions achieve an equilibrium density:

$$n_0 = \sqrt{Q/\alpha}. \tag{2.17}$$

With dust present, we can subtract Eq. 2.16 from Eq. 2.15, yielding:

$$(D_e n_e - D_i n_i) n_d = Q_e - Q_i = n_d \sigma_{geo} Y \Phi_p. \tag{2.18}$$

For simplicity, I here assume ions and electron energy distributions are Maxwellian (in thermal equilibrium with *themselves*), and that dust grains are spherical. The collection coefficients are thus:

$$D_i = 2r_d^2 \sqrt{\frac{2\pi k T_i}{m_i}} \left(1 - \frac{e\phi}{kT_i}\right) \tag{2.19}$$

$$D_e = 2r_d^2 \sqrt{\frac{2\pi k T_e}{m_e}} \exp\left(\frac{e\phi}{kT_e}\right). \tag{2.20}$$

Inputting this into Eq. 2.18,

$$2n_e r_d^2 \sqrt{\frac{2\pi k T_e}{m_e}} \exp\left(\frac{e\phi}{kT_e}\right) = 2n_i r_d^2 \sqrt{\frac{2\pi k T_i}{m_i}} \left(1 - \frac{e\phi}{kT_i}\right) + \pi r_d^2 Y \Phi_p. \tag{2.21}$$

If photoionization of the gas dominates photoemission from dust ($n_n \sigma_n \gg n_d Y \pi r_d^2$), we can approximate $Q_e = Q_i \equiv Q$. This is done for simplicity for the remainder of the calculation. The equilibrium condition thus becomes:

$$\frac{n_e}{n_i} \sqrt{\frac{kT_e}{m_e}} \exp\left(-\frac{e\phi}{kT_e}\right) = \sqrt{\frac{kT_i}{m_i}} \left(1 - \frac{e\phi}{kT_i}\right). \tag{2.22}$$

For consistency, we can put this in terms of H and ψ as before;

$$(1 - H) \exp\left(-\psi \frac{T_i}{T_e}\right) = \sqrt{\frac{m_e T_i}{m_i T_e}} (1 + \psi). \tag{2.23}$$

This gives the same equilibrium condition as before, Eq. 2.10. As our second equation, we can again use Eq. 2.12 (which came from charge conservation), but solve for n_i:

$$n_i = 4\pi\epsilon_0 k T_i r_d n_d \frac{\psi}{e^2 H}. \tag{2.24}$$

One more equation is required to define these three unknowns: H, ψ, and n_i. As the equilibrium relation (Eq. 2.23) combined the two rate equations, we can use the ion rate equation as our final independent equation:

$$\begin{aligned} 0 &= Q - \alpha n_i^2 (1 - H) - D_i n_i n_d \\ &= Q - n_i^2 \alpha (1 - H) - 2 n_i n_d r_d^2 \sqrt{\frac{2\pi k T_i}{m_i}} (1 + \psi). \end{aligned} \tag{2.25}$$

Given Q, α, r_d, n_d, and the temperatures, these three equations thus give H, ψ, and n_i, which can be used to find n_e and Z_d as well. While other literature use one or two of these equations, they do not employ OML in a self-consistent way [7, 42, 43], often assuming singly-charged grains or a distribution obtained through uncoupled simulations. [42, 44].

Results are plotted in Figure 2.2 over a range of r_d and n_d. There is a sharp transition between the $H \sim 1$ and $H \sim 0$ regimes as radii and dust number densities decrease. Meanwhile, dust charge increases with r_d while decreasing with n_d– this is expected, as at higher densities the charge must be shared among more grains.

The ion and electron densities are plotted relative to the density expected of pristine conditions ($n_0 = \sqrt{Q/\alpha}$), using the relation:

$$\Delta n_i(\%) = \frac{n_i - n_0}{n_0} \times 100\%. \tag{2.26}$$

The electron density map follows the contours of the Havnes parameter, depleted as H approaches unity. The ion density, meanwhile, is sometimes depleted along with n_e, and sometimes enhanced due to lack of electrons with which to recombine.

2.3 Charging by non-thermal electrons in an energetic tail

In Section 2.1, we found the equilibrium charge developed on grains in a plasma of given densities and temperatures. In Section 2.2, we found an equilibrium of *both* plasma densities *and* dust charge in a photoionized plasma at given temperatures. In this section, I expand this equilibrium to also include the electron energy distribution, accounting for the dominant effects of non-thermal electrons.

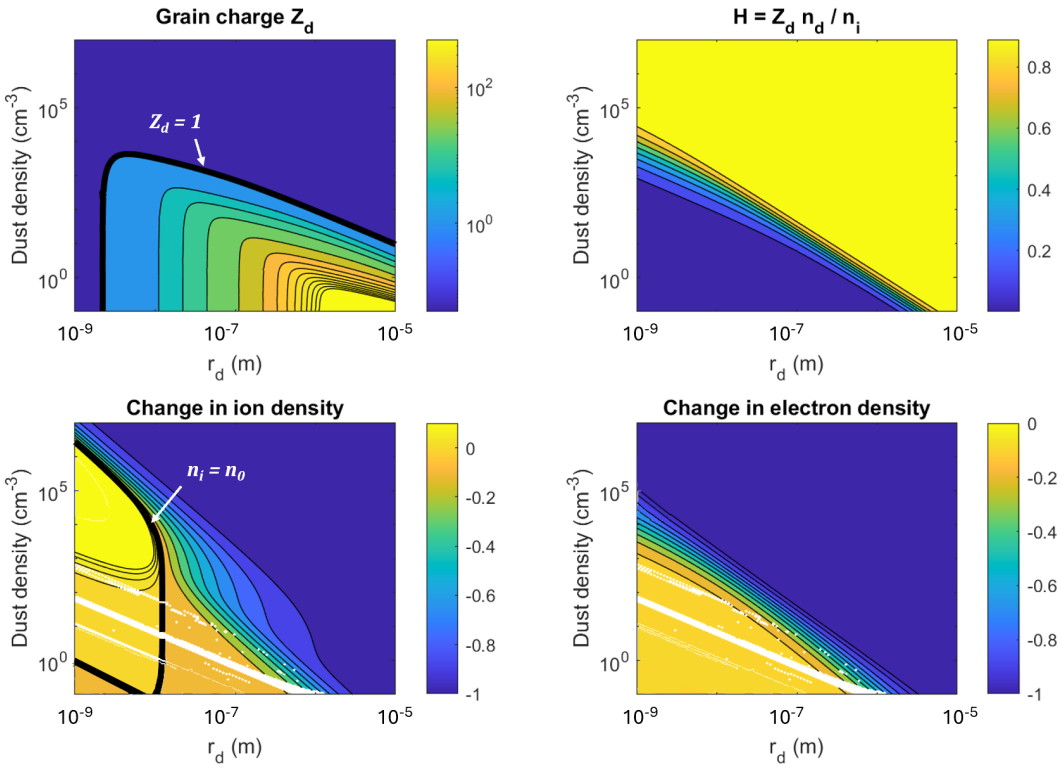

Figure 2.2: Solutions for the photo-ionized plasma model with $Q = 10\ \mathrm{cm^{-3}s^{-1}}$, $\alpha = 10^{-6}\ \mathrm{cm^3/s}$, $T_e = 10\ T_i$, and $m_i = 40\ m_p$. Electrons and ions are both well-depleted for larger grains at higher densities; ion density actually increases for small grains at low to medium densities, as no electrons are available to recombine with them. White artifacts in lower graphs are due to poor convergence in the nonlinear solver.

As shown in Eqs. 2.3 and 2.4, the calculation of grain charging from OML inherently depends on the distributions of electron and ion energies in the plasma. Applying a Maxwellian distribution is often justified by invoking the high collisionality of these plasmas. [7, 9, 32, 41, 45, 46] However, dusty plasmas generally maintain their state of weak ionization via energy input from some external ionization source; consequently, these plasmas cannot be considered isolated systems, and so may never come to thermal equilibrium.

Instead, even very collisional plasmas can have a high-energy tail of hot, newly-ionized free electrons that have not yet undergone sufficient collisions to cool to the neutral temperature. This is confirmed by many direct measurements: in laboratory RF plasmas have a tail of hot electrons due to stochastic heating in the sheath [13, 47], while electrons in the magnetosphere and

heliosphere are better modeled by kappa distributions that contain a larger high-energy tail [48].

Even slight deviations from a Maxwellian electron energy distribution can significantly affect dust grain charge and dynamics. For example, Havnes *et al.* [32] found that different electron distributions caused large variations in dust cloud density and grain potential, and Stangeby [49] and Chen [47] showed that small numbers of nonthermal electrons dominate current flux to probe surfaces. The shape of the nonthermal electron distribution is therefore essential to dust charging.

Energy evolution of a single electron

The neutral gas within weakly-ionized plasma is typically cold. A tiny fraction of the gas is continuously ionized, creating free electrons at energies of the order of a few eV. As neutrals greatly outnumber charged particles, the energetic electrons lose their initial energies through elastic collisions with the cold neutral population, until eventually undergoing recombination. This sequence is outlined in Fig. 2.3.

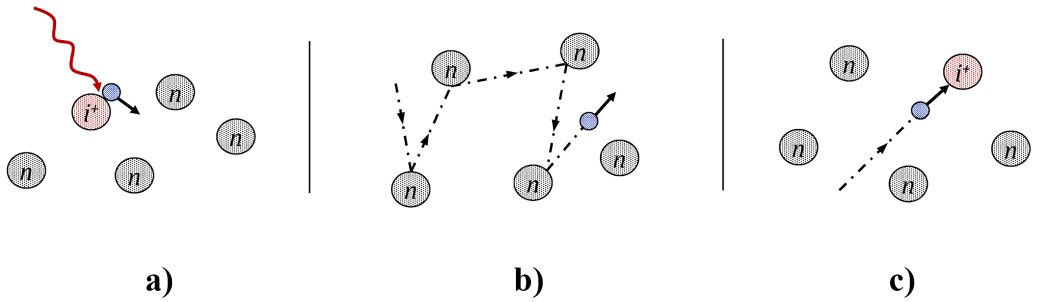

Figure 2.3: The life cycle of electrons: (a) a neutral atom is ionized by some source (red arrow), accelerating an electron (blue); (b) The electron collides with many neutral atoms which "moderate" its energy; (c) the electron collides with an ion and recombines.

This process is analogous to the energy moderation of neutrons used in nuclear fission reactors: in these devices, fast neutrons collide with heavier molecules, such as water or graphite, which "moderate" the kinetic energy of the neutrons and bring them towards a colder thermal distribution before entering a reactor. [50] Similarly, newly-ionized electrons can be modeled

undergoing energy "moderation" through collisions with cold neutrals before recombination. At any given moment, the plasma contains both "new" electrons at high energy and a range of other electrons at intermediate stages of the moderation process. The energy distribution then depends on the processes and rates of ionization, recombination, and electron-neutral collisions.

In each elastic collision between electrons and neutrals, assuming that monatomic neutral atoms are at a constant energy kT_n and that neutral mass $M >> m_e$, the change in electron kinetic energy per collision is estimated by:

$$\Delta w = -\frac{4M/m_e}{(1+M/m_e)^2}(w - kT_n) \approx -4\frac{m_e}{M}(w - kT_n). \tag{2.27}$$

The number of collisions in a time interval dt is dt/t_{en} where t_{en} is the electron-neutral collision time. The change of electron energy dw in the time interval dt is therefore:

$$dw \approx -4(w - kT_n)\frac{m_e}{M}\frac{dt}{t_{en}}. \tag{2.28}$$

The electron-neutral collision time is related to the mean free path of electrons, such that $v_e t_{en} = l_{mfp}$, where v_e is the electron velocity and l_{mfp} is the mean free path for electron-neutral collisions. The mean free path is related to the neutral number density n_n and the cross section for electron-neutral collisions σ_n, as follows:

$$l_{mfp} n_n \sigma_n = 1. \tag{2.29}$$

Using $v_e = \sqrt{2w/m_e}$, these relations can be used to substitute for t_{en} in equation 2 to obtain

$$\frac{dw}{dt} = -4\sqrt{\frac{2}{m_e}}\frac{m_e}{M}\sigma_n n_n (w^{3/2} - kT_n w^{1/2}). \tag{2.30}$$

Integrating from 0 to t and solving for w(t) gives,

$$w(t) = kT_n \tanh\left[2\sigma_n n_n \frac{\sqrt{2m_e kT_n}}{M} t + \tanh^{-1}\sqrt{\frac{w(0)}{kT_n}}\right]^2. \tag{2.31}$$

Equation 2.31 is plotted in Fig. 2.4. At t = 0, the electron is at its initial energy, $w(0)$, and energy decreases with time due to collisions.

This elastic model is appropriate for an atomic gas such as helium; for molecular gasses, the cooling rate is enhanced by rotational and vibrational

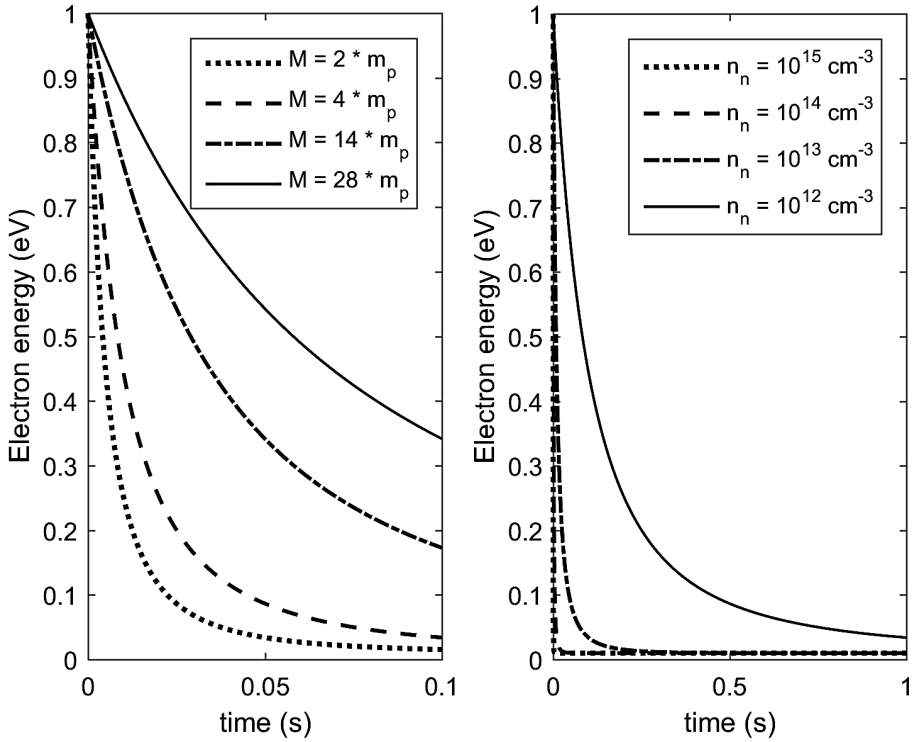

Figure 2.4: Time-evolution of the kinetic energy of a single electron. a) neutral atomic mass varying from 2 to 28 m_p (proton mass); neutral density fixed at 10^{13} cm^{-3}. b) neutral density varying from $10^{12} - 10^{15}$ cm^{-3}; atomic mass of 4 m_p. In all cases, initial energy $w(0)$ = 1 eV; target neutral particles have cross-sectional radius of 1 Å.

effects. In a molecular gas, energy drop per elastic collision, $4m_e/M$, is generalized to an overall cooling coefficient which is in general dependent on temperature. Studies by Huxley [51] and Smith & Dean [52] show that in inelastic collisions with molecular hydrogen, N_2, and O_2, electron cooling rates are larger by 2 to 4 times over their expected elastic cooling rates. The effect of inelastic collisions on the cooling curve (Eqn. 2.31) is therefore equivalent to the effect of decreasing the neutral mass by a factor of 2-4. As shown in Fig. 2.4a), reducing the mass causes the electron to lose its energy more quickly.

Ionization and recombination conditions

The initial energy of an electron produced by photoionization is the difference between the energy of the ionizing radiation and the ionization energy E_{iz} of

the neutral gas species. All free electrons ionized from a given gas species by a photon with a specific frequency ω thus have the same initial energy [53]:

$$w(0) = \hbar\omega - E_{iz}. \tag{2.32}$$

While in principle there is a broad spectrum of incoming ionizing radiation, and several neutral species in the gas, there are typically certain pathways that dominate electron production in any given situation. For example, electron production in the mesosphere is almost solely from ionization of nitric oxide by solar Lyman-α, which produce electrons at 1.1 eV [54]. While ionization of other molecules by other parts of the solar spectrum do occur, their contribution is orders of magnitude smaller. Typical solar system dusty plasmas, meanwhile, are mainly ionized by a few dominant H and He lines in the EUV range of the solar spectrum [55]. As these EUV solar lines generally decrease in strength for higher photon energy, [56] most neutrals are ionized with the lowest-energy line capable of doing so. This causes electrons to have a fairly uniform initial energy at ionization in the range of 1-2 eV.

In charge equilibrium, ionization and recombination occur at equal rates; the left-hand side of equation 2.15 is thus zero. Neglecting photoemission from the grain, as dust densities are typically much lower than neutral densities [10, 40, 54] and photoelectric yields are low [57], we approximate $Q_e = Q_i$ and $D_e n_e = D_i n_i$. The electron density is then given by:

$$n_e = \frac{Q_e}{\alpha n_i + D_e n_d} \equiv Q_e \tau_R. \tag{2.33}$$

Therefore, the electron density is proportional to the average lifetime of electrons in the plasma. Electron-ion recombination becomes more likely as energy is moderated, as α typically increases as energy drops in the < 1 eV range [58]. Meanwhile, the highest-energy electrons are more likely to be absorbed by dust grains, as negatively-charged dust easily repel slow electrons.

Analytical solution for the electron distribution

The energy evolution of an average electron is now completely defined by equation 2.31, electron production rate Q_e, initial energy $w(0)$, and recombination time τ_R. The fraction of the whole electron population with energy

between w and $w + dw$ is defined as $f(w)dw$, and is proportional to the time spent by a single electron in that range.

This electron energy distribution must also be multiplied by the probability $p(w)$ that an electron has *not* recombined before reaching an energy w. In general, the average electron will recombine after some lifetime τ_R, with a spread of lifetimes between different electrons given by $p(w)$. Thus, the electron energy distribution is given by:

$$f(w) = Ap(w) / \left| \frac{dw}{dt} \right|, \tag{2.34}$$

where $p(w)$ is the probability that an electron reaches an energy w without recombining, and A is a normalization factor.

The probability that a single electron recombines in some time step dt depends on the recombination cross-section, the electron velocity, and the density of ions it can recombine with. The functional form of $p(w)$ depends on the energy dependence of the recombination cross-section which increases quickly at low energy ($\sigma_R \sim 1/w$. The spread in electron lifetimes is therefore small in these plasmas, and thus we assume for simplicity that all electrons recombine upon reaching an energy $w(\tau_R)$. The probability $p(w)$ of *not* recombining can be approximated as 1 for energies between $w(\tau_R)$ and $w(0)$, and zero at energies below $w(\tau_R)$.

The normalization factor A must now be calculated, such that the integral of the distribution over all energies evaluates to unity:

$$1 = \int_0^{w(0)} f(w)dw = \int_{kT_n}^{w(0)} A \frac{p(w)}{|dw/dt|} dw. \tag{2.35}$$

When all electrons are taken to recombine after τ_R, the normalization coefficient is:

$$A = \frac{1}{\int_{w(\tau_R)}^{w(0)} \frac{dw}{|dw/dt|}} = -\frac{1}{\int_0^{\tau_R} \frac{1}{|dw/dt|} \frac{dw}{dt} dt} = \frac{1}{\int_0^{\tau_R} dt} = \frac{1}{\tau_R}. \tag{2.36}$$

Therefore, the electron energy distribution is expressed as follows:

$$f(w) = \frac{M}{4\tau_R \sqrt{2m_e} \sigma_n n_n} \frac{1}{w^{3/2} - kT_n w^{1/2}}. \tag{2.37}$$

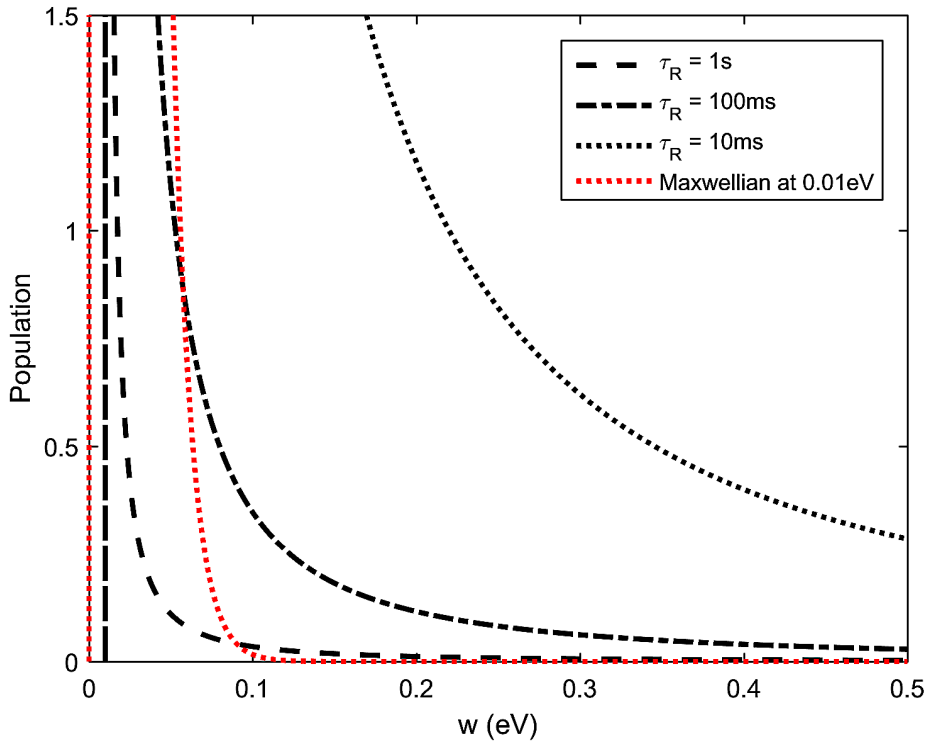

Figure 2.5: Electron energy distributions for various recombination times. Low-temperature Maxwellian (red dotted line) is at 0.01 eV. Target neutral particles have cross-sectional radius of 1 Å; neutral density is 10^{14} cm^{-3}, neutral atoms have mass $M = 4 * m_{proton}$, and initial electron energy $w(0)$ is 1 eV.

$f(w)$ is plotted in Figure 2.5 for lifetimes of 0.05, 0.1, and 1 seconds at a plasma parameters common to planetary and astrophysical environments. This is compared to a Maxwellian distribution at a temperature of 0.01 eV, expected if electrons were in thermal equilibrium with the neutrals. It is clear that the high-energy tail of the distribution is much larger than the Maxwellian tail. As recombination time increases, more electrons will reach low energies; however, the high-energy tail remains larger than Maxwellian. The Maxwellian tail trends towards zero at an exponentially faster rate, showing the moderation model will always have a larger hot tail than the Maxwellian distribution predicts.

Implications on charge equilibrium

The effect of this electron distribution on grain charge can be calculated using OML theory by inserting the electron distribution into equation 2.4 while assuming Maxwellian ions. For an arbitrary distribution, $f_e(w) = n_e g(w)$, the equilibrium condition ($I_i + I_e = 0$) can be written as:

$$\frac{2n_i}{\sqrt{\pi}}\sqrt{\frac{kT_i}{M}}(1+\psi) = \frac{n_e}{\sqrt{m_e}}\int_{kT_i\psi}^{\infty}(1-\psi\frac{kT_i}{w})\sqrt{w}g(w)dw. \tag{2.38}$$

Following the same methodology used in Section 2.1, Eqn. 2.38 is solved in terms for H as a function of ψ,

$$H(\psi) = 1 - \frac{\sqrt{m_e/M}(1+\psi)}{\frac{\sqrt{\pi}}{2}\int_{kT_i\psi}^{\infty}\sqrt{\frac{w}{kT_i}}(1-\psi\frac{kT_i}{w})g(w)dw}. \tag{2.39}$$

The electron distribution calculated in equation 2.37 is used for $g(w)$ in Eq. 2.39, which approximates the probabilistic collision process. As this distribution applies over the energy range $w \in [w(\tau_R), w(0)]$, the upper boundary of the integral in the denominator of equation 2.39 is decreased from infinity to $w(0)$. The lower boundary, $w = kT_i\psi$, is usually larger than $w(\tau_R)$, but care must be taken when dealing with very short recombination times. Solving results in the parameter curve:

$$H(\psi) = 1 - \frac{\sqrt{m_e/M}(1+\psi)}{\sqrt{\frac{\pi}{2m_e kT_i}}\frac{M}{8\tau_R\sigma_n n_n}\left(\psi\ln\frac{w(0)}{kT_i\psi} + (1-\psi)\ln\frac{w(0)/kT_i - 1}{\psi - 1}\right)}. \tag{2.40}$$

This curve is plotted in Figure 2.6, compared to a Maxwellian case with $T_e = T_i$. As the knee occurs at significantly higher ψ as recombination time drops, we conclude that a small fraction of hot electrons significantly affects the shape of the curve. This shows that the distribution's greater high-energy tail dominates the charging process.

In summary, we find that non-thermal electron populations are intrinsic to photoionized plasmas, become more significant when electron lifetime is short. Importantly, even small populations of hot electrons have a strong effect on dust grain charging, as hot electrons more frequently intercept grains— assuming a Maxwellian, thermal distribution of electrons thus will always underestimate dust grain charge.

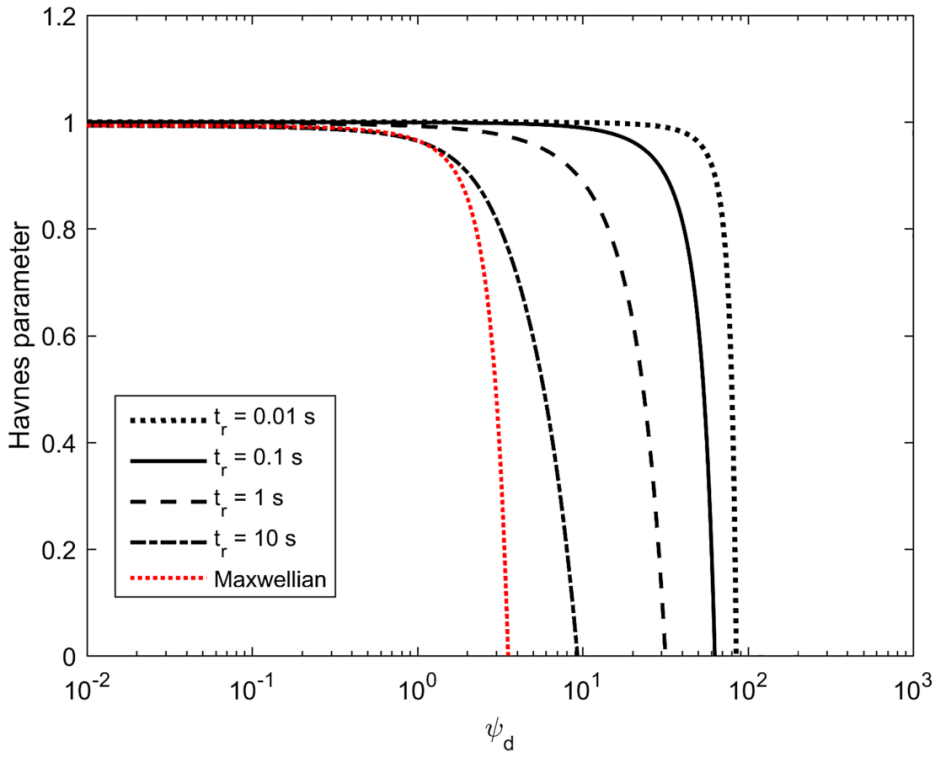

Figure 2.6: Parameter curve $H(\psi)$ for the calculated distribution of a weakly-ionized plasma at four recombination times, for $n_n = 10^{12}$ cm^{-3}, initial energy $w(0) = 1$ eV, and atomic helium gas at 0.01 eV.

2.4 Monte Carlo charging simulation with nonthermal electrons

The OML approach does not explicitly treat dust charge as discrete, and assumes that all grains have the same charge, it breaks down as Z_d approaches 1. When Z_d is large, as the spread of the charge distribution is small compared to the average value, and the effect of discretization is minor. In this section, I validate the model by comparing it to a numerical simulation of the plasma.

A Monte Carlo method is used to model a population of electrons, ions and dust grains of a given size, in which individual electrons are created at initial energy $w(0)$, cool over time through neutral collisions according to Eqn. 2.31, and eventually recombine with ions or dust grains. At each timestep in the simulation, the probability is computed for an electron colliding with an ion or a dust grain, and each electron is either chosen to recombine or remain, based on these probabilities. After a sufficient number of iterations,

the simulation reaches a steady-state electron and ion densities and yields equilibrium distributions of electron energies and dust charges.

Methodology

The simulation methodology is as follows:

1. A control volume the size of 1 cm^3 is considered, containing an arbitrary number N_e of electrons, each at initial energy w_0. An equal number of ions is initialized, as well as N_d dust particles of radius r_d.
2. In a small timestep Δt, each electron has its energy decreased by $\Delta w(w)$, calculated from Eqn. 2.28.
3. For each electron, the probability of a collision with an ion, a neutral dust grain, and a dust grain of any charge, are calculated. These are dependent on electron energy.
4. A random number between 0 and 1 is generated. Depending on the value, it is chosen based on calculated probabilities whether each electron recombines with an ion, a dust grain, or remains in the plasma.
5. If the electron collides with an ion, it is removed from the simulation, and both N_e and N_i are decreased by 1.
6. If the electron collides with a dust particle of charge Z_d, the electron is removed from the simulation, and N_e is decreased. The number of dust particles with a charge Z_d is decreased by 1, and the number of grains with $Z_d + 1$ is increased.
7. The probability of ions colliding with dust grains is calculated, and a corresponding proportion of them are subtracted from N_i. The charge number of incident dust particles is decreased.
8. A number $Q * dt$ electrons at $w(0)$ and ions are added to simulate photoionization.

This process is repeated for a large number of time steps, until N_i and N_e reach equilibrium values that cause the recombination rate to balance the production rate. At this point, the electron energy and dust charge distributions are also in steady state.

Numerical electron distributions

The steady state electron distribution depends on the competition between three rates, namely the rate of electron-neutral collisions, the rate of electron production, and the rate of electron removal. As neutral density is typically far greater than plasma or grain density, the electron-neutral collision rate is orders of magnitude larger than the rest. By defining a characteristic electron-neutral collision time $t_{en} = 1/\sigma_n n_n \sqrt{2w/m_e}$, Eqn. 2.31 can be rewritten in terms of the number of electron-neutral collisions $x = t/t_{en}$. This form, independent of neutral density and cross-section, is plotted in Fig. 2.7.

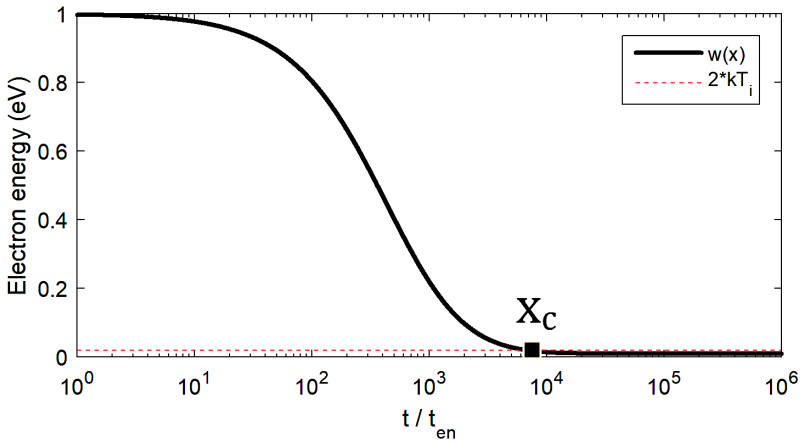

Figure 2.7: Decrease of single electron energy with number of collisions. Intersection point of $w(x)$ with $2 * kT_i$ defines the critical number of collisions x_c for each electron to cool. In this plot, $w(0) = 1$eV, $kT_i = 0.01$eV, and energy transfer per collision is that of molecular nitrogen. For these values, $x_c \approx 7500$.

The electron energy decays through neutral collisions until asymptotically reaching the neutral temperature. We define a critical number of collisions x_c in which electron energy has cooled to twice the neutral temperature. This critical collision number is compared to the rates of recombination. If most electrons undergo x_c collisions before recombining ($\tau_R/t_{en} > x_c$), there will be a bulk of cold electrons in the plasma. If most electrons recombine before cooling ($\tau_R/t_{en} < x_c$), electrons will remain much hotter than the neutrals. If the electron recombination is comparable to the cooling time ($\tau_R/t_{en} \sim x_c$), the energy distribution will contain both a cold bulk and a significant high-energy tail. Resulting electron distributions for each of these cases are shown in Fig. 2.8.

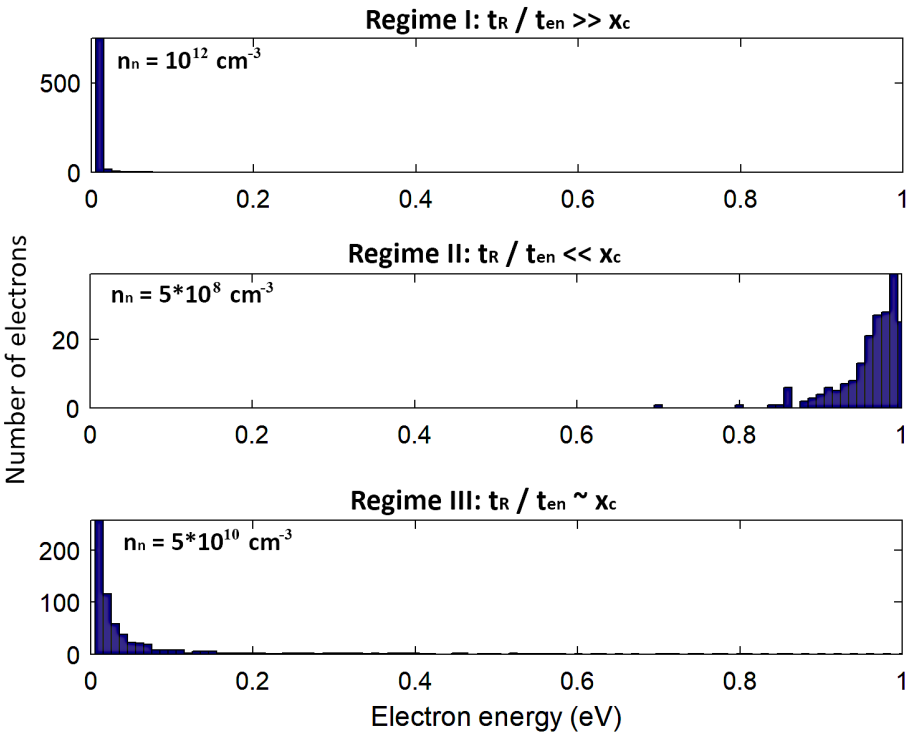

Figure 2.8: Computed electron distributions for each of three regimes. All simulations had $n_d = 1000$ cm^{-3}, $r_d = 10$ nm, neutrals corresponding with molecular nitrogen. Neutral density is varied by 4 orders of magnitude to reach various regimes.

In each of the three cases, different behavior can happen depending on if the electron production rate is large or small compared to the cooling rate. If electrons are produced more quickly than they cool, there can be a small population of hot electrons even with long recombination time. If electrons are not produced so quickly, the energetic tail will be mostly empty, and will have minimal effect on the dust.

Simulated dust charge distributions

When dust grains are charged to surface potentials such that $e\phi > w$, where w is the energy of an incoming electron, that electron will be repelled. Therefore, high-energy electrons can approach grains of higher charge. Therefore, it is expected that these high-energy tails in the electron distribution allow some grains to reach larger charges than expected for a cold Maxwellian electron population.

Fig. 2.9 shows the number of dust grains at various charges in four different simulations. The horizontal axis corresponds to the charge number Z_d on each charged particle, and the vertical axis shows the number of dust particles with that charge. The total number of dust particles in this simulation was 1000. In Fig. 2.9a), all electrons were created and remained at neutral temperature for all time. Fig. 2.9b), c), and d), are the distributions when electrons are created at high energy and cool, each with different neutral densities; these have the same parameters as those used in cases I, II, and III in Fig. 2.8.

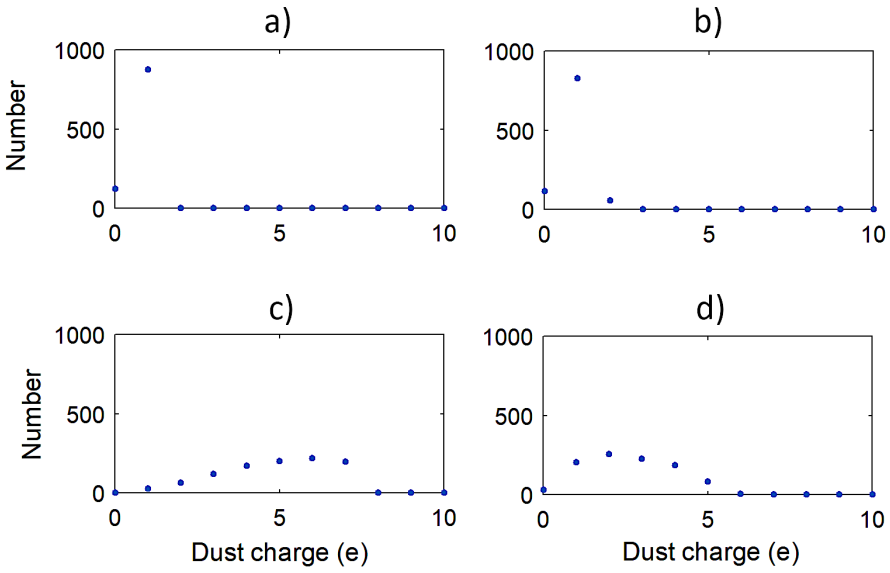

Figure 2.9: Computed distributions of dust charge for each of four cases. In a), all electrons at kT_i for all time. In b), c), and d), electrons are created at 1 eV and cool through collisions with neutrals at densities $n_n = 10^{12}$, $5 * 10^8$, and $5 * 10^8$ cm^{-3}, respectively. All simulations had $N_d = 1000$, $r_d = 10$ nm, and neutrals corresponding with molecular nitrogen.

Fig. 2.9b) corresponds to the case when electrons cool more quickly than they recombine. In comparison to 2.9a), the charge distribution is very similar; this is expected, as electrons only spend a tiny fraction of their lifetimes at energies above neutral temperature. However, a fraction of dust grains in case b) are doubly-charged, while case a) only allows singly-charged grains. This shows that even though nearly all electrons are cold, high-energy tail still allows some greater amount of dust charging.

Table 2.1: Comparison between results of simulation and analytical calculation, for the three cases in Fig. 2.8: (a) $n_n = 10^{12}$, (b) $n_n = 5 * 10^8$, and (c) $n_n = 5 * 10^{10}$ cm^{-3}. Dust has $r_d = 10$nm, n_d = 1000 cm^{-3}.

	H	ψ	$Z_{d,avg}$	n_e (cm^{-3})	n_i (cm^{-3})
Simulation (a)	0.46	15.40	1.07	1260	2330
Analytical (a)	0.34	14.39	1.00	1956	2956
Simulation (b)	0.96	70.04	4.86	185	5054
Analytical (b)	1.00	38.90	2.70	0.01	2703
Simulation (c)	0.73	37.49	2.61	924	3530
Analytical (c)	0.49	20.45	1.42	1470	2891

Fig. 2.9c) shows the charge developed when electrons do not cool much below 1 eV; here, the peak of the charge distribution is at $Z_d = 6$. As x_c is large, (e.g., 7500 in the case of Fig. 2.7), these plasmas are still very collisional, despite the considerable role played by a non-thermal tail of electrons. In Figure 2.9d), the dust grains have a distribution of charges ranging from $Z_d = 1$ to 5; this is the charge developed by electrons in the distribution shown in Fig. 2.8, regime III. Most electrons are still cold, but there is a larger hot tail, and this can increase the charge on dust five-fold.

Properties calculated from the simulations shown in Fig. 2.8 are compared to the properties calculated analytically from the same input conditions in Table 2.1. While the simplifications of the analytical model cause some divergence between the simulation and the analytical method, both show the same effect of the energetic tail on equilibrium values of ψ and H. It is noteworthy that $Z_d \sim 1$ in these cases, so OML is beyond its limits of applicability; we observe that it *underestimates* the average dust charge by neglecting charge discretization.

2.5 Model limits and applications to nature

Our model relies on several simplifying assumptions. We neglect photoemission from dust grains, assume electrons are produced at a single initial energy and recombine on a fixed timescale, treat electron cooling as purely elastic, and use OML theory for isolated grains. The applicability of these assumptions depends on the environment; Table 2.2 lists representative parameters for terrestrial and astrophysical dusty plasmas to provide context for evaluating model validity.

Table 2.2: Typical dusty plasma properties in a range of planetary and space environments. These are nominal parameters, and in general, all these plasmas have substantial ranges of parameters. Electron temperatures are based on average measured or predicted energies, and ignore non-Maxwellian effects.

	Neutral density (cm^{-3})	Plasma density (cm^{-3})	Grain density (cm^{-3})	Grain diameter (μm)	Neutral temperature (eV)	Electron temperature (eV)	Charge number (e)	Neutral gases
Comet tail	10^8–10^9	10^2–10^3	···	0.1–1	0.01	0.01	···	H_2O
Saturn's AB ring	10^3	40	10^{-2}	1	0.01	5	10^3	O, H_2O, O_2
Saturn's G ring	10^3	10	10^{-7}	1	0.01	1	10^3	O, H_2O, O_2
Molecular clouds	10^6	1	$<10^{-3}$	0.1	0.0001	1	100	H_2, He
Protoplanetary disk	10^{14}	10^2	10^{-9}–10^6	0.01–1000	0.01	0.01	1–10^4	H, He
Noctilucent clouds	10^{14}	4000	0–1000	10^{-3}–10^{-1}	0.01	0.01	1	N_2, O_2
Pluto's aerosols	10^{13}	10^2–10^3	10^6	0.01–100	0.01	0.005–0.01	1–10^3	N_2

Analytical and numerical treatments both assumed constant initial electron energy $w(0)$ and recombination timescale τ_R. This is reasonable in many solar system palsmas, as ionization is driven by discrete peaks in the solar UV spectrum. In molecular clouds, however, ionization is dominated by cosmic rays with a broad energy distribution, so a spread of initial energies must be included [11]. Similarly, a distribution of τ_R could be applied to simulate probabilistic recombination; this is discussed in the appendix of Nicolov & Bellan [39].

OML theory breaks down when grains interact strongly. This occurs if the spacing between grains is smaller than the Debye length [59], and electrons can become bound interstitially within a grain lattice [32]. Such conditions can occur when plasma density is lower than dust density, as in Pluto's atmosphere [60] and in the dustiest regions of protoplanetary disks [12].

Application to several natural dusty plasmas

Different plasmas cool to different extents: as shown through the Monte Carlo simulation, some have well-thermalized electrons, some remain quite hot, and some become mostly-thermal, but with a significant high-energy tail to the electron distribution. The electrons in Saturn's rings, for example, have been shown to be hotter [10]; as neutral density is low, electrons do not fully cool before recombining. Noctilucent clouds, comet tails, and protoplanetary disks, meanwhile, are typically assumed to have electrons and neutrals at

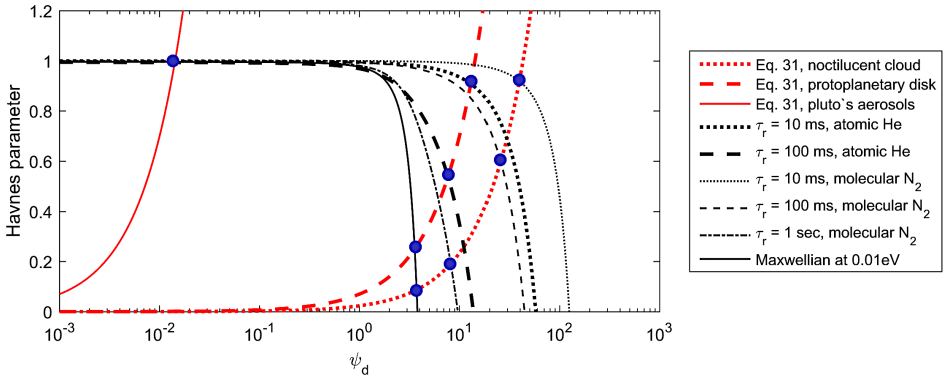

Figure 2.10: Black downsloping lines are from Eq.2.39 for four cases using the electron moderation model and for a maxwellian electron distribution; red upsloping lines are for typical noctilucent clouds ($r_d = 0.01\mu$m, $n_d = 1000$ cm^{-3}, $n_i = 4000$ cm^{-3}), protoplanetary disks ($r_d = 1\mu$m, $n_d = 1$ cm^{-3}, $n_i = 100$ cm^{-3}), and Pluto's aerosols ($r_d = 0.01\mu$m, $n_d = 10^6$ cm^{-3}, $n_i = 10^3$ cm^{-3}). All cases have neutral density of 10^{14} cm^{-3} and neutral temperature 0.01 K. Intersections of upsloping and downsloping lines shown as filled blue circles give equilibrium values of H and ψ for the specific configuration.

similar cold temperatures due to their collisionality; however this does not necessarily imply that the energetic electron tail can be neglected.

To illustrate, I here apply the analytical approach of Sec. 2.3 to noctilucent clouds, protoplanetary disks, and Pluto's aerosols: three plasmas with comparable neutral densities, temperatures, and ionization fractions. Fig. 2.10 shows Eq. 2.39 for various recombination times, as well as the curve predicted by a Maxwellian distribution. The relation from Eqn. 2.12 is plotted for the known dust densities and sizes in each environment. Intersection points between the two relations are highlighted in blue. A stronger hot tail shifts the curves, leading to higher dust charge and greater electron depletion than predicted by a purely Maxwellian distribution.

Equilibrium values vary strongly with environment. In Pluto's atmosphere, the extremely high aerosol density causes nearly complete electron removal: $H \to 1$ while ψ remains small. In contrast, noctilucent clouds and protoplanetary disks show strong sensitivity to the electron energy distribution. In the mesosphere, meanwhile, charged ice particles produce pronounced "bite-outs" in electron density of up to an order of magnitude [7, 61], consistent with a large Havnes parameter. Grains of 10-20 nm at $\sim 10^3$ cm^{-3} efficiently

capture electrons, while larger grains during cloud events are rarer and can become positively charged by photoemission [7, 42].

For typical noctilucent cloud conditions, OML predicts $H = 0.1 - 0.9$ and $\psi = 4 - 40$, depending on recombination time. Photoionization of NO produces electrons, while slow NO^+ recombination ($\alpha = 10^{-7} - 10^{-5}$ cm^3 s^{-1} [42]) gives lifetimes of tens of seconds to minutes. Monte Carlo simulations, meanwhile, calculate grains with $\psi = 12.6$, thus an average charge of $Z_d = 0.88$, yielding $H = 0.42$ and substantial electron depletion. By comparison, the aerosol charging model of Parthasarathy [43], applied by Rapp & Lübken [42], gave $H = 0.33$ and $\psi = 14.4$ (average $Z_d = 1$). Our model thus predicts stronger electron and ion depletion, attributed to the enhanced collision probabilities of the hot electron tail, which better explains the large observed bite-outs in the polar mesosphere during noctilucent cloud events.

In protoplanetary disks, grain sizes and densities span wide ranges, leading to large variations in electron lifetime and charge distribution. Without dust, electron lifetime is set by electron–ion collisions, with $\tau_{ei} \sim 1$ hour under typical conditions (Eqn. 2.2), so only a small hot electron population is sustained. With dust present, electron–dust collisions reduce the lifetime to ~ 5 s, enhancing the hot tail and raising both H and ψ (Eq. 2.33). As disks evolve, neutral, plasma, and dust densities change, altering electron cooling rates and energy distributions. Dust growth increases electron capture cross-sections, producing higher grain charging and deeper depletion of electrons and ions. These effects directly influence dust coagulation [11] and mass accretion rates [62], with measurable consequences for the dynamics and observable properties of protoplanetary disks.

Taken together, these cases illustrate how hot electrons shape dusty plasmas across diverse regimes: near-complete depletion in Pluto's atmosphere, measurable bite-outs in the mesosphere, and evolving charge dynamics in protoplanetary disks. The model therefore captures both terrestrial and astrophysical environments where non-Maxwellian electron populations play a decisive role.

Chapter conclusions and outlook

Through both OML-based analytical calculations and statistical Monte-Carlo simulations, I conclude that non-thermal electron populations have signif-

icant effects on acquired dust charge. I show that these effects are most pronounced when the electron lifetime is short, but notable even when these non-thermal electron populations are quite small. Modeling electron production and thermalization to obtain an electron energy distribution *in tandem with* calculating charge equilibrium (e.g., with the standard methodology of Section 2.1) can enhance charging models by significant amounts, $\sim 25\%$ in the case of mesospheric clouds.

Furthermore, the contents of this chapter provide a way forward for calculating the charge balance within dusty plasmas with arbitrary ion and electron distributions, and is easily extendable to non-spherical grains through adjusting grain capacitance. This is especially important to laboratory plasma discharges including our Ice Dusty Plasma Experiment, in which particles grow and agglomerate in unusual shapes, bathed in a highly-non-thermal electron population caused by nonlinear RF heating.

Chapter 3

THE ICE DUSTY PLASMA EXPERIMENT AT CALTECH

The Ice Dusty Plasma Experiment is designed to maintain a plasma at cryogenic temperatures that can synthesize and confine ice grains. The device described in this chapter, designed by Prof. Bellan and constructed by myself, is the second iteration of this experiment at Caltech and a significant upgrade from the device operated through the 2010s [34]. This chapter details the system's design, construction, working principles, and operation.

3.1 History and conception

Ice-dusty plasma research at Caltech began from a series of research in noctilucent clouds, made of ice particulates that form in the weakly-ionized mesosphere in certain seasons. While most models concerning these clouds assume that the ice grains are spheres, Prof. Bellan argued that electric charging would cause the ice to become decidedly non-spherical due to anisotropies introduced by electric fields [25].

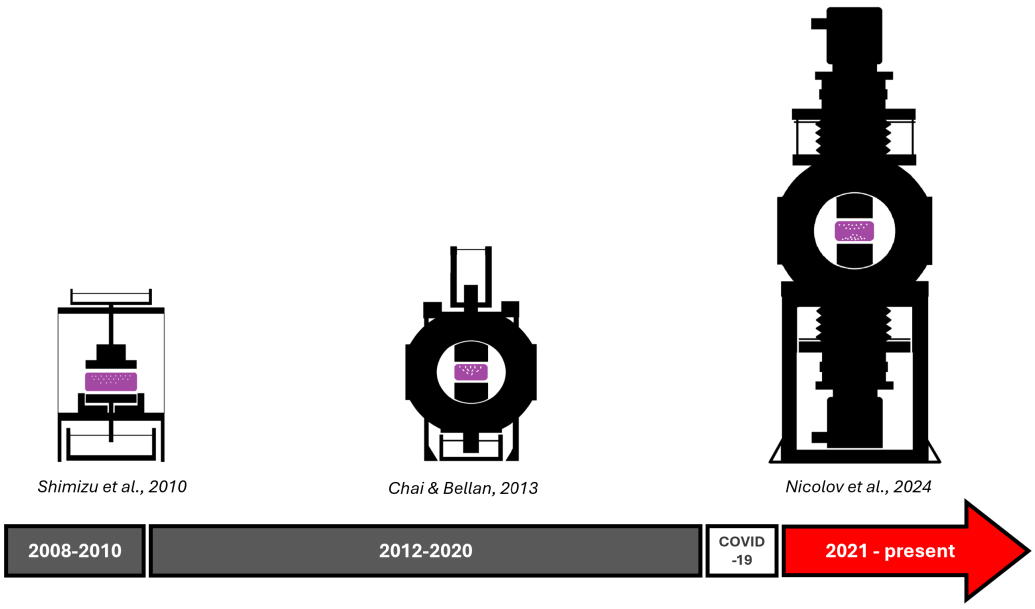

Figure 3.1: A timeline of ice dusty plasma experiments.

The first ice-dusty plasma experiment was conducted at the *Max Planck Institut für Extraterrestrische Physik* by Shimizu *et al.* [29], in which a radio-frequency (RF) plasma was produced from oxygen and deuterium. The electrodes were cooled by baths of liquid nitrogen (LN2), and upon ionization, particulates of heavy water (D_2O) ice spontaneously nucleated and levitated within the plasma.

Professor Bellan became interested in this experiment for studying ice grain morphology and supervised construction of a comparable device at Caltech— the "Mk. I" Ice-Dusty Plasma Experiment— which was primarily built by then-postdoc Dr. KB Chai. This device differed in that it formed ice by injected vapor into a plasma of *any* gas composition, rather than relying on gas-phase chemistry[1] [34]. In the eight years that the *Mk. I* device was operational, it was used to show that the ice grains were indeed highly aspherical [34], growing in dendritic structures to hundreds of microns through electically-enhanced vapor deposition [24, 63].

Both previous experiments, at the Max Planck Institute and at Caltech, maintained cryogenic temperatures by thermal contact between the electrodes and LN2 baths. The ice temperature was thus fixed around 170 K [64], arbitrarily above the LN2's boiling temperature of 77 K due to inefficiencies in heat transfer from the gas, through the electrodes, to the liquid nitrogen. This posed severe limitations, as the properties and formation mechanisms of ice can change drastically with the system temperature.

Precise temperature control is critical to extrapolating results to astrophysical systems. As demonstrated in recent years by numerous studies on astrophysical ice films formed in the laboratory [2], such as those by astrophysical ice expert Dr. Murthy Gudipati at NASA-JPL [22, 28], the phase structure, properties, and surface interactions of ice is extremely dependent on its temperature *history*.

To enable independent, precise temperature control of each electrode, Prof. Bellan designed a massive experimental upgrade. This "Mk. II" Ice Dusty Plasma Experiment employed technology developed over the previous decade of ice-dusty plasma research, and incorporated cryogenic techniques drawn from ice film experiments, developed in collaboration with Dr. Gudipati. I constructed this new apparatus in the first years my PhD, and though

[1] A much safer approach— $D_2 + O_2 \rightarrow D_2O$ is a combustion reaction.

progress was significantly delayed by the COVID-19 pandemic, a host of geopolitical events,[2] and the unyielding procession of Murphy's law, the Ice Dusty Plasma Experiment *Mk. II* has been fully operational since autumn of 2022.

3.2 Experimental design

A schematic of the new Ice-Dusty Plasma Experiment is shown in Figure 3.2. The main vacuum chamber is evacuated with a turbomolecular pump. During operation, the chamber is filled to a constant low pressure (typically $100 - 1000$ mTorr) with a background gas, typically argon or hydrogen.

Parallel-plate electrodes, mounted to the top and bottom of the chamber and adjustable in spacing, are driven by a radio-frequency (RF) voltage, of a couple hundred volts peak-to-peak, which causes gas breakdown and sustains a capacitively-coupled plasma (CCP) with an ionization fraction of about 10^{-6} ions per neutral gas molecule. The system operates at a standard frequency of 13.56 MHz; nothing about this frequency is particularly special, but it is an RF band allocated to Industrial, Scientific and Medical (ISM) applications by government regulations.

Each of the copper parallel-plate electrodes are mounted on a cold head of a cryogenic cooler, which provides continuous unregulated cooling. Embedded in the electrodes are temperature-sensitive silicon diodes and resistive heater cartridges, which are managed by a feedback control system to maintain steady, controllable temperatures between 50 and 250 K. The background gas cools due to contact with the cryogenic electrodes; the weakly-ionized plasma thus contains cold neutrals and ions; electrons, heated by the RF electric fields, maintain high energies of 1-2 eV.

A small flow of water vapor is injected into to the cryogenic plasma. On contact, the vapor cools and spontaneously nucleates into microscopic ice grains. The grains are well-confined, floating in the positive potential of the plasma, and grow over time.

[2] perhaps most critically, the 2021 Suez Canal Blockage Incident which crashed the semiconductor supply chain.

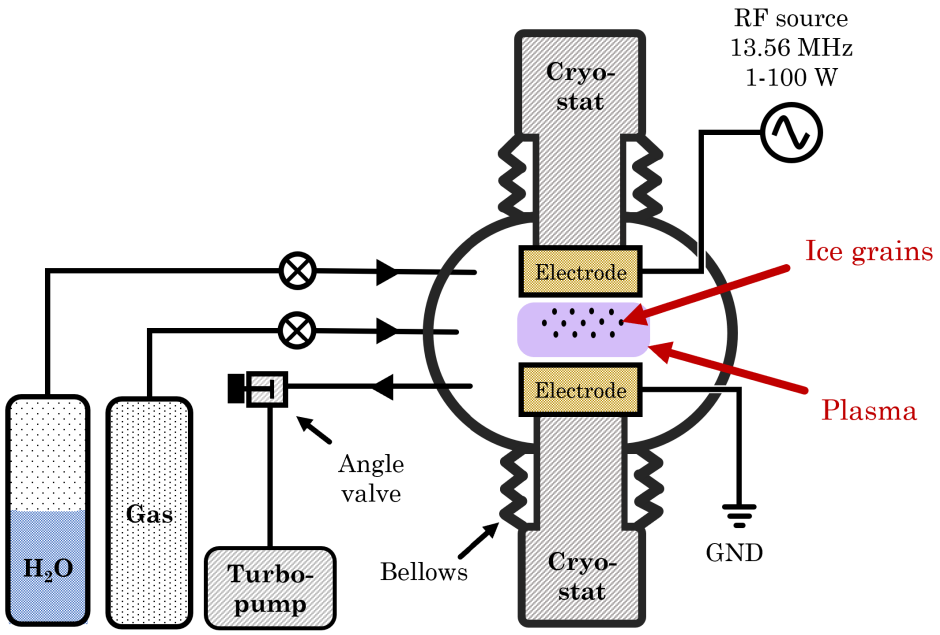

Figure 3.2: Schematic of the Ice Dusty Plasma Experiment at Caltech [1]

.

Mechanical design

When I joined Caltech in September of 2019, Prof. Bellan had already designed the blueprint for the experiment's upgrade. The design incorporates several new features— a mechanism for adjusting the electrodes under vacuum, mounting for the cryogenic coolers, electrical feedthroughs for the temperature control circuitry and the RF power input, and a new electrode design that incorporated the cryogenic system and allowed more flexibility in RF power configuration. Figure 3.3a shows a CAD model, created by Prof. Bellan, with the components labeled.

The main vacuum chamber, a 3.8-liter stainless steel chamber with 8-inch inner diameter, is supported by a frame built from 80-20 beams secured to an optical table. The whole apparatus stands about 1 meter high off the table.

Vacuum bellows are mounted on the top and bottom 8-inch Conflat flanges of the main chamber. The bellows are capable of expanding and contracting under vacuum, adjustable under vacuum by a mechanism of gears, lead screws, and a bicycle chain, illustrated in Fig. 3.3 b.

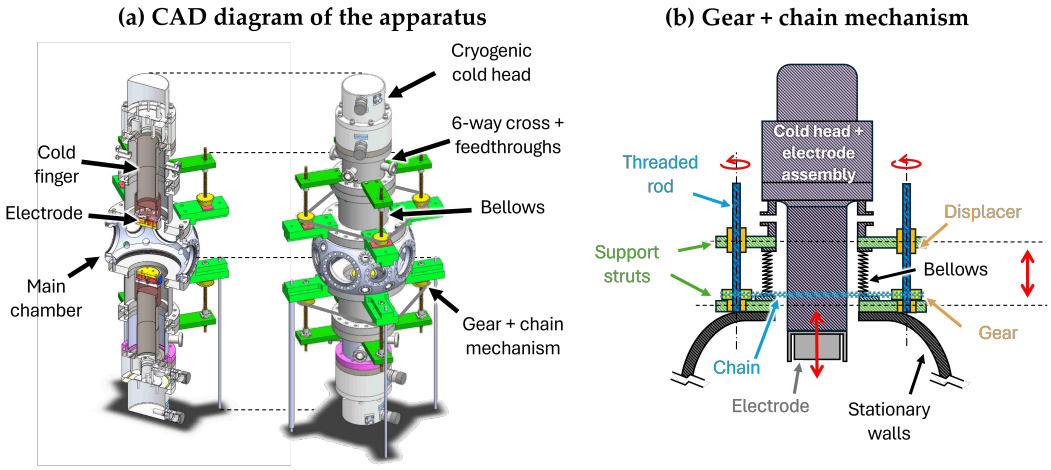

Figure 3.3: Experiment design: (a) CAD model of the device, created by Prof. Paul Bellan, with major components labeled; (b) diagram of the gear-chain mechanism for adjusting the electrode. Cryostat-electrode assembly (purple) moves up and down as the bellows extend and contract.

Mounted to the opposite side of each bellows are 6-way crosses which contain the electrical feedthroughs for each electrode's cryostat and RF power connections. Each cryogenic cold head is mounted to the far side of the cross, with a cold finger that runs down the center of the cross and bellows, reaching into the main chamber. The electrodes are mounted to the inner face of the cold fingers. Extending or contracting the bellows therefore translates the electrodes up or down, adjusting their spacing without breaking vacuum.

Assembling and testing this mechanical system was the first challenge of the build: the displacers, rods, and chain had to be robust enough to extend the bellows against atmospheric pressure, while nimble enough to be adjusted by hand.

Electrode design

The electrodes serve the dual purpose of both powering the plasma and acting as the heat sink, and thus required careful design. They are custom-machined from copper to ensure high heat conductivity and low electrical resistance.[3] Each electrode assembly consists of a grounded, cup-shaped

[3]The factory from which we ordered the electrodes, based in Wuhan, was shuttered due to the spread of an unknown virus. We canceled and used a US-based manufacturer to avoid delays, and our order was delivered quickly— two days before Caltech went into COVID lockdown for several months.

"shield," which mounts to the cold head of the cryogenic compressor. An electrically-floating electrode sits within it, which can be connected to RF power through an embedded SMA connector. This is shown in Fig. 3.4. The shield improves the uniformity of the electric field towards the edges of the electrodes and helps confinement of charged grains, while also providing a grounded surface to attach the temperature diode and embedded heating cartridge.

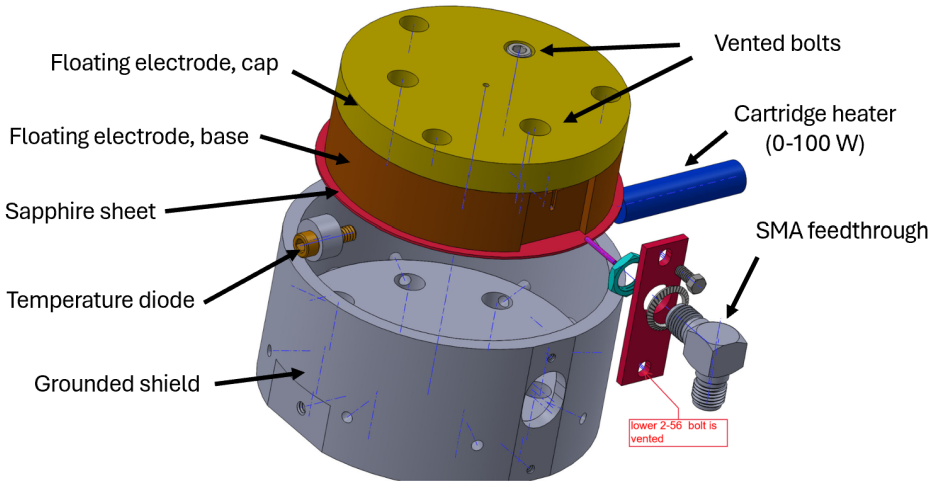

Figure 3.4: Electrode assembly (exploded view).

To efficiently cool the electrodes, each electrode must be in good thermal contact with its shield (which is mounted to the cryogenic cold head) while fully electrically insulated. To achieve this, a thin sheet of sapphire, cut from a single crystal, separates the electrode from the shield. Each contact surface is also coated in a layer of vacuum-grade thermal paste to improve thermal conductivity.

Vacuum and gas injection

The vacuum and gas system is illustrated in Fig. 3.5. The vacuum chamber is attached to a HiCube 80 Eco pumping station, which consists of a turbo-molecular pump capable of pumping ~ 30 L/s, backed by a diaphragm pump connected to its exhaust line. When fully engaged, the chamber reaches $\sim 10^{-6}$ Torr.

When operating, however, the chamber must be filled with 20-2000 mTorr of gas to maintain a capacitive discharge. To allow this, an angle valve between

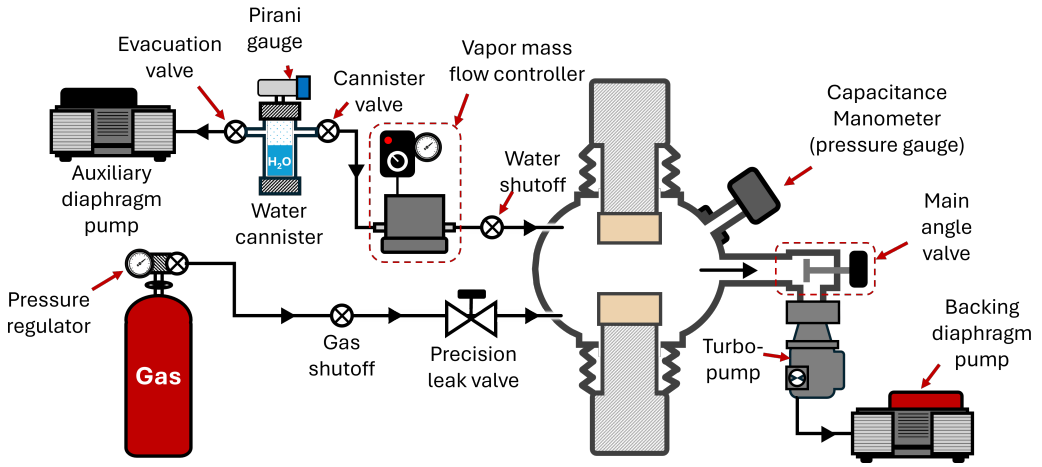

Figure 3.5: A diagram of the vacuum chamber, pumping, gas injection, and water flow control system.

the chamber and the turbo-pump is closed nearly all the way, limiting the outflow, while a gas flow is introduced. The chamber pressure is set by the balance of the gas inflow and the outflow to the pumping system.

The buffer gas is sourced from a standard, 250 cu. ft. gas cylinder, which is typically pressurized to 4000 psi. A pressure regulator is attached to the cylinder which is set to allow 60 psi of gas from the cylinder into the $1/4$-inch tubing running to the experiment. The gas flow into the chamber is then controlled using a precision leak valve, which passes a flow of 50-100 SCCM.[4]

Water vapor is sourced and input through a separate system. A vacuum-tight canister is filled partway with distilled water and sealed. At room temperature, the air above the liquid contains a partial pressure of water that is ~ 10 Torr, the saturated vapor pressure. Using a second diaphragm pump, the air is evacuated from the canister, leaving only the ~ 10 Torr of pure water vapor above the liquid. This pure vapor is directed through a shutoff valve into a vapor mass flow controller (MKS Type 1150C), which passes an adjustable 1-20 SCCM flow of water vapor into the chamber.

With the input flows of buffer gas and vapor, the chamber will reach an equilibrium pressure where the inflow is equal to the outflow to the turbo-pump. While continuously monitoring the pressure using a capacitance

[4]SCCM: Standard Cubic Centimeters per Minute

manometer, the main angle valve between the chamber and the pump can be adjusted to set the desired pressure.

Electrical circuitry

A 13.56 MHz sinusoidal voltage is produced, amplified to an adjustable 1-120 W by an off-the-shelf RF generator purchased from T&C Power Conversion[5] and applied across the electrodes. This generator essentially produces the RF signal using a push-pull MOFSET circuit and amplifies it to high voltage with a transformer. The output impedance of the generator is 50 ohms; the electrical load (the electrodes, cables, and the plasma itself) is in general *not* a pure resistive 50 ohms, but some complex number caused by the system's intrinsic capacitance and inductance.

Power transmission to the plasma therefore requires *impedance matching*. This involves inserting some intermediate, tunable circuit into the load circuitry, parallel to the plasma discharge, that makes the *combined* load impedance 50 ohms. Figure 3.6 (a) shows a simplified circuit diagram outlining the relevant components.

To ensure maximum flexibility and ease of use, we purchased an automatic impedance matcher from T&C power conversion, which automatically adjusts its internal capacitance to minimize the power reflected to the RF generator. This is internally optimized for a capacitive load, working out-of-the-box. It is worth noting that the power reading, 0-120 W, does not correspond with the "true" power entering the plasma: voltage amplitude across the electrodes reaches no more than 200 V, and current is typically below 50 mA, indicating that only 10 W enters the plasma at *maximum* input power. The system's efficiency thus hovers around 10 percent.

As the top and bottom electrodes and circuitry are symmetric, either electrode can be powered, and either can be grounded (see Fig. 3.6(b)) any asymmetries are adjusted for by the automatic impedance tuner, making producing a plasma trivial.

Many CCP systems operate in push-pull mode, in which *both* electrodes are powered in sync with each other, 90 degrees out of phase. This involves

[5]Though I attempted to build one myself, it quickly became apparent that this would require a second PhD in black magic.

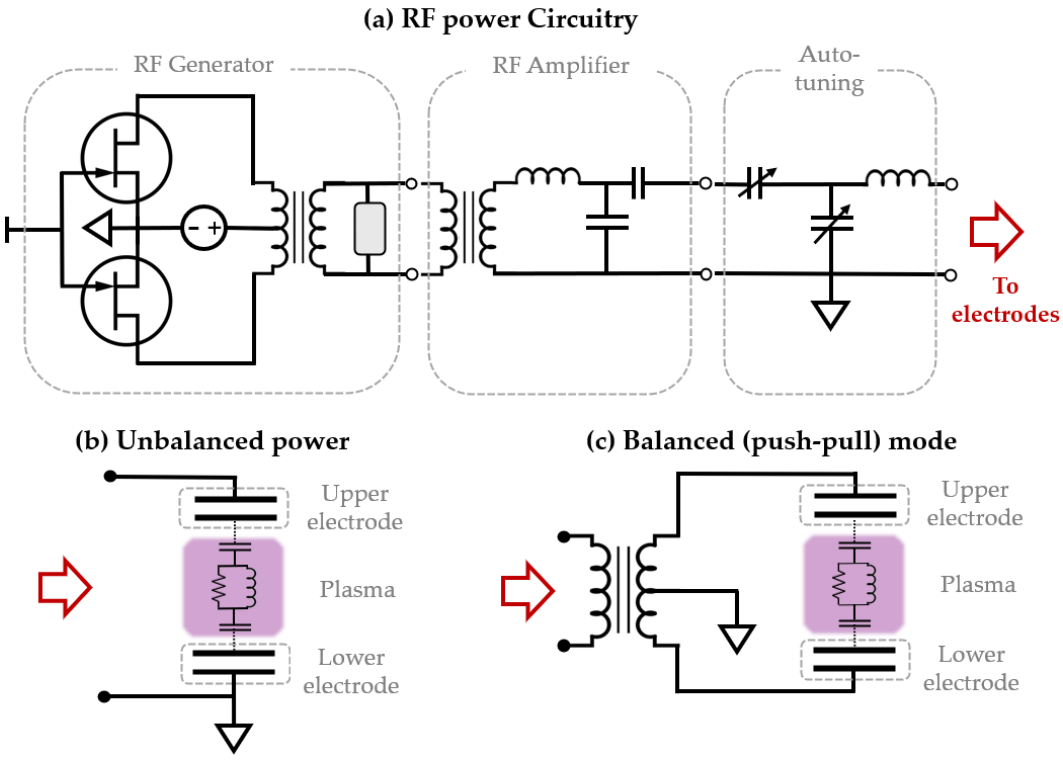

Figure 3.6: (a) Simplified circuit diagram of the RF generator and amplifier (T&C Power Conversion, AG 0113) and automatic impedance tuner (AIT-600-03); (b) typical connections when powering one electrode; (c) Push-pull mode, incorporating a balun.

putting a balun in line with the electrodes, a one-to-one transformer with a center tap, as shown in Fig. 3.6 (c). I mentored a high-school student D. Hajimiri in building one of these; however, because the transformer is a large inductive load, it puts the circuit outside of the range of the auto-tuner. We added quarter-wavelength-long coaxial cable, which effectively makes the load capacitive, and succeeded in producing an Argon plasma; however, it significantly decreased the efficiency of power transfer. I did not use it much further because of this inefficiency, though revisiting the effect of the balun on the system properties and improving efficiency could be an extremely valuable project for the future.

Assembly and timeline

I was tasked with making the design a reality: mechanical testing of the new components, overhauling the RF circuitry to accommodate the new electrode

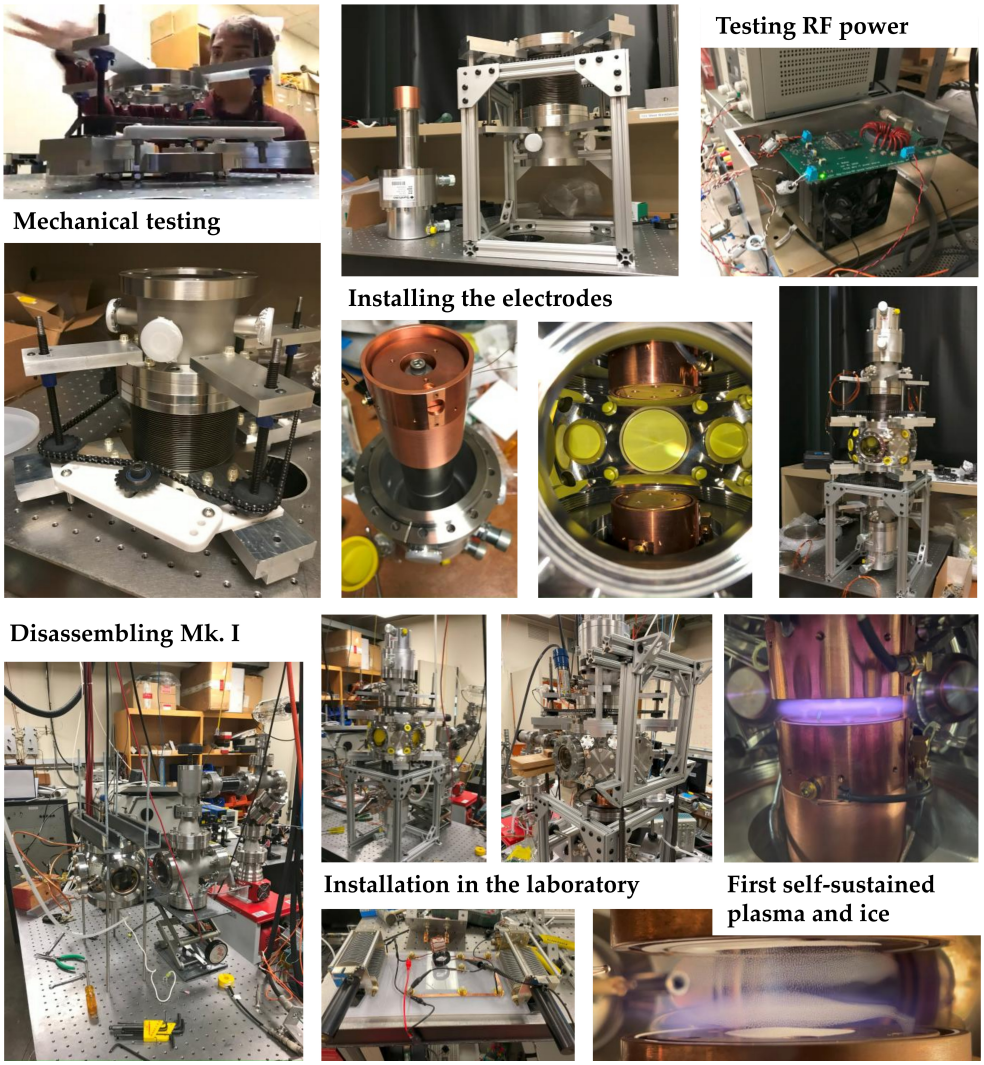

Figure 3.7: Construction of the upgraded Ice Dusty Plasma Experiment.

design, and cannibalizing the old "Mk. I" experiment for its parts. Figure 3.7 shows a photo montage of construction.

Starting in September of 2019, I began with building, testing, and iterating the design for the gear-and-chain mechanism for adjusting the bellows under vacuum. Once I achieved a working mechanism, I mounted them to the vacuum chamber— a new "spherical square" chamber from Kimball Physics— and began assembly of the electrodes.

Construction continued methodically until, when the chamber was about 70% complete, the COVID-19 pandemic hit. Lab access was revoked for months, and even when restrictions eased, we returned under strict, stag-

gered, part-time shifts[6]. These setbacks delayed completion for nearly another *year*, finally installing the chamber in the laboratory in February of 2021.

This was only the first step, however, as the vacuum and electrical systems were plagued with issues. It took yet another year of leak checking, impedance matching, and parameter tuning until I achieved reliable operation, finally reproducing the conditions of Chai & Bellan [34] and able to forge new ground.

In the end, every component of the *Mk. I* chamber had been replaced, apart from the turbopump, a pressure controller, and the gas leak valve. Much like Plutarch's Ship of Theseus, one could argue this apparatus was no longer an upgrade at all, but something entirely new.

3.3 Operating principles of a CCP

Capacitively-coupled plasmas are the most common device used in current dusty plasma research. In use since the early 20th century, they gained prominence in the 1960s with the rise of the semiconductor industry, in which CCPs are used for precise and efficient plasma processing techniques. As such, they have been extensively studied, often using industry-standardized setups such as the GEC reference cell for reproducibility. In 1994, Chu & I [18] showed that dust particles are efficiently contained within a CCP discharge and can self-arrange in Coulomb crystals, which kicked off thirty years of experimental dusty plasma research using CCP discharges.

This section contains a few simple models outlining the dominant physics behind our device. It does not seek to create a self-consistent description of the plasma— a more complete model of the plasma can be found in Lieberman & Lichtenberg [13] and is an active area of research— Including ongoing research by my undergraduate mentee, R.B. Morgan III.

The ionization cascade

Within any neutral gas, there are generally a few free electrons and ions, probably ionized by incoming cosmic rays, trace radioactive decays, or

[6]We were required to work alone to prevent virus transmission by institute policy, instead facing the much-higher risk of operating heavy machinery and handling high voltages unsupervised.

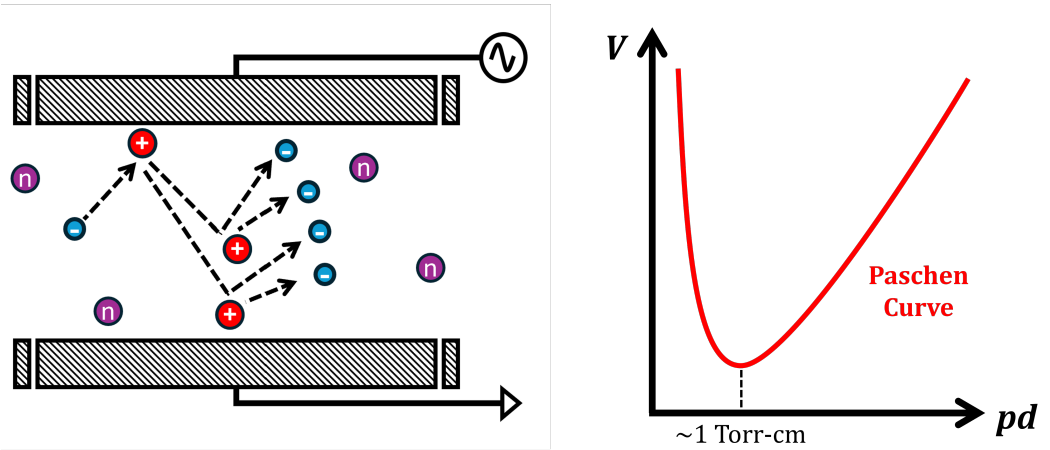

Figure 3.8: The ionization cascade (left) and the Paschen curve (right).

photoemission from low-intensity ambient UV light. The RF electric field accelerates the electrons to high energy, oscillating back and forth between the electrodes, as the driving frequency (13.56 MHz) is smaller than the electron plasma frequency; meanwhile, the ion plasma frequency is smaller still, and so ions remain relatively stationary.

As the few "seed" electrons traverse the plasma, they impact neutral molecules with a frequency,

$$\nu_{e,n} = n_n v_e \sigma_n \approx 10^8 \text{ collisions/sec.} \tag{3.1}$$

If the electrons are sufficiently accelerated, each electron-neutral collision ionizes the neutral molecule. This frees another electron, which itself accelerates and ionizes more molecules (Fig. 3.8), instigating a *cascade of ionization*, also known as "gas breakdown." The ionization fraction equilibrates when the impact ionization rate balances the loss rate of electrons to the walls and to recombination, typically leveling out around $10^{-6} - 10^{-7}$— very weakly ionized.

The required voltage for the ionization cascade, when plotted versus the product of pressure p and electrode spacing d, follows the *Paschen curve*, which has a minimum around 1 or 2 Torr-cm (varying with gas species). At lower $p \cdot d$, the seed electrons do not collide with enough molecules to cause a cascade, while at higher $p \cdot d$, they never accelerate to enough energy to impact-ionize the gas.

Sheath behavior

When sufficiently ionized, electrons move to screen the oscillating electric field (see §1.1). A Debye sheath forms at the plasma-electrode interface with an altered electron density profile and a strong localized field. As the electrons oscillate with the RF voltage, the sheath thickness $s(t)$ oscillates from 0 to s_{max}.

As the ion plasma frequency is lower than the RF driving frequency, they experience only the time-averaged electric field. In the simplest approximation, we assume that ions are evenly distributed throughout the inter-electrode gap; there is no ion sheath. This is called the "homogenous model" of a CCP, and it is good enough for the purposes of this summary, but is not self-consistent: it ignores ion acceleration by the time-averaged sheath field and thus breaks the continuity equations. A more in-depth treatment is outlined in Lieberman & Lichtenberg [13] and leads to (mostly) qualitatively-similar results.

Assuming ion density is constant in the sheath and the electron density is near-zero, Poisson's equation gives:

$$E = \int_{s(t)}^{x} \frac{en_i}{\epsilon_0} dx' = \frac{en_i}{\epsilon_0}(x - s(t)). \tag{3.2}$$

This drives a displacement current through the sheath. As the driving voltage is sinusoidal, so is the displacement current; this causes the sheath thickness to oscillate such that $s(t) = \bar{s} - s_0 \sin(\omega t)$. The voltage across the sheath can then be calculated:

$$\begin{aligned} V_{sheath} &= \int_0^{s(t)} \vec{E} \cdot dx = -\frac{en_i}{2\epsilon_0}(\bar{s} - s_0 \sin(\omega t))^2 \\ &= -\frac{en_i}{2\epsilon_0}\left[\bar{s}^2 - 2\bar{s}s_0 \sin\omega t + \frac{1}{2}s_0^2(1 - \cos 2\omega t)\right]. \end{aligned} \tag{3.3}$$

Now the system contains two sheaths, one at each electrode, which oscillate out of phase by π [13]. If we assume the sheaths are symmetric and ignore the minor resistive voltage drop across the bulk plasma, the total voltage across the electrodes is:

$$V_{sheath}(\omega t) - V_{sheath}(\omega t + \pi) = \frac{2e}{\epsilon_0} n s_0 \bar{s} \sin\omega t. \tag{3.4}$$

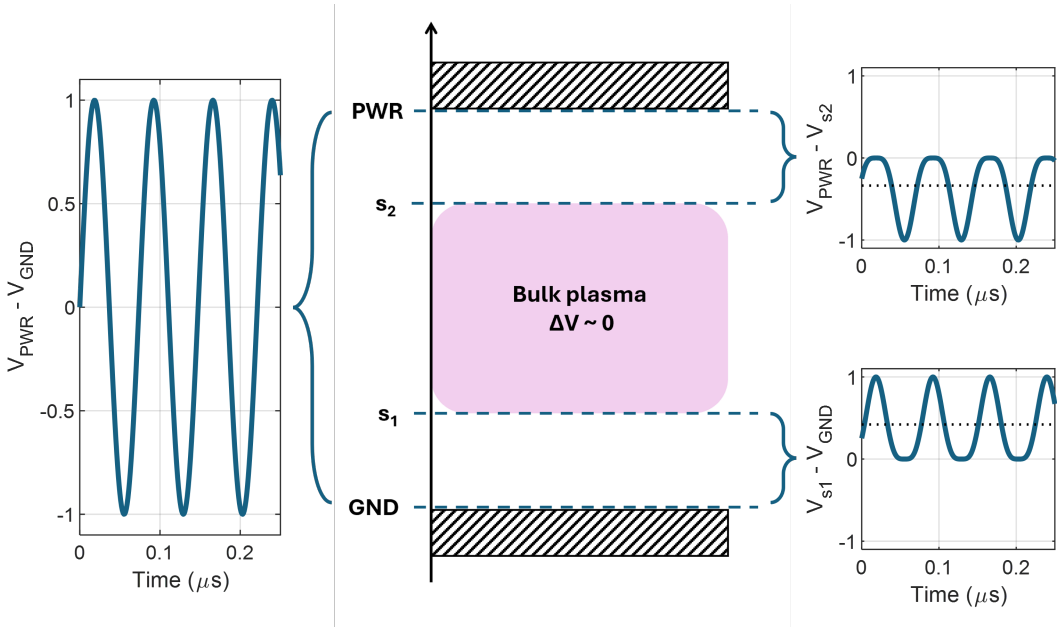

Figure 3.9: Schematic showing the positions of the sheaths and the voltage difference across each region.

Figure 3.3 shows the voltages across the electrodes and each sheath as given by the homogeneous model.

In a real CCP discharge, behavior deviates from this model for a few reasons. Most significantly, because we typically ground one of the electrodes, the two sheaths are *asymmetric*. Importantly, this causes a negative DC self-bias to develop on the powered electrode due to its capacitive coupling to ground.[7]

The sheaths do most of the work maintaining ionization. Electrons can be thought of like ping-pong balls, and the sheaths as the paddles. The electrons traverse the bulk plasma and bounce off the sheath field, given an extra "kick" by the interaction with the moving sheath edge. This kick, in bulk, manifests as stochastic heating, responsible for the high electron temperature (2-3 eV) in these plasmas. Because of these nonlinear sheath interactions, the sheath edges tend to have the highest electron densities and temperatures, and tend to glow the brightest.

[7]Note that the harmonic terms in Eq. 3.3 cancel in Eq. 3.4; this is a quirk of the homogeneous model and is not true in general, and asymmetry further amplifies the developed harmonics.

Ambipolar diffusion

Plasma is produced in the center of the chamber and diffuses radially outward to the walls, resulting in a density gradient of both electrons and ions. Because electrons have a higher temperature and lower mass, they diffuse much more quickly, causing a radially-outward "ambipolar" electric field. The electric field decreases the electron flux and increases ion flux from the plasma; the plasma potential rises to increase ambipolar field strength until the fluxes equate.

The ion flux and electron flux balance in equilibrium:

$$\Gamma = n_e \frac{e}{m_e \nu_e} \vec{E}_{amb} - D_e \nabla n_e = n_i \frac{e}{m_i \nu_i} \vec{E}_{amb} - D_i \nabla n_i, \tag{3.5}$$

where ν_e is the electron collision frequency and $D_e = kT_e/m_e\nu_e$ is the electron diffusion coefficient. Setting n_e = n_i,

$$\vec{E}_{amb} = -\frac{D_e - D_i}{e\left((m_e\nu_e)^{-1} - (m_i\nu_i)^{-1}\right)} \frac{\nabla n}{n} \approx -\frac{kT_e}{e} \frac{\nabla n}{n}. \tag{3.6}$$

Now by continuity, the divergence of the ion flux equates to the difference in ionization and recombination rates. The impact ionization rate is linear with ion density, while the recombination term is dropped as ions are more likely to escape to the walls than to undergo electron-ion recombination [65]. Rearranging Eq. 3.6, we get an equation of the form:

$$\nabla^2 n_i + a\, n_i = 0, \tag{3.7}$$

where a is a constant that depends on the ionization rate and diffusion coefficients. In cylindrical coordinates, Eq. 3.7 gives Bessel function solutions in the radial direction and sinusoids in the vertical direction. Treating boundary conditions properly, ionization occurs ($\alpha \neq 0$) only in the inter-electrode gap ($r < R$), while ions stream all the way to the chamber walls (at some $\rho > R$). Here I numerically solve these two regions separately using a finite difference method, and match the ion flux and density at the boundaries to obtain the ion density, plasma potential, and ambipolar field throughout the chamber shown in Fig. 3.10. Strong electric fields form at the radial edges of the bulk plasma, increasing in magnitude towards the chamber walls.

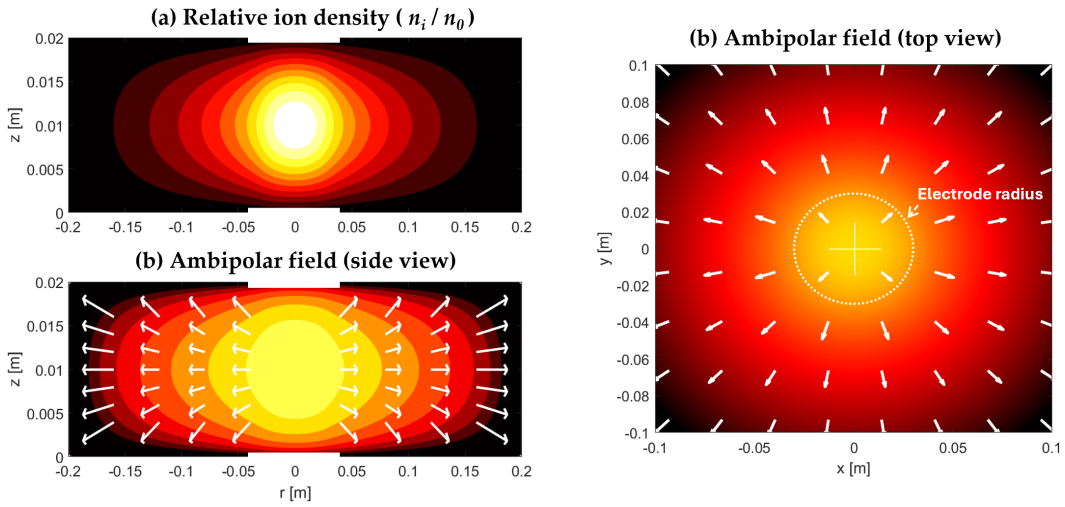

Figure 3.10: Solutions to the plasma equilibrium: (a) plasma density contour plot in side view; (b,c) electric potential overlaid with a vector field showing the ambipolar field, in side and top view.

Dust grain confinement

The dust grains thus experience two electric forces: the ambipolar field and the time-averaged RF field. As grains are negatively charged, both these forces act to confine the grains to the bulk plasma. When other forces are negligible, grains will sit at the density maximum of the plasma, as shown in figure 3.11. Other forces such as gravity and ion drag can force the grains toward the sheath edge(s) where the electric force is many times stronger and supports the grains against these forces.

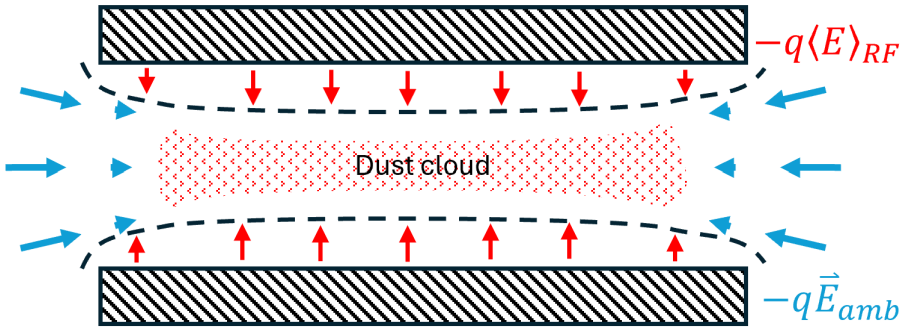

Figure 3.11: Electrostatic forces experienced by negatively-charged dust grains, including the time-averaged RF field (red) and ambipolar field (blue).

3.4 Principles of cryogenic cooling

The cryogenic system is essentially a very cold refrigerator, which pulls heat from the electrodes and dumps it into the room. Rather than using a vapor-compression cycle like a typical refrigerators or air conditioning units, it uses a *Gifford-McMahon* cycle, which uses helium gas as its working fluid. This design uses timed valves and thermodynamic regeneration to increase its cooling capacity. While our cryocoolers (SHI Cryogenics CH-104) are fairly low-caliber, single-stage systems rated to reach only 77 K, they can easily reach < 50 K in practice.

Helium refrigeration cycle

The cooling system consists of a Helium compressor and two cryogenic "cold heads," one mounted to each electrode. Two semi-flexible hoses connect to each cold head: a supply line carrying high-pressure helium to the cold head, and a return line carrying low pressure helium back to the compressor. A diagram of the cooling system is given in Fig. 3.12.

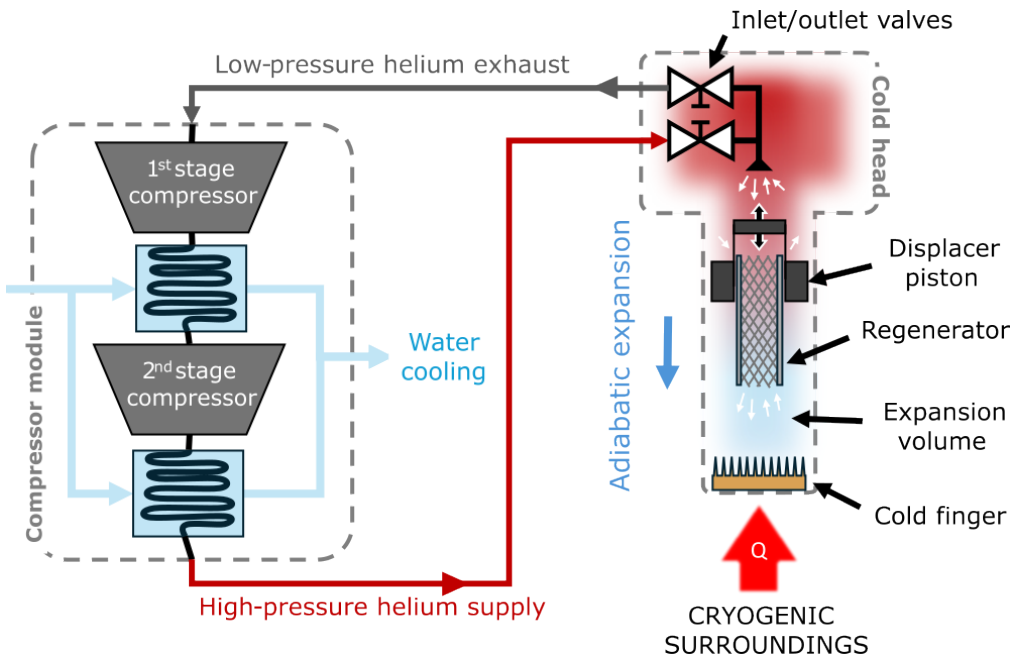

Figure 3.12: Cryogenic cooling using a Gifford-McMahon refrigeration cycle.

The refrigeration cycle works as follows: (i) high-pressure helium from the compressor enters the cold head when the inlet valve opens. (ii) The displacer

piston shifts, allowing the gas to expand adiabatically into the expansion volume, cooling to cryogenic temperatures. (iii) The cold gas absorbs heat from the surroundings (e.g., the electrode attached to the cold head). (iv) The outlet valve opens, and the warmed, low-pressure gas is drawn back to the compressor. The displacer piston moves back to the closed position, and the cycle restarts.

The "regenerator," a porous matrix inside the displacer, acts like a sponge for heat: the high-pressure helium input pre-cools as it travels through it into the expansion volume, and the low-pressure helium absorbs that heat on its way back to the compressor. This greatly improves the cooling efficiency.

Temperature control

To control the temperature of each electrode, a resistive heating cartridge and temperature-sensitive silicon diode are embedded in each. They connect to a temperature control system (CTC100, manufactured by Stanford Research Systems).

As the cryocooler applies a constant, uncontrolled cooling, the controller measures each electrode's temperature from the diodes. Using a PID control system, the controller drives 0-100 W of power into each cartridge heater, maintaining the temperature of each electrode at a steady value, independently controllable for each electrode. In practice, this system can easily maintain steady temperatures between 50 and 250 K.

Cryogenic gas equilibrium

The electrodes are held at a controlled uniform temperature. As gas enters the chamber at room temperature and the chamber walls are not cooled, the temperature profile will *not* be uniformly cold throughout the chamber. Rather, an equilibrium temperature profile will be reached through a balance of heat transfer from the cold electrode surfaces, the room-temperature input gas flow, and heating from the RF field.

If the gas flow rate into the chamber is large, the gas may never reach thermal equilibrium, as cryogenic gas is continuously replaced by the warmer inflow. To prevent this, we introduce the buffer gas far from the electrodes to minimize advection and net flows near the electrodes. Whether thermal

equilibrium is achieved thus depends on the ratio of gas residence time in the chamber to thermal diffusion time, called the Fourier number:

$$\mathrm{Fo} = \frac{\tau_{res}}{\tau_{diff}} = \frac{V/Q_V}{L^2 \rho c_p / k_{th}}. \tag{3.8}$$

Given the chamber volume V of 3.8 liters and a volumetric flow rate Q_V calculated to as $0.002\ \mathrm{m}^3/\mathrm{s}$ from pressure measurements, the gas residence time is approximately 20 seconds. For an argon gas at 150 K and 300 mTorr, we calculate a Fourier number of 25.5 across the full 8-inch chamber diameter, and 231.5 across the electrode diameter. Thermal diffusion therefore greatly outpaces gas replacement, so we can assume that the gas is rapidly quenched on input and a static thermal equilibrium temperature profile is achieved.

Next, I calculate the *Rayleigh number*, the ratio of the thermal diffusion timescale to the natural convection timescale, which dictates whether heat transfer is primarily conductive or convective— convection becomes dominant when $\mathrm{Ra} \geq 1708$. In a fluid layer of thickness L,

$$\mathrm{Ra} = \frac{\rho^2 g c_p L^3}{\mu k_{th}} \frac{\Delta T}{T}, \tag{3.9}$$

where c_p is the heat capacity, μ is the dynamic viscosity, and k_{th} is the thermal conductivity. In argon gas at 300 mTorr and 150 K, a temperature differential of 950,000 K would needed for convection across a 2-cm inter-electrode gap— heat transfer is thus purely *conductive*, following the heat diffusion equation in steady state:

$$\nabla \cdot (k_{th} \nabla T) = -\dot{Q}_{RF}, \tag{3.10}$$

where $\dot{Q}_{th}$ is volumetric heat generation from the RF field, mainly resistive heating from the hot electrons.

In the absence of plasma ($\dot{Q}_{RF} = 0$), the gas reaches an equilibrium profile given by the Laplace equation. This was solved numerically using a finite difference method in MATLAB for our chamber geometry. I here used constant-temperature boundary conditions were— a defined cryogenic temperature across each electrode surface, and outer walls at 300 K— and solved for the equilibrium temperature profile. The profile is plotted in Fig. 3.13 for two temperature configurations, one with both electrodes at equal temperatures (150 K), and one with the lower electrode 10 K warmer than the upper.

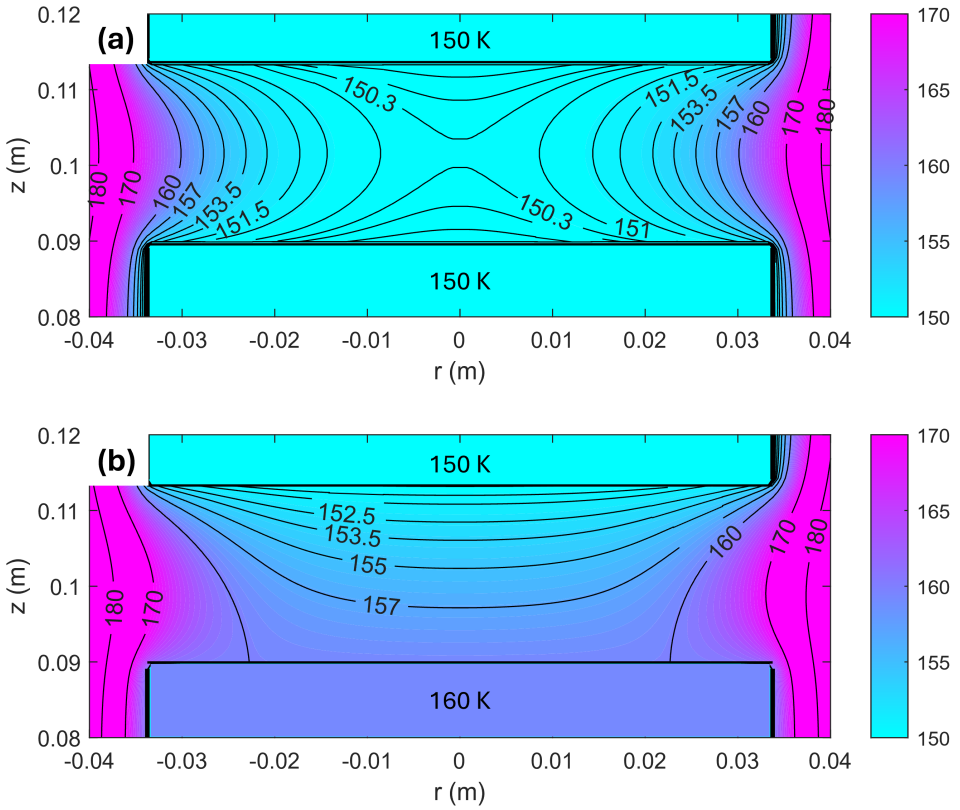

Figure 3.13: Temperature profile obtained from a numerical solution to the heat conduction equation; (a) outer walls at 300 K, electrodes at 150 K, (b) upper electrode at 150 K and lower electrode at 160 K.

The plasma introduces nonuniform heating throughout the inter-electrode gap, dependent on the plasma density profile and strongest along the powered electrode's sheath edge, which results in a more complicated temperature profile [64].

3.5 Operation and diagnostic methods

The experiment runs following this protocol:

1. The chamber is pumped out to low pressure.
2. Electrode positions are adjusted to the desired spacing.
3. The cryogenic compressor is started.
4. The desired temperature on each electrode is set on the temperature controller.

5. The gas manifolds are purged and set to supply a steady flow of bufer gas.
6. The main angle valve is adjusted to reach desired pressure in the chamber.
7. The RF power is turned on, ionizing the plasma.
8. Water is injected; under the appropriate parameters, ice forms spontaneously.

The device operates over a broad parameter space, with independent control of electrode temperatures, buffer gas species and flow rates, pumping speed, electrode separation, and RF power.

Tuning the gas input and pumping speed (via the angle valve) controls the total pressure, and indirectly changes the gas residence time and flow velocity through the chamber. The gas composition strongly affects the discharge physics and ice formation due to differing molecular masses, ionization energies, and electronegativity. Adjusting the electrode separation allows tuning around the Paschen minimum to vary ionization fraction, while the symmetric electrode design allows various RF configurations and DC biases to be applied to alter the plasma structure. Dynamic control of any of these variables can have significant effects both on the plasma and the ice contained within.

The versatility of the device is a blessing and a curse— it enables exploration of diverse plasma conditions but demands careful tuning for repeatable, reliable data.

Further details of the experimental hardware and operation are presented in Appendix A. The remainder of this chapter covers the diagnostic methods used the characterize the plasma and the ice grains, which are employed throughout this thesis.

Current and voltage traces

We monitor the electrical characteristics of the plasma reactor as the RF power turns on, the plasma lights, and ice grains form within. The voltage trace on the powered electrode is measured by a 100x voltage probe (Tektronix)

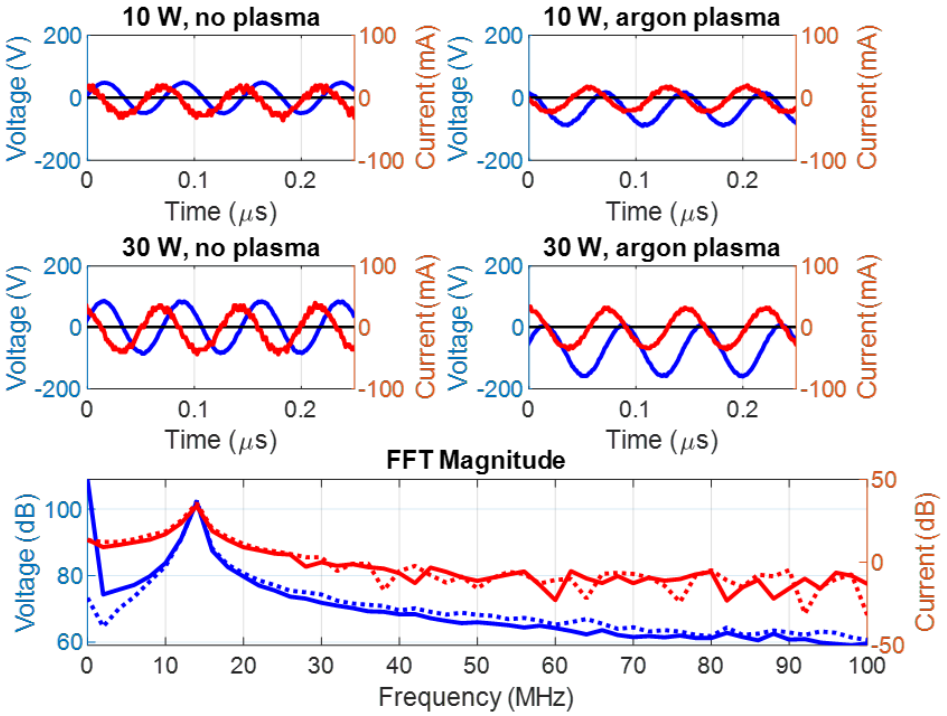

Figure 3.14: Voltage on the powered electrode and its current, both with and without plasma, at 10 and 30 W forward RF power. Also shown is the frequency spectrum at 10 W, with (solid line) and without (dotted line) plasma.

plugged into an oscilloscope with 1 MΩ input impedance. Meanwhile, a 1 V/A current transformer, wrapped around the coaxial power cable, measures the current driven to the powered electrode.

Figure 3.14 shows measured voltage and current traces over a few RF periods. These are captured for two RF power settings, 10 W and 30 W, both with plasma present (300 mTorr of pure Argon at room temperature) and with no plasma (chamber at vacuum). The frequency spectrum of the traces are also shown. Both the voltage and the current magnitudes increase as RF power is increased; in frequency space, they show a peak at 13.56 MHz as expected.

The input power $P = VI$. At a forward power set to 10 W, The voltage amplitude is 50 V, and the current is 20 mA— the power *delivered* to the plasma is thus around 1 W. With forward power set to 30 W, we measure a delivered power of 2.9 W. The efficiency of the power delivery is thus about

10 percent, while the rest of the energy is likely radiated from the cables. This is a common issue in RF electronics in general, and a great amount of effort in the field of RF plasmas is spent on this issue [66].

The voltage traces have similar magnitude whether or not the plasma is present. However, a DC offset, or "self-bias," is established when the plasma appears. The bias has a magnitude around 50-100 V, increasing nonlinearly with RF power.

The measured current waveform includes both the current *through the plasma* (that is, the displacement current across the sheaths and through the resistive bulk plasma) and an inductive current ($C\ dV/dt$) through the powered electrode's intrinsic capacitance to ground. As the current waveform is relatively unchanged whether or not plasma is present, the inductive current likely makes up most of the signal.

The offset between the plasma current and the voltage gives the impedance of the plasma. The plasma itself can also produce harmonics of the driving frequency in both the voltage and current waveform [13]. Both these observations can be used as diagnostics for the plasma's bulk electron density. [13, 67]. They are also particularly sensitive to particle formation, allowing detection of nanoscale grains invisible to optical diagnostics; I have worked with undergraduate R. B. Morgan III to probe early ice growth using this method.

Direct imaging

Photographing the plasma itself can reveal a lot of details about its composition and structure. In Fig. 3.15, three different plasmas are shown with three different power configurations: first with the top electrode powered and bottom grounded, second with the polarity reversed, and third in push-pull mode. Photographs, taken with a DSLR camera fitted with a wide-angle lens, are shown on the left; voltage traces across each electrode are shown on the right.

When only one electrode is powered, its sheath appears significantly brighter than the grounded electrode's sheath, highlighting the asymmetry of the discharge. This occurs because the chamber is at the same grounded voltage

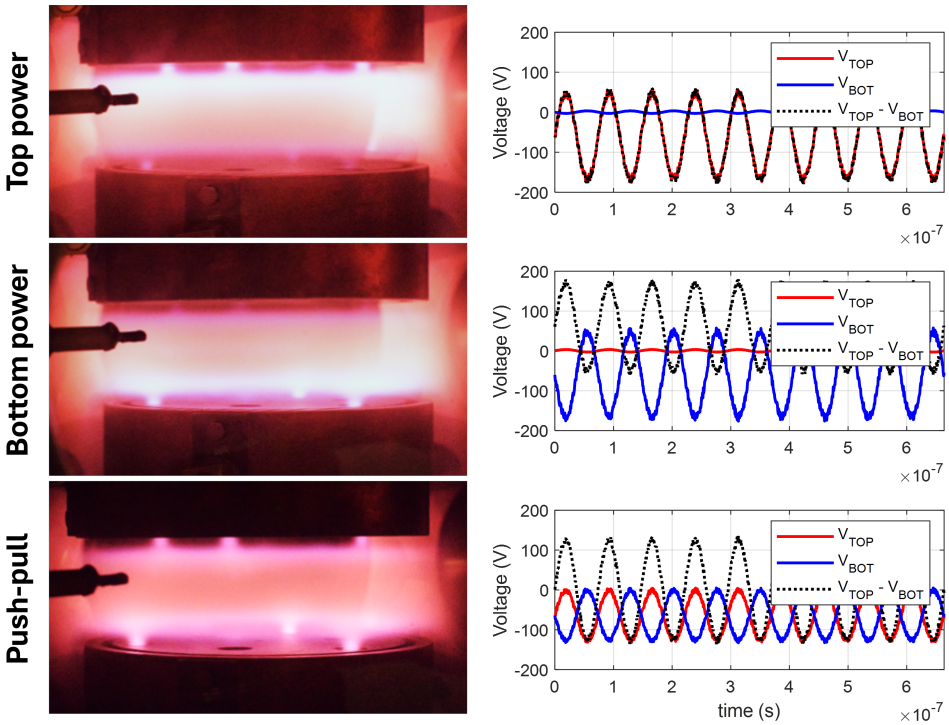

Figure 3.15: Photos of the plasma with three different power configurations: top-powered, bottom-powered, and push-pull (balun) mode. Also displayed are the voltage traces on each electrode.

as the electrode, "spreading out" the sheath. In push-pull mode, however, the sheaths appear much more comparable in brightness and width.

The sheaths contains prominent "spouts" that appear to emanate from the electrodes. This is *not* actually a spout, however, but plasma density maxima due to bolt holes on the electrode surface. The sheaths dip into the bolt holes, while the sharp edges cause concentrated electric fields that increase local ion density.

The color and brightness of the plasma tell us about the plasma temperature and composition: argon is bright pink, verging on white at high power, hydrogen leans more violet, nitrogen red, and high concentrations of water vapor (above the freezing point) as a deep, dull indigo. Optical emission spectroscopy could be used to quantify the colors, comparing ratios of the spectral lines, which also reveals the electron temperature.

Laser sheet scattering

The bulk behavior of the cloud of ice grains are generally visualized using a laser scattering scheme. In this scheme, a sheet of laser light is produced by directing a laser pointer— typically a 532 nm green laser ($Nd:YVO_4$) or a 633 nm red laser (HeNe)— through a cylindrical lens. This sheet illuminates a vertical cross-section of the ice cloud (Fig. 3.16 (a)), as the laser light scatters off the ice grains.

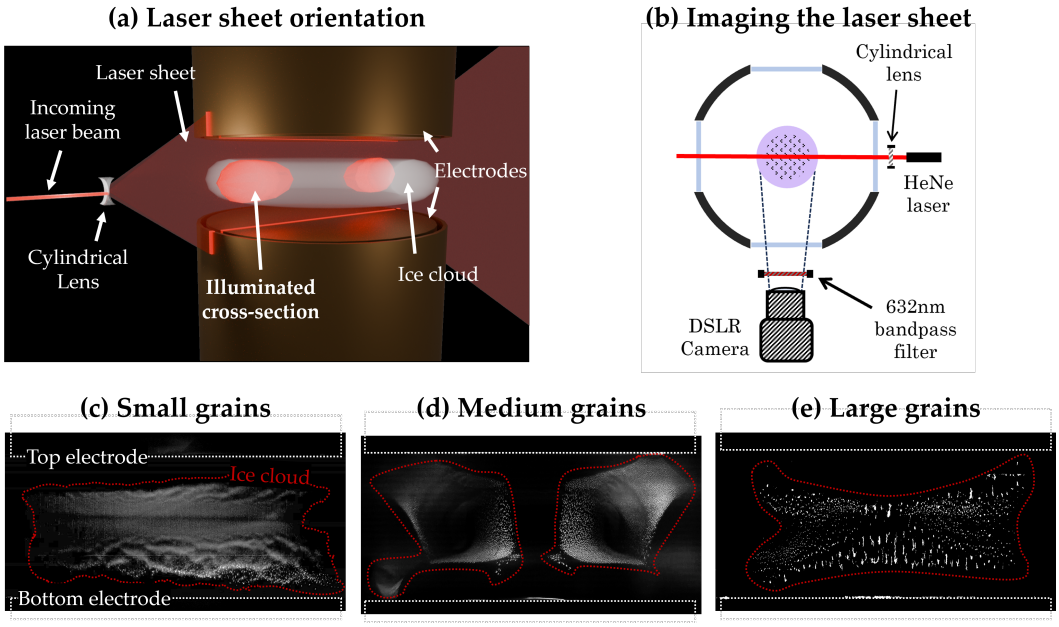

Figure 3.16: Laser sheet imaging diagnostic: (a) 3D render indicating the orientation of the cylindrical lens and the laser sheet; (b) illustration of the camera and laser layout (top view); ice cloud images with (c) small grains (< 1 nm) imaged soon after formation, (d) grains with intermediate size $10 - 100$ μm, and (e) large grains (> 500 μm) formed in low pressure hydrogen.

Scattered laser light is imaged by a camera oriented perpendicular to the beam path, as shown in Fig. 3.16 (b). The camera is fitted with a wide-angle macro lens on a tube extender, allowing a sharp focus at the position of the laser sheet. The images are taken through a bandpass filter tuned to the laser wavelength to block the light from the plasma.

The light becomes bright enough to see when the grains grow above $\sim 10\%$ of the laser wavelength, showing a diffuse glow due to Rayleigh scattering (grain size $\ll$ wavelength). As grains grow to the scale of the wavelength

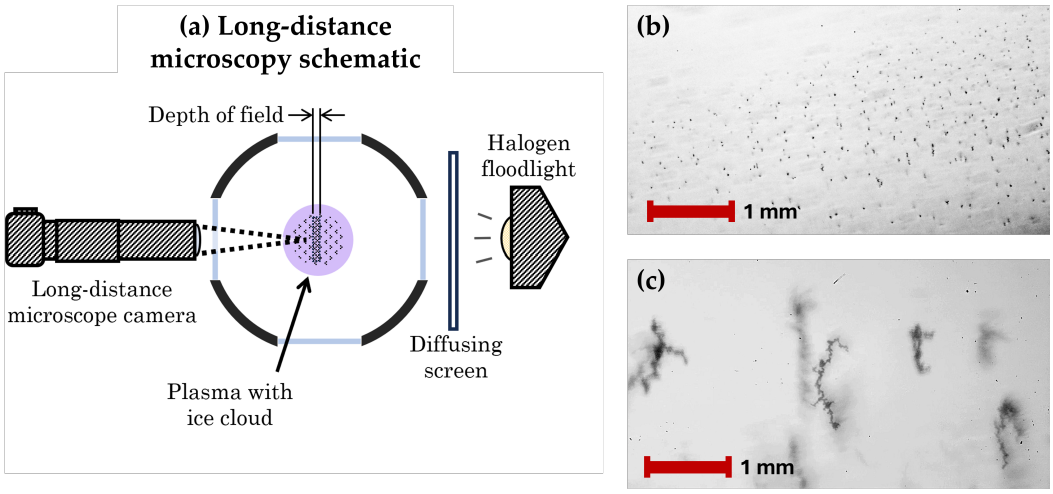

Figure 3.17: Grain imaging with a long-distance microscope: (a) schematic of the long-distance microscope camera, capturing within a ~ 30-micron depth of field and a 3×5-mm field of view, with resolution of about 3 microns. Grains are back-lit by a bright halogen lamp. Example photos are shown with grains averaging (b) 5-10 microns and (c) 1 mm in length.

and beyond, scattering enters the Mie, and then geometric optical regime, and individual grains become distinguishable through laser scattering [68]. Figure 3.16 (c-e) show images of the laser scattering for clouds with grains of various sizes, revealing the shape and structure of the ice cloud and capturing it's large-scale dynamical behavior.

Long-distance microscopy

To image the micro-scale structure of individual grains, a long-distance microscope lens (Infinity Photo-Optical) is mounted to a camera. The lens has a magnification of approximately 20, capturing a window of about 3×5 μm. It has a very shallow depth of field, $\sim 30 - 100$ μm depending on the lens's adjustable aperture; thus only a narrow cross-section of the ice cloud is imaged. This allows resolving individual grains in a small pocket of the ice cloud. Figure 3.17 (a) shows the microscope position and its depth of field.

A bright halogen flood lamp is placed at the window opposite the camera, backlighting the ice cloud, such that the camera captures silhouettes of ice grains in its depth of field against a background of unfocused white light. Figures 3.17 (b) and (c) show the resulting images for differently-sized grains.

Both this microscope lens and the wide-angle lens used for laser sheet scattering have Nikon F-type lens mounts. High-resolution photos are taken with a Nikon DSLR camera. Both lenses can also be attached to our Phantom v642 high-speed camera, which is capable of taking videos at 1600 frames per second at 1080p resolution. This allows recording motion of individual grains, as well as capturing large-scale waves and dynamic instabilities using laser scattering; these diagnostics are utilized in Part III of this thesis.

Infrared spectroscopy

The transmission spectrum of infrared light through the ice-dusty plasma reveals the composition, phase, and morphology of the ice and vapor contained in it. This is measured using a Thermo-Nicolet iS50 Fourier Transform Infrared (FTIR) spectrometer.

The FTIR spectrometer emits a modulated infrared (IR) beam. This beam is coupled to a 1.5-meter-long, hollow-core, IR optical fiber (Guiding Photonics) to guide it to the experimental apparatus. Upon exiting the fiber, the beam is collimated by a gold parabolic mirror and directed through a sapphire window on the vacuum chamber. The beam traverses the plasma and ice cloud, exits the vacuum chamber through another sapphire window, and is focused onto a mercuric cadmium telluride (MCT) detector by another gold-plated mirror. This is shown in Figure 3.18 (a). The beam is partially absorbed at some wavelengths by material in the beam path— by the sapphire windows, by various gas species in the air and within the plasma, and mainly, by the ice grains as they form.

The modulated beam is produced through a Michelson interferometer within the FTIR spectrometer's casing, shown in Fig. 3.18 (b). A broadband IR source emits a constant beam that is directed onto a beam-splitter, which divides it into two paths. One beam reflects from a fixed mirror, while the other reflects from a mirror that moves back and forth at constant velocity, creating a continuously-varying optical path difference between the two beams. When the beams recombine, different wavelengths interfere constructively or destructively depending on that path difference, producing a time-varying *interferogram.* The detector records the beam intensity with time, correlates it with the mirror position (which is precisely measured

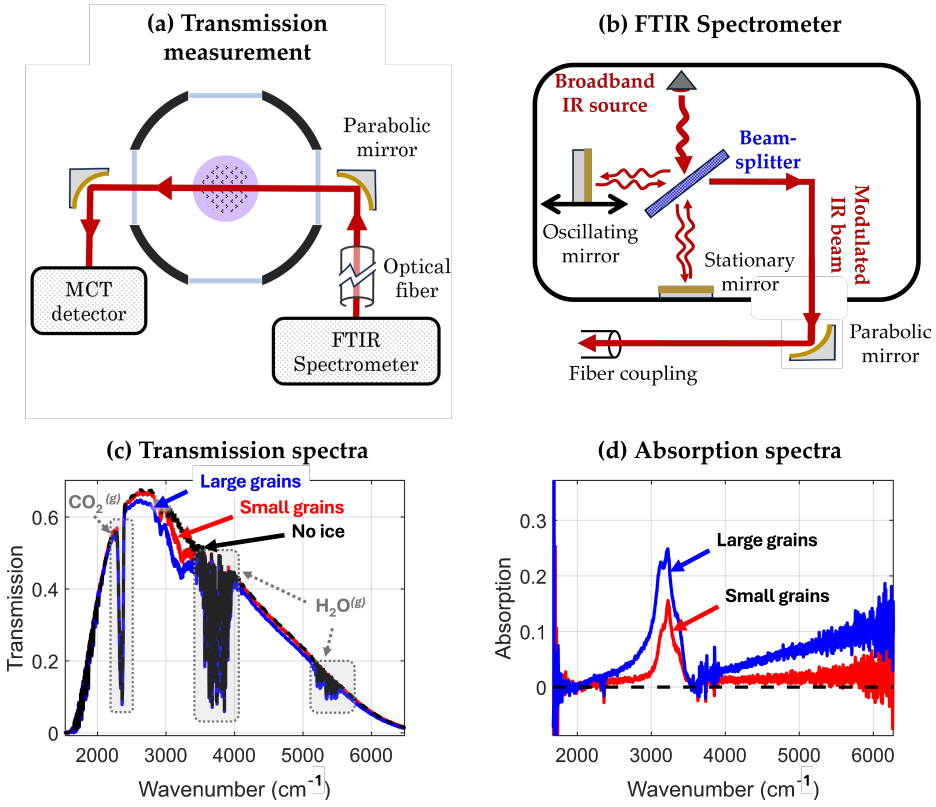

Figure 3.18: The FTIR spectroscopy diagnostic. (a) a schematic sketch of the measurement setup; (b) a diagram of the spectrometer's inner beam mechanics; (c) three raw transmission spectra obtained without ice (black), with a cloud of small ice grains (red), and with a cloud of large ice grains (blue); (d) absorption spectra obtained from the transmission spectra in (c).

internally by a HeNe laser), and Fourier-transforms the interferogram to obtain the frequency spectrum of the infrared light.

Each scan involves 60 separate spectra that are averaged to increase the signal-to-noise ratio, and takes roughly one minute. A baseline transmission spectrum is taken before any plasma or ice has been formed, shown by the black line in Fig. 3.18 (c). The scan shows the broadband "hump" produced by the IR source, and several absorption lines, mainly from atmospheric water vapor and carbon dioxide. When ice grains form and grow, additional transmission spectra are taken, shown by the red and blue curves. There appears a significant absorption around 3000-3500 cm^{-3}, associated with water ice: photons in this frequency range excite vibrations in the O-H bonds in the ice lattice.

The background scan can be subtracted from the signals containing ice grains to obtain an extinction spectrum of the grains themselves. This is computed using:

$$\text{Ice Extinction} = -\log\left[\frac{\text{Ice Transmission}}{\text{Background Transmission}}\right]. \tag{3.11}$$

Figure 3.18 (d) shows two extinction spectra obtained from the transmission spectra shown in Fig. 3.18 (c). The blue curve was taken in a plasma that contained larger grains than that with the red curve; the large offset baseline is due to significant light *scattering* by the larger grains, in addition to absorption.

FTIR spectroscopy is used extensively in Chapters 4 and 5 to characterize the ice composition, grain size, and phase structure.

Laser-induced fluorescence

Laser-induced fluorescence (LIF) is a powerful diagnostic for measuring the velocity distribution of neutral molecules or ions. Our scheme, developed by Marshall & Bellan [64], employs a diode laser at 696.735 nm to excite neutral argon atoms from one metastable state to another; they then decay, fluorescing at 772.6 nm (see Fig. 3.19).

The laser uses a piezoelectric material to vary its wavelength by ± 10 pm. As the laser shines through the plasma, each argon atom sees the laser Doppler-shifted by its velocity; in the lab frame, it fluoresces when illuminated by a wavelength appropriately shifted from the ideal 696.735 nm.

The intensity of fluorescence is measured by a photomultiplier tube (PMT) at a single point along the laser path, and the laser sweeps over its wavelength range, yielding a gaussian distribution. The mean laser wavelength corresponds to the Doppler shift by the mean flow velocity (projected along the laser path), while the spread corresponds to the temperature of the neutral argon gas.

Marshall & Bellan [64] used this setup to measure neutral gas flows as slow as 2 m/s; as this is slower than any expected flows in the experiments described here, I did not undertake a flow measurement, using the setup only for obtaining gas temperatures. For details on the setup, hardware, and operation, and analysis, see Ryan's thesis [69].

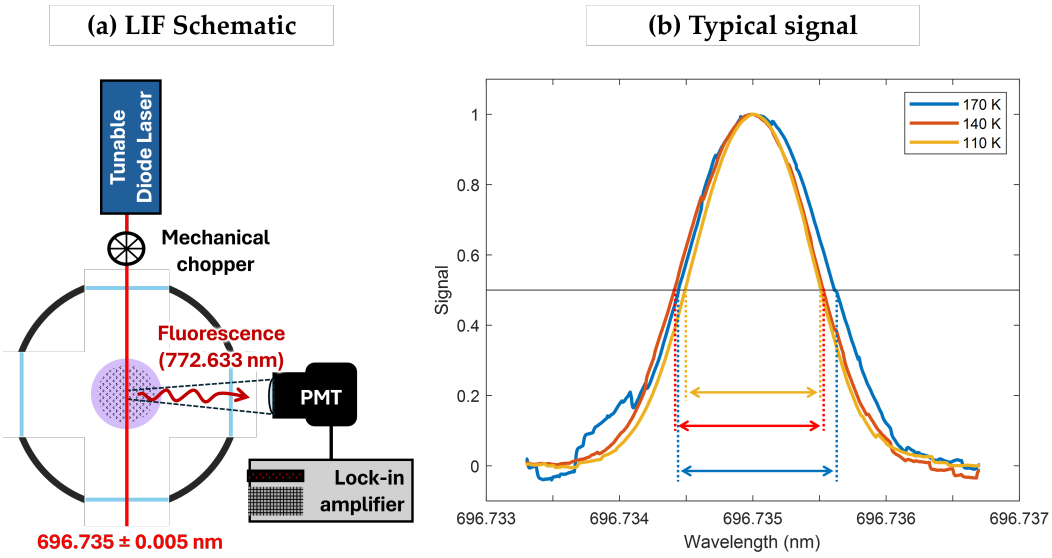

Figure 3.19: Details of the LIF diagnostic: (a) a schematic sketch, and (b) typical measurement of the fluorescence distribution at the midpoint of the plasma, at 3 different electrode temperatures. Note that at colder temperatures, the spectrum's spread is narrower.

I worked with undergraduate Zhe Yang to develop a planar LIF scheme, in which the diode laser beam is spread into a sheet, and the fluorescence is imaged by a camera throughout a whole 2D plane; this is still under development but has shown promising results.

Mass spectroscopy

The chamber was equipped with an ion energy analyzer (Hiden EQP-300) capable of measuring mass and energy of neutral atoms, positive, and negative ions.

At the top of the EQP is a quadrupole mass spectrometer (QMS). This separates ions according to their mass-to-charge ratio using combined RF and DC electric fields, applied across four rods; only ions with specific q/m pass through the quadrupole field without being deflected into the rods. The selected ions are finally detected by a secondary electron multiplier (SEM). By scanning the quadrupole field parameters, the instrument selectively transmits ions of different masses to the detector and records the counts per second at each measured q/m.

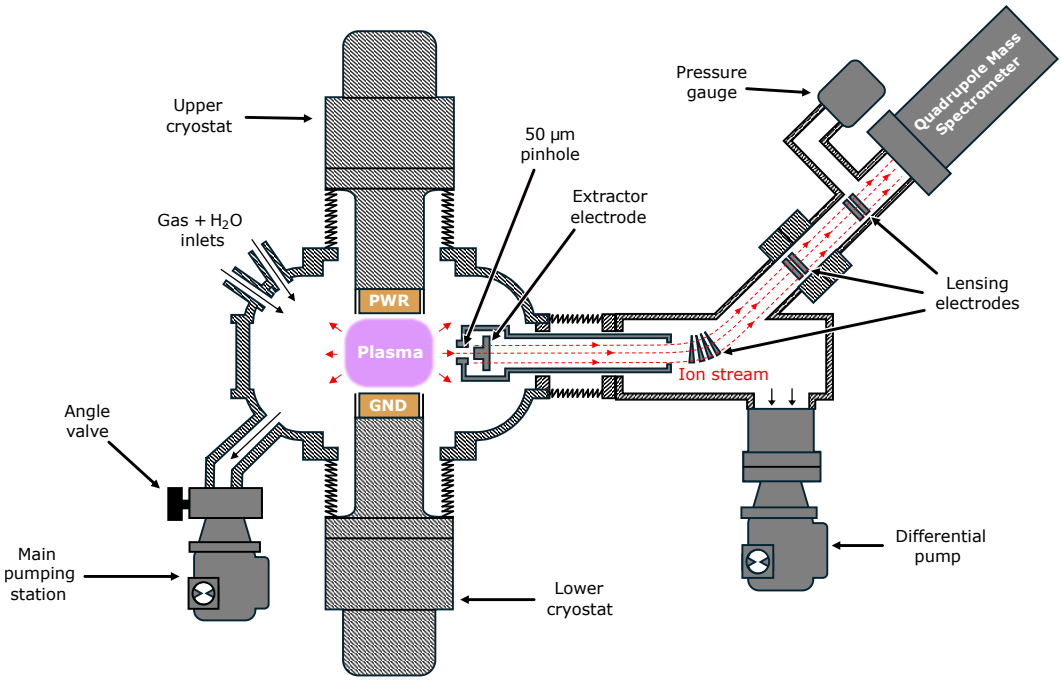

Figure 3.20: Schematic of the EQP-300 Ion Mass Spectrometer.

A series of electrodes placed throughout the EQP act as an Einzel lens. Einzel lenses use electrostatic fields to focus and direct ions beams without significantly changing their kinetic energy. By applying appropriate voltages to its electrodes, the lens focuses the beam of ions coming from the plasma, through the pinhole, and directs them into the QMS detector. In practice, the efficiency of the lens depends on the ion charge-to-mass ratio, and so the voltages must be tuned for the ion mass range that we desire to detect.

The EQP can also act as a residual gas analyzer (RGA) to detect the neutral gas species. Neutral particles enter the spectrometer through the pinhole and fill the spectrometer's differentially-pumped low pressure region. A heated filament emits electrons at a set energy, which impact-ionize the neutral gas within the quadrupole field. The SEM records the mass spectrum of these ions, which should match the mass spectrum of the neutral gas itself. As the Einzel lens is not active while running RGA mode, and neutral molecules greatly outnumber ions even in the bulk plasma, ions from the plasma do not enter the detector simultaneously and skew results.

In addition to the diagnostics mentioned throughout this section, I have used a variety of plasma-facing probes, namely Langmuir probes and variations

thereupon. These have not given reliable results and are thus relegated to Appendix B.

3.6 Looking forward

While the new Ice Dusty Plasma Experiment is based on a decade of previous research in ice grains within plasma, its capabilities are the first of its kind. Precision temperature control allows studying ion-induced ice grain nucleation in a controlled fashion [30], formation of amorphous ice at low temperature, and the effects of the ice's temperature history on its morphology.

As the electrodes can be set at different temperatures, we also can study large-scale dynamics much more effectively, separating ion motion from thermophoretic motion much more precisely than achieved in prior dusty plasmas [65, 70] and observing how thermal effects drive flows and instabilities of the ice cloud.

The remainder of this thesis focuses on extracting laboratory measurements and applying them, both to describing dusty plasma behavior in RF reactors, and to large-scale processes throughout planetary and astrophysical phenomena.

Part II

Ice Formation and Physical Properties

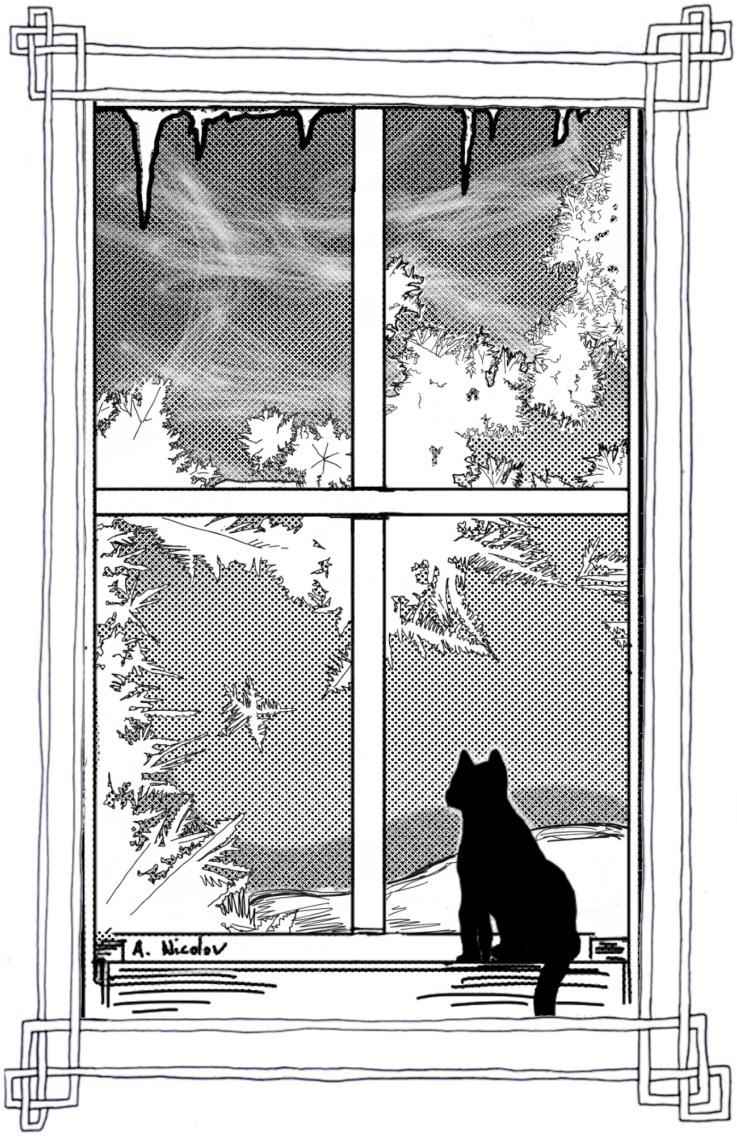

"One must have chaos in oneself to birth a dancing star." -Nietzsche

Chapter 4

ICE MORPHOLOGY AND GROWTH

Parts of this chapter have been published in:

> Nicolov, A. *et al.* Phase and morphology of water-ice grains formed in a cryogenic laboratory plasma. *The Astrophysical Journal* **966,** 66. `http://doi.org/10.3847/1538-4357/ad34b5` (2024).
>
> ...

In this chapter, I present a survey of ice grain shape, size, and growth rate. The results show much consistency with the work on the previous iteration of the experiment, as published by Chai & Bellan [63] and Marshall *et al.* [24]: grains grow with fractal scaling to the scale of hundreds of microns, form elongated, dendritic structures in vertical alignment, grow larger at lower pressures and in less-massive gases. The new iteration of the experiment allows adjustment of electrode temperature was well, opening a new parameter to explore.

4.1 Parameter space for grain formation

The Ice Dusty Plasma Experiment allows control of many parameters, namely the pressure, the background gas species, the flow rates of both the background gas and water vapor, the temperature of each electrode, the input RF power, and the spacing between the electrodes. Each of these variables affects the size, number density, and behavior of the ice grains that form.

In a typical experimental run, the cryostat is set to maintain the desired electrode temperatures. The chamber is filled with low-pressure gas, (typically 20-2000 mTorr), usually hydrogen or argon, and ionized by the RF power, set between 5 and 100 W. Finally, a steady flow of water vapor is introduced. Under the right conditions, the cloud of ice grains becomes visible to laser sheet scattering (see Section 3.5) within a couple seconds. Initially, a dim glow of laser light appears and intensifies as grains grow; eventually, individual grains become large enough to see individually, as shown in Fig. 4.1.

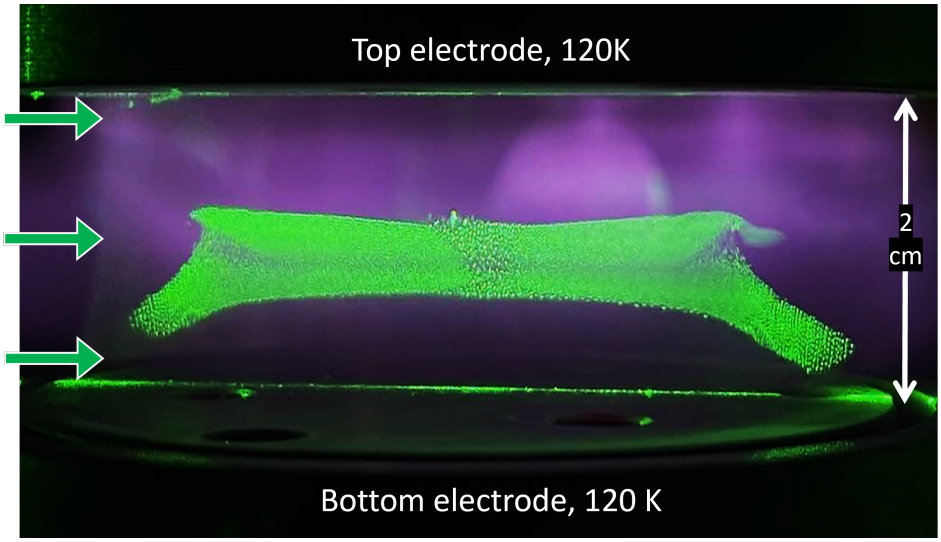

Figure 4.1: Micron-sized grains visible in the plasma.

To be visible through laser scattering, the ice grains must reach sizes comparable to the laser wavelength used to image them (here $\lambda = 532$ nm). When particle size $r << \lambda$, they Rayleigh-scatter the laser with an intensity that scales with r^6/λ^4. To be bright enough to see with the naked eye [71], the grain must grow to $r \gtrsim 30$ nm.

To be detected, therefore, the grains must both nucleate (that is, form a stable ice condensate from the vapor phase) *and* grow significantly by accreting additional H_2O— growing three orders of magnitude, from the Angstrom-scale of a small H_2O cluster to the ~ 10-nm scale that is optically detectable. It thus becomes difficult to distinguish experimentally between lack of grain *nucleation* and lack of grain *growth*.

With this in mind, we can map the experimental parameter space in which grains form and grow to a visible size. In hydrogen plasma, grains consistently appear at pressures between 400 and 2000 mTorr. Outside this range, formation is sparse, although grains can be formed within this window and then brought to lower or higher pressures. Grains form visibly only below electrode temperatures of about 180 K— significantly lower than water's freezing point (~230 K at these pressures).

RF power and electrode spacing show no clear influence on ice formation, in contrast to observations by Chai & Bellan [72]. At high power, grains tend to be displaced towards the electrodes, making them less visible, but they

still form and grow. If power is reduced, they again spread throughout the plasma.

Gas species play a major role in growth behavior. In agreement with Chai & Bellan [63], we confirm that lighter gases form larger grains: in hydrogen, grains illuminated by the laser become easily distinguishable from one another within a few minutes, while in argon, they frequently remain too small to distinguish individually, scattering only a diffuse glow of laser light; this is indicative of the Rayleigh scattering regime, in which particle size is below the wavelength of the scattering light.

Formation also depends on vapor flow rate and the procedure of its injection. Water vapor is introduced through a 1/4-inch pipe at the electrode midplane; above about 20 SCCM, the flow blows grains out of the plasma. Below roughly 5 SCCM, we do not observe new grain formation: vapor density is likely too low for effective nucleation and growth. Interestingly, steady vapor flow is not required in hydrogen plasma, especially at lower pressures. Instead, ice growth can actually *accelerate* after vapor shutoff, provided vapor was injected for at least several seconds initially. The ice grains then remain in the plasma for tens of minutes without significantly sublimating. In contrast, in argon plasma and at higher pressures of hydrogen, grains typically vanish within a few minutes of stopping the vapor injection.

4.2 Experimental sequence

Going forward, I focus solely on the effect of temperature and pressure on ice formation. To maintain consistency and narrow the experiment's daunting parameter space, data was collected using a standard procedure and run parameters (gas species, RF power, electrode separation, water and injection). There is nothing particularly special about these parameters, chosen just because they repeatably produced large, visible ice grains.

Each run followed this procedure: electrodes were brought to temperature, hydrogen gas was introduced at low pressure, and plasma was ionized with 75 W forward RF power. Electrode spacing was fixed at 2 cm. Experiments were conducted from 80 K to 150 K in 10 K increments, each with background pressures of 400, 800, and 1600 mTorr. Once the plasma was established, water vapor was injected at ~ 5 SCCM from a $1/4$-inch tube 3 cm from the outer rim of the electrodes. Ice grains spontaneously formed during this

"vapor deposition period." At $t = 2$ minutes, the water flow was halted, leaving ice grains confined in the plasma to evolve over time.

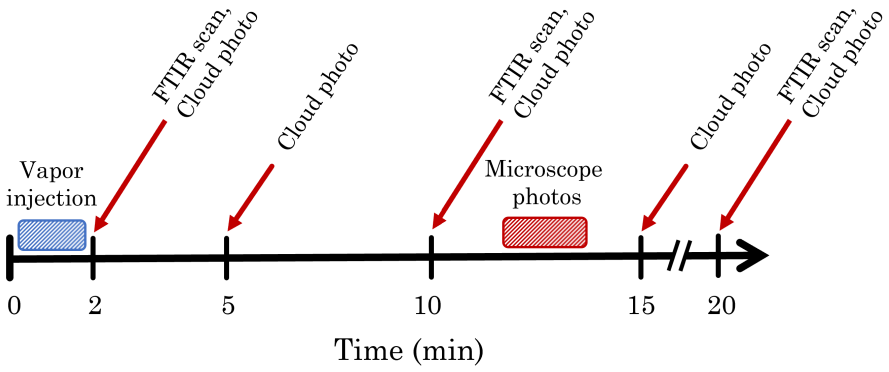

Figure 4.2: Experimental timeline. In the first two minutes, a steady flow of vapor is inputted. FTIR scans and wide-angle laser scattering photos of the ice cloud are taken at $t = 2$, 10, and 20 minutes; cloud photos are also taken at 5 and 15 minutes. Microscope photos are taken between 10 and 15 minutes.

Each experimental run lasted 20 minutes; a timeline is shown in Fig. 4.2. At $t = 2$ (at vapor shutoff), 10, and 20 minutes, IR transmission scans were taken with the FTIR spectrometer, and the ice cloud was imaged using laser sheet scattering. In addition, several photos were taken with the long-distance microscope photos between 12- and 15-minute mark.[1]

4.3 Results of direct imaging

Figure 4.3 compares laser scattering photos at two pressures (400 and 1600 mTorr), $t = 2$ and 10 minutes after ice formation. Panels (a) and (b) show two different temperatures. In experiments at 400 and 800 mTorr, scattering gets brighter over time, indicating ongoing grain growth. Conversely, at 1600 mTorr, the size and brightness of the ice cloud decrease significantly by 10 minutes. This suggests that at high pressure, sublimation outcompetes accretion of vapor molecules.

At all pressures, more ice generally appears at 130 K than at 90 K, suggesting that nucleation and/or growth is less efficient at colder temperatures. This

[1]The microscope had to be refocused in each run, so exact timing was not feasible.

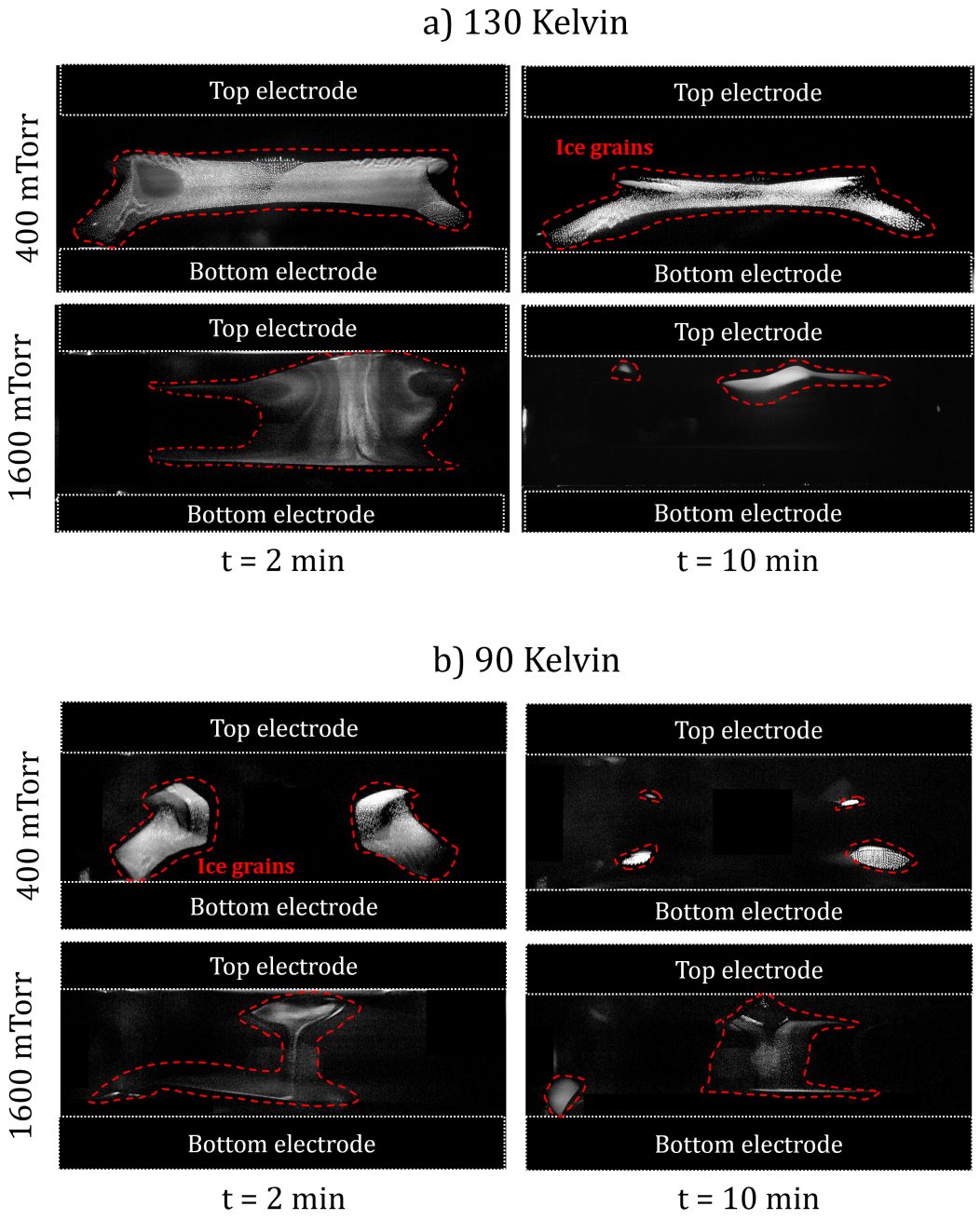

Figure 4.3: Wide-angle photos of laser sheet scattering. Panel (a) is at 130 K, and panel (b) at 90 K; each panel shows two pressures (400 and 1600 mTorr) and two points in time (t = 2 and 10 minutes). Photos at other parameters (p, T, t) are available through a data repository at doi:10.22002/x3qp1-3k378.

temperature trend persists across the entire 80 K to 150 K temperature range, with higher temperatures leading to larger and brighter ice clouds.

Images collected through the long-distance microscope lens are shown in Fig. 4.4 for various temperatures and pressures. Grains have a spindle-like, branching dendritic shape. They also tend to be elongated, and align in the vertical direction. This is similar to ice grains observed in previous experiments using the "Mk. I" apparatus [24, 63].

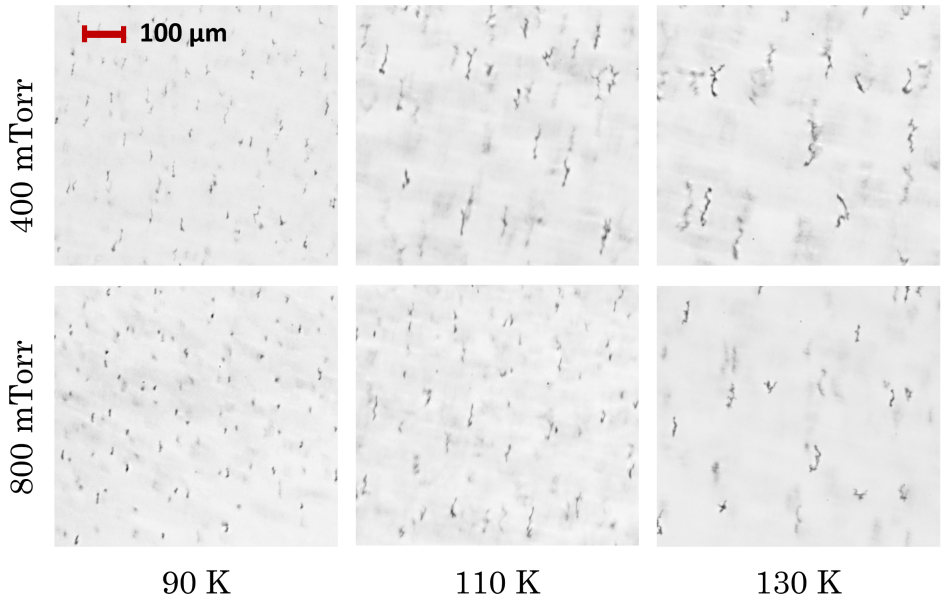

Figure 4.4: Microscope photos taken 10 minutes after grain formation. Four temperatures and two pressures are shown; at 1600 mTorr, grains were smaller than the microscope resolution.

Size dependence on pressure and temperature

Between 80 and 150 K, grains were generally larger under the *warmer* conditions. Grain size scaled inversely with pressure, consistent with observations by Chai & Bellan [63]; this indicates that grain size generally increases with the inverse of the gas density ($n \sim p/T$). The average grain size, measured from microscopy at $t = 10$ minutes in each experimental run, is plotted against electrode temperature in Fig. 4.5 at both 400 and 800 mTorr.

Notably, the dependence at 400 mTorr is not linear, instead reaching a peak around 130 K. This nonlinearity suggests a balance between multiple growth and decay mechanisms: for example, more molecular mobility at lower den-

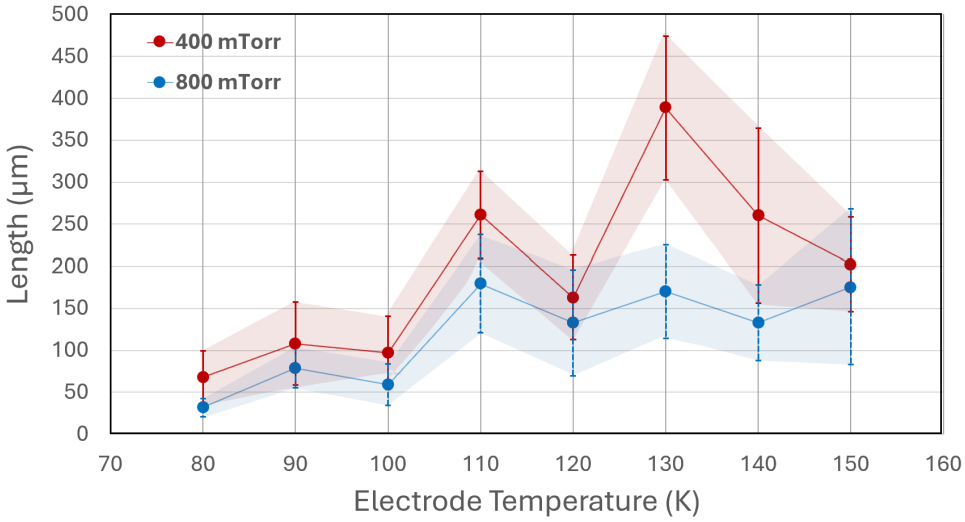

Figure 4.5: The average grain length obtained from long-distance microscope photography, taken at $t = 10$ min, and the standard deviation in length between various grains. Plotted against electrode temperature, for gas pressures of 400 and 800 mTorr.

sities allows faster accretion, while higher sublimation rates at temperatures above the peak disallow grains from becoming as large.

Fractal morphology of the ice grains

Larger grains appear to be more "fluffy," and smaller grains more densely-packed; this increasing porosity with size indicates that grains do not fill 3D space during growth, a characteristic of fractal morphology [73]. This is described by a fractal dimension, a measure of how well a grain fills its encompassing space, determined by the scaling law:

$$\text{Area} \sim L^{D_2}. \tag{4.1}$$

Quantitatively, the "box-counting" fractal dimension of a grain is defined by tiling the grain of size L with boxes of side length x, counting the number of boxes N_B, and plotting how L/x varies with N_B; on a log-log scale, the slope gives D_2 [74].

For each single grain, we vary the box size x and find the fractal dimension using:

$$D_2 \log_{10}(L/x) = \log_{10}(N_B) \tag{4.2}$$

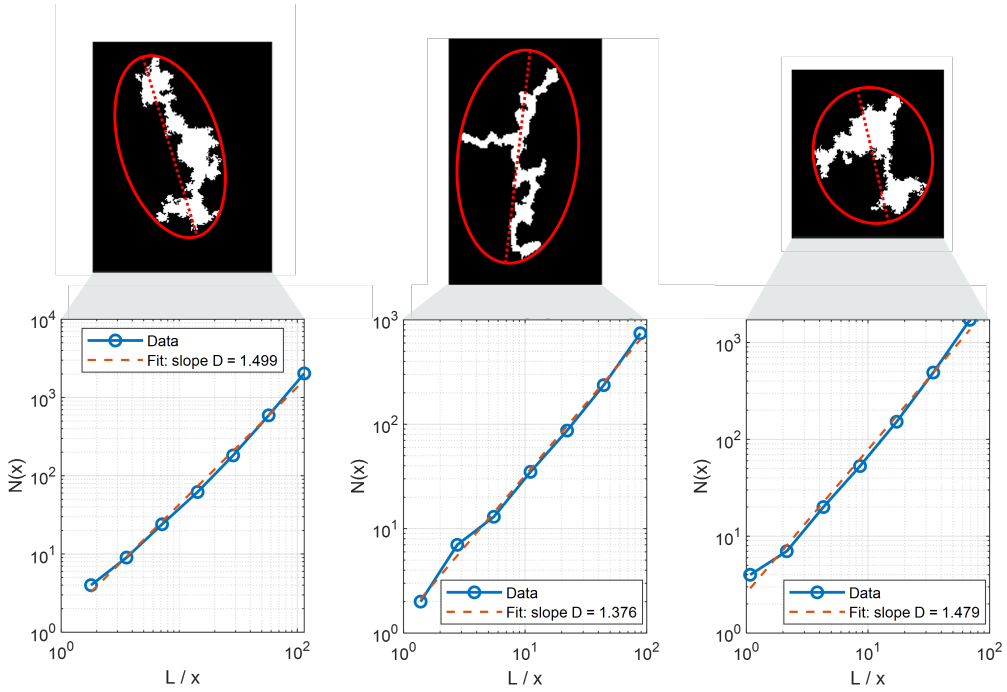

Figure 4.6: Box-counting results for three large grains. Total lengths L are defined by the major axis of a fit ellipsoid. Graphs show box-counting plots ($N_B(x)$ vs L/x) for the corresponding grains above, resulting in $D_2 \sim 1.5$.

Obtaining a reliable fractal dimension requires varying x by several orders of magnitude. This is shown for several large grains in Fig. 4.6. These grains show dimensions D_2 around 1.4–1.5. This is consistent across the large grains we have measured, with D_2 typically falling between 1.35 and 1.55.

Box-counting relies on varying L/x by several orders of magnitude to obtain D_2. As we cannot decrease x below the microscope resolution, about ~ 3 μm, box-counting does not give reliable results for grains smaller than 100 microns or so.

As most of our measurements— such as light scattering and absorption, dynamics of the ice cloud, and electrical properties— are bulk properties of the ice-dusty plasma, averaged over a large collection of grains, it is useful to have a "bulk" fractal dimension, that is, some average across all the grains of all different sizes [73, 75]. Rather than perform boxcounting for *each grain individually*, we here assume that *all* grains grow with roughly the same fractal dimension. We can then hold x fixed at the pixel size of the photos, and compare different grains of differing lengths L; this allows applying Eq.

4.2 over a wider range in L/x, giving a *bulk* D_2 that is valid over a wider range of grain sizes.

A plot of N_B vs. L is shown in Fig. 4.7, as well as several grains of different sizes. A linear regression yields $D_2 = 1.465 \pm 0.199$. We note that this value is in the same range as those of *single*, large grains; this affirms our assumption that the fractal dimension is relatively consistent between grains of different sizes.

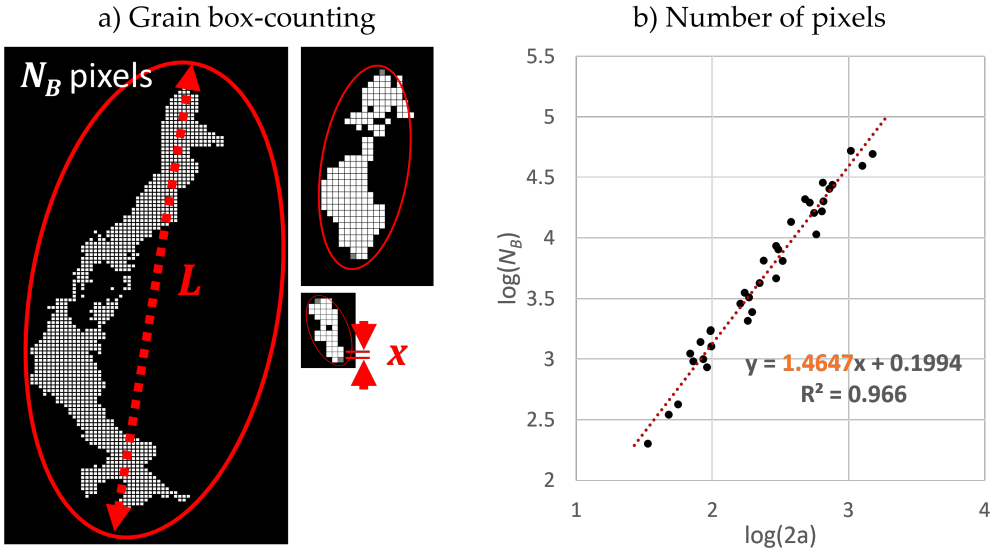

Figure 4.7: Computing the fractal dimension of the bulk of ice grains: (a) Grain images fit with an encompassing ellipsoid with axes $(a,\ b)$, tiled with N_B pixels of size x. (b) Length $2a$ plotted against N_B on a log-log scale gives a slope equal to the fractal dimension, $D_2 = 1.465 \pm 0.199$.

We note that this is the scaling dimension of the grain cross-sectional area; a volume-dimension D_3 would require a 3-dimensional model of the grain, which we have not yet achieved. Several correlations from simulations are available to relate D_3 to D_2 [76, 77], but these have underlying assumptions about aggregation mechanics or composition that likely do not hold under our conditions. The volume dimension *can* be extracted from grain dynamics, as shown by Rahmani *et al.* [75]; this is pursued in Chapter 7.

The fractal ice in this experiment is morphologically quite similar to grains made in diffusion-limited aggregation (DLA) simulations [73, 76, 77], in which accreting monomers collide and stick through Brownian motion. However, our ice has a lower fractal dimension— $D_2 \sim 1.5$, rather than ~ 1.7

for DLA [73]. This indicates that the ice grains are more "fluffy," with a less space-filling structure than DLA aggregates. We attribute this to electrostatic effects first cataloged by Bartlett [25] that fundamentally alter both deposition dynamics and internal restructuring. Electric fields become concentrated at the sharp tips of the dendrites, and lens polar H_2O molecules and small charged grains into the aggregate, promoting anisotropic growth [25, 26, 78]. These forces break the free-diffusion assumptions of DLA, leading to a more filamentary, sparsely-packed structure [75].

Furthermore, electrostatic effects can cause grain restructuring: simulations by Kritikos *et al.* [79] showed that electrostatic stresses lead to elongation of grains on the nanometer scale, which could stretch the dendrites. It has also been suggested that ion bombardment of the grains can cause a thin quasi-liquid layer to form on the ice surface, even at ambient temperatures far below what classical theory predicts [26]. This allows molecular mobility of the surface H_2O toward electric field maxima.

These observations are of particular relevance to astrophysics: fractal dust grains have long been postulated to exist across planetary, interstellar, and intergalactic environments [1, 37, 80–82]. Their proposed fractal dimensions vary with precursor chemistry [37, 83], acquired charge [24, 78, 84], and details of the aggregation dynamics [76]: for example, organic aerosols in Titan's atmosphere are thought to span a broad range of dimensions, depending on specific precursor compounds [37]. The optical properties and surface interactions of fractal structures are not well understood, limiting data collection through telescopes; these laboratory studies are thus the only direct window into their formation, optics, and behavior in these faraway environments.

4.4 Characterization from IR scattering

The Fourier Transform Infrared (FTIR) spectrometer transmits a modulated beam of infrared light, ranging from 800-4200 cm^{-1}, through the plasma and ice cloud (see Sec. 3.5). A detector measures the transmission spectrum; by subtracting a background scan taken in the absence of ice and plasma, we obtain an extinction spectrum, which measures the combined absorption and scattering from the ice-dusty plasma over this infrared wavelengths. The absorption spectrum is a material property, dependent on the ice composition

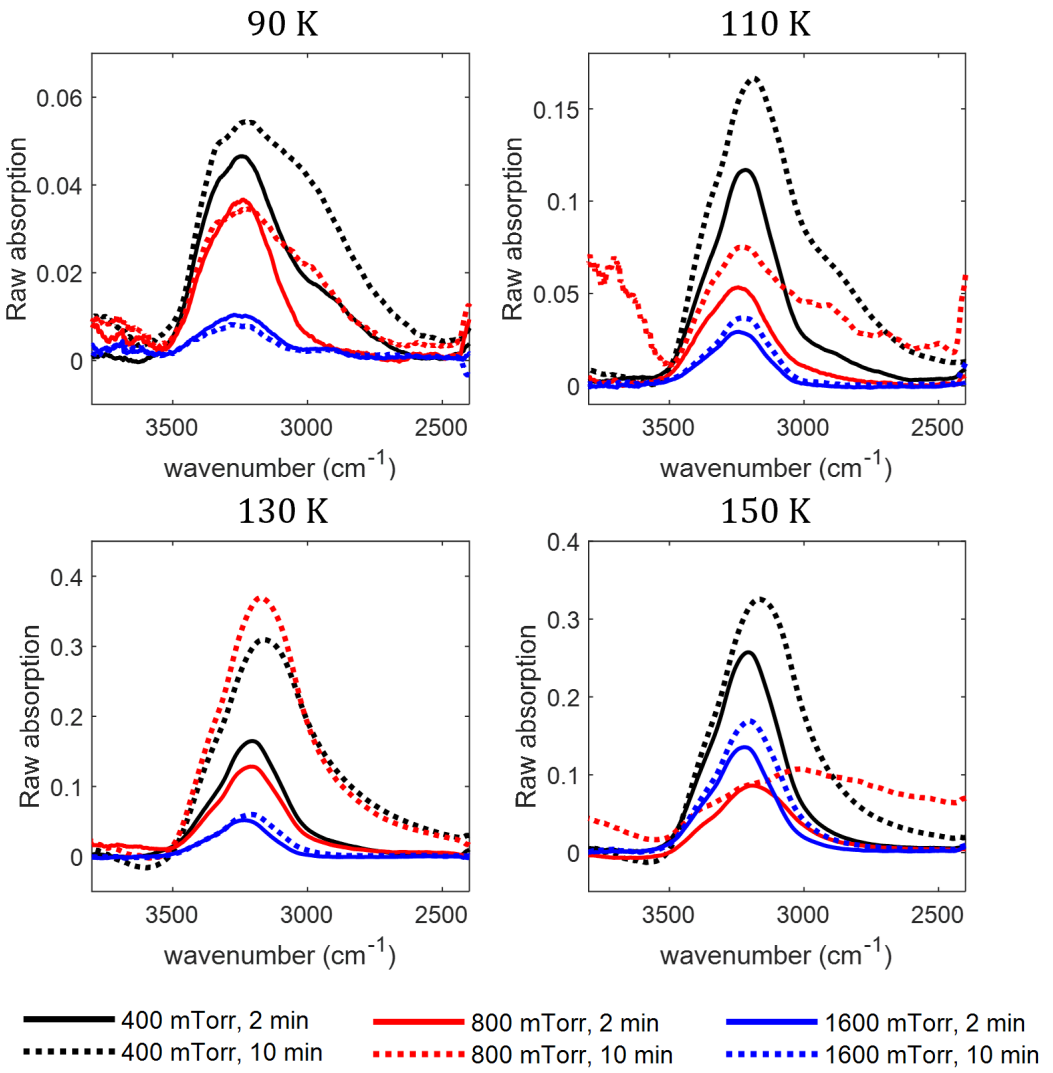

Figure 4.8: Spectra taken at 90, 110, 130, and 150 K. All three pressures tested are shown. Solid-line spectra are taken at $t = 2$ min, and dotted-line spectra at $t = 10$ min.

and phase structure, while the scattering depends also on the grain size and geometry.

Extinction spectra measured by the FTIR spectrometer in the range reveal strong absorption band by water ice in the region near 3200 cm^{-1} ($\sim$ 3 microns); this is shown in Figure 4.8. The magnitude and shape of the extinction curves vary with the temperature, pressure, and time since ice formation. This absorption band arises as photons excite vibrational energy in the ice lattice's O-H bonds. The shape of the absorption band thus depends on the phase structure of the ice, as detailed in the next chapter.

Absorption magnitude

The magnitude of the IR absorption peak varies with the quantity of ice that intercepts the IR beam, and the product of the number of grains and their volumes. The signal is thus sensitive both to changes in the total amount of ice deposited in the plasma and to movement of the ice cloud in or out of the IR beam path.

The magnitude of the absorption spectrum is larger when the electrode temperature is higher: At 90 K, the absorption magnitude is 3-5 times smaller than the absorption at 130 K. Additionally, the absorption magnitudes are considerably smaller at higher pressure; the absorption magnitude therefore correlates with the observed grain size. Thus, when grains are smaller, less total ice is contained in the plasma; the small grain size is *not* countered by higher densities of ice grains. This suggests less-efficient nucleation at lower temperatures, in agreement with laser scattering observations.

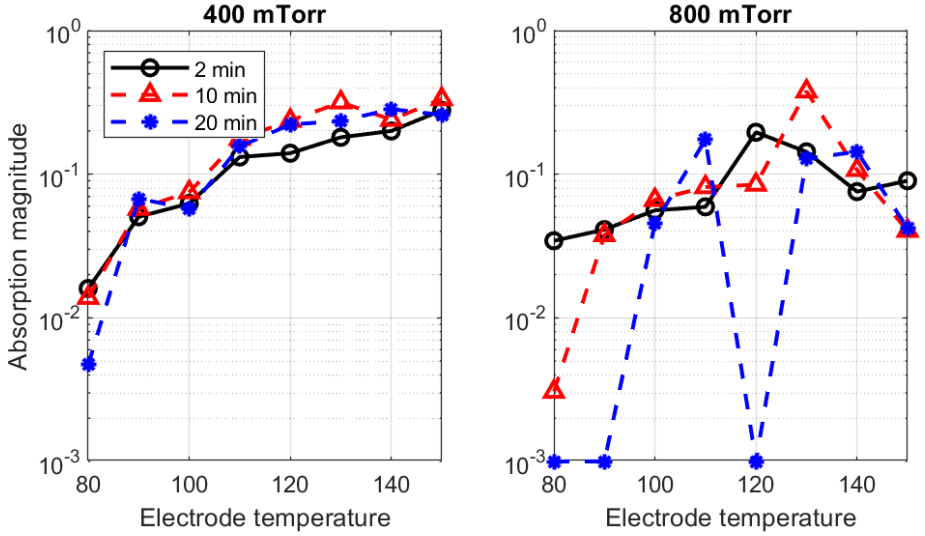

Figure 4.9: Peak intensity of the absorption spectrum with temperature, pressure, and time since formation.

The IR absorption changes in time to various extents typically more variable as the electrode temperature increases. In scans at 400 mTorr we observe little change in absorption between the 2- and 10-minute scans at 90 K , while at 130 K, the absorption peak magnitude increases significantly over time (see Fig. 4.9, left). At 800 mTorr there is more variation between temperatures, and a trend is less obvious (Fig. 4.9, right).

As the inflow of water vapor was shut off after $t = 2$ minutes, there is no "new" water in the chamber during these changes in absorption intensity. The increase in IR extinction in this time frame is therefore entirely due transport of the available water into the FTIR beam path: ice that initially deposited on the electrodes may sublimate and re-deposit on the ice grains, while small grains on the outskirts of the plasma may grow and be pulled into the IR beam by electrostatic forces, or sublimate away, re-depositing their vapor to other grains.

Because sublimation happens more readily at higher temperatures, grains at 130 K are immersed in a higher partial pressure of water vapor than those in colder conditions, and grow through accretion faster than do grains at lower temperature. Meanwhile, the diffusion time of water molecules is higher at higher pressures (at the same temperature), and thus deposition rates are lower, causing slower ice growth and higher variability.

Mie scattering and grain size

The shape of the extinction spectrum changes over time due to two effects: wavelength-dependent scattering of the IR beam from the grains, and phase transitions of the ice itself, which affects the absorption band. The former effect will be used to quantify ice growth in this section, while the latter will be explored in detail in the next chapter.

Light scattering by small particles falls into three regimes: [68]:

1. Rayleigh scattering: for particle size r much smaller than the incident wavelength λ, the intensity increases monotonically with r^6/λ^4.
2. Geometric scattering: for $r >> \lambda$, scattering intensity varies with the geometric cross section $\sim r^2$, and is independent of wavelength
3. Mie scattering: intermediate case for $r/\lambda \sim 1$. Scattering intensity shows nonlinear oscillations with r/λ.

As the FTIR beam sweeps over 1-10 μm wavelengths, grains much smaller than the wavelength ($r/\lambda \ll 1$) do not have significant scattering; the signal reflects pure absorption, similar to the signal from a thin film of ice [2, 85].

Grains much larger than the wavelength, meanwhile, attenuate all wavelengths equally, and thus do not alter the shape of the extinction spectrum. However, grains of comparable sizes to the beam Mie-scatter each wavelength with different intensity, skewing the shape of the absorption band quite considerably [68, 85].

The solid lines in Figure 4.10 show normalized extinction spectra taken at 400 mTorr over a range of temperatures, at 2, 10, and 20 minutes after ice formation. At $t = 2$ minutes, the spectrum has a band that matches the pure-absorption spectrum of ice in literature [22]; at later times, the grains grow, and the spectrum is broadened and shifted due to Mie scattering. These extinction spectra can thus be used to determine an effective particle size from Mie theory; I here apply a method developed by Clapp *et al.* [85] to extract the grain size.

Mie scattering theory requires knowledge of the grain's *complex index of refraction* $\bar{n} = n - ik$, a material property that varies with the frequency of light ω. The imaginary component $k(\omega)$ is the absorption coefficient, and the real component $n(\omega)$ is the traditional refractive index.

In the initial spectrum taken at $t = 2$ min, grain size $r << \lambda$, and thus we can assume the spectrum contains no wavelength-dependent scattering. This initial spectrum is therefore used as the absorption coefficient $k(\omega)$ of the ice.

Next, we require $n(\omega)$; because the complex index of refraction $\bar{n}$ is analytic in the complex plane[2], they are related by the Kramers-Kronig transformation [68]. Using its subtractive form [85],

$$n(\omega) = \frac{2}{\pi}(\omega^2 - \omega_0^2)P\int_0^\infty \frac{w'k(\omega')dw'}{(\omega^2 - w'^2)(\omega_0^2 - w'^2)} + n(\omega_0), \tag{4.3}$$

where P indicates taking the Cauchy principle value of the integral. The wavenumber ω_0 is an "anchor point" at which the index of refraction is known; here we use $\omega_0 = 4000$ cm^{-1}, at which $n(\omega_0) = 1.232$ [85]. These "optical constants" n and k are properties of the material, independent of the grain geometry.

[2]Note n and k are consequences of the same physical process— light interacting with a lattice of molecules— they are not independent phenomena, but two aspects of the same response function.

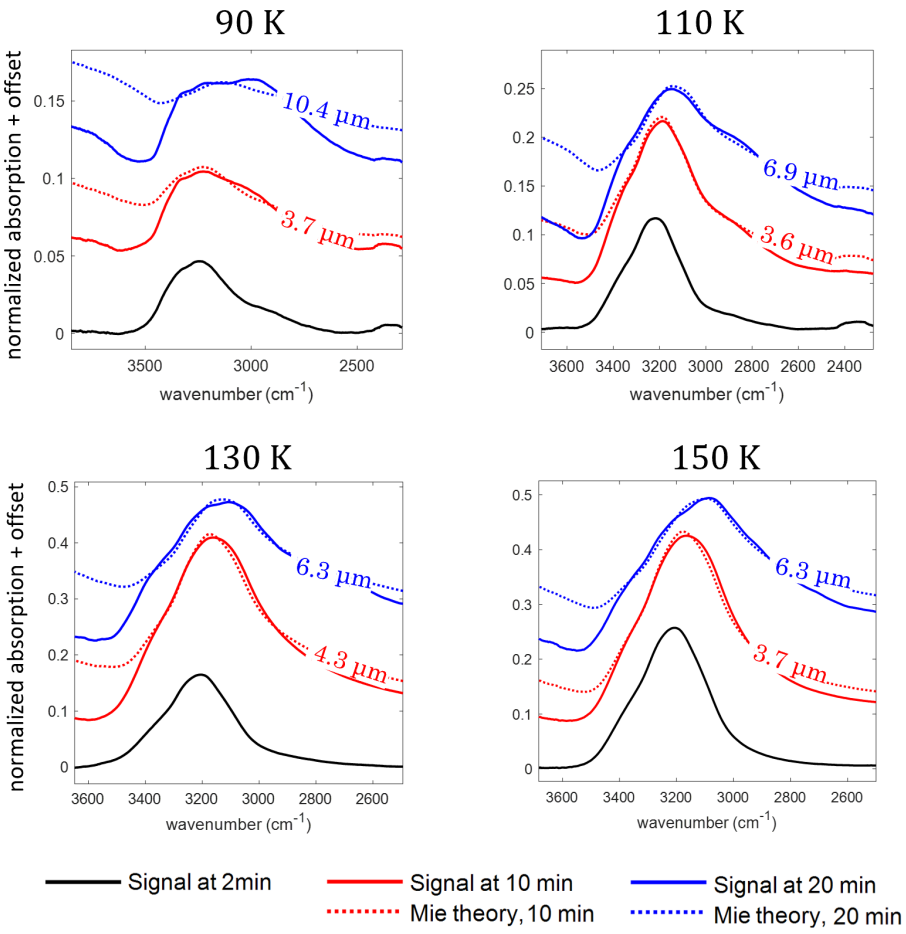

Figure 4.10: Spectra obtained at $t = 2$, 10, and 20 minutes, and Mie scattering fits to the $t = 10$ and 20-minute spectra. Shown are spectra taken at 400 mTorr, and temperatures of 90, 110, 130, and 150 K. Curves are offset in the y-direction for clarity. Mie fit radii and uncertainties at all pressures and temperatures are presented in Fig. 4.11.

The optical constants can then be used to predict the extinction spectrum off arbitrarily-sized particles. This method has associated challenges: most notably, Mie scattering is an unsolved problem for irregular grain morphologies—only scattering from spheres and infinite cylinders have known solutions. We here use a spherical model to obtain a decent fit to the data, noting that the multi-scale, fractal nature of the grains will cause some divergence in the fit [86].

The optical constants $n(\omega)$ and $k(\omega)$ are inserted into a Mie scattering algorithm by Bohren & Huffman [68] (the BHMie code), along with a "guess" of particle radius r. The algorithm calculates an extinction spectrum of uniform

spheres of size r with the input optical constants. Multiple spectra are computed for a large range of input radii. These are compared to the measured extinction spectra, taken at $t > 2$ min. The best fit between the theoretical and observed spectra gives the effective Mie scattering radius of the grains in the associated FTIR scan. These fits are plotted in Figure 4.10 (dotted lines) for the 400 mTorr spectra at a range of temperatures, and yield effective radii between 1 and 14 microns.

Overall, this simple Mie scattering method well-replicates the observed time dependence of the spectrum. The model fits observations very well around the absorption band, but diverges on the high-wavenumber side when grains are large. This is most likely due to the non-spherical grain structure and multitude of intrinsic length scales within the grain [86]. While scattering of the absorption band will be most strongly affected by grain structures of a similar scale (~ 3 μm), other grain structures of different length scales will contribute scattering that the BHMie code cannot replicate.

Comparison between Mie theory and direct imaging

Figure 4.11 (a) – (c) present effective radii from Mie scattering versus temperature. Generally, effective radii increase with temperature at 800 mTorr and 1600 mTorr, while this trend is not evident at 400 mTorr. At 400 and 800 mTorr, ice grains generally grew between the spectral scans at 10 and 20 minutes. At 1600 mTorr, ice vanished by the 20 minute mark due to more rapid sublimation.

In Figure 4.11 (d), grain lengths from microscope images taken just after $t = 10$ minutes are plotted against temperature. Similar to the Mie scattering results, grains are larger at higher temperatures at 800 mTorr, with a less clear trend at 400 mTorr. Notably, there is a tenfold difference between measured grain lengths and Mie scattering-derived radii shows. The ratio of grain length to Mie scattering diameter is displayed in Figure 4.12 (a). This ratio fluctuates anywhere between 4 and 20, with a modal average value around 12, and does not have an obvious dependence on temperature.

This discrepancy is attributed to the elongated, fractal grain shape and its low dimension. At most polarization angles, infrared radiation intercepts a cross-section on the order of the width of the ice grain, rather than its total length: the Mie scattering spectrum is dominated by this width of

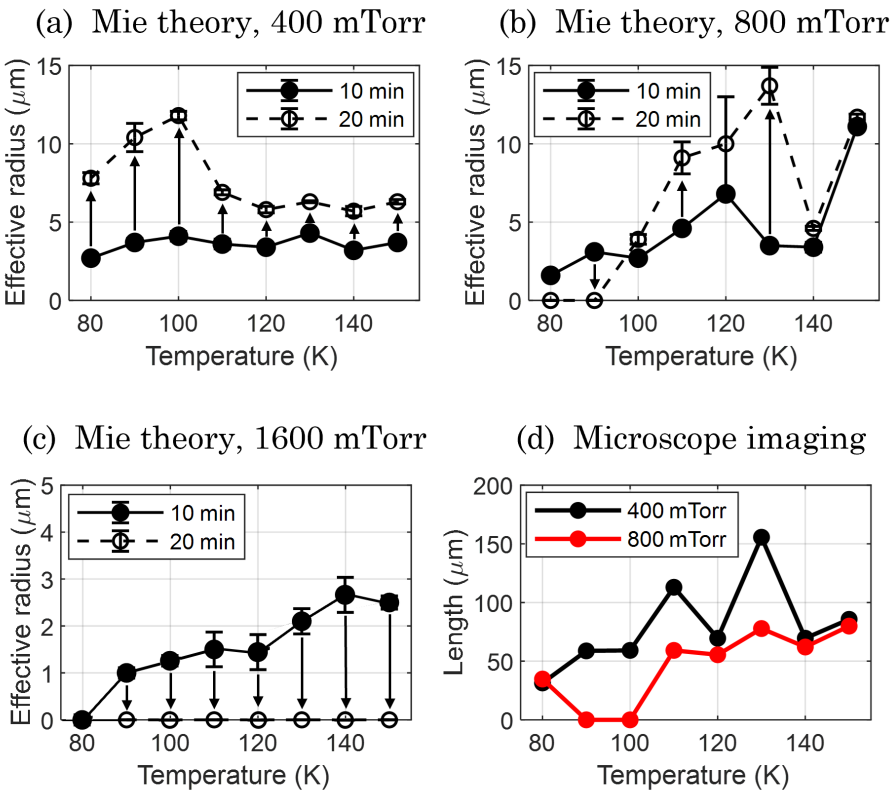

Figure 4.11: Trends of grain size with temperature and time. Graphs (a) through (c) show effective Mie scattering radii at different pressures; closed circles are radii at 10 minutes, and open circles are radii at 20 minutes. Arrows indicate size change over time. Graph (d) is the grain length from microscope photos, taken after $t = 10$ minutes.

a comparable size to the scattering wavelengths. Because of the limited resolution of the microscope photos, precision measurement of the width is not possible for most grains. Photos of some exceptionally large grains, in which their widths are within camera resolution, are shown in Figure 4.12 (b). These images exhibit aspect ratios ranging from 13 to 16. These are comparable in magnitude to the ratio of length to Mie scattering diameter shown in Figure 4.12 (a), providing some explanation for the discrepancy between microscope measurements and Mie theory calculations.

4.5 Toward a model of grain growth and demise

While our experiment provides novel measurements of ice grain growth rates, similar plasma-based particle growth has been well characterized in

(a) Ratio of Mie radius to grain length

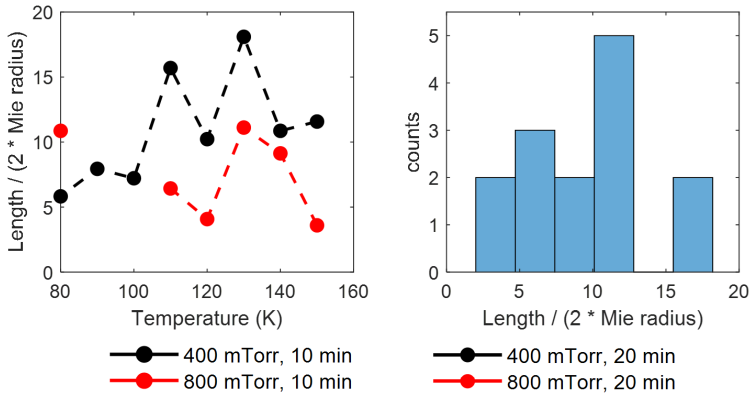

(b) Grain aspect ratio

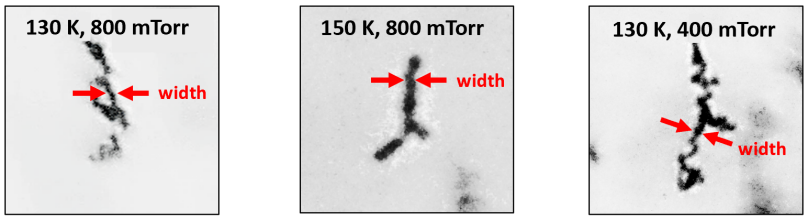

Length: 101px
Width: 7px
Aspect ratio: 14.4

Length: 85px
Width: 11px
Aspect ratio: 13.5

Length: 127px
Width: 8px
Aspect ratio: 15.9

Figure 4.12: (a) Plot of ratios between grain length (microscope photos) and Mie scattering effective radii ($t = 10$ min) for 400 and 800 mTorr configurations. Plot at left shows variation with temperature, and plot at right shows a histogram of all data points. (b) Microscope photos of grains in which the width can be resolved. Grain width is measured across the thinnest part of the grain. Images are compressed to roughly 2 microns per pixel.

argon-silane systems used in manufacturing [66, 87]. There, the accepted model of growth proceeds in three phases:

1. **Nucleation:** Nanometer-scale particles form but remain small until a critical number density is reached.

2. **Agglomeration:** The nanoparticles collide and form aggregates quickly (< 1 second). For some materials there is *restructuring*, where the aggregates collapse and fuse into a solid spherical particle; this clearly does *not* happen for our ice grains.

3. **Molecular Accretion**: Aggregates grow by accreting single molecules, a significantly slower process (10s of minutes).

Observations of ice growth mostly agree with this model, but are affected by the high volatility and dipole moment of water molecules. In this section I propose an analogous model for ice grain formation in our experiment, guided by observed growth behavior.

Nucleation and monomer growth

Nucleation occurs mainly through ion-induced nucleation around negative ions [1, 13, 30, 31, 88] (See Chapter 6); thus initially, grains are singly-charged negatively. Once grain radii begin to exceed about a nanometer, a significant current from colliding electrons causes grains to acquire high negative charge from the plasma.

Each of these spherical "monomer" ice grains can continue to grow in radius through molecular accretion or agglomeration with another ice monomer. The rates of these processes are both controlled by the grain charge: the accretion rate is increased as polar water molecules are attracted to the charged grains, while the agglomeration rate is decreased as the ice monomers are repelled by their like charges.

During vapor deposition, assuming high supersaturation ($p_{\mathrm{H_2O}} >> p_{\mathrm{sat.}}$),[3] the free mass flux of H_2O to the monomer surface is:

$$J_{H2O} \approx m_{H_2O}\, n_{H_2O} \sqrt{k_B T / m_{H_2O}}\,. \tag{4.4}$$

A charged monomer will attract surrounding water molecules through a charge-dipole force, associated with an electric potential energy that scales with distance as $1/d^2$ inside the Debye sphere. The deposition rate is therefore enhanced by a Boltzmann factor $\exp(-U_E/k_B T)$, where U_E. is the electric potential energy. For a spherical monomer of size r, the rate of change of the mass is equal to $4\pi r^2 J_{H_2O}$, and thus $\mathrm{d}r/\mathrm{d}t = J_{H_2O}/\rho_{ice}$: the radius grows linearly in time. This gives a growth rate:

$$\frac{\mathrm{d}r}{\mathrm{d}t} = \frac{m_{H_2O}\, n_{H_2O}}{\rho_{ice}} \sqrt{\frac{k_B T}{m_{H_2O}}} \exp\left(\frac{e Z_d\, p_E}{4\pi\epsilon_0 r^2\, k_B T}\right), \tag{4.5}$$

[3] Note at low p and T, saturated vapor pressure is very low, which makes it easy to be supersaturated

where p_E is the electric dipole moment of water. Using $p_E = 6 \cdot 10^{-30}$ C $\cdot$ m and $T = 150$ K, the argument in the exponential is approximately $4{\cdot}10^{-18}/r^2$—the growth rate of a singly-charged 1 nm grain is enhanced by a factor of $\exp(4) \approx 54$, while that of a 10 nm grain is enhanced by $\exp(0.04) \approx 1.04$.

Further, OML theory predicts a surface charge that increases linearly with radius ($Z_d \sim r$), so the argument of the exponential scales with $1/r$ rather than $1/r^2$ at larger size, causing electrostatic lensing to remain relevant as grains grow larger. Integrating Eq. 4.5, we estimate that a grain will grow from 1 nm to 100 nm in several milliseconds.

It must also be noted that these monomers are likely *not* spherical: as shown by Kritikos *et al.* [79], electrostatic stresses will cause charged, nanometer-scale grains to elongate into ellipsoids. Further, any surface perturbations will cause local electric field maxima that will more strongly attract incoming molecules, driving asymmetric growth [25, 26]. Both these effects increase the surface area of the ice monomer relative to its volume, increasing the accretion rate and the OML charge [66, 78, 84].

Onset of coagulation

The coagulation rate of two uncharged, spherical monomers in the cloud is given by:

$$\begin{aligned} \nu_0 &= n_{mono} \langle \pi r^2 v \rangle \\ &= n_{mono} \pi r^2 \sqrt{k_B T / m_{mono}}. \end{aligned} \tag{4.6}$$

If the monomers have identical charges and the velocity is thermally distributed, the coagulation rate must be multiplied by a Boltzmann factor $\exp(-U_{coag}/k_B T)$, where U_{coag} is the electric energy barrier:

$$U_{coag} = \frac{(eZ_{mono})^2}{4\pi\epsilon_0 (2r)}. \tag{4.7}$$

This barrier strictly forbids coagulation *unless* the monomers grow to tens of nanometers *and* charge is limited to 1-2 electrons per grain. This is only possible through the Havnes effect, when the monomer density is high enough to strongly deplete electrons ($H \to 1$), limiting grain charge. Practically, this can only take place when the grain density approaches the electron density.

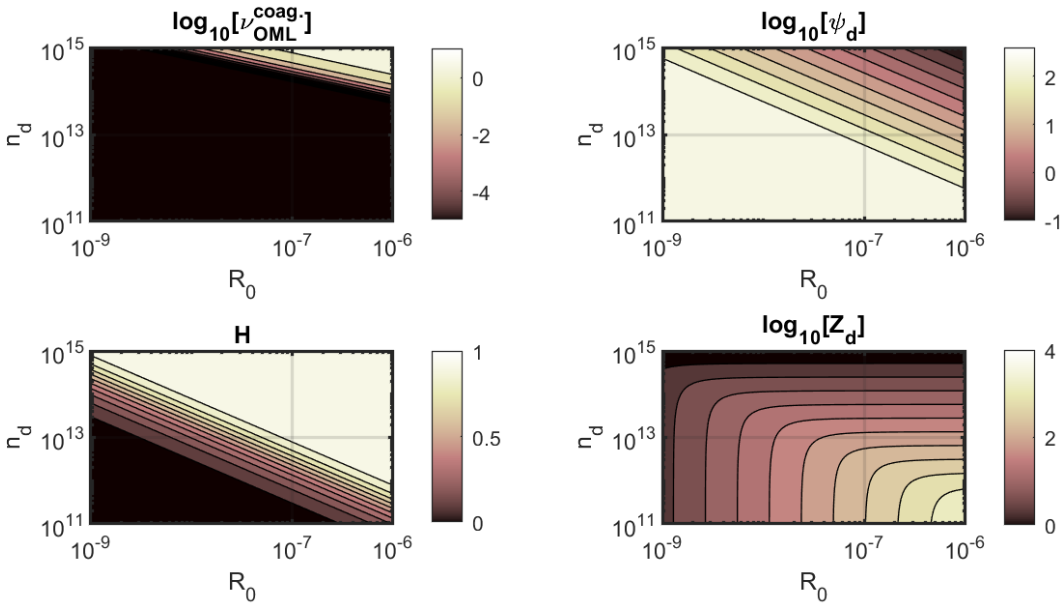

Figure 4.13: Coagulation frequency, incorporating OML charging and the Havnes effect, shows that monomers of size $r = R_0$ can coagulate at high radius and density, corresponding to high electron depletion and low grain surface potential. In this computation, $n_i = 10^9$ cm^{-3}, $T_i = 150$ K, and $T_e = 1$ eV.

Using a full OML treatment to calculate monomer charge (see Sec. 2.1), the dependence of coagulation frequency ν on monomer radius and number density is shown in Fig. 4.13, along with the developed grain charge, surface potential, and Havnes parameter H. This shows a sudden rise in coagulation frequency at high n_d and r, associated with a drop in surface potential. This is associated with measurable changes to the RF discharge parameters due to electron depletion, referred to in literature as the $\alpha \rightarrow \gamma'$ transition [66, 67, 89]

The "monomer growth" phase, therefore, continues until the density of grains approaches the electron density, resulting in an electron depletion, consistent with measurements by Eschbach [90]. At this point, grains > 10 nm suddenly become able to coagulate.

Coagulation cutoff, slow accretion, and demise

The shape of the grains is evidence towards this coagulation occurring: the fractal structure of the grains closely mirrors those formed in aggregation simulations [76], in colloidal fluid systems [73, 91], and in other dusty plasma

experiments [16, 37], in which a monomer structure has been verified through scanning electron microscopy. However, coagulation explicitly does *not* occur once grains reach the micron scale: as reported by Marshall *et al.* [24], grains observable to microscope imaging are never observed to collide or stick to one another. The coagulation of like-sized aggregates must therefore be suppressed; larger grains can only accrete invisible (<1 μm) monomers, individual molecules, or clusters of molecules.

Grain density drops quadratically ($\dot{n}_d \sim \nu_{\mathrm{coag}} n_d^2$) during aggregation, which causes the Havnes parameter (see Ch. 2) to decrease and grains to charge more highly. Furthermore, each collision between like-sized grains causes the charge to double, suppressing further agglomeration of charged grains. Aggregates then accrete only the remaining singly-charged monomers, and eventually charge enough to repel even these; thus ends the fast agglomeration phase of growth.

The growth rate slows significantly; as previously shown by Mie scattering measurements (see Fig. 4.11) grain size can increase by a factor of 2-3 over the course of 10 minutes. This is driven by competing rates of accretion of individual molecules, the formation and accretion of ion-water clusters, and the formation and accretion of new monomers. These growth rates are counteracted by the sublimation rate especially at higher temperatures and pressures; if the sublimation rate dominates grains shrink and disappear. If we assume single-molecule accretion dominates, we can write this in terms of the vapor pressure:

$$\frac{\mathrm{d}m}{\mathrm{d}t} = \alpha\, \sigma \frac{m_{H_2O}}{k_B T}(p_{H_2O} - p_{eq}(\sigma)), \tag{4.8}$$

where α is some constant of order unity, σ is the grain cross-sectional area, p_{H_2O} is the partial pressure of water, m_{H_2O} is the molecular mass of water, and p_{eq} is the equilibrium vapor pressure above the ice grain of area σ, which can be estimated from the Kelvin-Thomson equation [92].

While the precise calculation of $\mathrm{d}m/\mathrm{d}t$ depends on the grain charge and the temperature-dependent saturated vapor pressure, the takeaway is that there is a critical grain surface area σ^*: larger grains will grow ($\mathrm{d}m/\mathrm{d}t > 0$), while smaller grains will shrink ($\mathrm{d}m/\mathrm{d}t < 0$). This explains why when water input is halted small grains formed in Ar or H at 1600 mTorr disappear fairly quickly, while larger grains in lower pressure hydrogen remain.

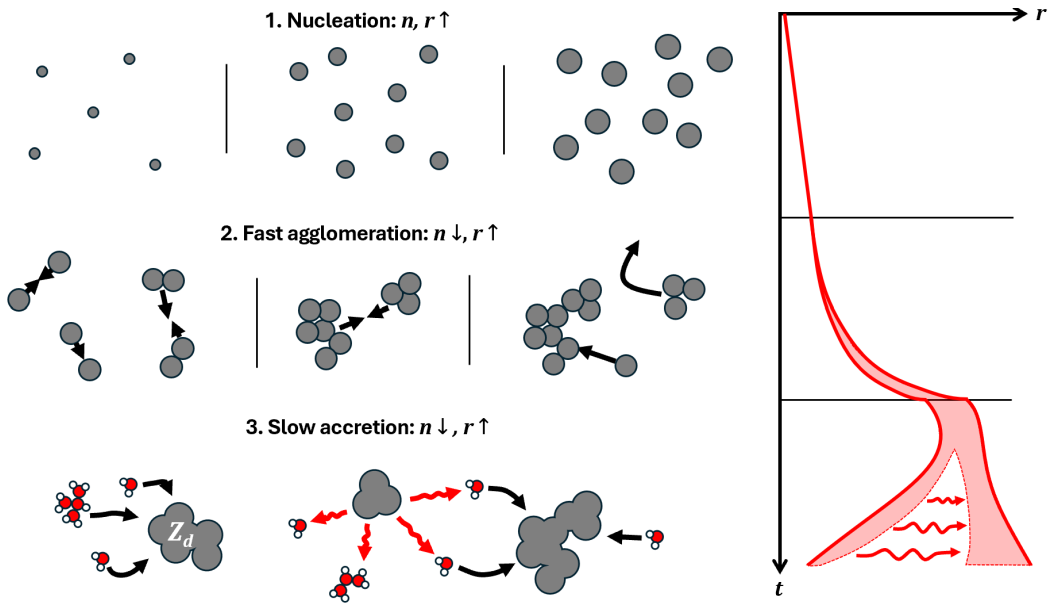

Figure 4.14: (left) Phases of ice growth, from nucleation to demise; (right) rough sketch of particle size over time during monomer accretion, coagulation, and sublimation.

Curiously, grains grow more quickly *after* water flow is shut off in hydrogen gas, especially at pressures 800 mTorr and lower. It is plausible that during vapor deposition, larger grains are "blown away" by the input water flow once they grow to a certain size, but as p_{H_2O} drops when the flow input is stopped, Eq. 4.8 would suggest a smaller mass accretion rate. The accelerated growth, and the increase in IR absorption, thus suggests a secondary source of water vapor to feed the accretion. This "new" ice is likely deposited from vapor that sublimated from elsewhere in the chamber, either from the electrodes or from other ice grains.

Due to the size dependence of the sublimation rate, smaller grains may sublimate away (along with ice from the electrodes), raising the ambient p_{H_2O} surrounding the larger grains. This leads to a consolidation of the ice from the small grains into the largest ones: a process analogous to Ostwald ripening in colloidal systems [93, 94]. This explains the peaks in growth rate around 130 K at lower pressures: this is a goldilocks zone for ripening, as sublimation dominates accretion for smaller grains, but is dominated by accretion for larger grains. Over the course of tens of minutes, the small grains, the poorest in ice, get poorer, while the rich grains get richer, hoarding water molecules. While this model of "ice capitalism" qualitatively matches

our observations, more work will be necessary to develop a quantitative predictive model of grain evolution.

4.6 Implications and lingering questions

These experiments demonstrate that water-ice grains grown in a plasma environment develop elongated, dendritic, fractal structures, that diverge from the spherical-particle assumption commonly used in dynamical simulations of ice clouds and in radiative transfer models.

The dependence of growth rate and equilibrium size with pressure and temperature are obtained, indicating that grains reach larger lengths at lower pressures and in warmer conditions up to 130 K. As experiments were at higher densities than in astrophysical situations such as protoplanetary disks or molecular clouds, these findings suggest that ice structures could stretch longer lengths and obtain more pronounced morphologies still. This could affect their charge accumulation and collisional properties, impacting rates of planetesimal formation.

As shown by microscopy and Mie scattering analysis, grains can reach lengths an order of magnitude greater than their effective scattering radii. This may cause size estimates of interstellar grains based on IR scattering to be systematically too low, and points towards a need for better models of scattering by fractal aggregates in interpreting astrophysical data.

The consistent alignment of grains along the electric field lines and the suppression of coagulation above the micron scale show that the ionized environment is critical to shaping the ice morphology. Future work should seek a more quantitative model to describe the entire grain life cycle, from nucleation to fractal aggregation to eventual removal from the plasma, which can be scaled to conditions between experiments, in the Earth's upper atmosphere, and across space environments. Further work is also required to improve scattering measurements, crucial to matching laboratory results to the spectra obtained from astrophysics observatories.

Chapter 5

AMORPHOUS AND CRYSTALLINE ICE

Some of this chapter's contents have been published in:

> Nicolov, A. *et al.* Phase and morphology of water-ice grains formed in a cryogenic laboratory plasma. *The Astrophysical Journal* **966,** 66. `http://doi.org/10.3847/1538-4357/ad34b5` (2024).

...

In the previous chapter, we examined how ice appears and grows into unique, dendritic structures, utilizing Fourier Transform Infrared (FTIR) transmission spectroscopy to measure the grain's scattering spectrum and obtain its characteristic size. In this chapter, I use this same data to probe an even smaller structure— the phase structure of the ice itself.

5.1 Low-density amorphous ice

Above 80 K, the stable phase of water ice is the common *ice* I_h, which has a hexagonal lattice of oxygen atoms. Each pair of neighboring oxygens is bridged by a hydrogen atom that is covalently bonded to one oxygen and hydrogen-bonded to the other. This phase is *proton-disordered*, meaning that "which side" has the covelant bond does not have an ordered structure, and these bonds fluctuate over time due to thermal energy. Below 80 K, the hexagonal lattice becomes proton-ordered to form *ice XI*[1].

These equilibrium phases take some time to establish, however, as water molecules require some thermal energy to reorient into a lattice. When ice is deposited from vapor at at low temperatures and densities, this molecular "reorientation" occurs more slowly than the deposition rate, and ice exists in a transient amorphous configuration before crystallizing [2].

Amorphous ice differs significantly from the properties of crystalline ice: it typically has a higher density, markedly lower thermal conductivity, and a much greater capacity to trap and retain volatile gases [22]. Its open, disordered structure increases internal surface area, enhancing adsorption and

[1] Refer to the phase diagram in Fig. 1.7.

diffusion of small molecules, which in turn can promote chemical reactions within the ice, especially under irradiation or thermal cycling relevant to astrophysical and planetary environments [23, 28]. The formation and transition of amorphous ice is thus of great interest to astrophysics, as it may allow distinct physics not predicted in crystalline ice.

Metastability and crystallization

Below about 140 K, the amorphous ice is *metastable*: why crystalline ice is still energetically favorable, its formation is hindered by the low thermal energy, and amorphous structures can persist for long periods. Once the amorphous-to-crystalline phase transition occurs, whether spontaneously over time or due to external heating, it is exothermic and thus irreversible [23]. The released heat can propagate through the ice, prompting crystallization in neighboring regions, and triggering runaway conversion throughout the ice grain. The heat released can also warm the surroundings and liberate volatile species trapped in the amorphous matrix.

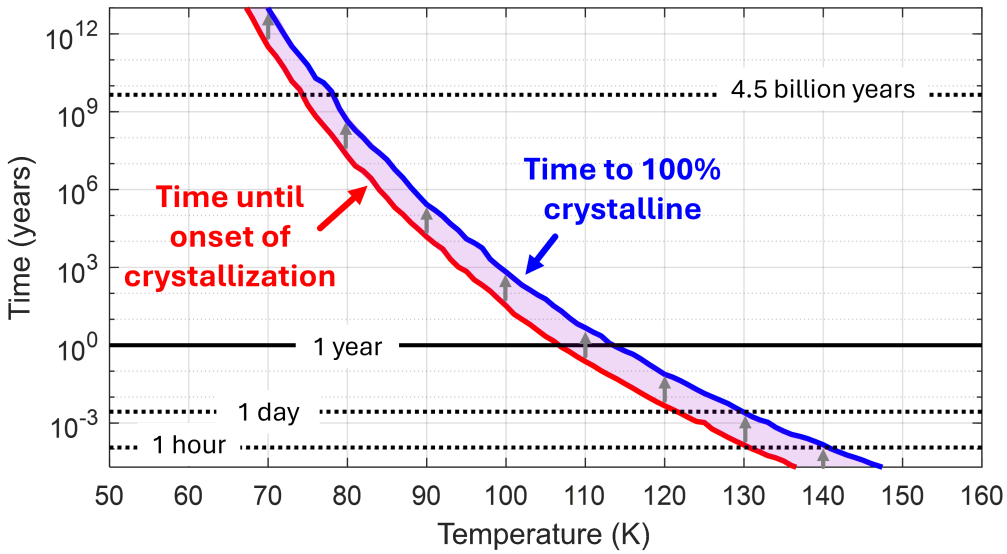

Figure 5.1: The spontaneous transition time for amorphous ice crystallization, reproduced from Mastrapa *et al.* [2]. The curves are theoretical and empirical estimations; Mastrapa *et al.* [2] stresses that these values are approximate and not well-reproduced.

The spontaneous crystallization timescale varies exponentially with temperature: at 140 K it lasts merely seconds, while at 80 K it exceeds a billion years.

Formation of *Ice XI*, which requires temperatures below 70 K, can therefore take longer than the age of the Earth. The transition timescale is shown in Fig. 5.1, reproduced from Mastrapa *et al.* [2].

In astrophysical environments, crystallization can be initiated or accelerated by energetic processes such as starlight, cosmic-ray irradiation, and impacts by ambient ions or electrons [1, 28]. The interaction between ice and plasma is thus a critical factor in the thermal and chemical evolution of icy grains.

Absorption spectra

To begin experimental studies of ice phase, I went to the Ice Spectroscopy Lab at JPL[2] to train on the instrument and take spectra of ice films. In this setup, a cryostat (identical to those in our apparatus) cool a KBr window, onto which ice is deposited and observed through various spectral methods.

Ice films were deposited at 30 K, heated to 150 K, and then cooled back to 30 K; transmission scans were taken of the ice film, using an FTIR configuration identical to the one used in the previous chapter, throughout the heating and cooling sequence; select absorption spectra are shown in Fig. 5.2.

These spectra show the broad absorption band surrounding 3 microns— the same band used for Mie scattering in the previous chapter— that arises from O-H stretching vibrations of the water molecules. In crystalline ice (black and dashed-red lines in Fig. 5.2) there arises a characteristic triplet structure that corresponds to vibrational coupling along the three axes of symmetry in the hexagonal network of hydrogen bonds. These peaks are sharp at low temperature and progressively blend at higher temperature as thermal motion distorts the lattice. In contrast, amorphous ice entirely lacks long-range order, yielding a smooth absorption band. The amorphous band is also shifted toward shorter wavelengths due to weaker hydrogen compared to the crystalline minimum-energy configuration [2].

Just after ice was formed at 30 K, the ice film's spectrum clearly showed amorphous ice, with a characteristically smooth O-H absorption band. As the ice was steadily heated, the entire ice film transitioned to crystalline ice around 130 K. After reaching 150 K, the sample was quenched back to 30 K,

[2]Special thanks to Dr. Murthy Gudipati, Dr. Bryana Henderson, and Dr. Lora Jovanovic for their mentorship and technical assistance.

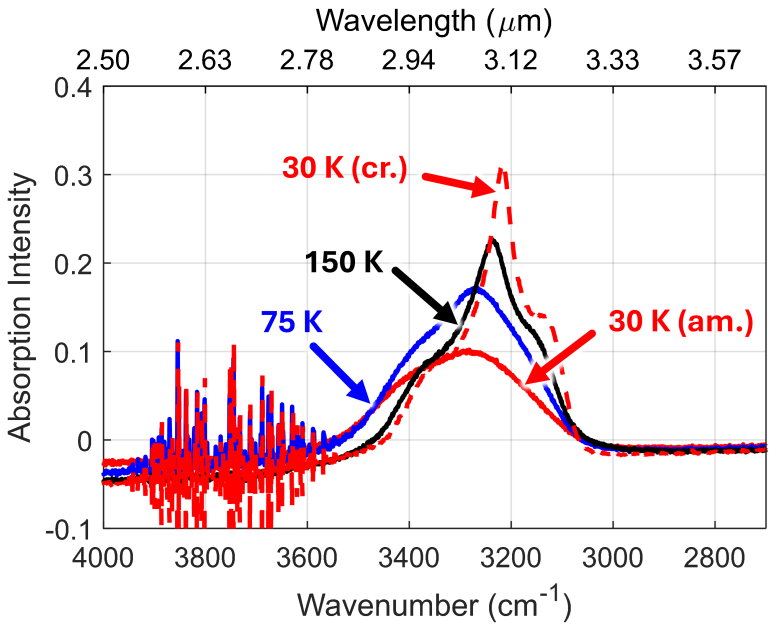

Figure 5.2: Absorption spectra of pure-H_2O ice films formed in the Acquabella device at JPL. Solid red line shows amorphous ice just after deposition at 30 K; dashed red line is the sample after heating to 150 K and cooling back to 30 K. "Hairy" region from 4000 to 3600 cm^{-1} is due to water vapor.

but retained it's crystalline structure. This *hysteresis* is characteristic of the irreversible crystallization process.

5.2 Phase measurements in ice-dusty plasma

Next, we return to the absorption spectra collected using the Ice Dusty Plasma Experiment at Caltech. In the previous chapter, we collected FTIR spectra throughout a 20-minute experimental sequence (Fig. 4.2) and used the measured extinction bands to retrieve the grain size (Fig. 4.10). When grains are considerably smaller than the IR wavelengths (Rayleigh scattering regime), as is the case for the $t = 2$ minute FTIR scans, scattering does not affect the spectrum significantly. In this case, the shape of the band is purely due to the phase structure of the ice. Figure 5.3 shows normalized absorption spectra, each at an electrode temperature ranging from 80 K to 130 K, each taken just after ice formation.

At 130 K, the spectrum displays the triplet shape, with a maximum at 3215 cm^{-1} and smaller humps at wavenumbers of 3360 and 3140 cm^{-1}, matching

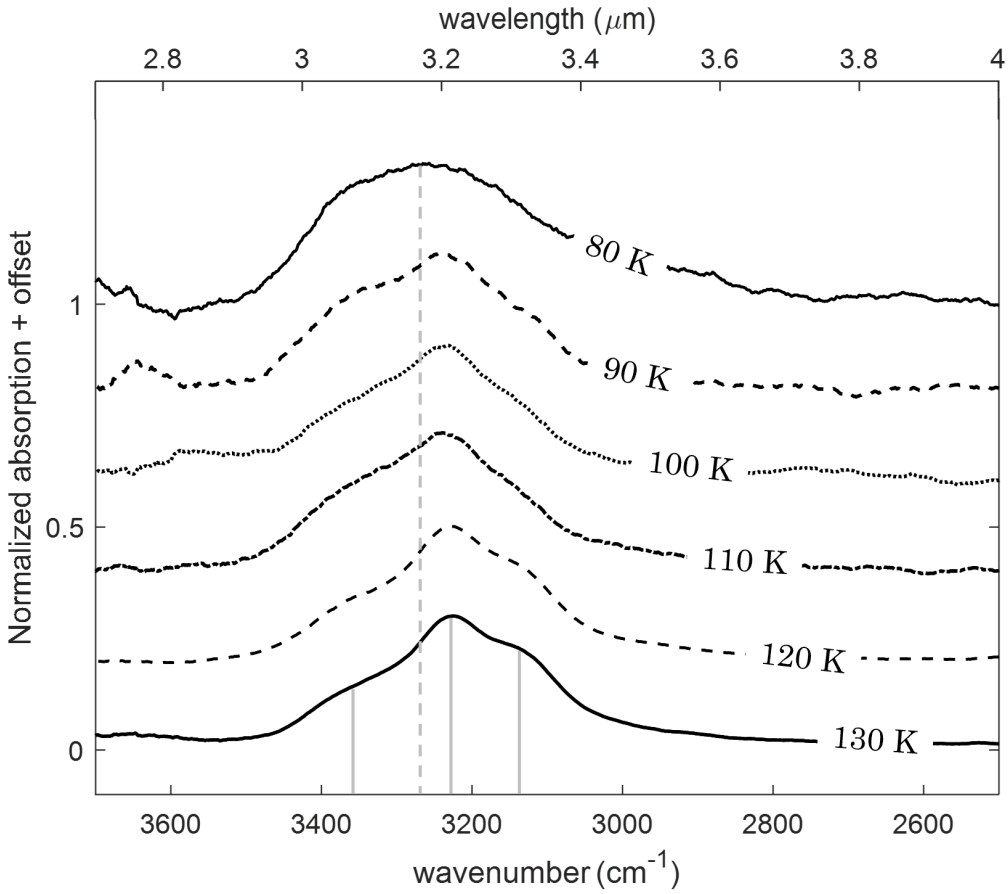

Figure 5.3: Ice absorption spectra with electrode temperatures ranging from 80 K to 130 K, and pressure of 800 mTorr. Spectra are offset in the vertical direction by an arbitrary amount for clarity. The positions of absorption peaks are indicated by vertical grey lines.

the *ice-I_h* structure observed in ice films. At 80 K, the spectrum broadens to become unimodal, with its singular peak shifted to 3270 cm^{-1}, signifying that the ice grains are amorphous.

The spectra from 90 to 110 K display a mix of both amorphous and crystalline properties: they contain a leftward-shifted broad spectrum, but retain a local peak at 3215 cm^{-1}. This indicates that both amorphous and crystalline ice are present within the cloud of ice grains: either individual grains contain both amorphous and crystalline ice domains, or some of the ice grains are crystalline and others are amorphous. The latter is more likely, as the heat release in the amorphous-to-crystalline phase transition would likely cause runaway crystallization throughout the entire grain [22, 23].

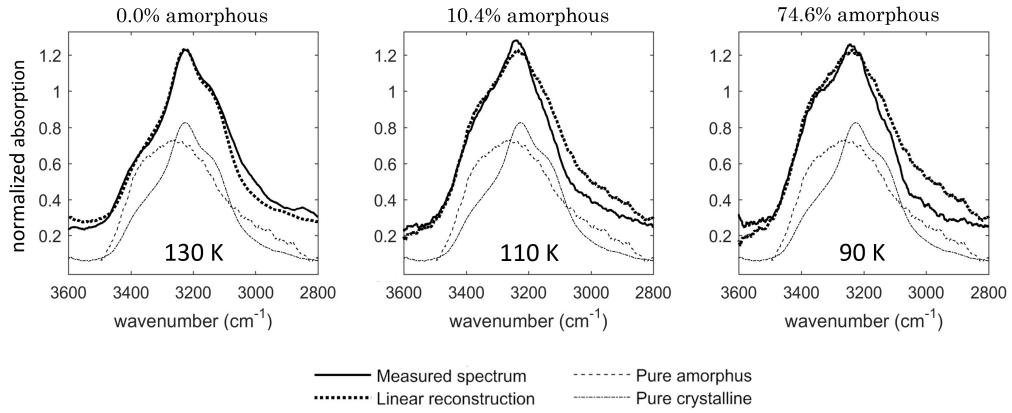

Figure 5.4: Spectra at 130, 110, and 90 K, in 400 mTorr of Hydrogen plasma (solid line), compared to the fitted linear combination of pure amorphous and crystalline phases (dotted line). Thin dashed and dot-dashed lines show the pure amorphous and crystalline spectra (shifted downwards by 0.2 for clarity). Table 5.1 gives percentages for all tested pressures and temperatures.

Fractional phase analysis

To determine the fraction of ice grains in each phase, a simple linear mixing model is devised; because grains are not densely packed, nonlinear mixing effects should be negligible [95]. Spectral mixing to quantify amorphous and crystalline ice has been successfully used in previous works [96, 97], and this analysis is in line with those previous works. The measured spectrum is fit to a linear combination of the pure-amorphous and pure-crystalline spectra,

$$A_{tot} = aA_a + (1-a)A_c, \tag{5.1}$$

where A_{tot} is the measured signal, A_a is the pure-amorphous spectrum, and A_c is the pure-crystalline spectrum. The parameter a is constrained within the range [0,1], representing the fraction of grains in the pure-amorphous state. All spectra were normalized before the fit. The fits for 130, 110, and 90 K at 800 mTorr are presented in Figure 5.4. Results for all $t = 2$-min scans are given in Table 5.1.

As is expected, the fraction of amorphous ice increases as temperature decreases. At 800 mTorr, no amorphous ice is observed above 130 K, nearly all ice is amorphous at 80 K, and intermediate temperatures show mixed compositions. Because amorphous ice is known to exist below 130 K [2], we conclude the warmest parts of the ice cloud are roughly 50 K above the

Table 5.1: Percentage of amorphous ice with pressure and temperature, derived from FTIR spectra taken immediately after closing H_2O inlet valve at $t = 2$ min. At all temperatures above 130 K, only crystalline ice was present.

	130 K	120 K	110 K	100 K	90 K	80 K
0.4 Torr	0%	0%	10.4%	64.1%	74.6%	60.5%
0.8 Torr	0%	1.7%	89.4%	73.4%	83.0%	94.5%
1.6 Torr	0%	33.1%	51.1%	76.1%	100%	100%

electrode temperature, such that they are 130 K when electrodes are 80 K; the coldest ice grains are within 10 K of electrode temperature, as amorphous ice is seen at 120 K. Pressure greatly affects this: at 1600 mTorr, 33.1% of the ice is amorphous at 120 K while there is little to none at lower pressures, while at 400 mTorr, there is still some crystalline ice at 80 K. This variation is likely because the cold background gas is less collisional at low pressure, and thus cools the incoming water vapor less efficiently. This also explains why grain size does not correlate with temperature at 400 mTorr as reliably as it does at higher pressures: the temperature profile is less consistent within the icy region. It is hypothesized that if the water vapor were cooled before entering the chamber, this effect would disappear, as vapor would not require as many collisions to equilibrate with the cold background gas.

Time-evolution of the phase composition

This method of phase determination is reliable only when grains remain small; once grains grow to micron size, wavelength-dependent Mie scattering interferes with direct spectral fitting. To account for this, the Bohren–Huffman Mie scattering algorithm [68] was used to modify the pure-crystalline (A_c) and pure-amorphous (A_a) absorption coefficients to include scattering, using the characteristic grain radii obtained from the previous chapter (Fig. 4.11). These modified extinction coefficients were then fit to the measured spectra to retrieve the fractional phase composition (Fig. 5.5). The time evolution of the fractional phase composition is shown in Fig. 5.5 over the 20-minute run time.

Overall, the ice tends to become more crystalline over time. Between 90 and 120 K the amorphous fraction decreased between 2 and 20 minutes, to varying extents depending on the pressure; below 90 K the ice remained largely amorphous independent of time, and above 120 K it crystallized

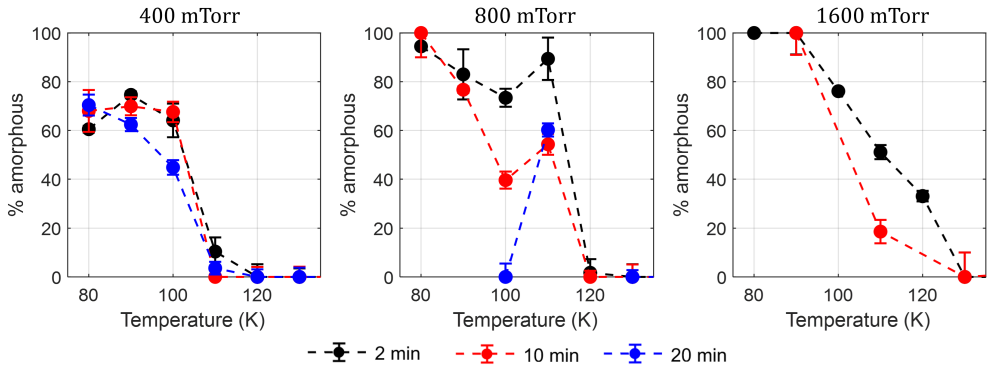

Figure 5.5: Percentage of ice in the amorphous phase in each FTIR scan. Each of the three plots shows the time-evolution of phase composition at five temperatures for a single pressure. Error bars give the root mean square (RMS) deviation of the fit to of the linear mixing model to the data. Gaps in data are due to the disappearance of ice through sublimation.

immediately upon formation. This window of measurable phase transition differs from literature values (see Fig. 5.1), which predict measurable phase transition over 20 minutes between 130 and 145 K.

Lifetime of amorphous ice grains

The probability for a single amorphous grain to undergo crystallization at any given time t is distributed about some average lifetime τ and a spread σ, which each depend on temperature:

$$\text{prob}[t, T] = \exp\left(-\left(\frac{t-\tau}{\sigma}\right)^2\right). \tag{5.2}$$

This assumes that each grain crystallizes instantaneously, in its entirety, in a cascade driven by the energy release from the exothermic transition. If a cloud of amorphous grains is formed at the same time, therefore, the percentage that are amorphous are given by the complementary error function,

$$A_a(t) = A_a(0)\ \text{erfc}\left(-\frac{t-\tau}{\sigma}\right), \tag{5.3}$$

As previously shown in Fig. 5.1, literature contains two timescales associated with the crystallization of an amorphous ice substrate: a time to *onset* and a time to *completion* of crystallization [2]. The difference between them

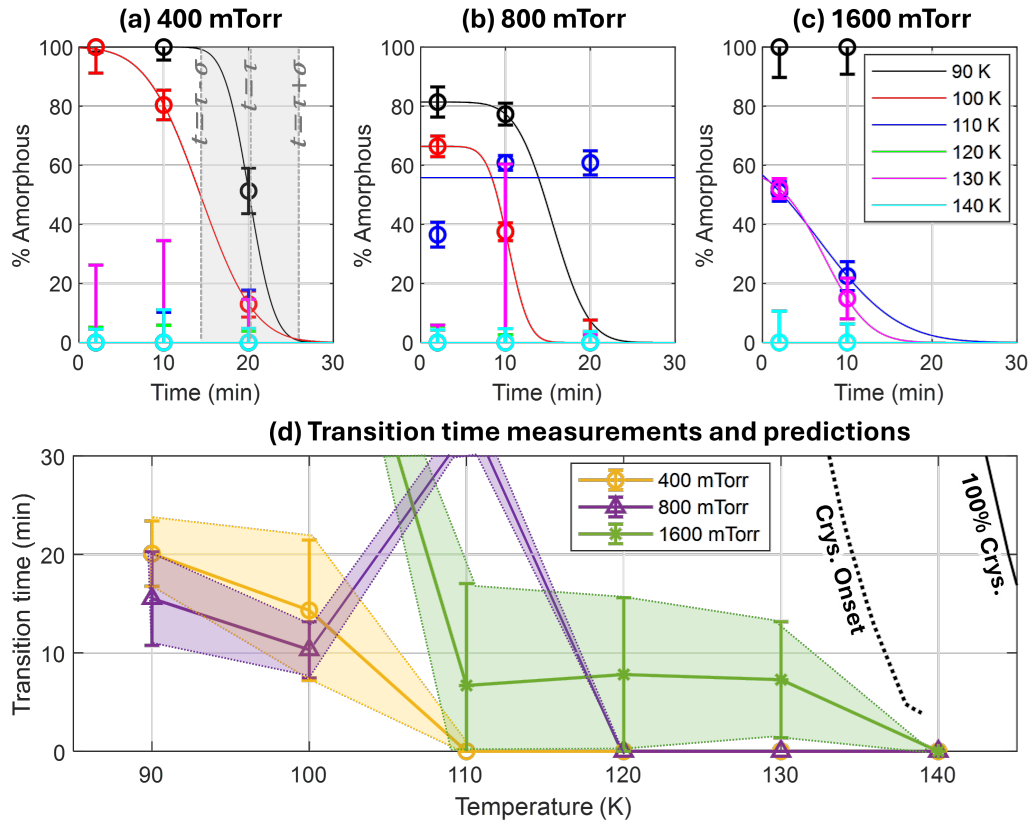

Figure 5.6: (a-c) The points show the relative composition of amorphous ice over time for various pressures and temperatures, with error bars due to fit uncertainties, as shown in Fig. 5.5; solid curves show the fit of a complementary error function to the decay. (d) Each data point shows the fit lifetime τ, and the bars show the spread σ in lifetimes through the cloud. These are plotted alongside the literature values for the transition time [2].

corresponds to the spread σ in the gaussian probability distribution defined above.

We previously collected A_a at $t = 2$, 10, and 20 minutes (Fig. 5.5); I here fit Eq. 5.3 to these three points to obtain the average lifetime τ of the amorphous phase, and the spread in transition times through the cloud σ. These fits are shown in Fig. 5.6 (a-c).

The lifetime and spread obtained from these fits are plotted in 5.6 (d) versus electrode temperature. In the same plot, the crystallization onset and completion times from Mastrapa *et al.* [2] are plotted versus *ice* temperature.

Our crystallization onset is shifted to significantly lower temperatures, between 90 and 120 K depending on pressure. This deviation is likely present because temperature is measured at the *electrode* surfaces, not in the gas or the ice itself. Due to RF heating, the bulk gas temperature sits about 20 K above the electrode temperature [64], and can be warmer still in the outskirts of the plasma, away from the electrodes.

The temperature range over which a phase transition is observed is also significantly wider than the values predicted by Mastrapa *et al.* [2]: at 1600 mTorr, the collection of ice grains became fully crystalline over 20-minute experimental sequence in runs at 110, 120, and 130 K, a 20 ± 10 K range, while literature values predict a transition only in the 15 K range between 135 and 150 K. This may be partially attributed to the nonuniform temperature profile, as some grains in the IR beam path are warmer and transition faster than others.

Also notable is the dependence on pressure: at 1600 mTorr, ice the phase transition occured at higher temperatures (though not as high as literature values), while at 400 mTorr, ice was observed crystallizing even at the lowest measured temperatures, and no amorphous ice was present at 110 K or higher. This could indicate that low-pressure runs also had greater nonuniformity in the temperature profile throughout the ice cloud, possibly due to higher RF heating (perhaps dependent on proximity to the Paschen minimum), slower cooling rate of input gas (see Sec. 3.4), or different nucleation and confinement conditions that allow grains to form further from the cold electrodes.

Overall, there is a great amount of error in each measurement, due to deviations in the fits for phase composition and transition lifetime, as well as experimental error due to variability between runs. In the future, significantly more data could be collected to decrease errors and provide more confident transition rates.

5.3 Mechanisms of phase transition

Measurements show that phase of ice grains within the cloud transitions from amorphous to crystalline over the course of tens of minutes. This occurs over a significant range of electrode temperatures, differing from transition rates in literature for any given temperature.

These differences may be due to a number of competing effects, some due to the thermal distribution of the background gas, some due to plasma interactions. These modify ice transition rates, instigating crystallization at lower temperatures while slowing it at higher temperatures.

Temperature distribution and particle drifts

When the electrodes are both held at some cold temperature T, the plasma has a neutral temperature distribution throughout, at T in the coldest region and up to $\sim 20 - 30$ K warmer at the outer edges and electron density maxima.

When ice grains form and T is in a range where crystalline and amorphous ice coexist, crystalline ice grains populate the warmer regions while amorphous grains form near the cooled electrodes. The amorphous ice on the warmer outskirts of these "amorphous zones" will crystallize first followed by the grains in colder conditions. As the FTIR beam is a line-integrated measurement, with a path encompassing colder and warmer regions of the ice cloud, the measured transition time will be stretched out compared to that of any single ice grain at any one temperature. This is illustrated in Fig. 5.7 (a).

This is further complicated because the ice grains are not stationary within the plasma. Vortex motion transports them throughout the plasma, mixing the originally-stratified amorphous and crystalline regions. As the amorphous-to-crystalline phase transition is irreversible, amorphous grains transported to warmer areas can crystallize and not revert. As ice grains circulate between the colder and warmer regions of the plasma, they transiently heat and quench again. The probability of transitioning thus oscillates in time. As the transition probability is highly nonlinear with temperature, the rate depends on the precise temperature distribution, the grain's path, and its velocity. This is sketched in Fig. 5.7 (b).

The motion thus accelerates the phase transition onset and can cause full crystallization even for low minimum temperatures, while also slowing its course: some amorphous grains are quickly transported into warmer regions for enough time to crystallize, while some cycle through warmer regions only briefly, stretching out their transition time.

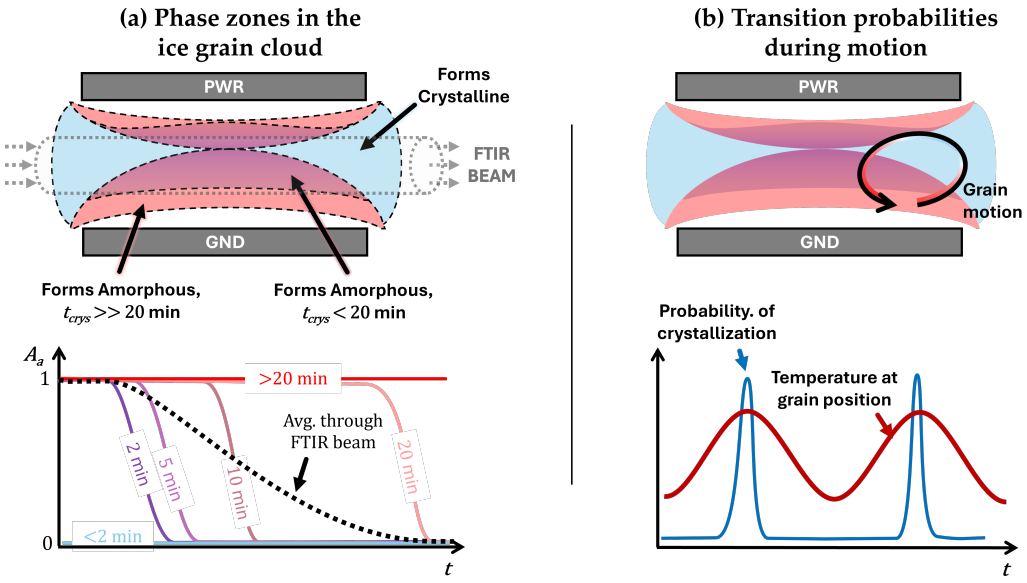

Figure 5.7: (a) Rough sketch of temperature "zones" in the grain cloud with varying crystallization times t_{crys}: ice crystallizes quickly (< 2 min) in blue zones, slowly (> 20 min) in red zones, and within the experimental run time in the purple zones; the graph sketches approximate composition curves over time in various regions and the expected measured curve, spatially-averaged through the FTIR beam. (b) Motion of an ice grain through the temperature zones, with an accompanying sketch of temperature at the grain (red) and probability of transitioning (blue) over time. Note all sketches are illustrative approximations, not based on precise measurements.

The relative strength of this mechanism in causing the measured amorphous transition rates, compared to other proposed mechanisms, would be quite difficult to measure. Tandem measurements with laser-induced fluorescence and high-speed videography could determine the time spent by each grain in a given temperature zone; if taken alongside FTIR results, one could test if the time-evolution of the ice's local temperature fully fits the measured transition rates of the bulk ice cloud.

Ongoing sublimation and deposition

All previous infrared scans were collected *after* the water vapor flow was shut off; thus no new water vapor was introduced to the chamber. However, as discussed in Section 4.5, ice from the electrode surfaces or other ice grains can sublimate and re-deposit on the grains. This may form amorphous films

on the surface of crystalline grains or nucleate into new fully-amorphous grains.

The formation of new amorphous ice would significantly affect FTIR scans, causing an increase or steady level of amorphous ice as time progresses. This could explain the odd cases in which the amorphous percentage increases over time, such as the scan at 110 K and 800 mTorr, but in general does not appear dominant: in most scans, the relative composition of amorphous ice trends to zero at later times.

The onset time to crystallization in literature [2, 98] is:

$$t_{crys.} \approx (3 \cdot 10^{-15}\ \mathrm{s}) \exp\left(\frac{5300\ \mathrm{K}}{T}\right). \tag{5.4}$$

To first approximation, we can assume that crystalline ice sublimates and re-deposits into amorphous ice at the sublimation rate, given by the Hertz-Knudsen equation:

$$J_{sub} \approx \frac{p_{vap}(T)}{\sqrt{m_{H_2O} k_B T}}. \tag{5.5}$$

Using the Clausius-Clapeyron equation for the vapor pressure and putting this in the form of an "amorphization" time, we obtain:

$$\begin{aligned} t_{amorph.} &= \frac{r n_{ice} \sqrt{2\pi m k_B T}}{3 p_0} \exp\left[\frac{L}{R}\left(\frac{1}{T} - \frac{1}{T_0}\right)\right] \\ &\approx (3 \cdot 10^6\ \mathrm{s\ m^{-1} K^{-1/2}})\ r\sqrt{T}\ \exp\left[6100\ \mathrm{K}\left(\frac{1}{T} - \frac{1}{180\ \mathrm{K}}\right)\right], \end{aligned} \tag{5.6}$$

where r is the grain's characteristic size. Based on these relations, $t_{crys.} > t_{amorph.}$ for all temperatures and grain sizes relevant to the experiment; while re-amorphizing may slightly slow down the measured crystallization rate, it is likely not measurable.

The formation of new amorphous ice may be measurable, however, if new water vapor is input to the chamber, the deposition rate of amorphous ice may continue to outpace crystallization.

The flux or water to the grain surface is given by:

$$J_{dep.} = \frac{\dot{N}_{in}}{N_{grain} 4\pi r^2 + 2A_{elec}}, \tag{5.7}$$

where $\dot{N}_{in}$ is the vapor input in molecules per second, N_{grain} is the total number of grains in the plasma, and $A_{elec.}$ is the surface area of the electrodes;

here I assume ice is equally likely to deposit on the electrodes as on the ice grains, and neglect new grain nucleation. For this to be comparable to the crystallization rate $J_{crys} = rn_{ice}/3t_{crys.}$,

$$\dot{N}_{in} \geq \frac{rn_{ice}}{3t_{crys.}}(N_{grain}4\pi r^2 + 2A_{elec}). \tag{5.8}$$

As this is inversely related to the crystallization time, it is vanishingly small until a temperature around 130 K; amorphous ice deposition thus always dominates crystallization at lower temperatures. At 138 K, at least 1 SCCM of input vapor is required to balance the crystallization rate; this is similar to the water inflow in the experiment, which can range 1-20 SCCM.

This is supported by experimental measurements: if the water flow was not shut off at $t = 2$ min, little to no change was observed in the spectra; no scattering, likely because larger grains were blown away by the incoming vapor, and no change in phase, probably because amorphous ice nucleated and deposited more quickly than it crystallized.

Non-equilibrium cooling of gas inputs

As both the water vapor and the buffer gas enter the chamber at room temperature and cool through conduction, some time is required for the gas to thermalize. While the lifetime of the gas in the chamber is sufficient for thermalization (see discussion in Sec. 3.4), it has been suggested that small amounts of higher-energy, out-of-equilibrium molecules may persist. Since the most energetic molecules have a higher speed, and thus larger collision frequency, they may sufficiently heat the ice's surface to induce crystallization.

If this was the case, we would expect to see a difference in crystallization rate with the temperature of the gas inputs. To test this, a heat exchanger was built from coils of copper 1/4-inch tubing and integrated into the backing gas or water vapor lines, just before their input to the vacuum chamber. The copper coils were placed inside a styrofoam cooler and attached to a thermocouple to monitor the temperature, and the cooler was filled by LN2 (77 K), a mixture of LN2 and isopropyl alcohol (variable between 77 K and $\sim$260 K depending on the ratio), or heated by putting a bright halogen lamp within the cooler.

Several runs were taken at 100 K following the same standard procedure (recall Fig. 4.2) under four cases: (i) control case with both water vapor and hydrogen gas at room temperature; (ii) hydrogen gas cooled to 77 K with LN2, (iii) water vapor cooled to $-20^{o}\mathrm{C}$ with a sludge of LN2 and isopropyl alcohol[3], and (iv) with the water heated to $+50^{o}\mathrm{C}$ by a bright halogen floodlight. The composition of amorphous ice was monitored over time from the FTIR spectrum.

If non-equilibrium cooling was dominant, changing the input temperature would be expected to impact the transition rate. However, though there was some variation between runs as shown in Fig 5.8, this did *not* show significant correlation with the temperature of the gas input. I thus conclude that this is not a dominant effect in instigating the phase transition of amorphous ice over longer timescales.

It is possible that this effect begins to matter at higher inflows of water vapor, as the vapor input line is much closer to the electrodes than the backing gas input and is capable of blowing the grains out of the plasma if sufficiently high, under sufficiently high flows. However, this would be most significant during the vapor deposition period at the start of the experimental sequence, rather than over tens of minutes. Future work could examine the dependence of the ice phase with varying flow rates and pre-cooling temperatures. We have also discussed applying a LIF scheme on water vapor molecules, currently under development by Dr. Yegeon Lim, which could monitor the velocity distribution of the water vapor as it enters the chamber and correlate it with regions of amorphous and crystalline ice.

Energetic processing by the plasma

When immersed in plasma, ice grains experience continuous bombardment by ions and electrons. Ion impacts sputter surface molecules and deposit kinetic energy, producing localized heating that enhances molecular mobility. This may enhance crystallization rates of amorphous ice grains [1]. It may also establish a quasi-liquid layer (QLL) on the grain surface, even at temperatures much lower than a QLL is ordinarily observed on ice, in which adsorbed molecules retain significant mobility and can reorient on short timescales [26].

[3]Any further cooling would cause the vapor to freeze within the line

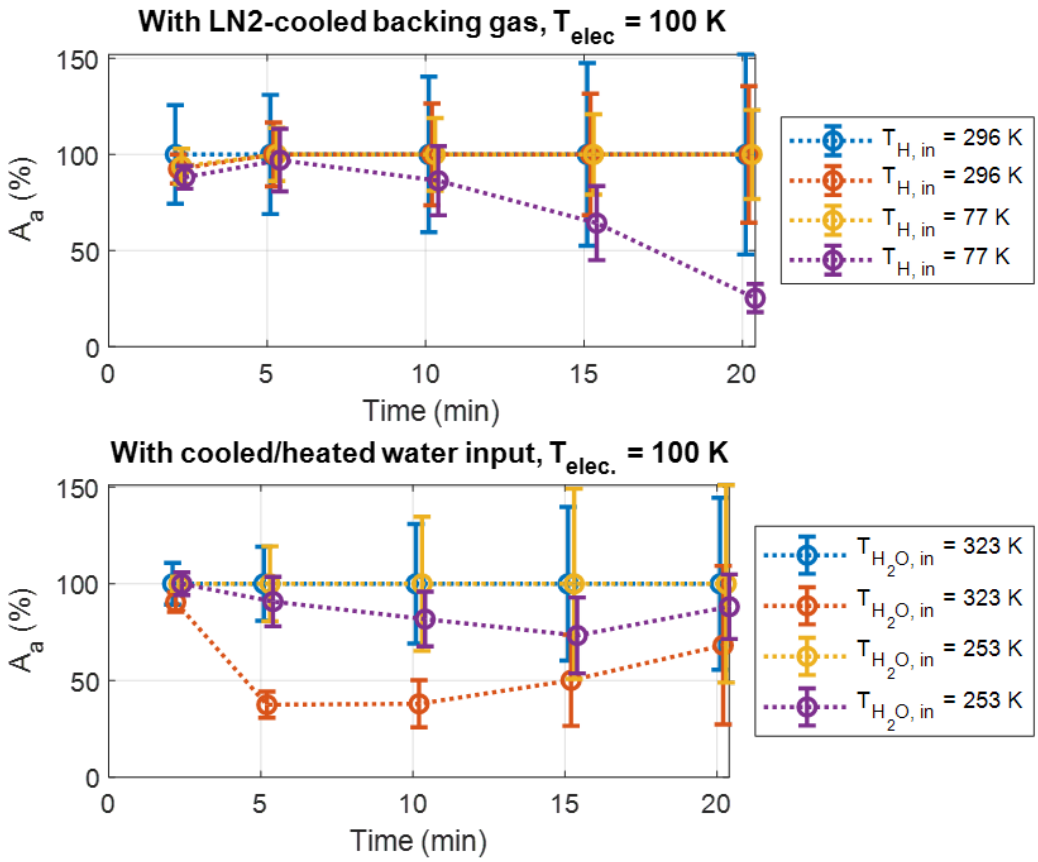

Figure 5.8: Time-evolution of phase composition with and without pre-cooled gas inputs: cooling H_2 and *not* H_2O (top) and cooling H_2O and *not* H_2 (bottom.

Energetic processing can also act in the opposite direction: electron and ion bombardment have been shown to re-amorphize crystalline ice by displacing molecules and disrupting long-range order [28]. In our system, this may compete with thermal crystallization, especially in colder plasma regions where grains spend long times under bombardment but below the thermal threshold for transition.

These effects are likely amplified near the Paschen minimum, where discharges reach higher plasma densities and electron temperatures [90]. High fluxes of energetic particles can shift the balance between crystallization and amorphization, such that plasma–ice interactions may dominate over purely thermal processes, even at temperatures where amorphous ice is normally

stable. Future experiments could probe this by varying electron density and temperature and testing for changes in crystallization rates.

The situation becomes even more complex under mixed deposition. In a pure H_2O ice matrix, the hydrogen-bonded lattice provides a relatively stable scaffold that resists radiation damage. However, when volatile molecules such as CO, CO_2, or CH_4 are co-deposited, they can introduce local structural heterogeneity and react strongly with plasma-generated radicals [22], which can be released during crystallization or increase the effects of energetic processing. effects are likely important in astrophysical environments, where ices are rarely pure, and may help explain observed spectral variations in planetary and interstellar ices.

5.4 Chapter conclusions

We have reported the first observation of pure low-density amorphous ice forming within a laboratory plasma. Alongside crystalline ice, this phase was detected under varying electrode temperatures, in agreement with astrophysical models that predict amorphous ice to dominate throughout much of the universe [2].

At intermediate temperatures, both amorphous and crystalline phases were observed to coexist in the IR spectra. Phase mixing analysis shows that ice becomes progressively more crystalline with time, consistent with a scenario where amorphous and crystalline grains nucleate in different plasma regions, or where amorphous grains undergo irreversible runaway crystallization. Individual grains crystallize suddenly, releasing latent heat that propagates through the system, and no measurable re-amorphization is observed.

Crystallization proceeds differently than in thin ice films: onset occurs earlier at lower temperatures, while completion is slower, suggesting the influence of plasma-specific effects. These include non-uniform temperature distributions, grain motion through temperature zones, and energetic impacts from electrons, ions, and UV photons.

In astrophysical contexts, these results imply that the lifetime of amorphous ice grains may be extended by plasma interactions, altering how ice is distributed across protoplanetary disks and how it evolves with time. Because amorphous ice efficiently traps volatiles and enhances reactivity, its persis-

tence has direct consequences for the chemistry of star- and planet-forming regions. Future experiments with mixed deposition, introducing volatiles into an H_2O matrix under plasma conditions, could provide more realistic analogs of astrophysical ices and test how energetic processing regulates both their phase state and the complex chemistry they host.

Chapter 6

ICE NUCLEATION

Nicolov, A. *et al. How anions induce ice nucleation in a cryogenic plasma* (in preparation). 2026.

. . .

When water vapor is introduced to a sufficiently-cold plasma, ice grains form spontaneously. This is a somewhat surprising observation: water is generally known for being quite inefficient at nucleating into droplets or ice grains *homogeneously*, that is, without some impurities around which to condense [30]. Throughout astrophysics, planetary, and atmospheric science, the default assumption is generally that *heterogeneous nucleation* dominates ice formation; for example, virtually every snowflake forms around some non-ice particulate like dust, smoke, or pollen [100].

Throughout the past decade of laboratory ice-dusty plasma research at Caltech, however, evidence points to a different nucleation pathway:

1. Nucleation occurs when plasma is present, and *not* in a neutral gas at the same temperature and pressure.
2. Grains appear in localized structures in the plasma density maxima, which are approximately in the middle of the two electrodes, rather than spread throughout the chamber emanating from the electrode surfaces.
3. Nucleation efficiency does *not* decrease when the vacuum chamber has been recently cleaned or has been pumped down for longer periods of time, so the impurity concentration is decreased.
4. Spectroscopy measurements do not detect aerosolized solid-state impurities that could seed nucleation.

It was suggested by Bellan [30] that ice formation in the Caltech experiments is likely dominated by ion-induced nucleation (IIN). This mechanism was first demonstrated in 1897 by Wilson [88], who discovered that the presence

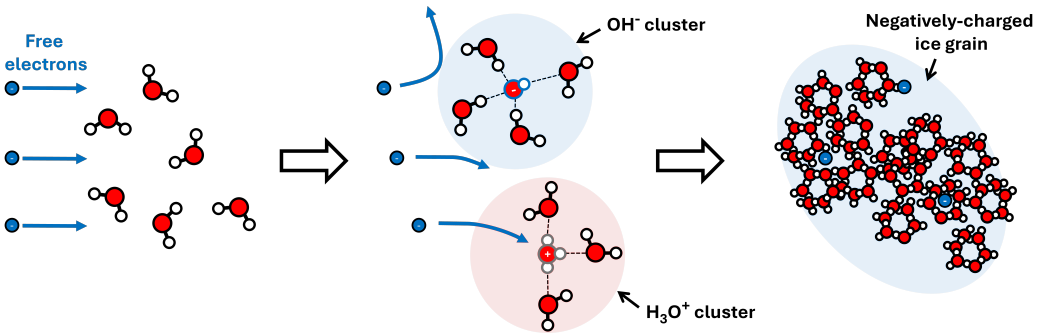

Figure 6.1: Free electrons collide with water molecules to produce $\mathrm{OH}-$ and $\mathrm{H_3O}+$ ions; water molecules cluster around the ions; positive clusters are neutralized by the electrons, while negative clusters grow into stable ice grains.

of ions increases the nucleation rate of vapor by millions of times.[1] Ions polarize and attract vapor molecules to form clusters held together electrostatically, nuclei around which more material can accrete. Specifically, the ion charge introduces an electric field gradient. Water molecules, which have a strong permanent dipole moment (around $p = 1.85$ D), are attracted towards the ion due to the polarization force. This is the dominant effect in *Wilson cloud chambers*, commonly used today for detection of radioactive decay products and cosmic rays [88, 101]. IIN has also been shown to dominate particle formation in silane plasmas used in the semiconductor industry [89, 102], and suggested to explain the correlation between aerosol and cloud formation in the troposphere and solar wind flux [103].

The IIN pathway proposed by Bellan [30] is *homogeneous*, catalyzed through ion products of $\mathrm{H_2O}$ itself, without need for gas or condensed-phase impurities. IIN had previously been discounted for ice formation in atmospheric and astrophysical plasmas because as clusters on positive ions were expected to be neutralized by electrons too rapidly to allow nucleation [104]. However, water vapor is electronegative and can form anions, most-notably $\mathrm{OH^-}$. Since ion-dipole attraction is agnostic to ion polarity, to first approximation, anions can form clusters, resist neutralization, and seed stable ice growth. This pathway, illustrated in Fig. 6.1, helps explain observations in the Ice Dusty Plasma Experiment, and by extension, in the upper atmosphere and protoplanetary disks as well [30]. This chapter investigates the efficiency

[1] For this, he won the Nobel Prize in Physics in 1927.

of this nucleation pathway for ice grain formation, using ion-mass spectroscopy to confirm the presence of anionic clusters in the laboratory and their dependence on ice formation.

6.1 Nucleation pathways

There are two common approaches to modeling nucleation: thermodynamic models and kinetic models [31]. Kinetic models follow the time-dependent growth and decay of individual clusters through molecular attachment and detachment. The models monitor the trajectories of individual atoms, ions, and electrons in real time and their interactions with nearby species, and are particularly useful because they make no assumptions about thermodynamic equilibrium, capturing fluctuations and transient effects with short timescales. However, they can have high computational cost and require detailed inputs to capture all relevant physics [79]. These methods are beyond the scope of this thesis, but are active areas of study within our group by postdoc E. Kritikos.

In a thermodynamic model, the particles are taken to always be in thermal equilibrium with their surroundings. Their possible states are described by energy distributions that depend on the system temperature and maximize entropy, yielding the *most probable* system configuration. Ensemble averages over the distribution functions give *bulk properties* such as pressure, density, surface tension, and chemical potential.

Thermodynamic models are powerful for describing large-scale behavior of a system and have long been used to predict nucleation rates. The Classical Nucleation Theory (CNT) is typically used in literature [31], which predicts whether a spherical collection of water molecules will grow or shrink, based on whether increasing its radius increases or decreases its Gibbs free energy. The nucleation rate of clusters with a given size is then calculated using a Boltzmann (or Arrhenius) function:

$$J_{nuc} \sim \exp(-\Delta G_{\mathrm{nuc}}/k_B T), . \tag{6.1}$$

where J_{nuc} is the nucleation rate. If $\Delta G_{\mathrm{nuc}} > 0$, nucleation becomes exponentially likely, while if $\Delta G_{\mathrm{nuc}} < 0$, it is exponentially suppressed.

As mentioned above, CNT cannot capture non-equilibrium effects. Since an RF plasma is highly non-equilibrium, dominated by constant ionization and

recombination of the ambient gas, the validity of CNT has been questioned for describing dusty plasma formation [30, 31].

Further, CNT requires extrapolating bulk quantities of stable-phase ice to the length scales of nucleation, in which the continuum assumption can break down. As such, properties such as surface tension, dielectric constants, and even ice temperature is not well constrained. The quantum-mechanical nature of single-molecule interactions and the geometry of the water molecules within small nuclei cause some deviation from classical theory, such as the appearance of so-called "magic numbers," in which clusters of specific numbers of H_2O are much more stable than others [105].

Homogeneous and heterogeneous nucleation

In homogeneous nucleation, $\Delta G_{\rm nuc}$ is the free energy associated with bringing together and bonding neutral water molecules together from a vapor. This contains two terms: a bulk volume energy and a surface term. The volume term is stabilizing ($\Delta G_v < 0$) when the ambient partial pressure of H_2O is higher than the saturated vapor pressure. The surface term is always destabilizing ($\Delta G_s > 0$), as molecules at the surface have a higher potential energy (due to missing water-water bonds). Classically, this is formulated as [31]:

$$\Delta G = \gamma A - n_{ice} V k_B T \ln\left(\frac{p_v}{p_{sat}}\right). \tag{6.2}$$

Here γ is the surface tension[2] of ice, V and A are the volume and surface area of the nucleus, n_{ice} is the number density of water molecules in the cluster, p_v is the partial pressure of water vapor, and p_{sat} is the saturated vapor pressure. When the vapor is supersaturated ($p_v > p_{sat}$), the volume term in ΔG is negative, such that it is energetically favorable for vapor to condense onto the nucleus.

The surface tension γ relates to the bonding energy of each molecule at the surface of the grain. The value for ice on a flat surface γ_∞ is tabulated in literature, generally following the correlation [100]:

$$\gamma_\infty[\mathrm{N/m}] = 0.109 - 1.1 \cdot 10^{-4}\,(T - 273\ \mathrm{K}). \tag{6.3}$$

[2] or, surface energy

For a spherical grain, it is altered by the Tolman correction,

$$\gamma = \frac{\gamma_\infty}{1 + 2\delta/r}, \tag{6.4}$$

where r is the grain radius of curvature. The "Tolman length" $\delta \approx -0.4$ to -0.8 Å, from $T = 100 - 300$ K, according to calculations by Kritikos *et al.* [79], though there is no general agreement in the literature about either the magnitude or even the sign of δ.

The saturated vapor pressure of water depends on the ambient temperature. I here use the Murphy-Koop equation [106]:

$$\ln(p_{sat}\ [\mathrm{Pa}]) = 9.5504 - \frac{5723.265}{T} + 3.53068 \ln(T) - 0.00728332\ T \tag{6.5}$$

Inputting these relations for p_{sat} and γ into Eq. 6.2, assuming a partial pressure of H_2O of 30 mTorr, using a linear interpolation for the Tolman length with temperature, and assuming spherical ice nuclei to compute V and A, we can graph ΔG_{nuc} with respect to the radius of the nucleus, as seen in Fig. 6.2 (a). In general, we observe that ΔG_{nuc} has a maximum at some radius r^*.

For the nucleus to grow on average, $d\Delta G/dr < 0$ must be satisfied, where r is the radius of the ice nucleus. Assuming a spherical nucleus, we can find a critical size for spontaneous growth by solving:

$$\begin{aligned} \frac{d}{dr}(\Delta G_{\mathrm{nuc}}) &= \frac{d}{dr}(\Delta G_v(T,p)) + \frac{d}{dr}(\Delta G_s(T,\gamma)) \\ &= 0. \end{aligned} \tag{6.6}$$

We can also find a critical number of water molecules for spontaneous growth,

$$N^* = n_{ice}\frac{4\pi}{3}\left((r^*)^3 - r_i^3\right), \tag{6.7}$$

where r_i is the radius of the central ion. The critical number is plotted versus temperature in Fig. 6.2 (b). We note N^* is an unstable equilibrium: ice particles with more H_2O grow spontaneously, and smaller ones quickly fall apart[3].

[3]This is an Ostwald ripening, not unlike the process described for *large* grains in section 4.5.

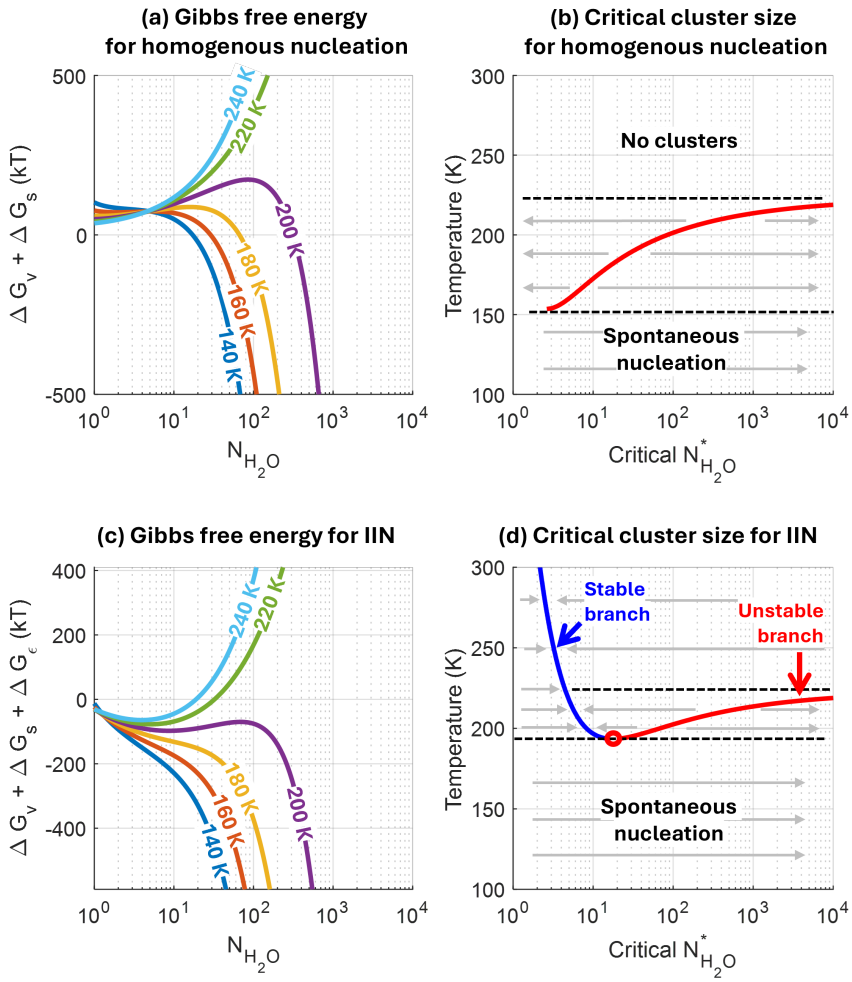

Figure 6.2: ΔG_{nuc} and associated critical points that satisfy $d(\Delta G_{\mathrm{nuc}})/dN = 0$, for (a-b) homogeneous nucleation and (c-d) ion-induced nucleation. Here $p_{\mathrm{H_2O}}$ is taken as 30 mTorr, ice density as 997 kg m^{-3}, and relative permittivity ϵ_r as 60 at all temperatures.

Below about 150 K, the energy barrier drops such that only a few water molecules are required to form a stable nucleus. In this case, homogeneous nucleation can proceed. At any higher temperature, this energy barrier can be bridged if ice forms around a particulate that is already near the size r^*. In this case, increasing the number of water molecules attached to the impurity always has a larger volume term than surface term, and ice always is favored to grow. This is heterogeneous nucleation; because a particle of sufficient size bypasses the energy barrier of forming a stable ice nucleus, it has an exponentially-enhanced nucleation rate.

Ion-induced nucleation

The barrier to spontaneous nucleation can be significantly reduced in the presence of ions, as the electrostatic attraction between free ions and polar water molecules stabilizes small clusters of H_2O [30, 107]. In the formalism of CNT, the ion-dipole attraction can be described by adding a new term to the Gibbs free energy that depends on a new bulk property ϵ_r, the dielectric constant of the ice [31]:

$$\Delta G_\epsilon = -\frac{q^2}{8\pi\epsilon_0}\left(1-\frac{1}{\epsilon_r}\right)\left(\frac{1}{r_i}-\frac{1}{r}\right), \tag{6.8}$$

where r_i is the radius of the central ion. The appropriate dielectric constant is not well known, especially above the freezing temperature, as no stable condensed phase exists at pressures below the triple point. However, simulations have suggested that the local dielectric constant approaches that of liquid water ($\epsilon_r^{(\text{liq.})} \approx 80$) at higher temperatures [108] and gradually increases to that of ice ($\epsilon_r^{(\text{ice})} \approx 100-180$) as temperature decreases [109]. For small clusters, the dielectric constant likely lies below bulk values due to the breakdown of continuum electrostatics.

The total Gibbs free energy is plotted in Fig. 6.2 (c), along with the new critical sizes, e.g. where $d\Delta G_{nuc}/dr = 0$, in Fig. 6.2 (d). This causes a few key changes to the nucleation dynamics: firstly, a local minimum in ΔG_{nuc} appears at cluster sizes of $1-10$ water molecules when above some critical temperature. This stable branch in N^* indicates "bare" ions are thus less stable than "hydrated" ions, surrounded by small clusters of H_2O.

Secondly, while there remains an energy barrier to unimpeded ice growth at higher temperatures, this barrier is smaller than that of homogeneous nucleation. The nucleation rate J_{nuc} will thus be significantly larger, as it is exponentially dependent on the size of this energy barrier.

Finally, the temperature for spontaneous, unimpeded growth is significantly higher than in the homogeneous case: accretion is always energetically favorable below about 180 K in IIN, while in homogeneous nucleation, this critical temperature is about 120 K. This 180 K temperature matches well with our observations of ice formation within the plasma.

6.2 Rates of ion-H_2O clustering and destruction

At the start of ion-induced nucleation, ions are *hydrated*, accumulating H_2O molecules one-by-one; as time progresses, the cluster evolves to the size that CNT theory predicts. As ions continuously ionize and recombine within the weakly-ionized plasma, these clusters are also continuously produced and destroyed. Collisions with high-energy ions and electrons may also break the clusters apart. If the destruction happens sufficiently quickly, the clusters within the plasma may never reach the size predictions of CNT.

The clustering rate for a single water molecule to stick to an ion is estimated as follows:

$$\begin{aligned} R_{i-H_2O} &\approx n_{H_2O} \left(\frac{q_i \ \mu_E / 4\pi\epsilon_0}{m_r v_T^2} \right) \ v_T \\ &\sim 4 \cdot 10^6 \ \text{collisions/sec} \end{aligned} \tag{6.9}$$

An ion will therefore accumulate a water molecule roughly every $1/R_{i-H_2O} \approx \mathbf{0.25}$ μs. Here n_{H_2O} is the number density of the *vapor*; the reduced mass $m_r \approx m_{H_2O}/2$, and $\mu_E \approx 6.2 \cdot 10^{-30}$ $\text{C} \cdot \text{m}$ is the permanent electric dipole moment of water. The rate constant is calculated at a partial pressure of H_2O of 30 mTorr and a temperature of 150 K. This estimation ignores the orientation factor and polarizability of the molecules; a more precise calculation should use Langevin capture with a correction for the permanent dipole moment [31].

Ion clusters can be destroyed through two methods: charge neutralization and escape from the plasma. If a positively-charged cluster absorbs an electron (or a negatively-charged cluster, an ion), it will no longer have a net electric charge to stabilize the cluster or to attract new water molecules, and will quickly dissociate. Meanwhile, clusters can also diffuse out of the plasma into the walls of the chamber.

In neutralization collisions, the H_2O cluster collides with an oppositely-charged particle. We can thus use an OML-modified cross-section to calculate the neutralization rate. For cationic clusters, they are neutralized by colliding with an electron at a rate:

$$R_{c^+-e} \approx n_e \pi r_c^2 \left(1 + \frac{e^2/4\pi\epsilon_0 r_c}{k_B T_e} \right) \sqrt{\frac{k_B T_e}{m_e}}. \tag{6.10}$$

Analogously, anionic clusters are neutralized by ions at a rate,

$$R_{c^- - i} \approx n_i \pi r_c^2 \left(1 + \frac{e^2/4\pi\epsilon_0 r_c}{k_B T_i}\right) \sqrt{\frac{k_B T_i}{m_i}}. \tag{6.11}$$

In these equations, m_c and r_c are the mass and cross-section of the cluster. Notably, the $\sqrt{T/m}$ dependence causes positively-charged clusters to be neutralized significantly faster than anionic clusters. Using $n_i = n_e = 10^9$ cm^{-3}, $T_i = 150$ K, $T_e = 2$ eV, and an ion mass of 19 amu (H_3O^+) in equations 6.10 and 6.11, the neutralization timescale of positive and negative clusters with 1 nm radius (roughly 100 water molecules) is 0.3 ms for positively-charged clusters, and 10 ms for negatively-charged clusters. Cation clusters are thus destroyed a hundred times faster than anion ones.

In the case of cluster escape from the plasma, the free diffusion rate of a 1 nm cluster through the argon background gas [70], from the center of the plasma to the electrode edge, is calculated as:

$$\begin{aligned} \tau_{\text{free}} &= 3.5 \text{ cm} \Big/ \left[\pi^2 \frac{\sqrt{k_B T/m_{Ar}}}{\pi r_c^2 n_{Ar}}\right] \\ &\approx 1.0 \text{ sec.} \end{aligned} \tag{6.12}$$

Free diffusion of clusters is thus quite slow compared to both neutralization and clustering rates. The outward-pointing ambipolar electric field vastly alters this rate: as positive clusters are therefore accelerated out, and negative clusters are confined, the timescale for ambipolar diffusion of cation clusters is given as [70]:

$$\tau^+_{\text{amb}} = \frac{2}{1 + T_e/T_i} \tau_{\text{free}} \approx 2.5 \text{ ms}, \tag{6.13}$$

while negative clusters are well-confined.

As τ^+_{amb} is larger than the neutralization timescale, neutralization is the dominant method of cluster removal. As both positive and negative clusters survive significantly longer than the clustering timescale, we expect to see ion clusters with both polarities. However, because negatively-charged clusters have significantly longer lifetime, their concentrations are expected to be larger at higher mass and to dominate collection of H_2O molecules over time, likely the dominant precursors to ice grain nucleation.

6.3 Ion formation and plasma chemistry

While the classical theory of IIN is independent of what ion species catalyzes nucleation, in practice the ion size, lifetime, and chemical behavior is important to the nucleation.

Low-temperature plasmas host rich, non-equilibrium ion chemistry. Because ions feel long-range Coulomb forces and the electric potential, reaction rates are enhanced and pathways open that are not favored in neutral gases. Charge exchange, impact ionization, and multi-body recombination reshuffle charge and expand the pool of radicals and ions. The resulting cascades of ion-conversion reactions can yield many species of cations and anions, rather than just ionized states of the neutral gas inputs [110].

Cation production

In a plasma containing Argon and H_2O, the input gas is impact-ionized by high-energy free electrons:

$$\mathrm{Ar} + \mathrm{e}^- \rightarrow \mathrm{Ar}^+ + 2\ \mathrm{e}^- \tag{6.14}$$

$$\mathrm{H_2O} + \mathrm{e}^- \rightarrow \mathrm{H_2O}^+ + 2\ \mathrm{e}^- \tag{6.15}$$

It turns out that the H_2O^+ ion is highly reactive, short-lived and thus never abundant in large amounts within the plasma. Instead, it undergoes:

$$\mathrm{H_2O} + \mathrm{H_2O}^+ \rightarrow \mathbf{H_3O}^+ + \mathrm{OH} \tag{6.16}$$

The hydronium cation H_3O^+ is highly stable and is generally the most abundant positive ion in water plasmas.

While argon, a noble gas, is generally known to be inert, the non-thermal nature of the plasma allows significant amounts of argon-containing molecular cations form. While these molecules are short-lived, their generation rates are high enough to exist in significant compositions within the plasma. The most common reactions are [110]:

$$\mathrm{Ar} + \mathrm{H_2O}^+ \rightarrow \mathbf{HAr}^+ + \mathrm{OH}, \tag{6.17}$$

and

$$2\ \mathrm{Ar} + \mathrm{Ar}^+ \rightarrow \mathbf{Ar_2}^+ + \mathrm{Ar}. \tag{6.18}$$

The chemical environment becomes even more rich when using a non-inert buffer gas, such as hydrogen or especially nitrogen. Hydrogen plasma most dominantly favors conversion to H_3^+ ions, while even trace impurities of nitrogen gas in the chamber will react with hydrogen and oxygen from the water to produce protonated nitrogen hydrides and oxides such as NH_x^+, NO_x^+, and N_2O^+ [27].

Anion production

Electronegative gases produce negative anions as well as cations within a low-temperature plasma. Lower-energy electrons, incapable of impact-ionizing, can attach to the neutral molecules through processes such as:

$$OH + e^- \rightarrow OH^-. \tag{6.19}$$

Of the radicals produced through H_2O reactions, hydroxide (OH) has the highest electron affinity [27].

Practically, however, these electron attachment reactions are fairly slow. as the product must dump its excess energy through radiation or coupling to a third body in the plasma. Anions are much more quickly formed through dissociative reactions such as

$$H_2O + e^- \rightarrow H^- + OH, \tag{6.20}$$

$$H_2O + e^- \rightarrow OH^- + H, \tag{6.21}$$

and

$$O_2 + e^- \rightarrow O^- + O. \tag{6.22}$$

Ion conversion reactions then quickly funnel the charge to hydroxide:

$$H^- + H_2O \rightarrow OH^- + H_2, \tag{6.23}$$

$$O^- + H_2O \rightarrow OH^- + OH. \tag{6.24}$$

Hydroxide anions are thus expected to dominate the anion composition in the plasma. Indeed, measurements by Eschbach [90] on the Ice Dusty Plasma Experiment showed that a significant amount of the negative charge in an Ar:H_2O plasma was carried by OH^- anions. Trace amounts of nitrogen impurities in the plasma can also cause significant concentrations of NO_x^-, and especially N_3^-, which is highly stable.

6.4 Laboratory methods

The vacuum chamber was fitted with an ion energy analyzer built by Hiden Analytics (See Chapter 3.5 for details). Cations, anions, and neutrals are extracted at its "collector," which sits at the outer edge of the plasma. The collected particles are then sorted by mass and directed into the detector.

Each mass spectrum takes a handful of seconds to collect. The instrument sweeps over a range of molecular masses (1-1000 amu), waiting for some "dwell time" (typically 50 ms) at each mass increment, and records the number of particle counts detected during this period.

When collecting the mass spectra in steady state, the anion collection is nearly always below the detection limit. This is due to the ambipolar field: while positive ions constantly flux out of the plasma and are easily collected, negative ions are well-confined and rarely make it to the collector. To remedy this, the plasma power was pulsed by modulating the RF power with a square wave at 500 Hz. The plasma thus repeatedly switched on for 1 ms, long enough for clusters to form and seed ice nucleation, and then switched off another 1 ms, long enough for the ambipolar field to decay and a significant amount of anions to reach the detector.

The 500 Hz modulation signal was also input to the mass spectrometer's control box, which can time its measurements in sync with the pulse. Instead of recording the particle counts at each mass increment over a *continuous* dwell time of 50 ms, it instead recorded the counts within a shorter "gating window" with a width of 100 μs, synced to a particular portion of the modulation signal, repeatedly over several pulses, until the sum of the recorded 100-μs gate widths reached the preset 50-ms dwell time.

This collection process could then be repeated with the gating window adjusted to a different portion of the modulation signal. We can thus obtain time-resolved ion concentrations as the plasma switches on and off, observing cations form and stream out of the plasma when powered, and anions be released from the afterglow. This is illustrated in Fig. 6.3.

The sensitivity is not even across the 1000-amu range of the mass spectrometer. When operating the instrument, its internal electrodes must be tuned to maximally transmit ions of a desired mass; the sensitivity will thus be highest within the surrounding ~ 50 amu, dropping as the mass diverges

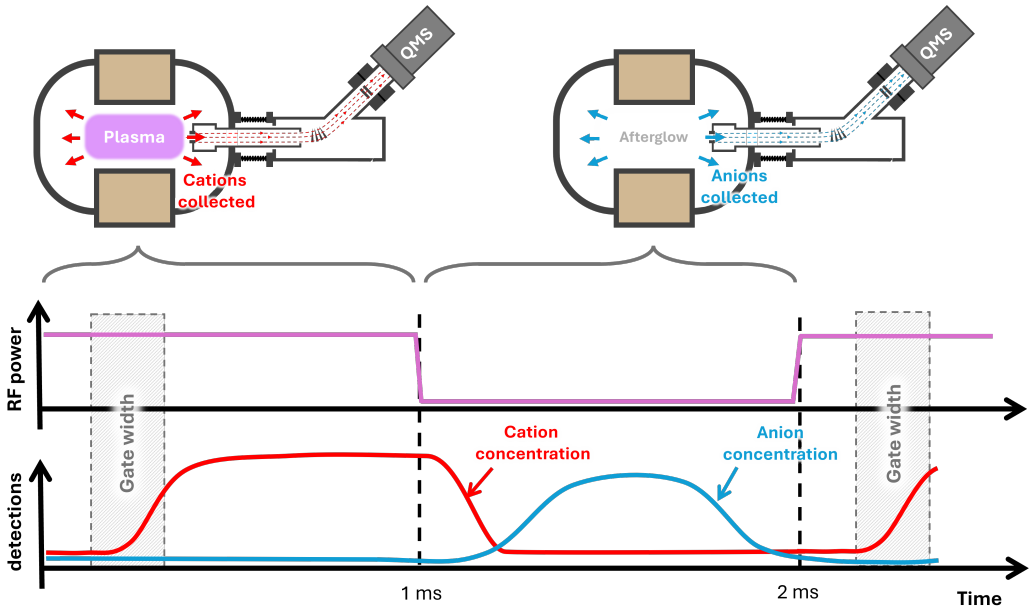

Figure 6.3: RF power is pulsed at 500 Hz. Cations continuously stream out of the plasma while the RF power is on; anions escape while the plasma is off, after the ambipolar field vanishes due to the escape of the remaining cations. The ion concentrations are measured by the mass spectrometer over some gate width, synced to the RF pulses.

from the tuned value. The relative magnitudes of lines far away from each other thus do not necessarily reflect the relative abundances of the ion species in the plasma.

6.5 Results from ion mass spectroscopy

A series of experimental runs were conducted at varying electrode temperatures between 100 and 250 K. Argon plasma was produced at a pressure of 300 mTorr and a forward RF power of 30 W, and mass spectra of the neutrals, anions, and cations were taken in 100 μs gating windows throughout the 2-ms period of the RF power modulation. Once spectra were collected in the pure-Ar plasma, water vapor was introduced to the chamber at $\sim 10\%$ the Argon flow rate, and a second sequence of spectra were collected. Time-averaged mass spectra are shown in Fig 6.4 for two temperatures: (a) 250 K, and (b) 100 K— note that because of the low pressure, 250 K is above the freezing temperature: vapor is the stable phase, and no ice forms.

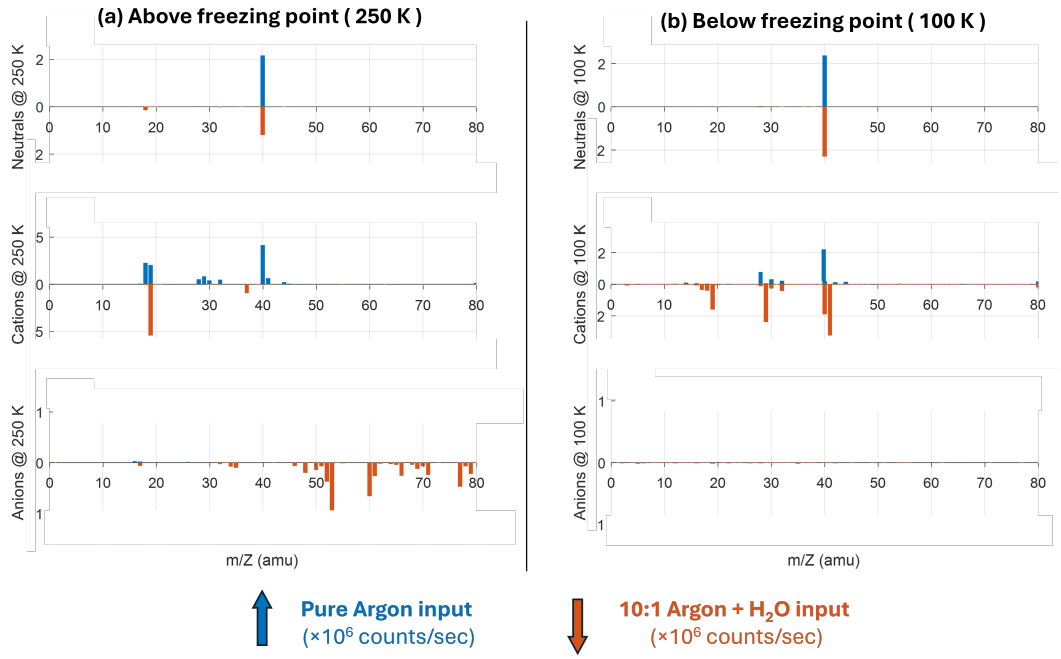

Figure 6.4: Mass spectra of neutral molecules, positive ions, and negative ions, time-averaged over the 500 Hz pulse cycle; two runs are displayed, (a) at 250 K, and (b) at 100 K. Blue bars show spectrum in Argon plasma *before* water injection, and red inverted bars were measured with steady water vapor injection at 10% the Ar flow rate.

At 250 K, we see that the neutral composition is predominately pure argon at 40 amu, with a small signal at 18 amu visible upon water injection (red bars). This 18 amu is not visible at 100 K, as the vapor freezes to ice grains or the electrodes before reaching the collector of the mass spectrometer.

The mass spectrum of positive ions changes considerably between the scans at 250 K and 100 K. Before water injection at 250 K, the plurality of cations are mass 40, corresponding to Ar^+, though it is *not* the only significant ion species. Despite the neutral composition being very pure argon ($< 99\%$), over half the positive ions are mass 18, 19, 28, 29, 30, or 32 amu— these correspond to molecules of water, nitrogen, and oxygen.

Further, upon water injection, nearly all argon ions disappear, and the plasma becomes nearly *entirely* H_3O^+, along with it's hydrated form $\mathrm{H_3O^+(H_2O)}$. This switch corresponds to the drastic color change in the plasma at high temperature, which goes from the characteristic bright pink-purple of an Argon plasma to a dull, deep purple concentrated near the powered electrode

[90]; as hydronium does not have dominant spectral line emission in the visible range, most of the plasma is invisible to the naked eye.

Interestingly, this is not as drastic a change at low temperature. While a significant amount of H_3O^+ does form upon water injection, a large population of Ar^+ ions remain, as well as trace Ar_2^+ at 80 amu. Furthermore, the most common ion species is 41 amu rather than 40, indicating argon ions are reacting to form HAr^+.

Finally, the negative ions show no signal before water injection at either temperature— this is expected, as argon is not electronegative. Upon water injection, however, a host of lines appear at 250 K. As expected, we see a small peak at 17 amu, indicative of OH^-. Much bigger are their hydrated forms— 35, 53, and 71 amu, corresponding to $OH^-(H_2O)_n$ clusters with $n = 1,\ 2,\ \text{and}\ 3$, respectively. Several other anions also appear— trace amounts of O^-, O_2^- and their corresponding clusters are detected, but significant unexpected peaks also appear at 46, 48, 60, 66, and 77 amu. These are likely stable anions formed from trace impurities of nitrogen and oxygen that were introduced with the water vapor, such as N_3^-, NO^-, NO_2^-, some with H-bonded water molecules.

Cluster detection

This experiment was repeated with the mass spectrometer tuned to heavier ions, scanning up to 300 amu. In Figure 6.5, the ion spectra are plotted, smoothed over mass with a 5-amu gaussian window. This clearly shows a sequence of ions, with a rough periodicity of 18 amu, reaching at least to 200 amu in the case of negative ions, characteristic of an anion species with $10-11$ water molecules attached. Positive ions, meanwhile, only reach about 100 amu. This is clear evidence for the formation of ionic water clusters especially around negative ions, matching predictions by Bellan [30], and mirroring similar processes in silane plasma [102].

The 18 amu periodicity is not perfect; clustering thus does not simply follow $OH^- + n(H_2O)$, but is a bit more "muddy" — this suggests that other molecular species can also bind to the clusters. For instance, some of the largest peaks above 100 amu are separated by 17 amu rather than 18, suggesting that clusters of this size are more stable if they collect a hydroxide molecule rather than H_2O. This is likely related to the precise bonding geometry of the

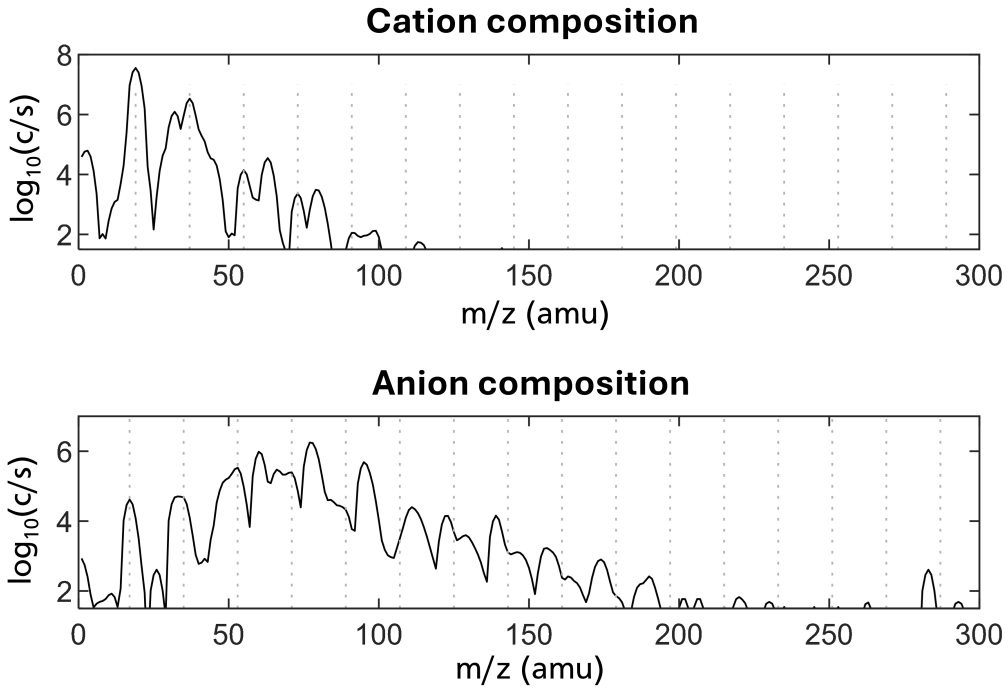

Figure 6.5: Mass spectra of cations and anions up to 300 amu, averaged over time, at 250 K. Spectra are smoothed with a 5-amu gaussian window to more clearly show clustering

molecules in the cluster, similar to the concept of "magic numbers," which is itself an active and complicated field of physical chemistry [105].

Time-dependence of ion detection

The time resolved measurements for ion concentrations over the 2 ms period of the RF power modulation are plotted in Fig. 6.6. Panel (a) shows the anion mass spectrum at five points within the 1 ms window when the RF power is off (the "afterglow"). Within 200 microseconds, lighter anions (< 100 amu) are detected streaming from the afterglow. Heavier ions reach the detector a few hundred microseconds later due to their longer transit times.

Panels (b) and (c) of Fig. 6.6 shows the concentration of hydroxide anions and hydronium cations, respectively, along with their corresponding clusters of 1-3 water molecules. Both are plotted over 1 ms, synced to the 500 Hz power modulation; anions are plotted while the RF power is switched off, and cations while the on. Results match our expectations, which are sketched in Figure 6.3. As the travel time to the detector is much longer than the

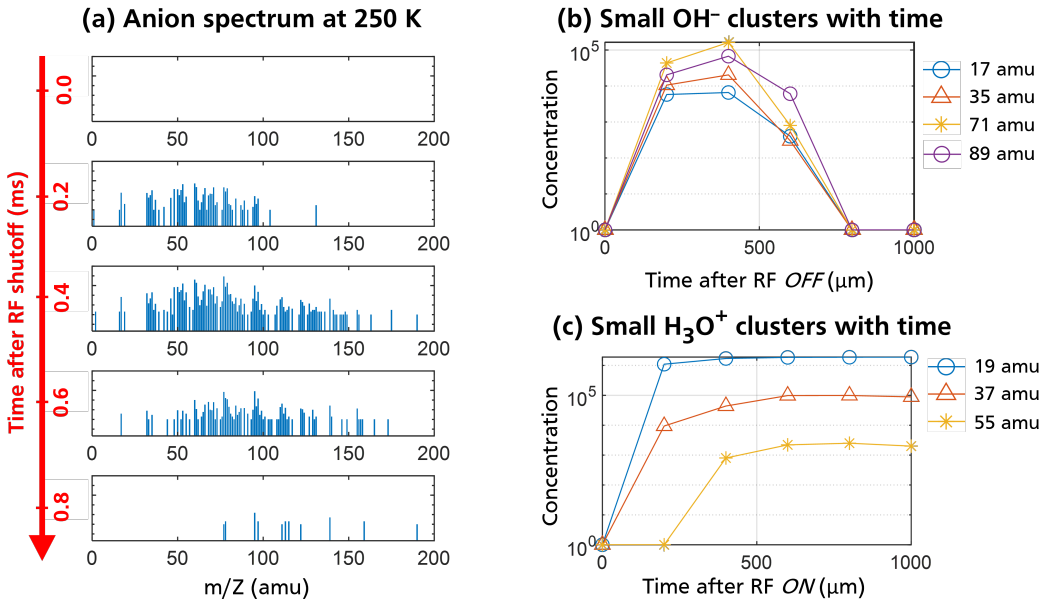

Figure 6.6: (a) Anion mass spectrum every 200 μs after plasma shutoff; (b) concentration of bare OH^- and clusters with $n = 1 - 3$, over the 1 ms plasma *off* window; (c) concentration of bare H_3O^+ and its first two clusters during the plasma *on* window.

clustering rate, the delay in detecting larger ion species is attributed to their slower diffusion velocities.

Ion composition with temperature

In Fig. 6.7, the mass spectra are plotted for each measured temperature, ranging from 120 to 260 K in 10 K increments, and compiled into a heat map. Each row of the map shows a mass spectrum from 1-80 amu, plotted on a logarithmic scale to reveal trace elements, at a different temperature; each column shows how the composition of the corresponding ion/neutral species varies with temperature.

Most notably, there exists a critical temperature at which the spectra suddenly change, at about 235 K. This is approximately the freezing point of water vapor at the system pressure. We must note that this is *not* the temperature at which ice grains are observed nucleating in the plasma; ice grains are never visible above about 180 K (see discussion in Sec. 4.1).

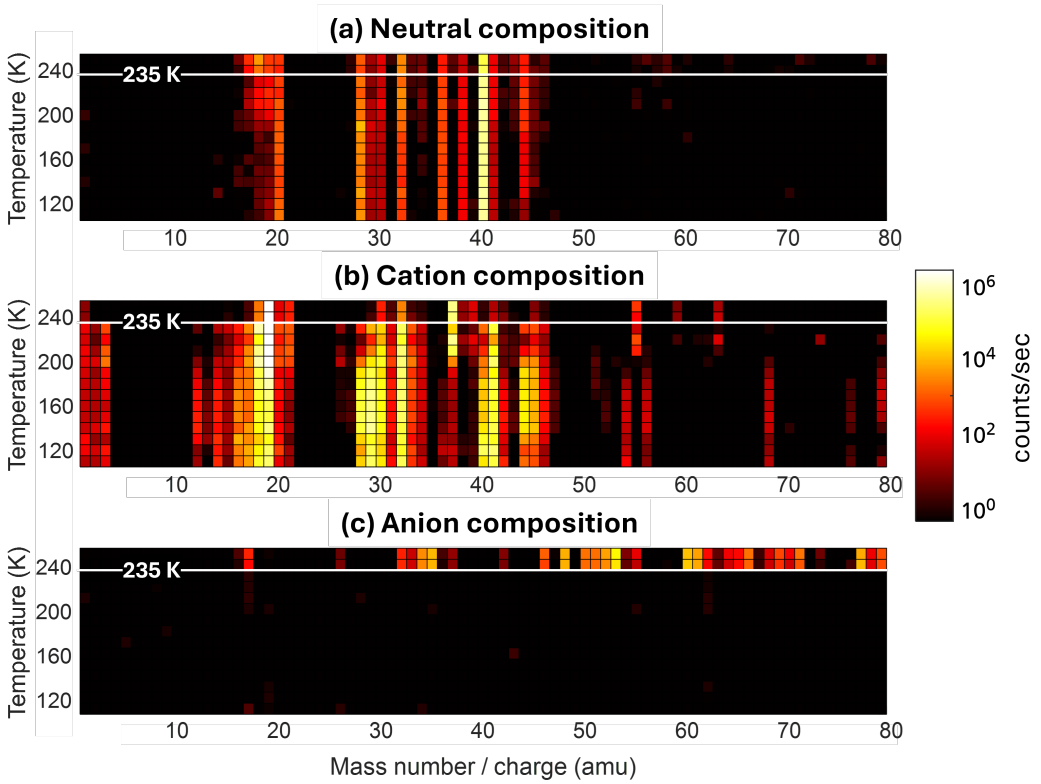

Figure 6.7: A heat map showing mass spectra in Ar:H_2O plasma varying with electrode temperature, ranging 120 to 260 K, in 10 K increments. The signal magnitude is shown in log scale ($\log_{10}(\text{counts/sec})$).

Below 235 K, neutral H_2O decreases in concentration by an order of magnitude. Simultaneously, the concentration of the 18-amu cation H_2O^+ *increases* by an order of magnitude, while concentration of 19-amu H_3O^+ does not show a significant change in composition. Several other cation species also become more abundant, especially H^+, H_3^+, HN_2^+, O_2^+ and HAr^+. It thus seems that neutral water molecules are increasingly dissociated into constituent hydrogen and oxygen and underwent more complex chemistry below the freezing temperature.

The negative ions, meanwhile, decrease by *several* orders of magnitude below this critical temperature. This may be due in part to the drop in ambient neutral water molecules at the freezing point, but this cannot explain the disappearance of nitrogen anions such as N_3^-, nor can it explain why H_3O^+ formation doesn't show a similar decrease.

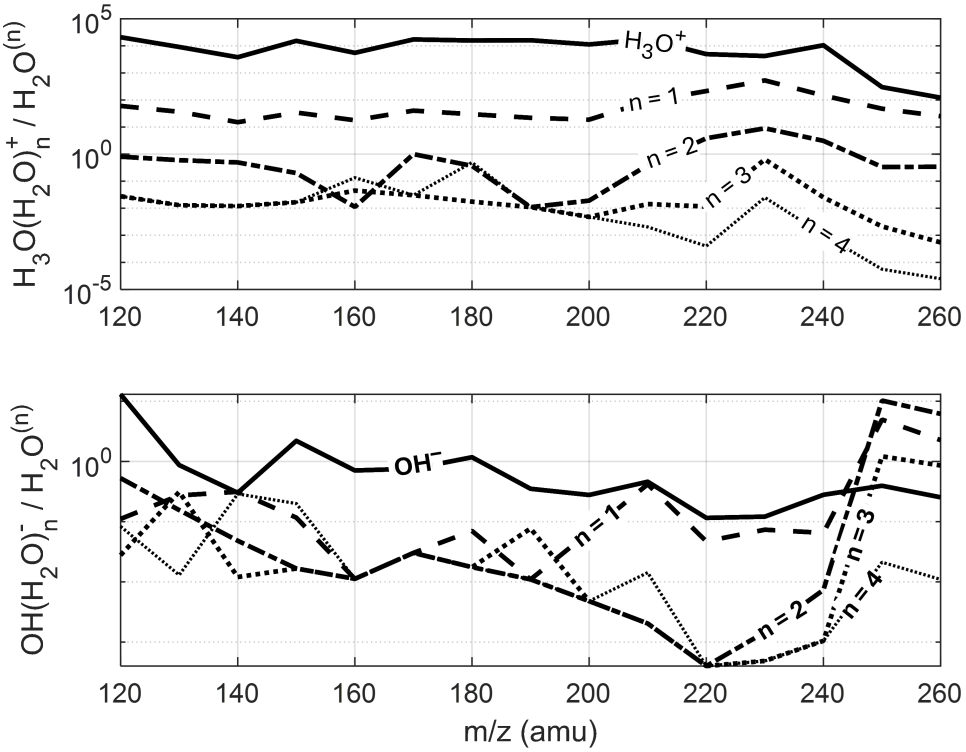

Figure 6.8: concentrations of $\mathrm{H_3O^+(H_2O)_n}$ (top) and $\mathrm{OH^-(H_2O)_n}$, for $n = 0$, 1, 2, 3, and 4, all normalized by concentration of neutral $\mathrm{H_2O}$.

Cluster behavior near the freezing point

Clustering about anions and cations shows very different behavior at the freezing point. If we normalize the data in Fig. 6.7 to the neutral mass-18 signal at the corresponding temperature, we account for the change in number density of water molecules as the temperature drops. Figure 6.8 shows the concentrations of $\mathrm{H_3O^+}$, $\mathrm{OH^-}$, and their first 4 clusters, divided by the concentration of neutral water at that temperature.

The normalized concentrations of bare hydronium cations and associated $\mathrm{H_2O}$ clusters show little variation throughout the temperature range; the change in their concentration with temperature observed previously is thus accounted for by the changing amount of ambient water. The same is true for the bare hydroxide anions: the composition is relatively stable, with no significant discontinuity at the freezing point.

The $\mathrm{OH^-(H_2O)_n}$ clusters, however, still have a sharp discontinuity at the freezing temperature: above 235 K, they are much more prevalent than bare

OH^-, while below, all clusters drop drastically in normalized concentration. This indicates that small anionic clusters suddenly become energetically disadvantageous when the temperature drops. This could be explained if the small clusters can suddenly overcome surface forces to grow unimpeded, such that all clusters of 1-10 H_2O are efficiently turned into ice nuclei that are too massive for the mass spectrometer to detect. However, it must be noted that no *do not optically detect* ice grains until much lower temperatures.

6.6 Evaluating anionic clusters as ice precursors

Comparison to IIN predictions

Recall that the classical theory for ion-induced nucleation is stable predicts equal clustering about any ion species, positive or negative, as the stability of small clusters is induced by the electrostatic dipole-ion interaction. All ions would thus hydrate to some stable cluster size. This is *not* supported by our data: certain ions seem much more capable of clustering than others. For example, $H_3O^+(H_2O)_n$ clusters are observed up to n=5, while no $HAr^+(H_2O)_n$ clusters are observed, despite bare HAr^+ being abundant. This asymmetry between species is not unexpected, as CNT's continuum assumption breaks down at small sizes and quantum mechanics is required to predict the true bonding structure and stability.

We also predicted that larger anion clusters should be achievable compared to cation clusters, as positive clusters attract electrons and are rapidly neutralized and lose stability. This is supported by observations: Fig. 6.5 shows anion clusters within the entire scanned mass range, while no cations are detected larger than 120 amu, a maximum cluster size of $5 - 6$. The cation destruction is thus *much faster* than predicted: as we calculate the timescale of clustering is 2-3 orders of magnitude shorter than the timescale for electron capture, we would expect much larger cation clusters to exist. This could indicate an unknown, faster pathway of cation cluster neutralization, such as interactions with nearby negatively charged clusters, or a weakened ion-dipole interaction for positive ions compared to negative ones.

Finally, CNT predicted a stable cluster size in the range of $n = 1 - 10$, increasing as temperature drops, when above some critical temperature $T_c \approx 190$ K, as shown in Fig. 6.2 (d). Below the critical temperature, spontaneous

nucleation is predicted as the stable equilibrium at low N_{H_2O} vanishes and ice grows unimpeded. This is a good *qualitative* match to the data: we also observe stable anion clusters up to a critical temperature, and then a sudden drop in all anion concentrations below this temperature. Their disappearance plausibly suggests the small clusters very efficiently grow into much larger ones, outside the mass range of these measurements, and thus the lifetimes of small clusters are too short for them to appear in any detectable concentration.

It must be noted that plasma-induced particle formation in silane plasmas does not show this same pattern: using similar instrumentation and a similar RF modulation timescale for ion detection, Howling *et al.* [102] detected anionic clusters of silicon through the entire mass range concurrently with visible particle formation. However, as the unique chemistry of water greatly changes the form of the Gibbs free energy of nucleation, driven by its high permanent dipole moment (note silane is nonpolar), hydrogen bonding, and large surface tension— because of this, water cluster growth is many times faster, and may be responsible for the apparent removable of all small $\mathrm{H_2O}$ clusters on the timescales of our measurements.

While our measurements qualitatively match the temperature behavior predicted by ion-induced nucleation theory, it quantitatively deviates in two important ways:

1. The critical temperature ($\approx$ 235 K) is significantly higher than that predicted in Fig. 6.2 (d)

2. Ice grains are not optically visible until 180-190 K, significantly lower than this critical temperature.

Further evidence is therefore required to conclude with any certainty that these anion clusters observed at high temperature are indeed the precursors to ice grains seen at lower temperatures; that is, to determine that fast-growing anion clusters are indeed the *dominant nucleation sites* within the ice-dusty plasma.

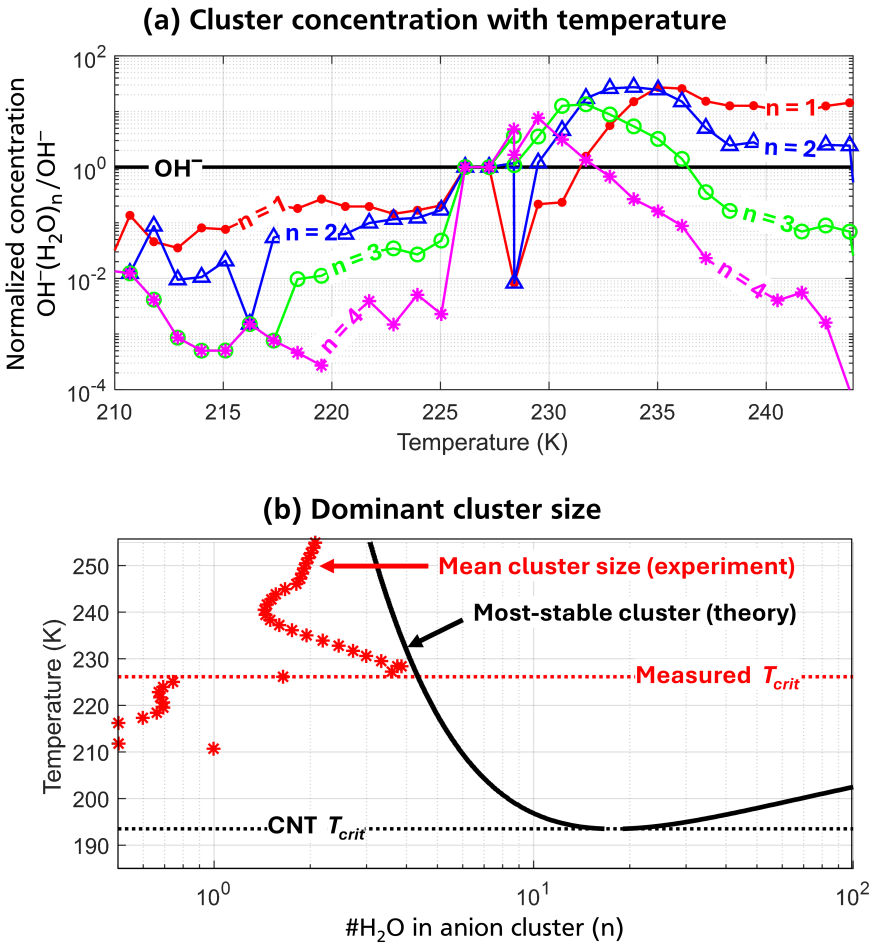

Figure 6.9: (a) Concentrations of $\mathrm{OH^-(H_2O)_n}$, for $n = 1$, 2, 3, and 4, normalized by the concentration of bare $\mathrm{OH^-}$; (b) Average cluster size versus temperature from measurements, plotted alongside the predictions from IIN theory.

Anion disappearance at the freezing temperature

To examine the behavior of anions at the critical temperature, a new set of data was taken between 210 and 250 K, with much higher temperature resolution. Figure 6.9 (a) presents the concentration of the first four clusters about $\mathrm{OH^-}$, normalized to the concentration of the bare hydroxide ion. In this run, we observe that $n = 1$ is the most stable cluster above about 236 K. As temperature decreases from 236 and 227 K, larger and larger clusters become stable, while smaller ones decrease in abundance; at 227 K, $n = 4$ dominates. Below 226 K, all the clusters are significantly less abundant than bare hydroxide.

The average cluster size is obtained from this data, and is plotted in Fig. 6.9 (b), alongside the cluster stability graph obtained from the theory of ion-induced nucleation. This illustrates the deviation between experiment and theory: the critical temperature is significantly higher in experiment, while the stable cluster sizes at higher temperatures are smaller than the theoretical predictions, and the shape of the size increase near the critical temperature is altered.

It is likely that the deviation is fully due to inaccuracies in the theory: we made a lot of assumptions about the environment, such as the partial pressure of water, the saturated vapor pressure, and the values of ice dielectric constant and surface tension. If the partial pressure in experiment is significantly higher than we assumed, this would increase the theoretical critical temperature. It also did not account for any change in partial pressure as temperature dropped.

The continuum assumption used in calculating the most favorable number of water molecules in the cluster is also flawed, as individual clusters cannot have non-integer sizes; in practice, a distribution of cluster sizes are present, and it is not clear that the average of these should match theory to begin with. Further, the dependence of cluster stability on number of H_2O is not monotonic due to quantum mechanical effects, which could allow smaller clusters to grow past the critical size for runaway nucleation at higher temperatures. Due to the non-thermal nature of the plasma, clusters may bridge the ΔG barrier to grow unimpeded at higher temperatures than expected.

The critical temperature in the measurements is very close to the freezing point and the experiment's pressure. Though the notion of freezing is not completely well-defined for collections of 1-10 molecules, the bonding energy and electric permittivity (and thus the clustering rate) may in fact change at this temperature, an effect not captured in our IIN computation. As classical nucleation theory invokes bulk properties, such as surface tension and dielectric constant, it is unclear if they change when the freezing temperature is traversed— especially as we are below the triple point, so no condensed phase exists above the freezing temperature from which to extrapolate the bulk properties.

There is also a possibility that the measured decrease in anions is *not* due to nucleation, and instead the ions are destroyed by other means. This seems

unlikely, as cations do not show this temperature dependence precisely because they are destroyed before growth, but the possibility cannot be discounted entirely. Resolving these issues will require further theoretical and computational modeling, employing kinetic simulations and incorporating quantum chemistry to better predict clustering rates and stability.

Gap in ice detection

A second discrepancy lies between measurements of anion disappearance, which we suggest arises due to ice nucleation, and detection of ice grains themselves. While we suggest that clusters grow rapidly below 230 K, our proposed "nucleation temperature," we do not observe ice optically until about 180 K, whether through laser scattering, FTIR extinction, or microscope imaging. We thus have not directly observed clusters "become" ice grains, i.e. a smooth increase from $n = 1 - 10$ to $n \sim 10^5$.

This 50-kelvin temperature difference between the critical temperature for nucleation and ice observation could simply be due to the limits of our detection methods. As the mass spectrometer can only detect up to 1000 amu, we cannot detect clusters larger than about 55 molecules, a radius of about 0.7 nm. Meanwhile, as particles much smaller than $\sim 10\%$ of the wavelength of light are virtually undetectable through scattering and extinction methods, it is plausible that ice *does* exist within this temperature gap, but is limited to the scales $\ll 100$ nm, which does not significantly scatter our 532-nm laser. There is just a gap of two orders of magnitude in grain size in which behavior remains mysterious.

According to the model proposed in Section 4.5, grain size experiences a sudden increase at the onset of fractal agglomeration, which occurs when reaching both a critical grain density ($n_d \sim n_e$) and a critical grain size (~ 100 nm). Practically, grains are likely undetectable to our optical methods before the onset of agglomeration.

As sublimation rates are larger at higher temperatures due to the larger equilibrium vapor pressure of water, ice cannot reach sizes as large as it can at lower temperatures, as less ice is needed to deplete the ambient vapor pressure below the saturation point. Furthermore, higher temperatures have lower gas densities at the same pressure, leading to fewer anions to act as nucleation sites. Both these effects may prevent the onset of the fast

agglomeration phase of growth, explaining why ice is not visible until the temperature decreases.

Solid evidence of grain formation directly from clusters must therefore probe this "mysterious size gap." One such option would be using much shorter wavelengths of light to detect smaller particles, such as an XUV scattering scheme. Another option would be to probe the perturbation of the plasma by ice formation: Boufendi *et al.* [67] showed that the impedance of the plasma and harmonic generation of the RF sheaths is strongly sensitive to particles 1-5 nm in size. If these methods can detect nanometer-scale ice grains begin forming at the same temperature as anionic clusters disappear, this would effectively bridge the gap to tie anions directly to ice formation and rule out other nucleation pathways. Investigation of those two methods is left for future work.

6.7 Summary and implications to astrophysics

In summary, we present direct evidence that *negative ions* efficiently seed ice nucleation within cold, weakly-ionized plasmas. Time-gated ion mass spectra show efficient clustering of water molecules around anions, consistent with predictions of [30], showing anion hydration extending to $\gtrsim 200$ amu with approximate 18-amu periodicity; this indicates successive additions of water molecules around the anion species. Departures from perfect 18-amu periodicity are consistent with co-adsorption or radical addition (e.g., OH) that stabilizes specific cluster sizes. Cations, meanwhile, show clustering only up to about 100 amu, as they have significantly smaller lifetimes due to fast neutralization by ambient free electrons.

Further, we observe strong clustering about OH^- and O_2^- anions formed through disassociation of water vapor itself, showing that the this ion-induced nucleation can be *homogeneous*— i.e., it does not require pre-existing solid or gaseous impurities. Notably, we see that nitrogen impurities cause anions that also induce clustering; future work, both experimental and theoretical, can examine how such ion species can enhance the rates of ice nucleation and measure its affect on the emergent phase structure of the ice.

A sudden drop in anion concentration below the freezing temperature is supporting evidence of their growth into much larger ice grains, as the lifetime of small clusters would significantly drop as they grow beyond

the 1-nm scale. Future experiments should search for currently-undetected nano-scale grains around this critical temperature to directly connect anion disappearance with nucleation.

Implications and extensions to astrophysics

The ability of ice grains to self-nucleate from cold water vapor under weakly-ionized plasma conditions carries profound implications for ice grain formation in interstellar and protoplanetary environments. Experimental results demonstrate homogeneous nucleation of ice, catalyzed by anions. Further, we show that both metastable amorphous and stable crystalline ice grains can arise through this nucleation process, depending on the prevailing thermal conditions.

In protoplanetary disks, we predict a radial stratification: at very low temperatures ($\lesssim$130 K) far beyond the ice line, we would expect to find small amorphous grains; closer in, higher temperatures favor growth and reordering into crystalline ice. In dense molecular clouds, where temperatures are even lower and electronegativity is high, ion-induced nucleation can seed small amorphous grains even without refractory dust; in dust-rich regions, heterogeneous and homogeneous pathways likely operate in parallel, with their relative weights set by dust surface area, plasma parameters, and local supersaturation.

As recent advances in space telescope capabilities, promoted by JWST and SPHEREx[4], delivering high-fidelity spectra of interstellar and circumstellar ices and dusts, understanding the formation, chemistry, and optical properties of these ices has never been more critical to advancing the frontiers of astronomy.

Future work, both theoretical and experimental, should quantify how anion-induced homogeneous rates and heterogeneous rates of nucleation scale as pressure and temperature approach in-space conditions, and how they are modulated by the composition of the gas. In particular, trace admixtures common to astrophysical ices such as CO, CO_2, NH_3, PAHs, and gas-phase metals may alter electron attachment, anion lifetimes, and the energetics of H_2O clustering. Laboratory campaigns that combine ion mass spectroscopy

[4]JWST: James Webb Space Telescope; SPHEREx: "Spectro-Photometer for the History of the universe, Epoch of Reionization and ices EXplorer"

with measurement of absorption spectra would help bridge the gap between complex telescope data and models of interstellar and protoplanetary dusty plasmas.

Part III

The Dynamics of an Ice-Dusty Plasma

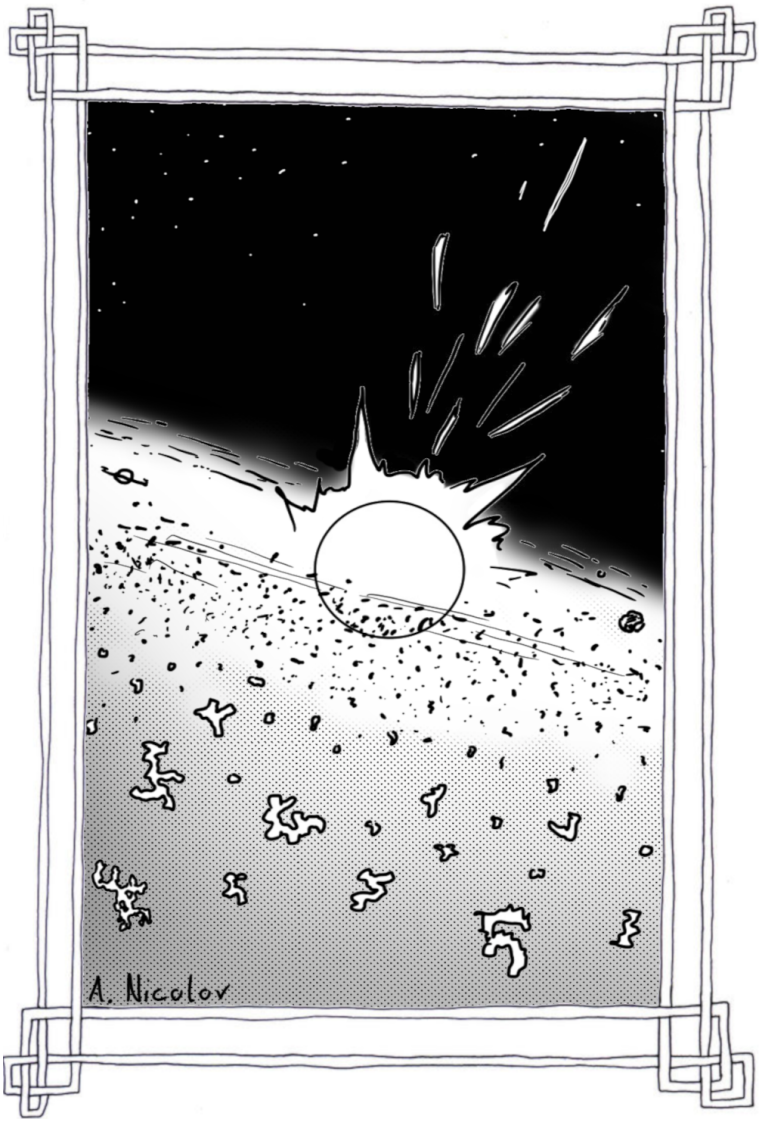

"No snowflake in an avalanche ever feels responsible." -Voltaire

Chapter 7

MEASURING THE DYNAMICS OF FRACTAL ICE GRAINS

> Nicolov, A. *et al.* The dynamics of fractal ice grains in cryogenic plasma. *Physical Review Letters.* accepted. `http://doi.org/10.1103/rx5l-k7f9` (2025).
>
> ...

We observe a host of complex, nonlinear dynamics of the ice grains within our laboratory plasma that evolve in unexpected ways over time. This behavior is difficult to describe, however, as the grains have an irregular, fractal morphology that causes deviation from existing dynamical models, which typically assume spherical grains. We thus have not yet been able to formulate an accurate and predictive dynamical description of the ice-dusty plasma's behavior over time.

In this chapter, therefore, I take the first step towards a more robust dynamical description. Through high-speed imaging of grain dynamics within the plasma afterglow and employing a host of plasma diagnostics, I determine the masses and collisional cross-sections of the ice grains and their scaling laws with grain length. This foundation can be used in future work to better model the dynamical behavior and understand the mysterious behavior we observe.

7.1 Dynamic evolution of the ice cloud

Within seconds of water injection, grains become visible to the laser sheet imaging scheme (see Sec. 3.5) filling the plasma– this is shown in Fig. 7.1 (left). In contrast to similar dusty plasma experiments [87, 112], in which spherical grains larger than a few microns settle to a layer just above the lower electrode due to gravity, these ice grains can span hundreds of microns and yet remain dispersed through the bulk plasma. This lack of sedimentation suggests that the relative effect of gravity has been greatly reduced compared to the electric confinement forces despite the ice grains growing orders of magnitude larger than the solid spheres grown in the other

experiments– we propose that this is due to the grains' fluffy, fractal structure, as seen in Fig. 7.1 (right).

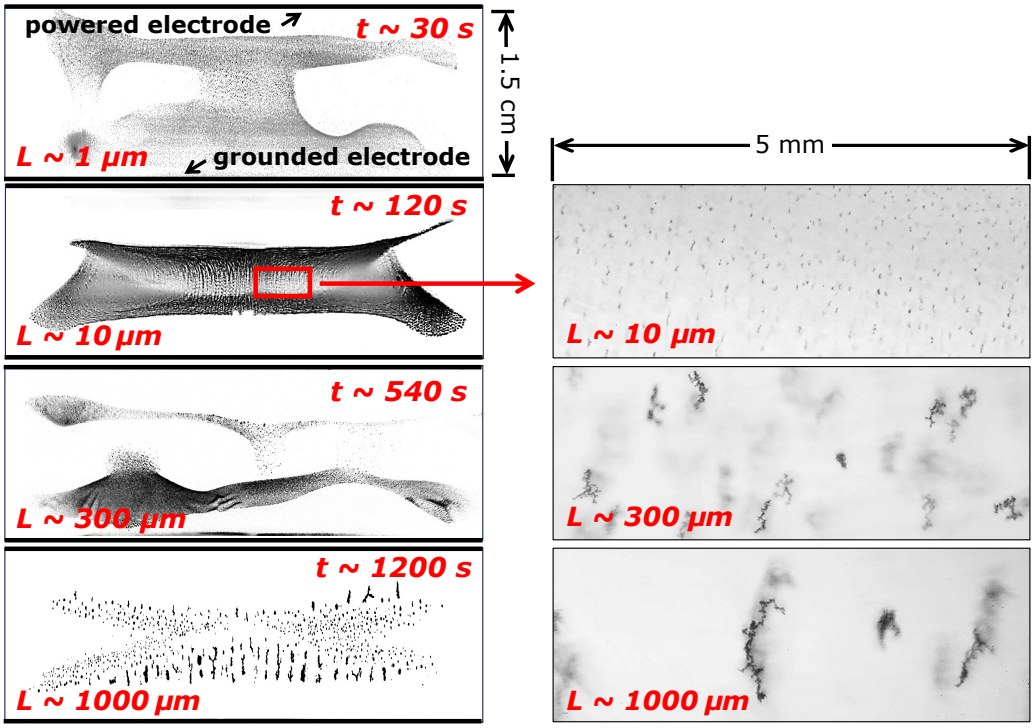

Figure 7.1: Photos of the grain cloud and individual grains at several times throughout a 20-minute period, showing the presence of waves, emergence of instabilities, and self-organization into lattice structures. Laser scattering photos (left) have been color-inverted for clarity.

The ice cloud contains complex motion, including vortices, waves, and dynamic instabilities. These dynamics evolve over time as the grains grow. In the first few minutes after grain formation, the grains rapidly move through vortices in the (r,z) plane of the plasma: along the vertical centerline of the plasma, they speed away from the powered electrode (downward in Fig. 7.1; this flips when electrode polarity is inverted), and return the opposite direction along the outer edges of the cloud.

As the grains grow, the vortex begins to slow down: when they reach about 10 microns in length, they rotate at tens of centimeters per second. When the grains hit some critical size, the vortex suddenly becomes unstable: the downward and upward motions start pulsing, rather than being smooth flows, while the rest of the cloud "ripples." The pulsing frequency slows as

grains continue to grow, until it stops altogether– at this point, the grains settle into two stable clouds, one on the top and one on the bottom.

This sequence of vortex $\rightarrow$ pulsing instability $\rightarrow$ "quiescent" clouds varies with system properties. It is most prominent in hydrogen, while in Argon, the pulsing often doesn't occur– this could be because the grains remain too small, or because it is stabilized by the much-higher neutral drag force (20 times larger for Ar vs. H_2). The criteria for the onset and end of instability also depends on the power and electrode separation– if the power is low or the separation is large, the vortex stops more quickly.

This dynamical sequence also progresses only when vapor flow is shut off once ice has nucleated; if it is left on, the vortex motion doesn't become unstable, and if waterflow is re-introduced once the grain cloud has become quiescent, the vortices can re-start.

Throughout the experimental timescale, we observe traveling dust density waves throughout the cloud. These waves are on a scale observable by the naked eye, with wavelengths of a few millimeters, and speeds of tens of cm per second. As grains get larger, the waves have slower speeds and longer wavelengths. It is most likely (though has been disputed) that these are dust acoustic waves [41, 113], though the dispersion relations do not match well with predictions via conventional theory. These waves may be involved in driving the large-scale instabilities, but further work will be required to investigate this.

Because of the irregular shapes of the grains, we do not know the mass or cross-section of any given grain. This makes it nearly impossible to extract key dynamics from these observations, such as the modes or mechanisms behind the dynamic instability, as dynamical models that utilize uniform, spherical grains do not fully reproduce this behavior.

7.2 Dominant forces

Five forces control grain dynamics: electric field, ion drag, neutral gas drag, thermophoretic force, and gravity. [40]. For a single grain, the equation of motion can be estimated:

$$m\frac{d\vec{v}}{dt} = \vec{F}_E + \vec{F}_{d,i} + \vec{F}_{d,n} + \vec{F}_{th} + \vec{F}_G. \tag{7.1}$$

This equation ignores grain-grain interactions, which are typically modeled using a repulsive Yukawa potential [114] as well as coupling and feedback between grain and gas flows, which require a multi-fluid description.

Electrostatic and ion drag forces

The electric force and the ion drag force tend to dominate within the RF discharge, competing to drive the intricate flows and vortices of dust grains [65, 114]. The electric force,

$$\vec{F}_E = Z_d e \langle \nabla \phi \rangle, \tag{7.2}$$

depends on the time-averaged electric potential profile; this is dominated by the ambipolar field, in which $\nabla\phi \sim \nabla n_i$. As discussed in Section 3.3, this is determined by the electrode geometry, plasma density distribution, and intricacies of the sheaths.

Meanwhile, the ion drag force arises due to streams of ions out of this same electric field; the electrostatic and ion drag forces are thus intimately linked. The force is described as follows:

$$\vec{F}_{d,i} = n_i m_i v_i \left[\sigma_{geo} \left(1 - \frac{2e\phi_d}{m_i v_i^2} \right) + 2\pi b_{\pi/2}^2 \ln \left(\frac{b_{\pi/2}^2 + \lambda_D}{b_{\pi/2}^2 + \frac{\sigma_{geo}}{\pi} \left(1 - \frac{2e\phi_d}{m_i v_i^2} \right)} \right) \right] \vec{u}_i, \tag{7.3}$$

where $\vec{u}_i$ the ion flow velocity, ϕ_d is the potential at the grain surface, and $b_{\pi/2}$ is the impact parameter for Rutherford scattering. The first term in parentheses is the drag cross-section for OML ion collection (see Sec. 2.1); the second term is the cross-section for small angle Coulomb collisions [40, 115]. The velocity v_i is the sum in quadrature of the thermal velocity $v_{T,i}$ and the ion flow velocity $|\vec{u}_i|$.

As shown by Chai & Bellan [65], the curl of the OML-component of the ion drag is typically nonzero, following:

$$\nabla \times F_{d,i}^{OML} \sim \nabla |\vec{u}_i| \times \nabla n_i. \tag{7.4}$$

The ion velocity points along the ambipolar electric field $E_{amb} \sim \nabla n_i / n_i$, and so:

$$\nabla |\vec{u}_i| \times \nabla n_i \sim \nabla \left| \frac{\nabla n_i}{n_i} \right| \times \nabla n_i = \frac{1}{n_i |\nabla n_i|} (H(n_i) \nabla n_i) \times \nabla n_i, \tag{7.5}$$

where $H(n_i)$ is the Hessian matrix. In the cylindrical geometry with azimuthal symmetry, $(H(n_i)\nabla n_i) \times \nabla n_i$ points along the azimuth; $F_{d,i}$ thus induces vorticity in the dust grain motion within the (r,z) plane. These qualitatively match the observed vortex motion in experiments [65, 114].

The interplay between the electric and ion drag forces during grain growth, combined with the asymmetry of the system due to the asymmetric discharge, gravity, and nonuniform gradients, are likely responsible for the growth of dynamic instabilities in the dust flow field as time progresses. Because these two forces are highly nonlinear, varying with plasma density, ion velocity, and grain charge, it is impractical to compute grain dynamics with sufficient precision to determine grain mass, collisional cross-section, or charge from observed motion.

Gravity

Computation of the other main forces on the grains is relatively simple. Gravity (on earth) is described by

$$\vec{F}_G = -mg\hat{z}. \tag{7.6}$$

Though in many other dusty plasma experiments gravity tends to dominate, causing grains to drop to a monolayer on the bottom sheath or even fall out of the plasma [18, 112], it has minimal effect in our device: we observe even large grains distributed through the bulk plasma, rather than falling to the lower sheath [39], while measurements by K.B. Chai on the Mk. I device indicate that even tilting the experiment on its side does not significantly change grain positions [69].

Neutral-collision forces

The net force due to collisions with ambient neutrals can be separated into two forces: the *neutral drag force*, which depends on the velocity difference between the grain and the neutral gas fluid, and the *thermophoretic* force, which arises due to local gradients in the neutral gas temperature[1].

The functional forms and magnitudes of the neutral drag and thermophoretic forces depend on the gas regime, characterized by the Knudsen number Kn,

[1]This assumes an isobaric system– pressure gradients would introduce a third collisional force.

the ratio of the gas molecule mean free path λ_{mfp} to an intrinsic grain size R_{Kn}. If Kn $>> 1$, the gas is *rarefied*, with ballistic collisions between gas molecules and the grain. If Kn $<< 1$, the gas is *hydrodynamic*, approximating a continuous medium that flows and deforms around the grain.

Under experimental conditions, the mean free path is

$$\lambda_{mfp} = 1/(n_n \sigma_{n-n}) \approx 200\ \mu\mathrm{m}, \tag{7.7}$$

where σ_{n-n} is the neutral-neutral collisional cross-section.

The appropriate choice of R_{Kn} is itself dependent on the gas regime for nonspherical grains, since in the hydrodynamic limit, gas entrained in the boundary layer increases the effective dynamical mass and cross-section. Simulations by Gopalakrishnan *et al.* [116] show that for fractal aggregates, the *Smoluchowski* radius is most appropriate within the hydrodynamic limit, while in the rarefied limit, one can base R_{Kn} on the projected area orthogonal to the direction of motion, $R_\sigma = \sqrt{\sigma/\pi}$, where σ is the grain's projected area. For the elongated fractal grains we observe, both these radii are much smaller than the total grain length L, remaining smaller than λ_{mfp} even when L reaches the millimeter scale. We can therefore safely assume that the gas is rarefied and use R_σ as the effective radius.

The form of the drag force is given by:

$$F_{d,n} = -f\sigma(v - v_n), \tag{7.8}$$

where f is a frictional coefficient and σ is the collisional cross-section of the dust grain. For the purposes of this analysis, I assume that the neutral gas is stationary ($v_n = 0$).

In the rarefied gas regime, the frictional coefficient f is given by the Epstein formula [40]:

$$f = \frac{4\delta}{3}\sqrt{\frac{8}{3}} v_T n_n m_n (1 + \pi/8), \tag{7.9}$$

where σ is the collisional cross-section of the grain, n_n is the neutral gas density, m_n is the molecular mass, and v_T is the neutral gas thermal velocity, and δ is a dynamic shape factor of order unity.

For larger grains, as Kn approaches 1, some deviation is expected from the Epstein formula, but we find this to be negligible. When $Kn \ll 1$, the

Reynolds number remains low under experimental conditions, and thus drag follows the Stokes formula. The corresponding frictional coefficient $f_{\mathrm{St.}}$ intersects with that of the Epstein formula $f_{\mathrm{Ep.}}$ around Kn = 1, and thus $f(\mathrm{Kn}) \approx f_{\mathrm{St.}} \approx f_{\mathrm{Ep.}}$ through transitional regime ($\mathrm{Kn} \sim 1$).

The thermophoretic force arises when there is a local temperature gradient in the neutral gas at the grain position. The warm side of the grain experiences more energetic collisions with gas molecules than the cold side of the grain, inducing a net force along the temperature gradient, from hot to cold. This gives a form:

$$\vec{F}_{th} = -h\sigma\nabla T, \tag{7.10}$$

where σ is the collisional cross-section of the grain in the direction of the temperature gradient, and h is a constant that depends on the gas conditions.

A precise computation of the h in the rarefied gas regime was carried out by Waldmann [117] by solving the Boltzmann equation using a Chapman–Enskog expansion with Lennard-Jones intermolecular potentials, yielding net momentum transfer from the gas kinetics to the grains:

$$h = \frac{32}{15\pi}\frac{15k_B}{4m_n v_T}\mu_{ref}\left(\frac{T_{gas}}{T_{ref}}\right)^{\nu}. \tag{7.11}$$

The dynamic viscosity μ and correlation exponent ν are obtained from literature for Argon gas at comparable pressure to the experiment; using a reference temperature $T_{ref} = 273$ K, $\mu_{ref} = 2.117 \times 10^{-5}$ Pa $\cdot$ s and $\nu = 0.81$ [70, 118].

7.3 Fractal aggregate model for area and volume

For a spherical ice grain, the cross-section and volume are simply given by πr^2 and $4\pi\rho_{ice}r^3/3$, respectively. For fractal grains, the cross-section and mass are nontrivial to determine.

The morphology is well described by fractal geometry as developed by Mandelbrot [74], such that grain geometric cross-section σ scales with L^{D_2}, and grain volume with L^{D_3}, where D_2 and D_3 are non-integers. We used this formulation in Section 4.3 to find the average fractal dimension D_2 of the grains, employing a box-counting algorithm on microscope photos, and obtained $D_2 = 1.465 \pm 0.048$.

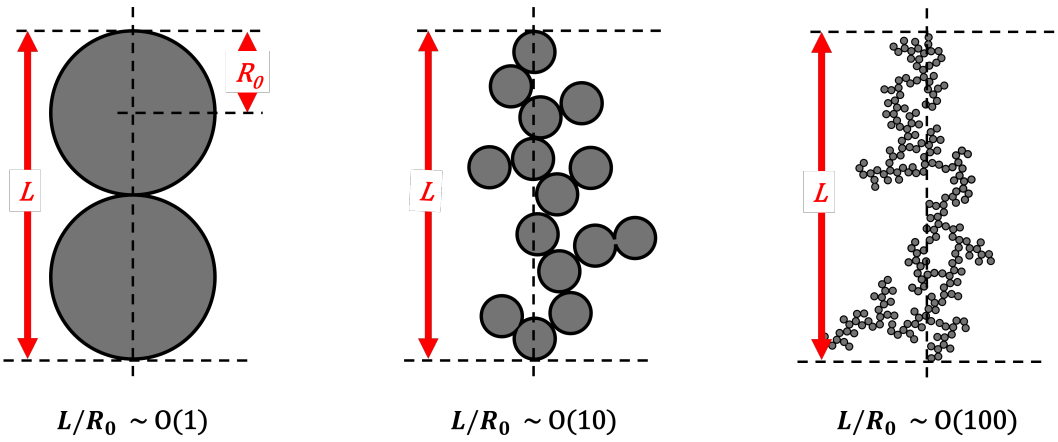

Figure 7.2: Aggregates of spherical monomers with radius R_0 agglomerate into complex shapes, characterized by a maximum length L. Fractal scaling emerges as L/R_0 increases.

However, these fractal scaling laws *must* break down at a minimum size because physical objects cannot be arbitrarily small: there is always some minimum size at which the grain area and volume *no longer scale fractally*, as matter is built of particles with three spatial dimensions. Because our microscope lens resolution has a minimum resolution of about a few microns, we likely cannot resolve this minimum size, and thus cannot directly estimate the true cross-sectional area experienced by the angstrom-scale gas molecules from the photos.

Instead, we model the grains as an aggregate of spherical monomers, each with unknown radius of R_0, clustered together in 3D space with a fractal dimension D_3. Figure 7.2 illustrates this minimum monomer size R_0 and fractal scaling as L/R_0 increases.

Following the formalism of Feder [73], each grain's cross-section is given by:

$$\sigma = \pi R_0^2 \left(\frac{L}{2R_0} \right)^{D_2} \tag{7.12}$$

where πR_0^2 is the cross-sectional area of one monomer and $(L/2R_0)^{D_2}$ approximates the number of monomers visible in the 2D projection when $L >> R_0$.

Analogous to equation 7.12, the grain volume is given by

$$m = \frac{4}{3}\pi \rho_{ice} R_0^3 \left(\frac{L}{2R_0} \right)^{D_3} \tag{7.13}$$

where ρ_{ice} is the mass density of ice. Just as D_2 was determined from box-counting microscope photos in Section 4.3, D_3 could be obtained using box-counting of a 3D model of the grain, but this is currently beyond our capabilities. Further, while several simulations have related D_3 and D_2 for fractal aggregates of specific sizes, no universal relation has been experimentally verified for arbitrary L/R_0 [76, 77, 119].

Note that the cross-sectional area σ from microscope photos (taken from a side-view) is not necessarily the same as the cross-section for the drag or thermophoretic force, which point mainly vertically; the fractal dimension and cross-sectional area may differ with the viewing angle. That being said, as the fractal dimension is less than 2, the grain is relatively porous in the 2D plane, such that not much of the grain structure is blocked from view by other parts of the grain at any one angle. We thus approximate that D_2 is independent of viewing angle, and thus σ is the same for the drag and thermophoretic force. Future work could verify this with additional imaging and simulations.

7.4 Dynamics in the afterglow

Grain behavior changes abruptly (within ~ 1 ms) when the plasma is extinguished by turning off the RF power. As seen by comparing Fig. 7.3b to Fig. 7.3a, when the RF is turned off, the ice grains stop their usual vortex motion and, instead, follow distinctly-different trajectories, mostly drifting towards the electrodes. Because the grain dynamics simplifies significantly in the afterglow, we use grain motion in the afterglow to determine grain properties.

As the electrons and ions escape in the afterglow, the electric field and ion drag forces, previously dominant, disappear. Then, only neutral drag, gravity, and thermophoretic forces determine grain motion, along with grain inertia [3, 70].

Timescale of ion escape

We desire to track grain motion within the afterglow and fit their trajectories to dynamics. In order to neglect electrostatic and ion drag forces on grain

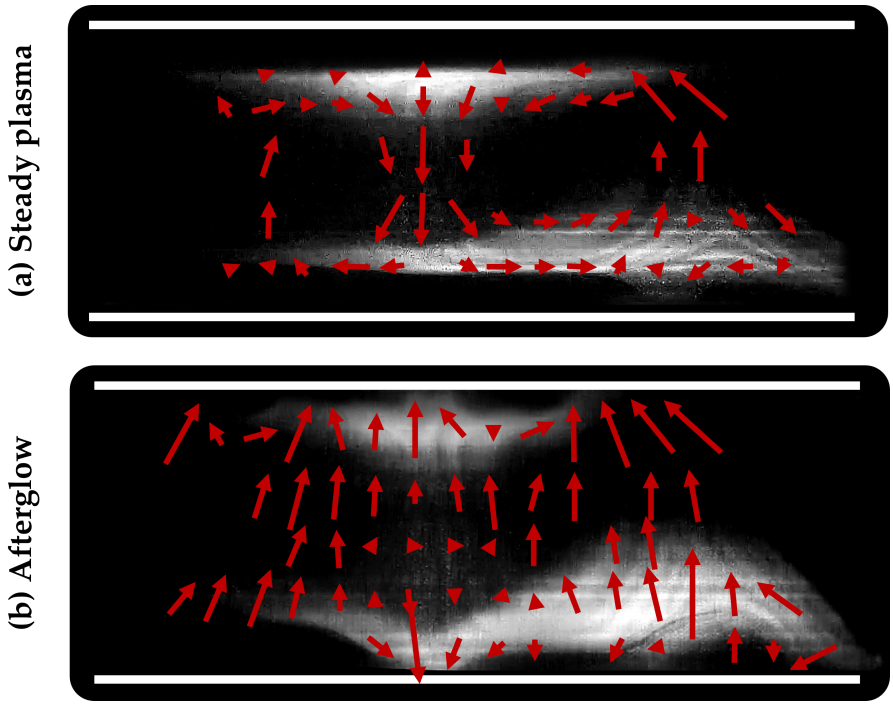

Figure 7.3: Grains in the steady plasma (a) and the afterglow (b), imaged at high frame rate using laser scattering and averaged over 40 ms; red arrows indicate grain motion at that location, extracted from the high-speed video.

motion in the afterglow, these forces must decay to insignificant levels well *before the grains leave the plasma*, which occurs in 50 to 100 ms.

Electrons and ions continuously escape the plasma. When the plasma is turned off (i.e. the afterglow), the particles are no longer replenished by continuous ionization, and the electron and ion densities decay as they defuse to the walls.

Plasma ions in our experiment are located in the cylindrical volume between the electrodes, with radius of 3.25 cm and height of about 1.5 cm. The nominal time for argon ions to freely diffuse out of this volume through the background neutral argon gas is

$$\tau_{\text{diff}} = \frac{(3.25\ \text{cm})^2}{D_{Ar/Ar}}, \tag{7.14}$$

where the diffusion coefficient is:

$$D_{Ar/Ar} \approx \frac{1}{3}\lambda_{mfp} v_T = \frac{1}{3} * 600\ \mu\text{m} * 280\ \text{m/s} = 560\ \text{cm}^2/\text{s}; \tag{7.15}$$

here $\lambda_{mfp} = 600\ \mu\text{m}$ is the mean free path and v_T is the argon thermal velocity.

This predicts a nominal **19 ms** diffusion time. However, this greatly overestimates the ion loss time, as it neglects the electric field. Importantly, ions experience an outward force from the ambipolar electric field, which Couedel *et al.* [70] calculates to accelerate the diffusion time according to:

$$\tau_{amb} \approx \frac{2}{(1 + T_e/T_i)} \tau_{diff}. \tag{7.16}$$

Because $T_e \sim 2$ eV, the ambipolar diffusion time is two orders of magnitude shorter than free diffusion. Using $T_i = 150$ K, the ambipolar diffusion time is **250 μs.**

Ion density decays in the afterglow as $n_i(t) \sim \exp(-t/\tau_{diff})$. As the ion density is about 10^{14} cm^{-3}, it is negligible within 8 ms ($\exp(-7/0.25) \approx 10^{-14}$).

Moreover, the DC self-bias field between the electrodes of $\Delta V \sim 70$ V at $t = 0$ even further accelerates ion depletion from the plasma in the early afterglow. Thus, after a few ms, *only dust grains and neutral molecules remain in the afterglow.*

Decay of the electrostatic field

The electric field from the plasma particles decays at the same rate as the ion drag, as both these phenomena are dependent on ambipolar diffusion. Meanwhile, a secondary electric field is caused by the DC bias across the electrodes. These fields can cause an electric force to persist into the afterglow, as grains may maintain some residual charge [3]. I show here that these forces become negligible within a few milliseconds, and thus can be neglected when tracking grain motion.

A 1 MΩ voltage probe connected to the powered electrode measured the electrode potential both before and after $t = 0$ where $t = 0$ is defined as the time when the RF was turned off. The intrinsic capacitance of the powered electrode was measured by an LCR meter to be 640 pF. Because the voltage probe has a 1 MΩ internal resistance, the electrode capacitance and probe resistance comprise an RC circuit with a 640 μs decay time.

As shown in Fig. 7.4, when $t < 0$, the electrode potential (blue in figure) oscillates at the RF frequency with a ~ 100 V amplitude and this oscillating potential is centered about a -70V DC self-bias [13]. When the RF power is

shut off ($t = 0$) the oscillation ceases and the self-bias decays (afterglow, blue line in Fig. 7.4 for $t > 0$).

Immediately after $t = 0$ the electrode self-bias (blue line) undergoes an initial rapid decay and then for $t > 0.5$ ms, follows the 480 μs RC time (dashed red line) associated with the probe resistance and electrode capacitance. The rapid decay occurring during $0 < t < 0.3$ ms is much faster than the RC time. This initial rapid DC self-bias decay is attributed to an ion flux impacting the powered electrode [3]. The disappearance of this ion flux after 0.3 ms indicates that the ions are fully depleted at 0.3 ms.

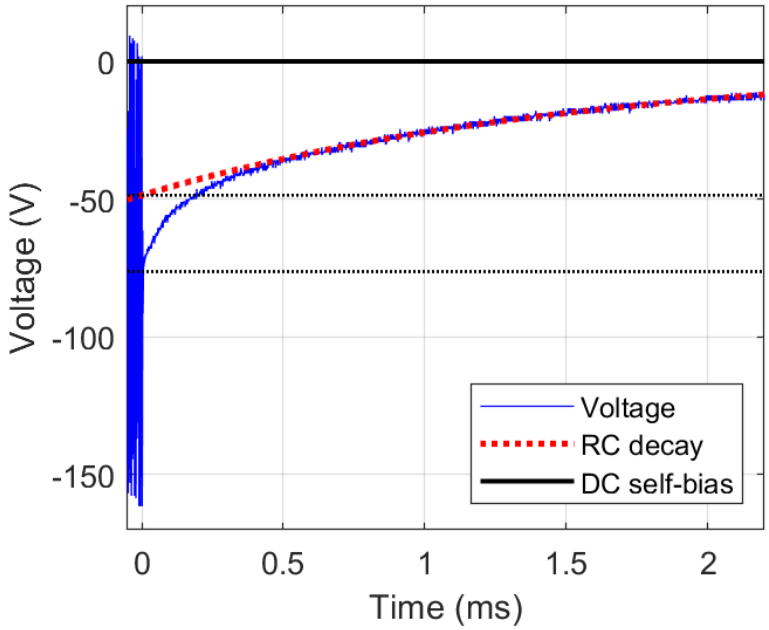

Figure 7.4: Trace of electrode voltage during the afterglow. At $t < 0$, RF voltage oscillates from with a magnitude of about 160 V and a self-bias of 72 V; at $0 < t < 0.5ms$, DC self-bias decays faster than exponentially due to ion collection [3]; at $t > 0.5ms$, voltage closely follows the RC decay of the circuit, indicating no charged particles are being collected.

Thus, the convergence of the blue line (measurement) with the RC decay (red dashed line) at $t \approx 0.3$ ms indicates that plasma ions are depleted within the first half millisecond of the afterglow, in agreement with the ambipolar diffusion time of 250 μs. Using the methods of Chaubey & Goree [3], an ion density of $n_0 = 4.4 \times 10^9$ cm^{-3} was calculated, consistent with Langmuir probe measurements; this further supports that the rapid drop in electrode

potential in the first 0.3 ms of the afterglow is caused by ion collection by the electrode and that ions are depleted rapidly by the DC self-bias potential drop across the electrodes.

Couedel *et al.* [70] and Chaubey & Goree [3] show that grains can retain a residual charge in the afterglow and so mutually repel each other. However, our measurements do not show evidence of Coulomb repulsion between grains in the afterglow, indicating that interactions between grains are small compared to drag and thermophoresis. This is *not necessarily* evidence that the grains are no longer charged, but does suggest that the effect of any residual charge is small on the scale of the inter-grain distance compared to thermophoresis, drag, and/or gravity.

Dynamical model at $t > 10$ ms

In the "late" afterglow (i.e., after ~ 10 ms) each grain follows a simplified trajectory, following the equation of motion:

$$m\frac{d\vec{v}}{dt} = -f\sigma\vec{v} - mg\hat{z} - h\sigma\nabla T_n. \tag{7.17}$$

It was observed that the grains reach terminal velocity within 20-30 ms after RF shutoff, and thus Eq. 7.17 is simplified:

$$-mg = f\sigma v_\infty + h\sigma\nabla T_n. \tag{7.18}$$

This can be solved to relate mass and cross-section:

$$\frac{m}{\sigma} = -\frac{f}{g}v_\infty - \frac{h}{g}\nabla T_n. \tag{7.19}$$

Thus only the terminal velocity and the local temperature gradient are required to relate the mass and cross-section of the grains.

7.5 Experimental methodology

Temperature mappings

To find the temperature gradient throughout the ice cloud, T_n was mapped using laser-induced fluorescence (LIF) scheme [64]. Fifty-two spatially separated LIF scans were taken in a vertical 2D plane to obtain a temperature map of the plasma.

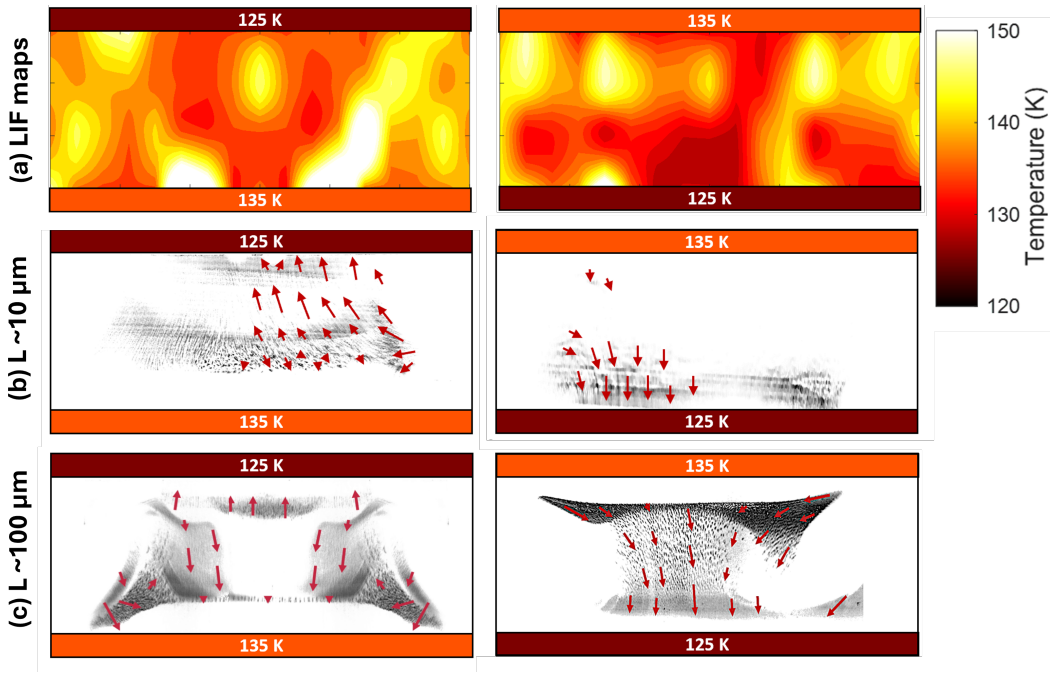

Figure 7.5: (a) Temperature maps of the Argon plasma obtained from LIF; (b-c) Grain cloud dynamics in the afterglow, with grains averaging (b) $L \sim 10$ and (c) $L \sim 100$ microns. Each panel shows two temperature configurations. Color is inverted, such that grains are dark against a white background, for clarity.

Maps are shown in Fig. 7.5 (a) for two electrode temperature configurations: one with the top electrode at 125 K and the bottom electrode at 135 K and the other with the temperatures interchanged. In both ∇T configurations, the gas was coldest near the electrodes and warmest at the edges; a warm spot below the center of the powered electrode was likely caused by stochastic electron heating at the RF sheath edge.

To illustrate the strength of the thermophoretic force, grain motion was tracked using laser sheet scattering and is shown in Fig. 7.5b-c. When grains were small ($L < 10$ μm), they closely followed the temperature gradient in the afterglow, for both temperature configurations: when the top electrode was colder, the grains predominantly moved upwards, and vice versa.

For larger grains ($L \gtrsim 100$ μm), vertical motion was predominantly downward (Fig. 7.5c), except where the temperature gradient was very strongly upward (e.g., right below the colder top electrode). This shows gravity's

increasing influence; however, the observed horizontal motion suggests that thermophoresis still plays a key role for grain dynamics.

This data further confirms that ion drag and electrostatic forces do indeed disappear in the afterglow– if they still contributed to grain motion, the grain motion would not depend so strongly on the temperature profile.

Grain tracking in the late afterglow

A data set was taken with the microscope focused to a region of the plasma where the temperature gradient was approximately 3.5 K/cm upward, and nearly-uniform through the frame. The plasma was pulsed off for 50 ms, during which grain motion was filmed at 1080p, 1200 fps using the long-distance microscope lens on a high-speed camera (Phantom v642). After 50 ms, the RF power was restored, and grains moved back to their equilibrium positions. This was repeated for several runs, containing grains of varying sizes, each imaging the same region of the plasma.

Each collected video was analyzed as follows:

1. The length of each grain visible in the video was measured from the initial frame.
2. Each video was sliced into 0.5×5 mm vertical sections and summed horizontally, forming a column vector of light intensity with vertical position.
3. This column vector was plotted over time, producing a color map that shows the grain trajectories.
4. The terminal velocity of each grain was recorded at 40 ms into the afterglow.

Figure 7.6 gives an example of the experimental sequence with dotted white lines showing the fitted terminal trajectories.

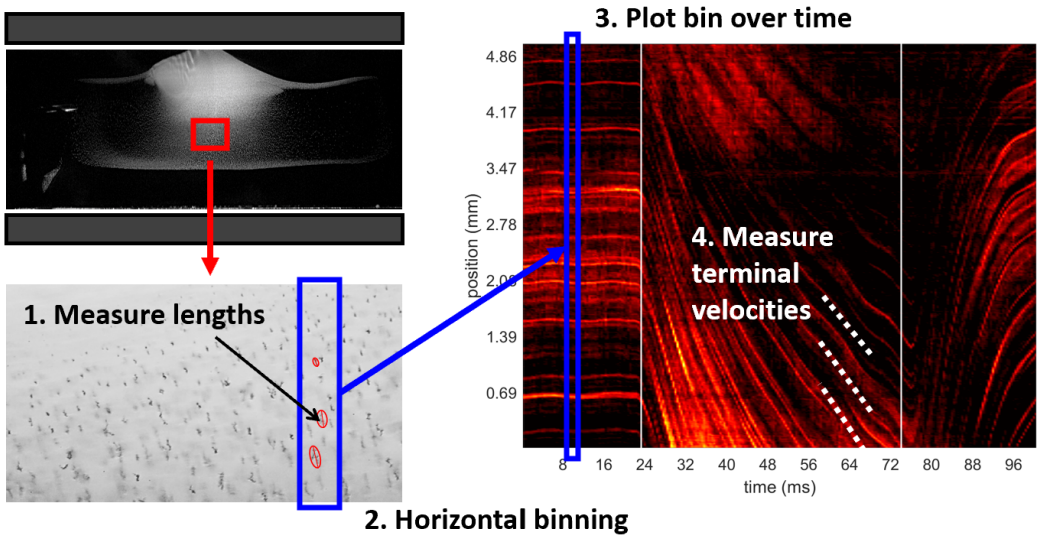

Figure 7.6: Methodology for obtaining terminal velocities vs. grain length in the afterglow

The resolution of the microscope was 3 microns, while the time resolution was $1/1200$ seconds; the terminal velocity thus has an uncertainty:

$$\begin{aligned}\delta v =& \sqrt{\left(\frac{\delta x}{\Delta t}\right)^2 + \left(\frac{v_\infty \cdot \delta t}{\Delta t}\right)^2} \\ =& \sqrt{(0.03\ \mathrm{cm/s})^2 + (0.083\ v_\infty)^2}\ \approx 0.083\ v_\infty\end{aligned} \tag{7.20}$$

Relating mass and cross-section

Results of terminal velocity ranged between 3 and 30 cm/s, increasing as grains get larger. From these values, m/σ for each grain was computed from Eq. 7.19; using a dynamic shape factor $\delta = 1.2$ [76], we obtain $f = 1.48\ \mathrm{kg\ m^{-2}\ s^{-1}}$ and $h = 3.73 \cdot 10^{-5}\ \mathrm{kg\ s^{-2}\ K^{-1}}$. The resulting values are shown in Fig.7.7 on a log-log scale. Each point retains an 8.3% relative uncertainty, propagated from the terminal velocity, as variation in ∇T is comparatively small.

A linear fit to the plot of $\log_{10}(m/\sigma)$ vs $\log_{10}(L)$ gives a slope of 0.383 ± 0.027 and a vertical offset of -0.648 ± 0.114. This ratio increases with L considerably *more slowly* compared to a sphere of the same size, for which m/σ would increase linearly with L.

Obtaining m and σ independently requires a second equation, typically obtained through geometry.[2] Employing the fractal aggregate model described in Sec. 7.3, we divide Eq. 7.13 by Eq. 7.12 to obtain

$$\frac{m}{\sigma} = \frac{4\rho_{ice}R_0}{3}\left(\frac{L}{2R_0}\right)^{D_3-D_2}. \tag{7.21}$$

Taking the log of both sides results in:

$$\begin{aligned}\log_{10}\left(\frac{m}{\sigma}\right) = (D_3-D_2)\log_{10}(L) + [1-(D_3-D_2)]\log_{10}(R_0) \\ + \log_{10}\left(\frac{4\rho_{ice}}{3}\right) + (D_3-D_2)\log_{10}\left(\frac{1}{2}\right).\end{aligned} \tag{7.22}$$

The slope of the linear fit to m/σ thus gives $D_3 - D_2$, while the vertical offset is a function of R_0. From the linear fit, we therefore obtain $D_3 = 1.848 \pm 0.201$, and $R_0 \approx 1.18 \pm 0.84$ μm.

Finally, inserting D_2, D_3, and R_0 into Eqs. 7.12 and 7.13 gives independent relations for grain cross-section and mass with the measured grain length.

7.6 Grain properties, scaling laws, and implications

Figures 7.7a and b show that both σ and m grow *more slowly* with L for fractal grains than for compact spherical or ellipsoidal grains. Both m and σ are also significantly smaller than for a similarly-sized compact grain. Fractal grains therefore become increasingly porous and fluffy as they grow. To quantify this, we define a packing fraction p, the ratio of the grain mass to the mass of the smallest-encompassing ellipsoid, so

$$p = \frac{3}{4\pi}\frac{\kappa^2}{(L/2)^3}\frac{m}{\rho_{ice}} \sim L^{D_3-3}. \tag{7.23}$$

Figure 7.7c plots p vs. L on a log-log scale; a linear fit confirms $p \sim L^{-1.10} \approx L^{D_3-3}$. The packing fraction rapidly decreases with L, such that the growing fractal grains fill progressively less of their encompassed volume.

Grain charge estimation

Fractal geometry also significantly impacts grain charging. Although ice grain charge has not yet been directly measured, previous numerical studies

[2] This is traditionally where one would assume grains are spherical.

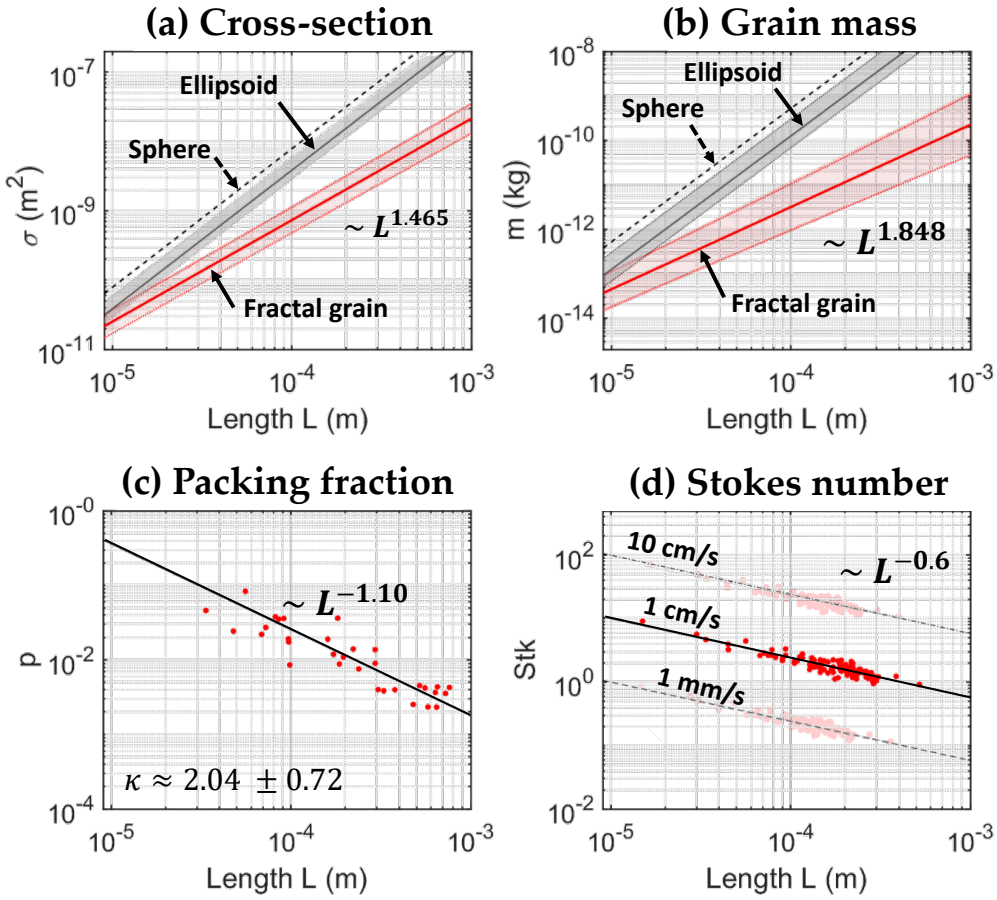

Figure 7.7: Grain length vs. (a) geometric cross-section (Eq. 7.12), (b) mass (Eq. 7.13), (c) packing fraction (Eq. 7.23) and (d) Stokes number for various grain velocities (Eq. 7.25). Panels (a,b) compare fractal grains with spheres (diameter L) and ellipsoids (major axis L, aspect ratio κ); grey bands show uncertainty propagated from κ, red bands show uncertainty in σ and m propagated from R_0, D_2, and D_3.

reveal that fractal grains accumulate more charge than compact grains of the same mass. Matthews *et al.* [78] and Ma *et al.* [120] suggest that fractal grains acquire a charge linearly proportional to $R_\sigma = \sqrt{\sigma/\pi} \sim L^{D_2/2}$; its charge-to-mass ratio q/m then scales with $\sim L^{-D_3+D_2/2} = L^{-1.1}$, decreasing with L more slowly than the L^{-2} scaling of spherical grains. Meanwhile, Asnaz *et al.* [84] and van Minderhout *et al.* [121] suggest that the acquired charge is proportional to the radius of the smallest-enclosing sphere, $q \sim L$, and thus $q/m \sim L^{1-D_3} = L^{-0.848}$, even further enhancing the charge-to-mass ratio. Therefore in Eq. 7.24, both the electrostatic force and the ion drag are further enhanced for fractal grains. This distinct force balance drives grain dynamics

that are inaccessible to solid spherical grains. The grain morphology also perturbs the plasma environment in distinct ways: together with the high surface area of the fractal grain, it increases electron depletion from the plasma [7] and accelerates chemical processes within the plasma [27].

A distinct dynamical regime

The fractal scaling of m/σ causes a unique dynamical balance in the experimental plasma, demonstrated by Eq. 7.17: as m/σ increases more slowly for fractals than for solid grains, the m-dependent terms do not dominate the σ-dependent terms until a significantly larger L is reached. Thus the effects of fractal geometry on dynamics is not a mere perturbation to solid grain dynamics but, instead, a fundamentally-different regime.

This difference extends to the steady plasma discharge, in which the electric force and ion drag must be included in the equation of motion, giving

$$\frac{d\vec{v}}{dt} = \frac{q\tilde{E}}{m} + \frac{\vec{F}_{d,i}(q,\sigma)}{m} - \frac{f\sigma\vec{v}_{rel}}{m} - \frac{h\sigma\nabla T}{m} - \vec{g}. \tag{7.24}$$

The neutral drag and thermophoretic force depend inversely on m/σ, electrostatic force depends on the charge-to-mass ratio q/m, while ion drag depends on both σ/m and q/m [40]. Due to the fractal scaling of m/σ, the ion drag, the neutral drag, and the thermophoretic terms are comparatively strong, while the gravitational and inertial ($d\vec{v}/dt$) terms remain negligible. This explains why millimeter-scale fractal ice grains remain dispersed in the bulk plasma, whereas the solid spheres in other experiments gravitationally sediment to the lower electrode [112].

Effects on gas coupling

An important effect of this force balance is stronger coupling between the dust grains and their surroundings. The settling time of a grain to terminal velocity due to neutral drag is $\tau = m/\sigma f$. This is non-dimensionalized to obtain a Stokes number,

$$\mathrm{Stk} = \frac{m|v - v_{gas}|}{\sigma f L} \sim L^{D_3 - D_2 - 1}. \tag{7.25}$$

When Stk $<< 1$, grains are entrained in the gas and quickly equilibrate with the neutral flow; at Stk $>> 1$, grains move independent of the gas flow. For

spherical grains, Stk is independent of grain size, and under our experimental conditions the grains would not be entrained. For fractal grains, however, $\mathrm{Stk} \sim L^{-0.6}$, *decreasing* as grains grow. Fractal grains therefore become more tightly coupled to gas motion as they increase in size: as shown in Fig. 7.7d, grains moving at 1 cm/s become fully entrained when they reach a few hundred microns in length.

Prior treatment assumed that the gas remains stationary; this is appropriate for the short timescales of the afterglow. However, in plasma environments with high densities of large fractal grains, grain motion can produce a significant force on the surrounding gas, and a multiphase flow treatment is required to capture all behavior. Grains can be accelerated by ion streams, electromagnetic forces, or radiation pressure, which have little direct effect on the gas molecules. As grains grow and Stk becomes small, the grains efficiently transfer momentum to the surrounding gas via the neutral drag force– the gas then becomes entrained in the motion of the grains, rather than entraining the grains itself.

7.7 Implications to experiment and beyond

The complex dynamics we observe in the steady plasma– vorticity, wave modes, and large-scale instabilities– depend on the relative magnitude of grain charge, mass, and cross-section. As we observe distinct size-dependent behavior of the ice cloud, such as the "pulsing" instability of the ice flow in hydrogen plasma, description of this behavior necessitates us to consider the fractal scaling of the grains; no spherical grain model can access the same dynamical regime, or balance of forces in Eq. 7.24 as the grains grow. The measurements and formulism developed in this chapter are thus integral to any future characterization of these behaviors.

For instance, the dispersion relation of dust density waves within the plasma is an ongoing matter of study. Previous observation of dust density waves within laboratory ice-dusty plasmas has shown significant deviations from theoretical predictions of dust acoustic waves. Marshall [69] measured phase velocity of these waves as $\omega/k \sim 0.5$ m/s. To first approximation, theory predicts [41] $\omega/k \approx \sqrt{q_d n k_B T_i / m_d}$; estimating mass and charge by modeling the grain as a porous ellipsoid, Marshall [69] predicted phase velocities 10 times smaller than those measured. This was later addressed by Chai

[113], who showed that much of this gap can be bridged by modifying the dispersion relation with an anomalous high "temperature" of the collection of dust grains,[3], and attributed the remaining deviation between theory and measurements to grain elongation. However, as mass scales with L^{D_3}, while charge scales either with L^1 or $L^{D_2/2}$ depending on the appropriate model, using theory based on a fixed grain aspect ratio [113] or a constant packing fraction [24] should not be expected to produce accurate predictions in the phase velocity over any range of grain sizes.

Across natural environments, the increase of fluffiness with size caused by fractal scaling has profound implications for grain evolution. Large fractal grains can form from minimal amounts of contaminants, strongly perturbing the plasma despite their low mass. In the mesosphere, fractal ice grains larger and fluffier than predicted by spherical solid grain models would alter cloud electrical and radiative transfer characteristics [7]. The high cross section per mass of fluffy grains could significantly influence planetesimal formation in protoplanetary disks by promoting faster capture of gas or water molecules than for a same-mass solid grain [12].

The impact of fractal growth on dusty plasma dynamics can thus have wide-reaching implications to the large-scale dynamical behavior across the cosmos. As dust grains nucleate and aggregate fractionally within stellar and galactic outflows, they are accelerated by radiation pressure and can couple to their surroundings, driving large-scale winds. Although gas density in astrophysical environments is usually orders of magnitude lower than in the laboratory, weakening drag and thermophoretic forces, the fractal scaling of m/σ will still alter the force balance: as radiation pressure scales with cross-section, it is similarly enhanced compared to gravity and inertia [122]. Fractal aggregation increases both the radiative force on the dust grain and gas entrainment by the collective of dust grains, amplifying dust-driven winds, enhancing mass loss during stellar evolution, shaping galactic feedback processes, and influencing metal enrichment by interstellar dust [12, 81].

In conclusion, we demonstrate that fractal ice grains exhibit a distinct dynamical regime driven by the unique scaling of m and σ during grain growth. Compared to solid grains, fractal grains have enhanced interactions with neu-

[3] that is, an increase of their average kinetic energy in their center-of-mass frame

tral molecules, ions, and electrons, leading to stronger collisional forces and higher charge-to-mass ratios that fundamentally shift the balance between drag, electromagnetic forces, and gravity.

Chapter 8

FROM LABORATORY TO ASTROPHYSICAL DYNAMICS

In the previous chapter, it was observed that the fractal nature and growth of ice grains cause distinct dynamics in plasma experiments. These fundamental effects can have wide-reaching implications to dusty plasmas in technology, the atmosphere, and across astrophysics. In this chapter, I apply our findings to various astrophysical systems, addressing key problems in interpreting telescope data and outlining how continued laboratory research in ice-dusty plasmas supplements the frontiers of observational astronomy.

Much work remains to be done in this field– I present three areas here in which our research can directly be applied to astrophysical models, performing elementary computations and suggesting routes for continued research.

8.1 How micro-scale grains drive galactic-scale flows

A substantial fraction of the visible matter in galaxies is contained in the interstellar medium (ISM), which is $\sim 99\%$ gas and $\sim 1\%$ dust by mass. The ISM is multiphase: supernovae carve hot, highly-ionized bubbles that can fill large volumes but hold little mass, while most of the mass is neutral hydrogen with temperatures of 0.01-1 eV, only weakly-ionized by distant starlight or cosmic rays. Dust is supplied by both stellar winds and supernova ejecta, with additional growth in the ISM [81]. Within the cold neutral medium, clouds can collapse gravitationally to form dense molecular clouds which catalyze star formation; once stars form, surrounding matter collapses to form protoplanetary disks, in which dust and ice grains eventually coalesce into planets [12]. The physics of dusty plasmas is thus critical to understanding the structure, properties, and evolution of the entire galaxy.

Interstellar dust grains are often elongated and in alignment with each other [26]. Clouds of grains polarize the starlight passing through them, as well as their own thermal emission, letting us map the direction of the magnetic field on galactic scales [123]. Neutral gas, especially the cold neutral medium, often appears in filamentary structures along these field directions.

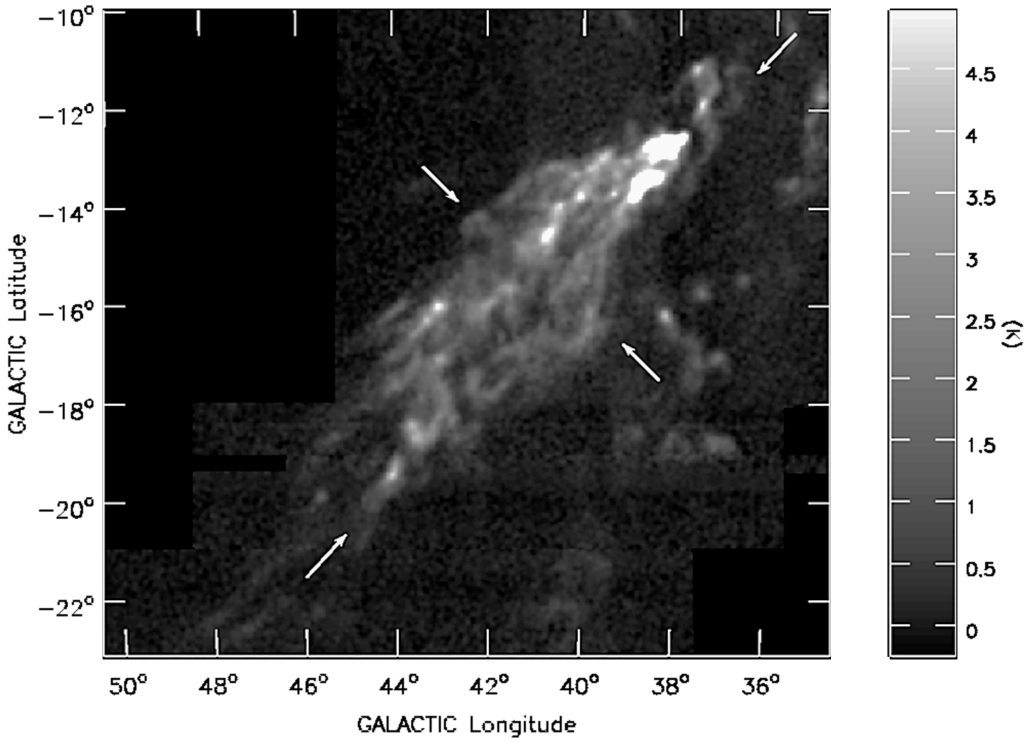

Figure 8.1: The Smith cloud, an H I feature of the cold ISM, imaged by the Planck mission; reproduced from Lockman *et al.* [4].

Neutral coupling to magnetic fields is generally attributed to momentum transfer between the neutral atoms and a small population of ions, coupling through collisions and charge exchange. Radiation pressure and electromagnetic forces can also accelerate dust grains, which also affect gas motion through drag forces, driving outflows and influencing the structure of the neutral ISM.

The interactions between neutrals, ions, and dust are also critical to the behavior of low- and intermediate-mass stars as they reach end of life, in which they shed their gaseous envelopes through radiation pressure, driving outflows of metals and silicates into interstellar space [122]. Ongoing grain nucleation, aggregation, and interaction between the multi-phase flow and magnetic fields are key to understanding the distribution of heavy molecules throughout the galaxy. Similar flows, albeit on much larger scale, are ejected from active galactic nuclei (AGNs); as outflows cool, dust nucleates and is strongly driven by radiation pressure [124].

Gas coupling to grain motion

As shown in the previous chapter, dust grains couple to the flow of a neutral gas through the Epstein drag force, and to ions through an ion drag force, which depends on both ballistic ion impacts and small-angle Coulomb deflection. Fractal grains experience much stronger acceleration in ion and neutral flows due to their increased ratios of cross-section-to-mass and charge-to-mass.

As dust grains couple to both ions and neutrals more strongly than they couple with each other, they can mediate momentum transfer between ions and neutrals: ions can accelerate dust, which then in turn accelerates neutrals. Dust could play a similar role with radiation pressure, gravity, and electromagnetic forces– these forces ordinarily have minimal effect on neutrals, but strong effect on charged dust grains, which can then accelerate the gas surrounding them.

In experiment, due to the small scales and closed boundaries, we can generally assume the neutral gas is not effected by ion and dust motion, and thus apply a Newtonian force balance as our equation of motion. In astrophysical systems, however, large-scale flows and open boundaries allow ion and dust flows to significantly accelerate the ambient neutral gas. As the mass density of dust grains approaches that of the gas, *the gas can become entrained in a flow of grains*, rather than grains following the gas. In this case, we must instead treat the dynamics using a system of four coupled fluid equations: electrons, ions, neutrals, and dust grains.

The calculation here is a first step toward applying the findings from experimental results to astrophysical systems, calculating the effect of fractal grains in mediating momentum transfer between ions and neutrals in a simple, 1-dimensional geometry. More complex simulations in future can extend this to cases more realistic to specific astrophysical phenomena.

Multi-fluid equations

Each fluid has a continuity equation given by:

$$\frac{\partial}{\partial t} n_j + \nabla \cdot (n_j \vec{u}_j) = 0, \tag{8.1}$$

and a momentum relation,

$$\begin{aligned}\frac{\partial}{\partial t}(m_j n_j \vec{u}_j) + m_j n_j \vec{u}_j \cdot \nabla \vec{u}_j + \vec{u}_j \nabla \cdot (m_j n_j \vec{u}_j) + \nabla p_j \\ = -\sum_{k \neq j} m_j n_j \nu_{jk} (\vec{u_j} - \vec{u_k}) + \sum_{\text{forces}} F_j.\end{aligned} \tag{8.2}$$

Here F_j contains gravity, Lorentz force, and anything else not accounted for by pressure and collisions.

This is a system of 8 equations (continuity and momentum for four fluids), and 12 unknowns (n_j, p_j, and u_j). We need an equation of state for closure. In the simplest case, we can apply isothermal closure, valid when $u_j << v_{T,j}$. In this case,

$$p_j = n_j k_B T_j = m_j n_j v_{T,j}^2, \tag{8.3}$$

where $v_{T,j}$ is the thermal speed $\sqrt{k_B T_j / m_j}$. It is worth noting that this assumption is questionable for the dust fluid, which has a low sound speed due to its neutral mass; future study should analyze whether an adiabatic closure is more appropriate.

Dust charging

Dust charges primarily through two mechanisms: photoemission and collection of ions and electrons. At any time, therefore, the grain charge is described by:

$$e\frac{dZ_d}{dt} = I_i + I_e + I_{\text{photo}}, \tag{8.4}$$

The photocurrent scales with the product of the incident flux, the photoemissive cross-section, and a quantum yield, the latter two of which are depend on the dust material's work function. The collection currents depend on the collision rates with ions and electrons, $I_e + I_i = e(\nu_{id} - \nu_{ed})$, with exact forms that are calculated using OML theory. The charging currents should also couple to the ion and electron continuity relations: the OML currents deplete free ions and electrons, while the photocurrent produces free electrons.

For the purposes of this calculation, I will neglect the photocurrent and assume dust charge remains at the floating potential of the plasma, effectively assuming a small Havnes parameter: $Z_d n_d << n_i \approx n_e$. This is approximated

as follows [40]:

$$\begin{aligned} Z_d &= -k_B T_e \frac{4\pi\epsilon_0 r_d}{e^2}\left[\frac{1}{2}\ln\left(\frac{T_i m_e}{T_e m_i}\right) + \ln\left(1 + \frac{e^2}{k_B T_i}\frac{Z_d}{4\pi\epsilon_0 r_d}\right)\right] \\ &\approx -2.5\ k_B T_e \frac{4\pi\epsilon_0}{e^2} r_d. \end{aligned} \tag{8.5}$$

This allows treating dust charge as fixed, rather than dynamically solving for charge alongside the fluid equations. Note that this is not necessarily representative of most astrophysical systems, in which dust photoemission can outpace OML collection and instigate positive charging, or plasma can be depleted through the Havnes effect. Future work can apply a full OML treatment and include a photocurrent, coupling these electron and ion sources and sinks to the continuity equations.

Treatment of collisions

The coupling between the fluid species is handled through collision operators in the momentum equation. Each collision term in the Equation 8.2 has the form:

$$F_{jk}^{\text{coll.}} = m_j n_j \nu_{jk} (\vec{u}_j - \vec{u}_k). \tag{8.6}$$

The collision frequency can be expressed generally as:

$$\nu_{jk} = \frac{m_k}{m_j + m_k} n_k \langle \sigma v \rangle_{jk}. \tag{8.7}$$

The angle brackets indicate an average over the velocity distribution:

$$\langle \sigma v \rangle_{jk} = \int d^3 v_j d^3 v_k\ f_j(\vec{v_j}) f_k(\vec{v_k})\ \sigma(|\vec{v}_j - \vec{v}_k|)\ |\vec{v}_j - \vec{v}_k|. \tag{8.8}$$

To first approximation, we can approximate the cross-section as the value at average energy $\sigma_{jk}(\langle v \rangle^2)$, and the averaged velocity as a sum in quadrature of thermal and bulk velocities:

$$\langle v_{jk} \rangle^2 = |\vec{u}_j - \vec{u}_k|^2 + v_{T,j}^2 + v_{T,k}^2 \tag{8.9}$$

When at low Mach number, it's sufficient to ignore flow velocities and use the faster thermal velocity, such that $\langle v_{jk} \rangle = v_{T,\max}$.

Each collisional term therefore has the form:

$$\begin{aligned} F_{jk}^{\text{coll.}} &= n_j n_k \left(\mu_{jk}\sigma_{jk}\langle v_{jk}\rangle\right)\left(\vec{u}_j - \vec{u}_k\right) \\ &\equiv n_j n_k R_{jk}\left(\vec{u}_j - \vec{u}_k\right), \end{aligned} \tag{8.10}$$

where μ_{jk} is the reduced mass between the two colliding species. The specifics of the collision operator is contained in the factor

$$R_{jk} = \frac{m_j n_j \nu_{jk}}{n_j n_k} = \frac{m_j m_k}{m_j + m_k}\sigma_{jk}\langle v_{jk}\rangle. \tag{8.11}$$

Collisions between like particles transfer no momentum. Each inter-species collision (e-i, e-n, e-d, i-n, i-d, and n-d) has a coupling coefficient R_{jk} that must be calculated independently.

Collisions between neutrals and other species can be treated as ballistic, hard-body impacts with an effective radius r_n,

$$R_{nj} = \mu_{nj}\langle v_{jk}\rangle\ \pi(r_n + r_j)^2. \tag{8.12}$$

The neutral radius $r_n \sim 2$ Å, an effective dust radius is $r_d = \sqrt{\sigma_{d,\text{geo}}/\pi}$, and electron radius can be approximated as zero. For ions, an enhanced radius $r_i^{\text{CX}} \sim 5 - 10 \times\ r_{i,\text{geo}}$ can be used to account for the larger cross-section due to charge exchange [41, 125].

For collisions between two charged species, R_{jk} must be calculated from Rutherford scattering, incorporating collision operators for both head-on ($R_{jk}^{\text{ball.}}$) and small-angle ($R_{jk}^{\text{Coul.}}$) collisions separately. The small-angle collisions have a form,

$$R_{jk}^{\text{Coul.}} = 4\pi\mu_{jk}\langle v_{jk}\rangle b_{\pi/2}^2 \ln\left(\frac{\lambda_D}{b_{\pi/2}}\right), \tag{8.13}$$

where the Coulomb logarithm $\Lambda_{jk} = \lambda_D/b_{\pi/2}$, the ratio of the Debye length to the 90^{o} impact parameter for Rutherford scattering,

$$b_{\pi/2} = \frac{|Z_j Z_k| e^2}{4\pi\epsilon_0\mu_{jk}\langle v_{jk}\rangle^2}, \tag{8.14}$$

Between electron and ions, the small-angle term dominates (i.e., $R_{ie}^{\text{ball.}} \ll R_{ie}^{\text{Coul.}}$). The ballistic term thus applies only to dust-ion and dust-electron

terms, and takes the form of the OML particle fluxes, as computed in Chapter 2.

Table 8.1 summarizes the appropriate coupling coefficients, assuming low-Mach number ($\langle v \rangle \approx v_T$), singly-charged ions. and negatively-charged dust, such that $q_d = -Z_d\, e$.

$j \to k$	R_{jk}^{ball}
e → i	~ 0
e → n	$\pi m_e r_n^2 v_{T,e}$
e → d	-
i → n	$2\sqrt{2}\pi m_n (r_n + r_i^{\text{CX}})^2 v_{T,i}$
i → d	$m_i v_{T,i} \sigma_d^{\text{geo}} \left(1 + \frac{2 Z_d e^2}{4\pi\epsilon_0 m_i v_{T,i}^2 \sqrt{\sigma_d^{\text{geo}}/\pi}}\right)$
n → d	$m_n \sigma_d v_{T,n}$
	$R_{jk}^{\text{Coul.}}$
e → i	$4\pi m_e \sqrt{\frac{k_B T_e}{m_e}} \left(\frac{e^2}{4\pi\epsilon_0 k_B T_e}\right)^2 \ln\left(\sqrt{\frac{\epsilon_0 k_B T_e}{e^2 n_e}} \frac{4\pi\epsilon_0 k_B T_e}{e^2}\right)$
e → n	–
e → d	$4\pi m_e \sqrt{\frac{k_B T_e}{m_e}} \left(\frac{Z_d e^2}{4\pi\epsilon_0 k_B T_e}\right)^2 \ln\left(\sqrt{\frac{\epsilon_0 k_B T_e}{e^2 n_e}} \frac{4\pi\epsilon_0 k_B T_e}{Z_d e^2}\right)$
i → n	–
i → d	$4\pi m_i \sqrt{\frac{k_B T_i}{m_i}} \left(\frac{Z_d e^2}{4\pi\epsilon_0 k_B T_i}\right)^2 \ln\left(\sqrt{\frac{\epsilon_0 k_B T_e}{e^2 n_e}} \frac{4\pi\epsilon_0 k_B T_i}{Z_d e^2}\right)$
n → d	–

Table 8.1: Collision operators $\mathbf{R}_{jk}$ for our four fluids, assuming slow flows ($u << v_T$), dust charge $Z_d < 0$ defined by the plasma's floating potential, and $\lambda_D > b_{\min}$.

By momentum conservation, the coupling terms are reciprocal, such that:

$$R_{jk} = -R_{kj}. \tag{8.15}$$

Dimensionless form

Let us consider a domain with a characteristic size L. Our system has a characteristic thermal velocity of neutrals $v_{T,n}$; let us therefore define a characteristic timescale using this velocity, $\tau = L/v_{T,n}$. We can also define an intrinsic neutral density $n_0 \equiv n_n(t=0)$. With these variables, we can perform a change of coordinates, $\bar{x} \to x/L$, $\bar{t} \to t/\tau$. Similarly, we shall nondimensionalize masses as $\bar{m}_j = m_j/m_n$, velocities as $\bar{u}_j = u_j/v_{T,n}$ and $\bar{v}_{T,j} = v_{T,j}/v_{T,n}$, and densities as $\bar{n}_j = n_j/n_0$.

The continuity equation is thus:

$$\begin{aligned} 0 &= \frac{\partial}{\partial t} n_j + \nabla \cdot (n_j \vec{u}_j) \\ &= \frac{v_{T,n}}{L} \frac{\partial}{\partial \bar{t}} \bar{n}_j n_0 + \frac{1}{L} \bar{\nabla} \cdot (v_{T,n} n_0 \bar{n}_j \bar{\mathbf{u}}_\mathbf{j}) \\ &= \frac{\partial \bar{n}_j}{\partial \bar{t}} + \bar{\nabla} \cdot (\bar{n}_j \bar{\mathbf{u}}_\mathbf{j}). \end{aligned} \tag{8.16}$$

All the extra factors divide out, and we are left with the same functional form.

First, examine the left-hand side of the momentum relation:

$$\begin{aligned} \text{LHS} &= \frac{\partial}{\partial t}(m_j n_j \vec{u}_j) + m_j n_j \vec{u}_j \cdot \nabla \vec{u}_j + \vec{u}_j \nabla \cdot (m_j n_j \vec{u}_j) + m_j v_{T,j}^2 \nabla n_j \\ &= \frac{m_n v_{T,n}^2 n_0}{L} \left[\frac{\partial}{\partial \bar{t}} (\bar{m}_j \bar{n}_j \bar{\mathbf{u}}_j) + \bar{m}_j \bar{n}_j \bar{\mathbf{u}}_j \cdot \bar{\nabla} \bar{\mathbf{u}}_\mathbf{j} + \bar{\mathbf{u}}_\mathbf{j} \bar{\nabla} \cdot (\bar{m}_j \bar{n}_j \bar{\mathbf{u}}_\mathbf{j}) + \bar{m}_j \bar{v}_{T,j}^2 \bar{\nabla} \bar{n}_j \right] \end{aligned} \tag{8.17}$$

Next, the right-hand side:

$$\begin{aligned} \text{RHS} &= -\sum_{k \neq j} n_j n_k R_{jk} (\vec{u_j} - \vec{u_k}) + \sum F_j \\ &= -v_{T,n} n_0^2 \sum_{k \neq j} \bar{n}_j \bar{n}_k R_{jk} (\bar{\mathbf{u}}_\mathbf{j} - \bar{\mathbf{u}}_\mathbf{k}) + \sum F_j \end{aligned} \tag{8.18}$$

Dividing the pre-factor from the LHS, we obtain:

$$\begin{aligned} &\frac{\partial}{\partial \bar{t}} (\bar{m}_j \bar{n}_j \bar{\mathbf{u}}_j) + \bar{m}_j \bar{n}_j \bar{\mathbf{u}}_j \cdot \bar{\nabla} \bar{\mathbf{u}}_\mathbf{j} + \bar{\mathbf{u}}_\mathbf{j} \bar{\nabla} \cdot (\bar{m}_j \bar{n}_j \bar{\mathbf{u}}_\mathbf{j}) + \bar{m}_j \bar{v}_{T,j}^2 \bar{\nabla} \bar{n}_j \\ &\qquad = -\frac{n_0 L}{m_n v_{T,n}} \sum_{k \neq j} \bar{n}_j \bar{n}_k R_{jk} (\bar{\mathbf{u}}_\mathbf{j} - \bar{\mathbf{u}}_\mathbf{k}) + \frac{L}{m_n v_{T,n}^2 n_0} \sum F_j \end{aligned} \tag{8.19}$$

Let us define:

$$\bar{R}_{jk} = \frac{n_0 L}{m_n v_{T,n}} R_{jk}, \tag{8.20}$$

noting that the units work out to make the term dimensionless.

Let us also define the dimensionless force:

$$\bar{F}_j = \frac{L}{m_n v_{T,n}^2 n_0} \sum F_j. \tag{8.21}$$

We have thus obtained our system in dimensionless form:

$$\boxed{\frac{\partial \bar{n}_j}{\partial \bar{t}} + \bar{\nabla} \cdot (\bar{n}_j \bar{\mathbf{u}}_\mathbf{j}) = 0,} \tag{8.22}$$

$$\boxed{\begin{aligned} \frac{\partial}{\partial \bar{t}}(\bar{m}_j \bar{n}_j \bar{\mathbf{u}}_j) + \bar{m}_j \bar{n}_j \bar{\mathbf{u}}_j \cdot \bar{\nabla} \bar{\mathbf{u}}_\mathbf{j} + \bar{\mathbf{u}}_\mathbf{j} \bar{\nabla} \cdot (\bar{m}_j \bar{n}_j \bar{\mathbf{u}}_\mathbf{j}) + \bar{m}_j \bar{v}_{T,j}^2 \bar{\nabla} \bar{n}_j \\ = -\sum_{k \neq j} \bar{n}_j \bar{n}_k \bar{R}_{jk} (\bar{\mathbf{u}}_\mathbf{j} - \bar{\mathbf{u}}_\mathbf{k}) + \sum_{\text{forces}} \bar{F}_j \end{aligned}} \tag{8.23}$$

Numerical solution for 1-D unmagnetized plasma

Consider a 1-D system, along a single coordinate $\bar{x}$, in which each fluid has a density $\bar{n}_j$ and a velocity $\bar{u}_j$ in the x-direction, varying over the domain $\bar{x} \in [0, 1]$. We can simplify continuity as follows:

$$0 = \frac{\partial \bar{n}_j}{\partial \bar{t}} + \frac{\partial}{\partial \bar{x}}(\bar{n}_j \bar{u}_j) \tag{8.24}$$

and momentum,

$$\begin{aligned} \bar{m}_j \frac{\partial}{\partial \bar{t}}(\bar{n}_j \bar{u}_j) + \bar{m}_j \frac{\partial}{\partial \bar{x}}(\bar{n}_j (\bar{u}_j^2 + \bar{v}_{T,j}^2)) \\ = -\sum_{k \neq j} \bar{n}_j \bar{n}_k \bar{R}_{jk} (\bar{u}_j - \bar{u}_k) + \sum_{\text{forces}} \bar{F}_j. \end{aligned} \tag{8.25}$$

Note all quantities in Eq. 8.25 are barred; bars will be dropped going forward, and all quantities can be assumed dimensionless.

We have 4 continuity relations and 4 momentum relations here; we also have 8 unknowns: the density and velocity of each fluid. However, an electric force must be included for consistency, arising due to charge separation, causing a force:

$$\begin{aligned}\bar{F}_{E,j} &= \frac{L}{m_n v_{T,n}^2 n_0}\frac{n_0 k_B T_n}{L} Z_j \bar{n}_j \bar{E} \\ &= Z_j \bar{n}_j \bar{E}.\end{aligned} \tag{8.26}$$

We normalize electric fields here by $E_0 = k_B T_n / eL$. This field must be solved for in tandem with the fluid equations, requiring an additional equation for closure. The simplest approximation is a zero-current closure,

$$J_x = n_i u_i - n_e u_e - Z_d n_d u_d = 0. \tag{8.27}$$

To simplify the system of equations, we can replace the electron continuity equation with quasineutrality, $n_i = n_e + Z_d n_d$. We can also neglect the inertial term in the electron momentum equation, giving:

$$m_e v_{T,e}^2 \frac{\partial n_e}{\partial x} = -\sum_{k \neq e} n_e n_k R_{ek}(u_e - u_k) + n_e E, \tag{8.28}$$

as the electron mass is small, and incorporating it causes a stiff system of equations that is difficult to solve numerically.

The electron momentum equation can be solved algebraically for the electric field:

$$E = \frac{m_e v_{T,e}^2}{n_e}\frac{\partial n_e}{\partial x} + \sum_{k \neq e} n_k R_{ek}(u_e - u_k). \tag{8.29}$$

This system now has 9 unknowns: n_j, u_j, and E ($j \in [e, i, n, d]$). It contains 9 equations: the quasineutrality condition, the continuity equation for ions, dust, and neutrals, the momentum equation for each of the four fluids, and the zero-current closure.

This system can be solved numerically using periodic boundary conditions. I apply an intrinsic length $L = 1$ AU, a neutral density comparable to the cold neutral ISM $n_n = 10^8$ m^{-3}, and $v_{T,n} = \sqrt{k_B * 100 \text{ K } / m_p} \approx 900$ m/s. I take the electrons to be cold, causing the dust to be weakly-charged; for a 10-nm spherical grain, $Z_d \approx 2$. The ion density was initialized as $\bar{n}_i = 10^{-2}$ (1% ionization).

The relative strengths of the collision operators $\bar{R}_{jk}$ control the coupling between the fluids; the equations in Table 8.1 are made dimensionless using

$\bar{R}_{jk} \approx 10^{43}\ \mathrm{s\ kg^{-1}\ m^{-3}}\ R_{jk}$. Approximate values for these conditions are given in Table 8.2. We thus see that the collision operator between dust and ion is extremely strong, and that the dust-neutral operator is significant as well; meanwhile, neutrals are not well-coupled to ions or electrons.

Collision operator	Ballistic	Coulomb
$\bar{R}_{in}$	0.04	~ 0
$\bar{R}_{en}$	0.04	~ 0
$\bar{R}_{dn}$	260	~ 0
$\bar{R}_{de}$	~ 0	$4 \cdot 10^6$
$\bar{R}_{di}$	$2 \cdot 10^5$	$8 \cdot 10^9$
$\bar{R}_{ei}$	~ 0	$2 \cdot 10^6$

Table 8.2: Approximate collision operators

Ions and electrons are initialized with a rightward velocity $\bar{v}_i = 0.1$, and the neutrals and dust at initially rest. Periodic boundary conditions are invoked. The solution, presented in Figure 8.2 gives the average velocity of the ions, dust, and neutral gas over normalized time, with and without the presence of dust grains.

With negligible dust densities, neutrals are very slowly accelerated by ion coupling (dominated by charge exchange). With dust grains present in sufficient amounts, meanwhile, the neutrals are accelerated orders of magnitude more in the simulated timescale. Dust acts as a mediator of momentum: ions efficiently accelerate the dust, and the dust efficiently accelerates the neutrals.

We must also note, however, that as dust slows down the ion flow, it indirectly lessens coupling between ions and neutrals themselves; under some circumstances, the absence of dust causes *faster* neutrals, as they couple to the faster neutral population. The overall effect is thus highly sensitive to the relative densities and initial conditions of the fluids.

Influence of fractal dimension

The previous simulation used spherical grains of radius R_0. Now suppose these grains were to aggregate to form grains with length L. The mass density of the dust fluid, $m_d n_d$, would be unchanged; the mass would thus

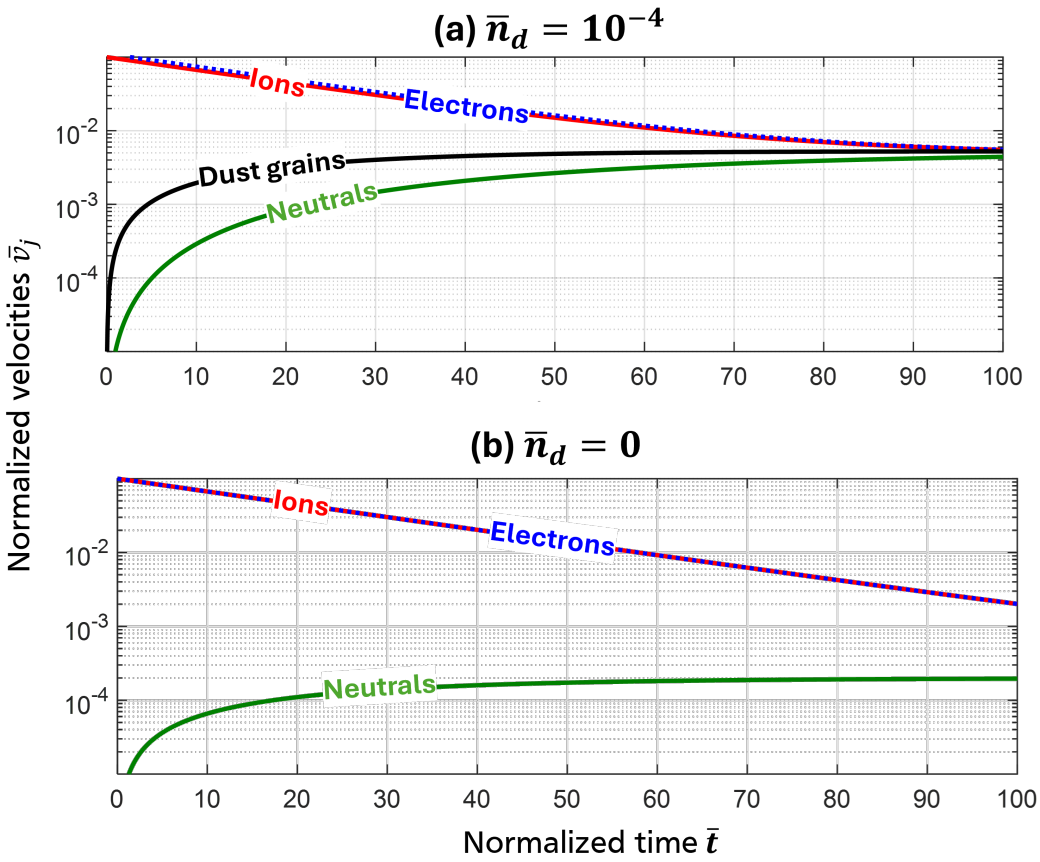

Figure 8.2: Results of the 4-fluid simulation, with (a) and without (b) dust present. Dust mass and cross-section are consistent with 10-nm spherical grains.

scale with:

$$m_d = m_0 \left(\frac{L}{2R_0} \right)^{D_3}, \tag{8.30}$$

and thus the number density must decrease with:

$$n_d = n_0 \left(\frac{L}{2R_0} \right)^{-D_3}. \tag{8.31}$$

The mass of each grain would increase with L^{D_3}, and thus the density would decrease as L^{-D_3}. The cross-section of each grain, meanwhile, would increase with L^{D_2}, and the charge with L, according to the smallest-enclosing sphere model [84]. This will affect the collision operators:

$$\bar{R}_{nd} = \bar{R}_{nd}^{(0)} \left(\frac{L}{2R_0} \right)^{D_2} \tag{8.32}$$

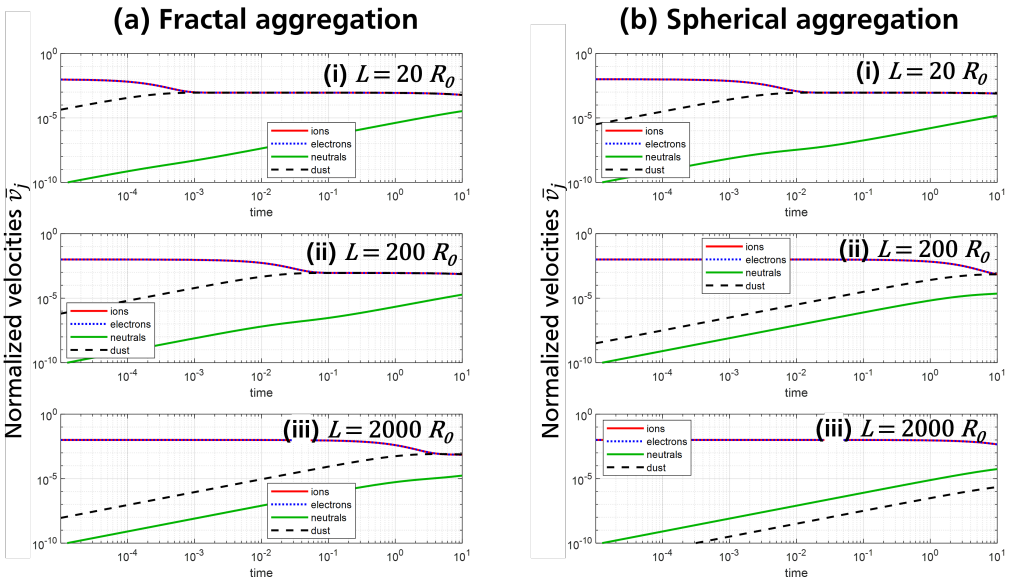

Figure 8.3: Comparison of fluid couplings between fractal and spherical aggregates.

$$\bar{R}_{id,ed} \approx \bar{R}^{(0)}_{id,ed} \left((L/2R_0)^2 - \ln(2R_0/L) \right), \tag{8.33}$$

as the Coulomb term tends to dominate ion-dust and electron-dust collisions.

Figure 8.3 shows how fluids change during aggregation, for fractal ($D_2 = 1.45$, $D_3 = 1.85$) and compact ($D_2 = 2$, $D_3 = 3$) cases. During fractal aggregation, dust much more quickly equilibrates with the ion flow. The neutral gas, meanwhile, has different acceleration rates depending on the case, illustrating the significant effect of fractal dimension on the system dynamics.

Extensions to radiative and magnetized environments

To capture all physics, we must include the current, couple Maxwell's equations into the fluid model, and incorporate magnetic fields. Instead of zero-current closure, we can solve Poisson's equation for the electric field at every step of the simulation,

$$-\nabla^2 \phi = \frac{e}{\epsilon_0}(n_i - n_e - Z_d n_d), \tag{8.34}$$

where $E = -\nabla\phi$. In addition, the $v \times B$ force can be incorporated to the equation of motion.

Further, it is crucial to incorporate two of the dominant forces in astrophysics: gravity and radiation pressure. Both of these are strongly affected by grain geometry [122], and thus active nucleation and agglomeration of dust grains introduce changes to the dynamical regime through these forces.

By developing these models, including accurate forms of the ion drag force, and the appropriate charge and cross-sections for fractal-shaped grains confirmed in dusty plasma experiments, we can produce more robust and accurate models of astrophysical dusty plasma.

8.2 Elongation and alignment

Starlight becomes partially polarized as it passes through the interstellar medium [123]. This polarization, as well as polarization of the thermal emission from dust and ice grains, arises from the alignment of elongated grains with magnetic fields, which selectively absorb, scatter, and emit light anisotropically. Consequently, polarimetry serves as a powerful tool for mapping magnetic fields across scales, from galaxies and AGNs [124, 126] to star-forming regions and stellar outflows [122, 127, 128]. The star forming region within the Orion nebula is shown in Fig. 8.4 with overlaid magnetic fields measured by SOFIA[1].

Observatories such as ALMA, JCMT, and SOFIA, alongside all-sky surveys such as Planck, have advanced our understanding of dust polarization and its role in cosmic evolution, and the proposed PRIMA mission seeks to extend high-resolution polarimetry into the far-infrared. However, uncertainties in grain morphology, including structure, size, and porosity, limit the accuracy of polarization models.

Nearly every astrophysical measurement must contend with dust emission, extinction, and polarization, due to its abundance throughout the ISM. Improved modeling of dust alignment to radiation sources and magnetic fields are thus vital to understanding both the environments in which they are contained, as well as any objects behind them, for which foreground dust signatures must be subtracted from measurements.

[1]SOFIA: Stratospheric Observatory for Infrared Astronomy; ALMA: Atacama Large Millimeter/submillimeter Array; JCMT: James Clerk Maxwell Telescope; PRIMA: PRobe far-Infrared Mission for Astrophysics

Figure 8.4: The OMC-1 region of the Orion nebula, photographed by the ESO Very Large Telescope [5], with overlaid magnetic field lines as measured by SOFIA, credited to Chuss *et al.* [6]

Alignment theory in astrophysical plasmas

The precise reason for grain alignment to magnetic fields has been debated for over half a century. In recent years, Radiative Torque (RAT) alignment theory has had widespread success in explaining observations. This theory posits that differential radiation pressure causes aspherical grains to spin about their principal axis (that is, the axis with the maximum moment of inertia) to supra-thermal speeds. A magnetic moment is induced along this axis of rotation, both due to electric charge on the grains, imparted by photoemission or collected from the surrounding plasma [129], and due to the Barnett effect [82]. This magnetic moment precesses about the external magnetic field, eventually relaxing paramagnetically to an aligned configuration. This process is outlined in Fig. 8.5

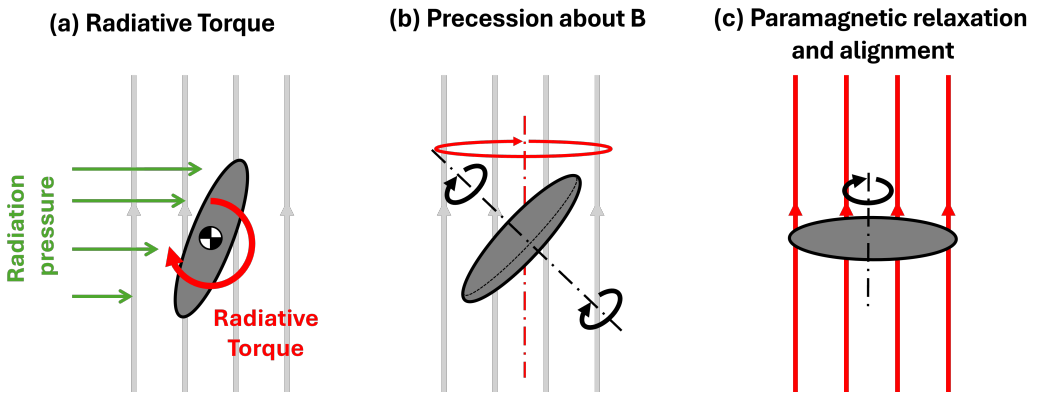

Figure 8.5: Radiative alignment of elongated grains to the magnetic field

While RAT theory outperforms alternatives such as paramagnetic or drag-induced alignment in agreeing with observation, challenges remain: in dense clouds and weak-field regions, it incorrectly predicts alignment with the radiation field [82], and in high-radiation environments, extreme radiative torques are predicted to fragment larger grains [130], sometimes contradicting direct observations. This may be remedied by better consideration of grain morphology, which affects the radiation pressure profile, torque efficiency, inertia tensor, and tensile strength to rotational disruption.

Grain alignment in experiment

In the experiment, grains tend to align vertically. As discussed by Chai [131], the alignment of longer grains matches well both with the electric field structure and the temperature gradient, which point outward and mainly in the vertical direction.

As there does not appear to be significant change in alignment as the temperature differential between the electrodes is altered, it appears that the alignment is with the electric field. This may be due to interactions between the grains' multipole moments with the electric field, or most likely, due to streams of ions along the field lines from the plasma density maximum. It has also been suggested that this mechanism is responsible for the spin of the dust grains, with the ion flow imparting rotation on the grains similar to a stream of water spinning a propeller.

Alignment efficiency may also be enhanced by interactions between the grains themselves. As they form a lattice, interacting through a Yukawa

potential, perfect alignment maximizes the distance between them, and thus minimizes the potential energy.

The fractal, irregular shape of the grains complicates the theory of alignment. In general, the grain has some inertia tensor $\mathbf{I_d}$ oriented to its longest axis $\hat{n}$ (that is, the principal axis of the inertia tensor); in the lab frame, the inertia tensor is written as:

$$\mathbf{I}(\theta) = \mathbf{R}(\theta)\ \mathbf{I_d}\ \mathbf{R}^{\mathrm{T}}(\theta) \tag{8.35}$$

where θ is the angle between the grain's axis and vertical in the lab frame, and $\mathbf{R}$ is a rotation matrix. The equation of motion is thus:

$$\mathbf{I}(\theta)\frac{d\vec{\omega}}{dt} + \vec{\omega} \times (\mathbf{I} \cdot \vec{\omega}) + b_{rot}\vec{\omega} = \sum_j \tau_j, \tag{8.36}$$

where $\vec{\omega}$ is the angular velocity, b_{rot} is the rotational damping coefficient, and the right-hand side represents the sum of torques on the grain.

Suppose the grain has a net charge and some multipole distribution. The potential is expressed as:

$$U(\hat{n} \cdot \hat{E}) = \sum_{n=1}^{\infty} \frac{p_n}{n!}[(\hat{E} \cdot \nabla)^n E](\hat{n} \cdot \hat{E}) \tag{8.37}$$

and the torque as:

$$\vec{\tau}_E = -\frac{dU}{d\hat{n}} \times \hat{n}. \tag{8.38}$$

There is no torque if there are no multipole moments, $p_n = 0$ for $n \geq 1$; note that p_0 is equal to the grain charge.

As the ions stream through the electric field, they exert two torques: an *alignment* torque that tends to align $\hat{n}$ to the flow direction, and a *spin* torque, which induces rotation $\vec{\omega}$ along the flow direction. Both scale with the product of $m_i n_i u_i^2$, with strengths that must be derived from the particulars of the grain shape, alongside the inertia tensor.

The thermophoretic alignment must be similarly computed from the grain's inertia tensor, but aligns to the preferred axis perpendicular to ∇T instead of along $\hat{u}_i$. This can be illustrated by considering a prolate ellipsoid with long axis a and short axes b. The cross-sectional area varies with orientation as

$$A(\theta) \approx \pi b^2 \cos^2\theta + \pi ab \sin^2\theta, \tag{8.39}$$

thus the potential energy associated with the temperature gradient is $U_{th}(\theta) \approx -\nabla T \ A(\theta)$ and the torque varies with $-dU_{th}/d\theta$. As A is maximized at $\theta = \pi/2$, and since $b^2 > ba$, the $\hat{n} \perp \nabla T$ orientation is more stable.

A more complete 3D model of the grain, along with charging simulations, could compute the inertia tensor, the multipole moments, and the alignment and spin torques due to thermophoresis and ion flows. The strengths of each could be compared, determining the dominant alignment mechanism.

A line of future experimental work

Chai & Bellan [72] applied magnetic fields to the ice-dusty plasma and observed that the grains that formed were less elongated and more compact. This suggests that the magnetic field impacted the growth process, preventing the formation of elongated fractal agglomerates. To study the alignment of elongated fractal grains, therefore, a magnetic field could be introduced *after* grains have formed, and any effect on the rotation or alignment could be studied.

Measuring alignment to magnetic fields would be of the utmost importance to observational astrophysics, as it would help predictions and interpretation of dust polarimetry measurements from telescopes. As dust in the Ice Dusty Plasma Experiment is already highly-elongated and aligned, in-situ polarimetery measurements could be performed across various wavelengths. Signatures of the dust geometry could be compared to simulations, such as the DDSCAT code [132], the industry standard for simulating dusts of nonspherical geometries.

In addition, the RAT mechanism itself could be tested. With an applied magnetic field, a radiation source could be applied to grains, and their re-alignment with the magnetic field could be recorded using high-speed videography. Such an experiment has only been performed once before, by Abbas *et al.* [38] in 2004, which measured induced spin rates of grains within an electrodynamic balance due to radiative torques. Monumental progress both in RAT theory and dusty plasma technology over the past two decades make this problem ripe for laboratory testing, especially in the highly radiative conditions in which theory predictions disagree with astronomical observations. The limits to radiative disruption, predicted to

take place when grains are spun to speeds their tensile strengths cannot withstand, could also be directly observed.

8.3 Conclusions and lingering mysteries

From controlled laboratory experiments to the diffused reaches of galaxies, the physics of dusty plasmas are fundamental to a vast range of phenomena. The structure of grains on small scales—from crystalline or amorphous phases at the nanoscale to fractal branching at the microscale—impacts plasma densities, flow speeds, and interactions with galactic fields and radiation. These grain-plasma interactions shape the interstellar medium, regulate stellar outflows, and drive planet formation from proto-planetary dust clouds. The details of many of these processes are still not well understood [12, 81].

Dust also imprints itself on virtually every astronomical measurement. Extinction, scattering, and thermal emission by irregular grains alter the light from distant sources, making grain properties, alignment, and dynamics essential to the interpretation of telescope data [132]. Much work remains in describing these processes, including the effects of irregular grain shapes, fractal structures, ice mantles, and coherent dusty plasma structures on their optical behavior.

It is a very exciting time to study ice-dusty plasma. As new measurements by the James Webb Space Telescope now allow us to resolve clouds of dust and ice in unprecedented detail, and planned missions will allow high-precision polarimetry and spectra covering sweeping portions of the sky, data is abundant and questions are numerous. In the near future, research into the interplay between ice and plasma– both theoretical and in the laboratory– is poised to greatly advance our understanding of the universe.

. . .

Appendix A

ADDITIONAL EXPERIMENTAL HARDWARE

A.1 The temperature control system

The cryocoolers supply unregulated cooling power of the electrodes. To control the temperature, a feedback system is implemented that contains:

- A temperature-sensitive silicon diode (CryoCon S950 or Lakeshore DT-670) on each electrode
- A resistive cartridge heater embedded in each electrode
- A Stanford Research Systems CTC100 temperature controller.

A vacuum feedthrough (a conflat flange with a 9-pin connector, made by Accu-glass) connects the diode and heater wires to the wires of the CTC100. When current is applied across the silicon diodes, they produce a voltage that corresponds to the temperature. Each diode has 4 leads, labeled $V+$, $V-$, $I+$, and $I-$. Nominally, a constant current of 10 μA is driven from $I+$ to $I-$, and a voltage drop is developed, read across the $V+/-$ pins.

For each polarity ($+$ or $-$), the I and V pins are actually shorted together. They can be soldered together, and only the $I+/-$ pins used to read both voltage and current; the $V+/-$ pins are used separately to avoid signal distortion by the resistance of the wires.

The CTC100 uses a PID feedback cycle read the temperature from the diode and drive 0-100 W of power (up to 50 V, 2 A) through the resistive heater cartridges, which have intrinsic resistance of 25 Ω.

Diagram of wiring

Figure A.1 shows a schematic and pinout of the connections. The output (heater) wires go to the Output +/- inputs on the back panel, while each diode goes to a DB9 socket. Each DB9 connector has the pins for two temperature sensors; as of 2025, each sensor is connected to its own DB9 connector, populating pins 1, 2, 6, and 7; pins 4, 5, 8 and 9 are empty.

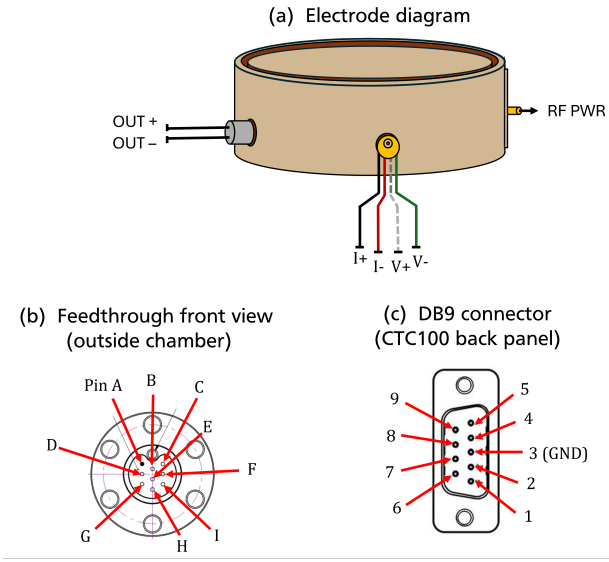

(d) Connections

Connection	Wire color	Feedthrough Pin No.	DB9 Pin No.
Out +		**G**	--
Out –		I	--
V+		**F**	**6, 8**
V-		D	7, 9
I+		**C**	**1, 4**
I-		A	2, 5

Figure A.1: Schematic of the wiring for the temperature controller. (a) Diagram of the electrodes. (b) Conflat 9-pin feedthrough, (c) DB9 connector at the back panel of the CTC100 chassis. (d) Pinout table for connecting the temperature sensor and heater to the back panel.

Programming the CTC100

In normal operation, the temperature is set as follows:

1. Press "setup" physical button at the middle-left of the front panel.
2. On screen, press the tab corresponding to the output of the electrode you want to set (e.g., "Out T" for the top electrode, "Out B" for the bottom.).
3. Press "Set Temperature" and input the desired value.
4. Double-click the physical red button ”Output Enable" at the bottom left of the front panel to engage the heaters and run the cycle. The red indicator light should turn on when engaged.
5. Press the "Show Data" button to display the temperature readings and output power. Press the tabs at the top of the screen to switch between numerical and graph views.

(a) Setting temperature

(b) Temperature readout

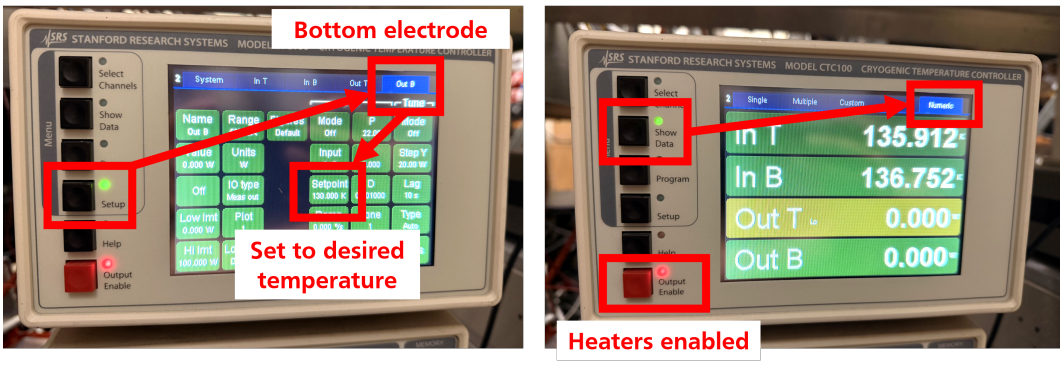

Figure A.2: CTC100 Interface

If not all of the readings are displayed (e.g., only the inputs are shown, not the outputs), hit the "Select Channels" button and make sure the working ones are selected. Figure A.2 shows the steps on the instrument's user interface.

If there are issues, such as temperatures not displaying or the heaters not engaging at the appropriate times, make sure the PID cycle is configured correctly, the outputs are responding to the correct inputs, and that the current is being driven in the right direction. Refer to the CTC100 user manual for troubleshooting details.

Common faults

If the diodes fail, check the connections inside the DB9 connectors at the back of the CTC100 chassis. Most likely, the wire was yanked, and one of the wires in the connector came loose.

The leads of the temperature diodes inside the chamber are extremely sensitive: 36-gauge wires, 125 microns in diameter. This is smaller than a human hair. Because of this, monkeying about in the chamber may cause them to snap, so one must be extremely careful. making repairs.

The diodes are also not rated for contact with water, or for use in electrically noisy environments. We treat them very poorly. Make sure not to vent the chamber when ice is present, as water can liquefy and mess the diodes up. As CryoCon is out of business, any replacements should be DT-670 diodes from Lakeshore Cryogenics.

Noise from the RF source and the current driven through the heaters can sometimes mess with the diode signal. This is because the 10 microamp driving current to the diodes is extremely small and thus quite sensitive to electrical noise.

A.2 Water vapor flow control

The water injection system inputs a steady flow of vapor into the chamber. It uses a MKS Type-1150C mass flow controller. Traditional thermal mass flow sensors do not work well with water vapor, especially as the vapor is sourced from a low-pressure canister rather than a pressurized gas cylinder, so the setup of this controller is quite different from that of the neutral gas injection.

Distilled liquid water is contained in the gas canister, and any trapped air is pumped out by the auxillary pump. A Pirani gauge displays the pressure, ensuring it is ~ 9 Torr, the saturated vapor pressure of water at room temperature. Vapor is sourced from the top of the canister and injected to the chamber through the mass flow controller. This is all outlined in Figure 3.5.

Flow controller circuitry

The 1150C unit requires a +/- 15 VDC input. For this, we purchased a MKS Type 360 PS-3B power supply which is made precisely for this flow controller. The +- 15 V are supplied both to the controller's internal heater and its relay. A schematic of the flow controller, power relay, and pinout are shown in Fig. A.3

When the power is properly connected, an indicator light in the flow controller turns on. If it has been disconnected, the light is orange, indicating it is not at equilibrium temperature. After about an hour, the light turns green, indicating that the controller is ready for use. There is no reason to turn off the power source; leave it on, so the controller remains in operable state.

A 0-5 VDC input signal sets the flow rate between 0 and 100 SCCM of water vapor. I designed a custom control box, a simple voltage divider circuit, to input an adjustable 0-1 V (0-20 SCCM) and display the output for manual

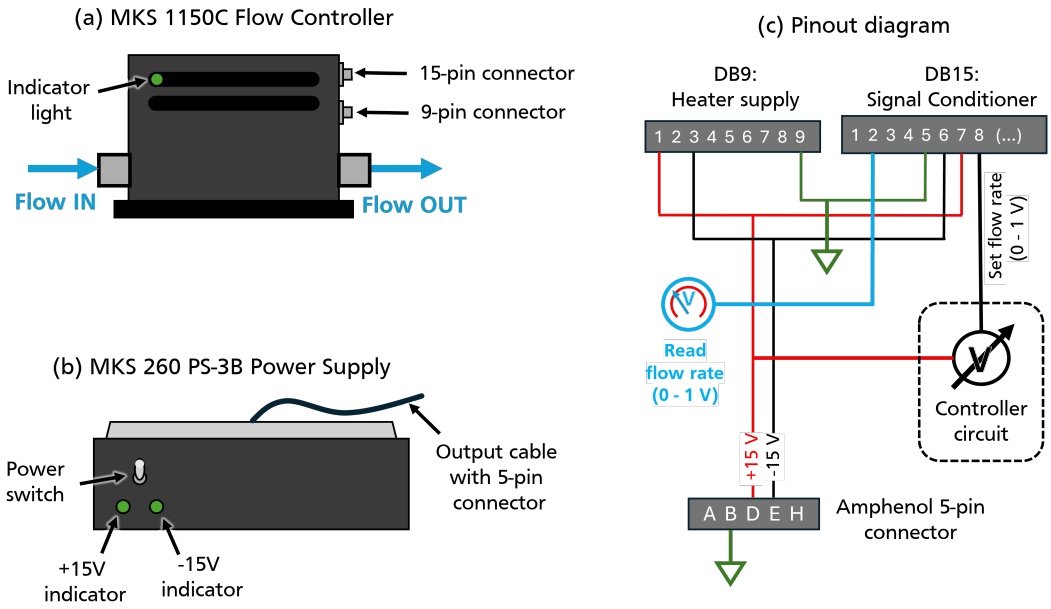

Figure A.3: Water vapor flow controller details.

control. The box is shown in Fig A.4, along with the circuit diagram and pinout.

An analog voltage meter attached to the box reads out the flow output from the controller (Pin 2 of the DB15 connector) to ensure that the meter is responding properly. The interface between the control box and the MKS flow controller is a DB9 connector, with pinout displayed in Fig. A.4 (c).

The switch must be on, and the LED illuminated, to input a flow. When the knob is turned, the flow setting is input to the flow controller, which takes about a second to adjust; the analog meter shows the actual state of the flow controller.

Troubleshooting

When the chamber is at high pressure ($\gtrsim 10\%$ the pressure in the water canister), it displays some baseline flow reading; this is normal and can be ignored.

When opening the valve, the knob may need to be turned further than you expect. This is because a higher voltage is sometimes needed to trigger the valve to open. Turn the knob up, wait for the flow reading to start increasing, and then quickly decrease the set point so it stabilizes at your desired value.

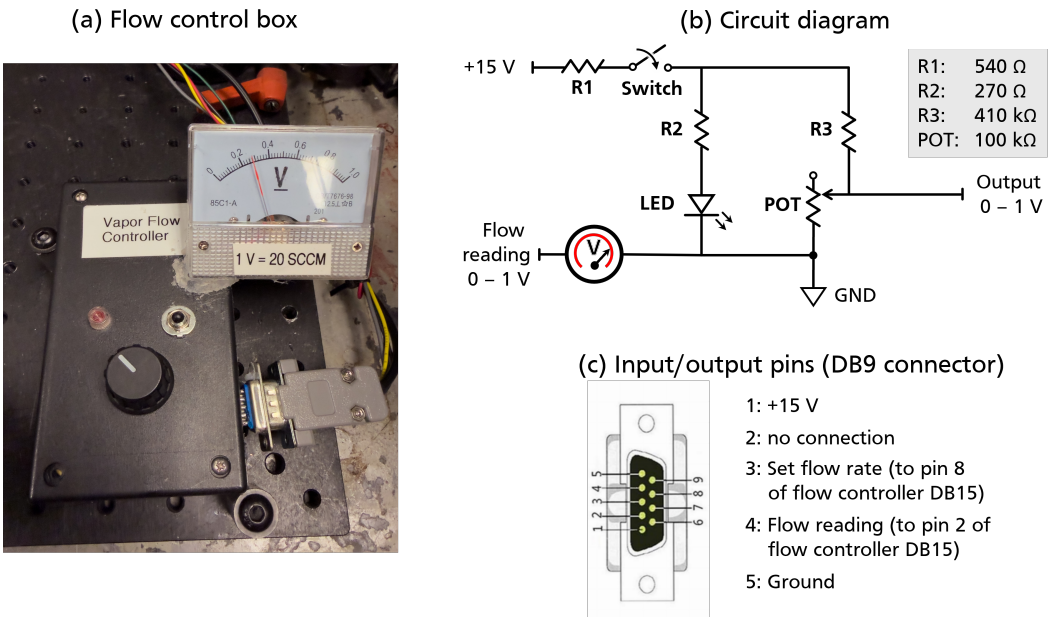

Figure A.4: Signal control box for vapor mass flow controller. (a) A photo of the box; (b) the circuit diagram; (c) pinout of the DB9 connector that connects to the type-1150C controller.

If the flow reading is at maximum whenever the DB9 connector is plugged in, there is probably a short inside the box. This is most likely because the dial was over-turned, spinning the internal wires and shorting the leads across the potentiometer.

Open up the control box and make sure the pins on the back side of the knob are not shorted. Check that all the proper wires are in the right places, and that no connections are broken.

This control box was intended to be a temporary solution. In the future, you may desire to get a standard flow controller for the neutral gas, as well as a motorized main angle valve for the chamber. The entire system, including this water vapor flow controller, could then be controlled centrally by LabView or an Arduino. The capacitance manometer gauge is also made by MKS, and therefore should interface well with the flow controller in an automated setup.

A.3 RF Power modulation

Control of the RF power is typically managed by the front panel of the RF generator. The AG-0113 RF generator (made by T&C Power conversion) has a knob to adjust the input power, from 0-120 W, and an on/off key for steady power delivery.

However, it is often desired to run the generator "burst mode," turning the generator on or off for a set window or modulating it with a TTL square wave of a set frequency. For this, the AG-0113 must be switched from Local to Remote control, controlled by inputs to the DB25 connector on the back panel.

Control circuit (by S. Pree)

Photos of the components for RF power modulation are shown in Fig. A.5 (a) and (b). The relevant pinout of the DB25 connector is outlined in (c). The remote control box circuitry, designed and built by Dr. Seth Pree, is outlined in Fig. A.5 (d).

When set to remote mode, the "RF" switch turns the RF power on or off. This is functionally the same as pressing the "RF Out" key on the AG-0113's front panel, (disabled in remote mode). The potentiometer knob controls the setpoint power, as the main control knob on the AG-0113 does in local control mode. However, in remote mode, the power can only be tuned up to 70 W— this is an internal calibration setting, and can be changed in the mode settings on the AG-0113's front panel.

The "Burst" switch sets the generator to burst mode, controlled by the pulse generator, which is connected to the remote control box by a BNC cable. The RF power being delivered to the plasma (LP) typically lowers when burst mode is turned on, even if the pulse generator is not modulating the signal (i.e., outputting a constant nonzero voltage).

When pulsing, the power setting on the front panel will appear to jump around randomly due to some aliasing effect; this is normal operation. For reliability, it is best to turn on burst mode, adjust to the desired input power while the pulse generator is outputting a constant nonzero voltage (something between 2 and 5 volts to ensure it is triggering the "on" configuration in the AG-0113), and then start modulating the signal with the pulse generator.

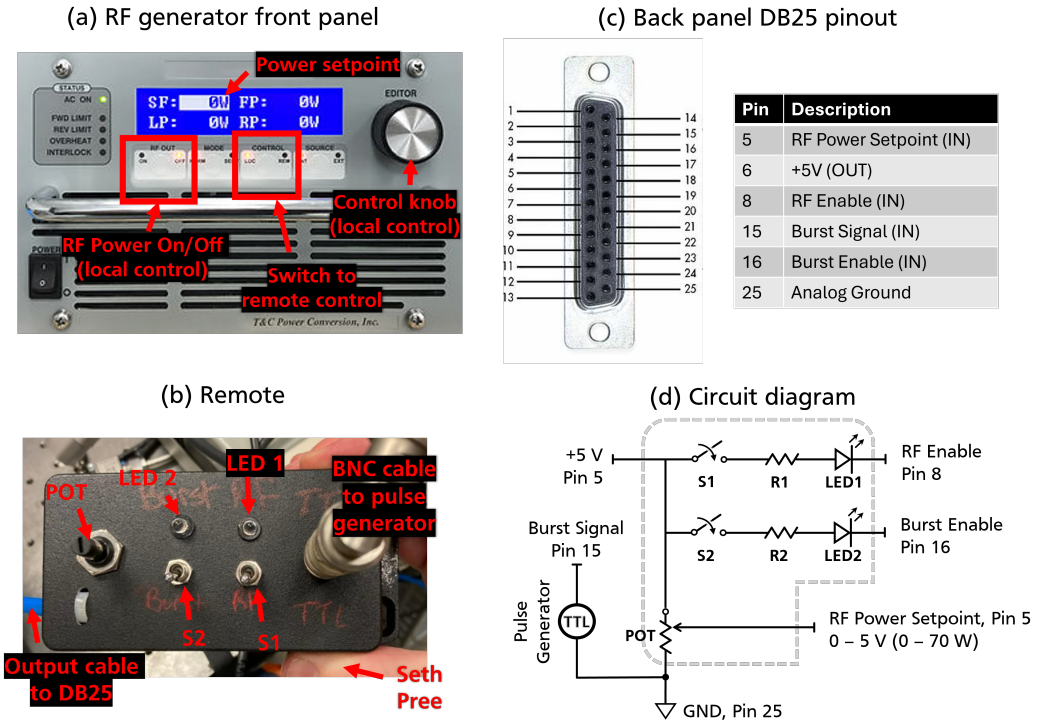

Pin	Description
5	RF Power Setpoint (IN)
6	+5V (OUT)
8	RF Enable (IN)
15	Burst Signal (IN)
16	Burst Enable (IN)
25	Analog Ground

Figure A.5: Control over RF power. (a) RF generator, (b) remote control box, (c) DB25 pinout for remote control, and (d) remote box circuitry.

Pulse generator

The pulse generator we use is an Stanford Research Systems DS345. A user manual for this function generator is available online, and a photo is shown in Fig. A.6. The output signal is input to the remote control box for RF pulsing; it can simultaneously be fed into the mass spectrometer, high-speed camera, or an oscilloscope, to trigger the diagnostics in sync with RF pulsing.

The RF generator's "burst signal" pin requires a TTL (square wave) with amplitude of a few volts. It delivers power at the "on" portion of the square wave, and shuts off the power during the $V = 0$ period. The function generator should thus be set to supply such a square wave.

Using the "Function" section of the DS345 front panel (see Fig. A.6), use the arrow keys to select a square wave. The amplitude can be set to 4 V peak-to-peak, and the offset to 2 V, so that the square wave oscillates from 0 to 4 volts. The frequency f can be set to the desired value; the gate width of each pulse is $1/2f$. Set the phase to 180 degrees, so that each pulse begins by switching the plasma off, and then turns it back on.

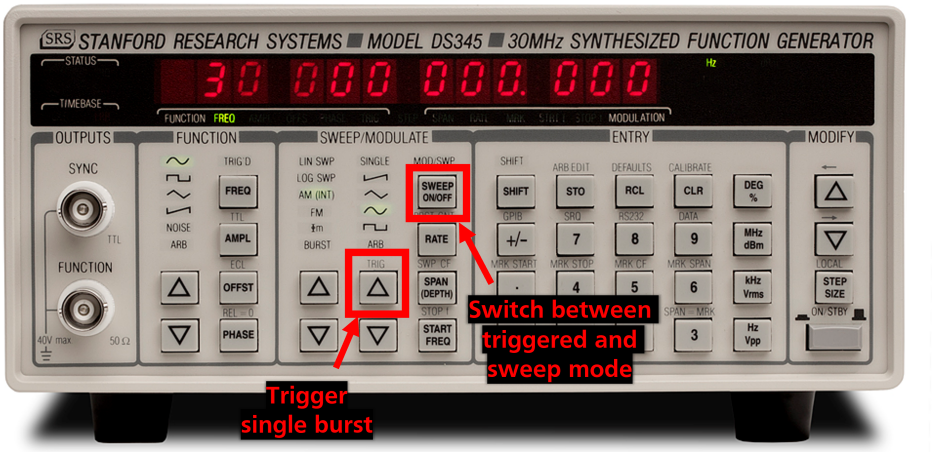

Figure A.6: Photo of the SRS DS345. Outlined in red are buttons to trigger the set burst, and to switch to continuous pulsing.

We typically use the power modulation for two applications: a single pulse off to study the afterglow (used in Chapter 7), or constant RF modulation at a fixed frequency (for mass spectroscopy in Chapter 6). This is configured in the "Sweep/modulate" section of the DS345 front panel.

To drive a single pulse, which shuts off the plasma for the pulse width, press the "SWEEP ON/OFF" button (label will light up). Using the left-hand set of arrow keys in the Sweep/modulate section to select "BURST" mode. Pressing "SHIFT" + "RATE," set the burst count to 1. A single pulse will now commence when triggered. By default, the up-arrow with "TRIG" written above it triggers the burst, as indicated in Fig. A.6.[1]

For continuous modulation, press the "SWEEP ON/OFF" button. This disables the sweep/modulate settings, giving a continuous waveform. It is useful to monitor the output with an oscilloscope to ensure it is behaving as expected.

[1]If it is not working, press "SHIFT" + "0" and make sure the trigger is set to "single" and not "external."

Appendix B

PLASMA-FACING PROBES

Plasma-facing electrical probes are the most common diagnostic for low-temperature plasmas. These consist of wires that stick into the plasma, interact with the electrons and ions, and output some signal. The response function of the probe tells us something about the plasma. In general, the more simple the probe is, the more complicated your analysis must be to extract anything useful from the readings

The simplest configuration is the standard Langmuir probe. This is a single wire that floats with respect to the chamber. Biasing the probe allows tracing an I-V characteristic of the plasma, which theoretically gives the ion density, electron density, and electron temperature. However, Langmuir probes are notoriously unreliable in RF plasmas [47] due to noise and RF oscillations in the probe's Debye sheath.

While there are methods of compensating Langmuir probes for RF plasmas, these are quite intricate and have not yet been attempted. Instead, we have attempted several other types of probes for measuring electron density.

I supervised undergrad G. Pomraning in using a method developed by Shirakawa & Sugai [133], in which an emissive filament is used to drive electron waves at the plasma frequency, which can be detected by a nearby Langmuir probe; preliminary measurements gave values around 10^8 electrons per cubic centimeter, but this method proved extremely unreliable.

We had more success with a hairpin resonator probe, developed by J. Eschbach for his M.S. thesis [90]; this showed that electron density is extremely variable, sometimes dropping to 10 percent of the ion density, depending on the electronegativity of the plasma and the presence of ice grains.

I also supervised a high-school student, J. Boskovich, at building a magnetic filter for a Langmuir probe for detecting both positive and negative ions. This method showed some promise, but the resulting data proved complicated to interpret and many technical challenges would need to be addressed for quantitative measurements.

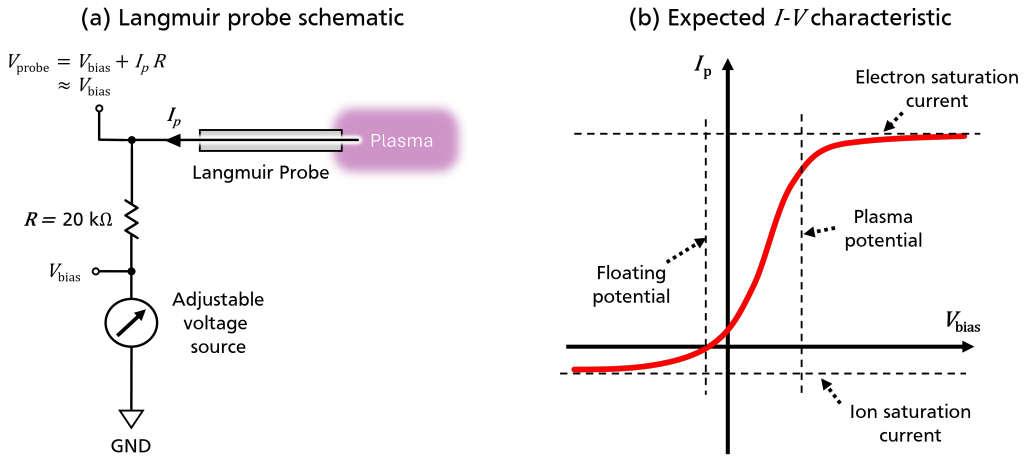

Figure B.1: A sketch of Langmuir probe operation. (a) circuit diagram, (b) sketch of a "typical" I-V curve.

This appendix gives some data and overview for those probes that had less success; see Eschbach [90] for a comprehensive overview of the hairpin resonator probe.

B.1 Langmuir probe readings

A Langmuir probe consists of a single wire that pokes into the plasma. We typically accomplish this by putting a thin tungsten wire through a ceramic (alumina) 1/4-inch tube with a hole through it, sealing it with vacuum glue (Torr-seal), and putting the ceramic rod through a vacuum feedthrough mounted to a Conflat flange.

The wire is biased to some DC voltage. As electrons and ions are collected from the plasma by the wire, a current flows through the probe. which is measured using a resistor in series with the probe. This circuit is shown in Fig. B.1 (a).

By sweeping the bias voltage and measuring the I-V characteristic, we can extract a number of characteristics of the plasma. An ideal I-V curve is sketched in Fig B.1 (b). In theory, the ion density, electron density, and electron temperature can be obtained from this I-V curve using an OML approach quite similar to dust charging problem in Chapter 2.1 [41].

When biased highly negative, all electrons are repelled, and the maximum number of ions are collected– this is the ion saturation current. Conversely,

when biased highly positive, the probe collects an electron saturation current. These saturation currents can be used to calculate the ion and electron densities in the plasma. In the region between, probe current increases exponentially, which depends on the temperature (or velocity distribution) of the electrons impacting the probe.

At a certain voltage, the electron and ion collection equate, and $I_p = 0$; this is the *floating potential* of the plasma. The plasma potential is the value at which there is a "knee" in the I-V curve, where the exponential increase in current flattens out the the electron saturation current.

Chen [47] gives a thorough overview of Langmuir probes, analysis with OML theory, and technical concerns in RF plasmas.

Measurement and analysis

An I-V trace, taken in a 400 mTorr helium plasma at 40 W, is shown in Figure B.2. It is clear that the curve deviates from ideal behavior for a few reasons. Firstly, the saturation regions are *not* flat. The ion saturation has some linear slope, likely due to sheath expansion. The electron saturation region shows much noise, and the "knee" at the plasma potential appears somewhat smeared.

As discussed by Chen [47], the potential in an RF plasma oscillates at the driving frequency. The current through the probe thus oscillates with $V_p - V_{\text{bias}}$, as the bias voltage is DC. The I-V curve thus has a funky time-averaging that "smears out" the curve, messing with the exponential transition region and plasma potential measurements.

We calculate the electron temperature from the slope of the linear fit in Fig B.2 (bottom) to be 32.5 eV. This is clearly nonsense, a classical symptom of this RF smearing [47], and why some sort of RF compensation must be used in CCPs.

Extracting ion density is much more reliable without RF compensation. From the measured ion saturation current, we compute $n_i = 3 \times 10^8$ ions per cubic centimeter. This is in line with expected values in CCPs at these conditions, as well as with our other diagnostics.

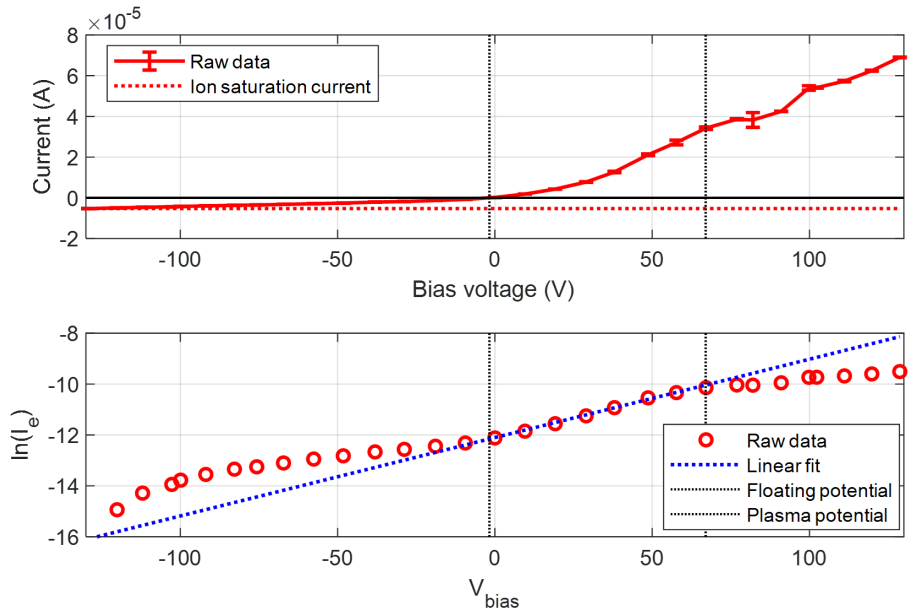

Figure B.2: I-V characteristic from Langmuir probe. Top: linear scale, with ion current indicated; bottom: electron current plotted with a log scale on y-axis.

B.2 A magnetically filtered Langmuir probe (with J. Boskovich)

As simple Langmuir probes are more reliable at measuring ion densities, as the ion current has less oscillation with the RF field, it may be possible to determine the electronegativity of the plasma by measuring relative composition of anions and cations. This requires somehow filtering out electrons from being collected by the probe, while leaving ion trajectories mostly unchanged.

I mentored high school student J. Boskovich, through a collaboration between Caltech and Westridge School, to develop a novel magnetically-filtered probe that collects only ions from the plasma. While it turns out that extracting quantitative results is quite complicated, we succeeded in deflecting most electrons, and measuring fluxes of anions.

Working principle

Because electrons are ~ 2000 times more massive than protons, the electron current is larger than the ion current by $\sim \sqrt{2000} \approx 45$. Even for very

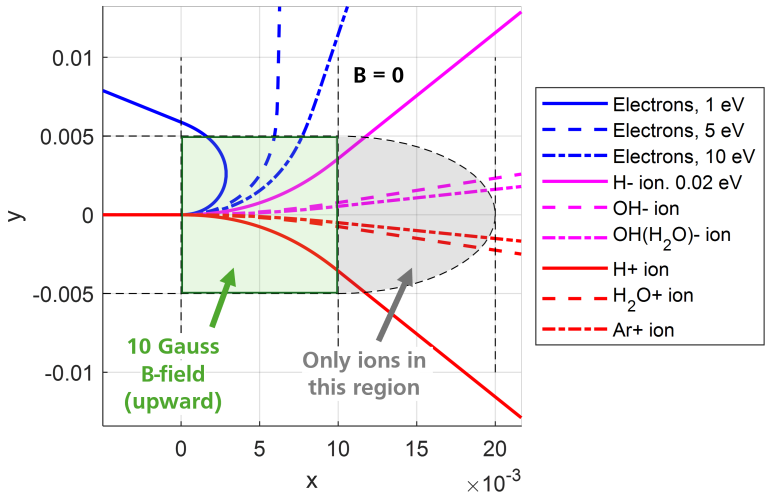

Figure B.3: A simulation of electrons and ions with various energies and masses passing through a region of 10 Gauss magnetic field.

electronegative plasmas ($n_i^- >> n_e$), electrons usually still dominate the Langmuir probe current at positive probe biases, obscuring any anion signal.

My proposition was as follows: if a magnetic field is held just in front of the Langmuir probe, it will deflect electrons more readily than ions due to their smaller cyclotron radius. If the probe dimensions are right, only ions will be collected by the probe. The cyclotron radius is

$$r_c = \frac{mv}{|q|B} \approx \frac{\sqrt{mk_BT}}{|q|B}. \tag{B.1}$$

As electrons are at ~ 2 eV, and ions at 0.02 eV, the electron cyclotron radius is only about $4\times$ larger than that of the lightest ions ($H^{\pm}$, 1 amu). The radius difference is even smaller for hot tail electrons. Therefore, the magnetic field strength and probe dimensions must be carefully optimized. Figure B.3 shows the trajectories, computed with a Leap Frog particle motion solver as described in Chapter 1 of Bellan [41].

This is not dissimilar to techniques used for anion energy and density analysis in negative ion beams and electronegative plasmas. However, these are typically much more intricate and expensive devices that use polarized meshes for ion energy measurement; our design would allow anion density characterization with minimal resources.

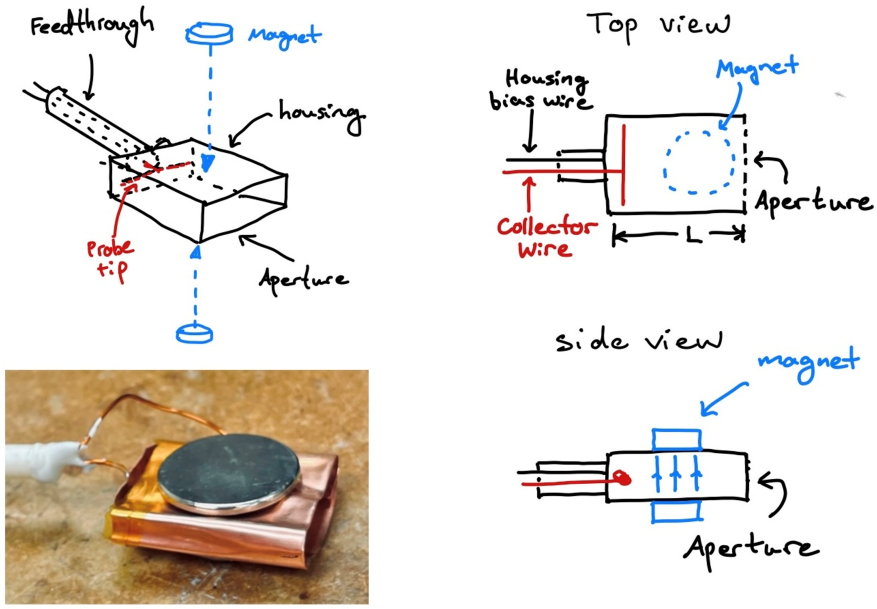

Figure B.4: Diagram sketches and photo of the magnetically-filtered Langmuir probe.

Probe design

The first challenge to designing the magnetic filter is holding the magnets in place. Firstly, the magnets and any structure holding them will acquire charge from the plasma, up to the floating potential if they are conducting. This will cause electric fields which attract electrons, ruining the probe's filtering efficiency, or repelling anions and depleting the signal. Therefore, we elected to make the filter housing from a conducting material and bias it to the plasma potential.

Secondly, the filter housing should encompass the probe tip, so that no particles can enter from the sides without passing through the magnetized region.

We purchased a set of permanent neodymium magnets, each 1 cm in diameter. I had Jordan measure the magnetic force between them at various spacings, and she determined that the field was 30 mT when they are spaced 4 mm apart. Iterating the design, we determined a length of 1.5 cm was appropriate for collecting OH^- ions (and heavier) and not electrons. One iteration Jordan built is shown in Fig B.4, along with my sketches of the geometry.

Measurements and challenges

Biasing the "body" (housing and mount for the magnets) to the plasma potential proved imprecise. Ideally, one could sweep the body bias and measure the current, locating the plasma potential at the knee of the I-V characteristic; however, because the body is much larger than the Debye length, sheath broadening obscures the peak. Future work could go into a better biasing mechanism; in our measurements, we simply biased the body to a few different values and observed how it affected the I-V characteristic of the probe itself.

In initial measurements, we created an Argon plasma, which should contain no anions. As a control, no magnets were attached to the body of the probe. The body was set to various biases, and at each, the probe was swept from -60 to 60 V of the body bias. Next, magnets were added to the probe, and the process was repeated. Figure B.5 (a) compares the I-V traces with and without the magnets.

Notably, the magnets do seem to function as expected: the probe current does not increase dramatically until significantly higher voltages, indicating that lower-energy electrons are indeed being prevented from entering. It is also noted that the floating potential increases with the body bias. The effect is more pronounced when magnets are attached.

This process is repeated for an argon + H_2O plasma, which we expect to be highly electronegative. The resulting I-V curves are shown in Fig. B.5 (b). These curves look quite different; at higher body biases, the magnet does not seem to make a difference; this could indicate that the plasma potential is lower when water is present, such that electrons were accelerated into the probe and unaffected by the magnetic field.

At the 20V body voltage, the magnets did filter out current at higher probe biases, indicating it was blocking electrons as intended. However, there also appears to be *more* negative current at intermediate probe biases, in the range of -20 to 40 V. We hypothesize that this hump in relative current indicates the presence of anions, a signal that can only be isolated due to the absence of electrons.

It is difficult to interpret the results; if all electrons were repelled, an enormous space charge would build up at the probe tip, so some quasineutrality

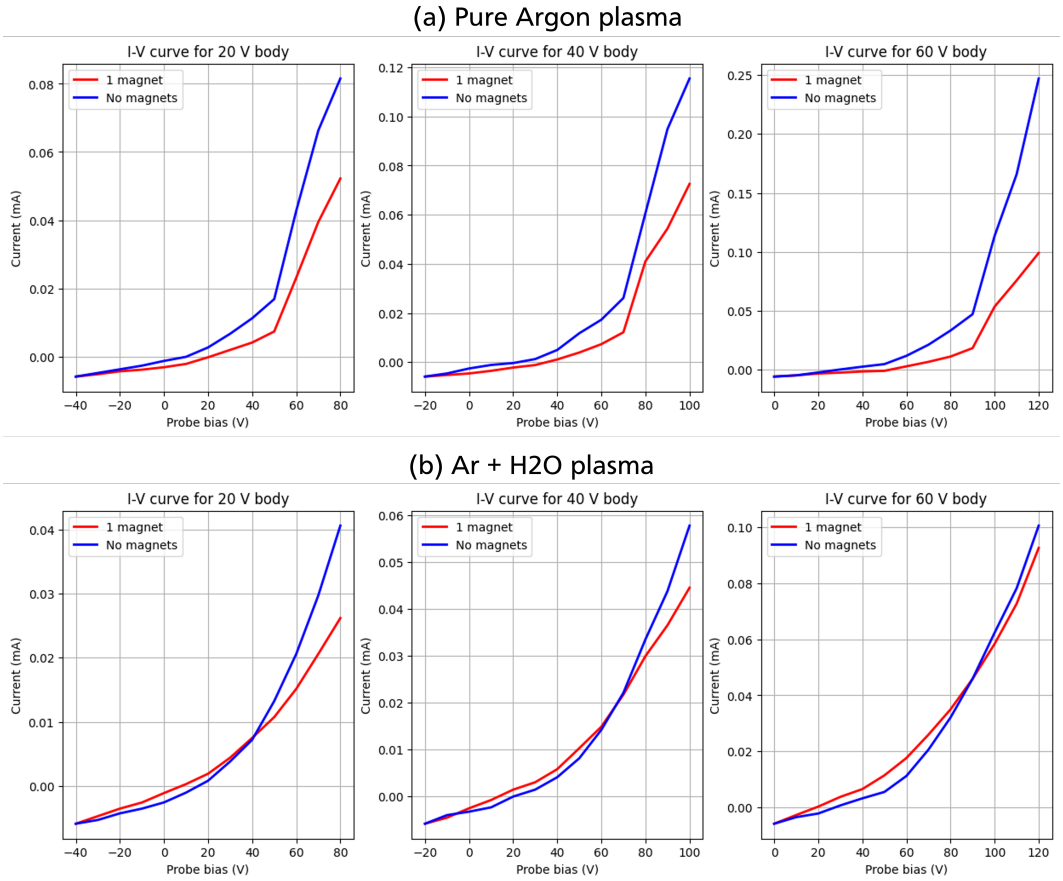

Figure B.5: Data from the filtered probe, both with and without attached magnets; (a) for a pure argon plasma, and (b) for an Ar + H2O plasma.

condition must be reworked to better interpret our results. Developing this theory is left for future work.

In addition to this difficulty in data interpretation, several technical challenges remain. Firstly, the the probe is highly perturbative, as the housing is large compared to the Debye length, so we cannot expect to detect same properties as the unperturbed plasma. Decreasing the probe size would require increasing the magnetic field strength.

Secondly, the biasing of the body to the plasma potential must be improved. As we note that the floating potential of the probe changes with the bias on the body, A second Langmuir probe could be inserted alongside the filtered probe, and the filter body biased until the floating potentials of both probes match. The biasing of both the body and the probe could also be RF

compensated, so no transient sinusoidal electric fields accelerate electrons to pass through the filter.

B.3 Using an electron-emission-induced instability as a density diagnostic (with G. Pomraning)

A study by Shirakawa & Sugai [133] measured the plasma frequency of an ICP using a novel mechanism, in which an electron beam generated from an emissive tungsten filament instagated electron plasma waves via the two-stream instability. The waves could then be detected by a Langmuir probe, connected to a frequency spectrum analyzer, and the electron density could be obtained from the wave frequency.

This technique addresses some shortcomings of the traditional Langmuir probe, such as the dependence on ion composition, and is relatively immune to RF noise, as it operates in a different frequency band.

With mentorship from Prof. Bellan, I supervised then-undergraduate Geoff Pomraning, now a graduate student at Princeton, to construct and test this probe in his summer research program.

Probe design

Both probes were formed from alumina rods with 1/4-inch diameter, which go through vacuum feedthroughs at the chamber walls and stick into the plasma.

For the emitter, the ceramic rod contained two through-holes along its length. A tungsten wire of 0.1 mm diameter was threaded through one hole, made a small loop at the vacuum end of the rod, and ran back through the other hole in the rod.

Geoff then used a chemical etching technique to make the wire loop a much smaller diameter (something like 0.025 mm), such that the current density would be much higher through that part of the wire. This causes the loop to glow and emit electrons when a current passes through, while no other parts of the tungsten wire experience that much heating.

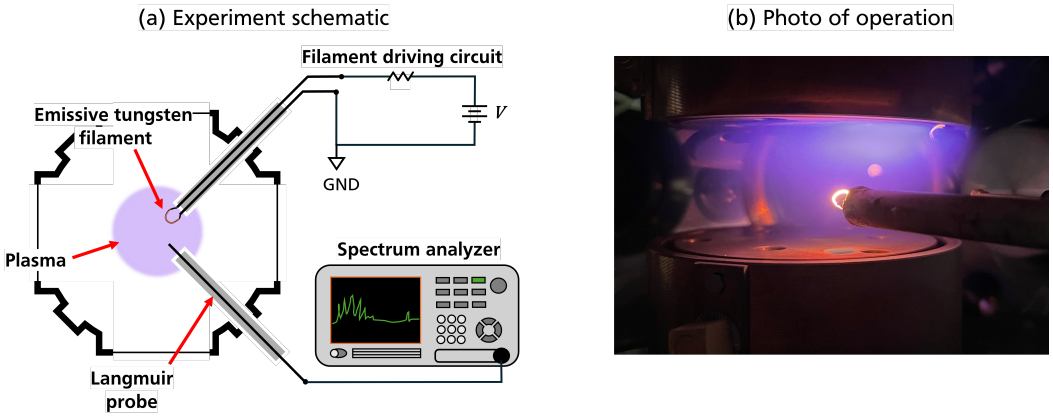

Figure B.6: The electron emission instability probe. (a) A schematic of the probes and their relevant circuitry. (b) A photo of the probes in operation.

The ends of the two wire-containing holes, on the atmosphere size of the rod, were sealed with Torr-seal. Note that glue could not be used on the vacuum side, as it contaminates the tungsten and prevents electron emission.

The "collector" was a simple Langmuir probe. The alumina rod had one through-hole, which simply contained a tungsten wire, with a tip sticking into the plasma. A spectrum analyzer monitored the frequency spectrum of the voltage on this probe.

The two probes were oriented at 90 degrees from each other, close together in the plasma. A diagram is shown in Fig. B.6. A current of 1 A was driven through the emitter, which induced an emission current from the filament of 2 μA when properly functioning.

Experimental challenges and results

Producing a stable filament turned out to be extremely challenging: too thin a filament and it would burn out with negligible emission, and too thick and the whole wire would start to glow, breaking the probe (and often the vacuum seal). Many sparks and small flames were created in this process. Part of this difficulty may be the relatively high pressure in the plasma, which increases resistive heating of the filament; as Shirakawa & Sugai [133]'s probe operated on an ICP, which has lower pressure, emissive filaments may be somewhat more stable.

(a) Plasma without emission

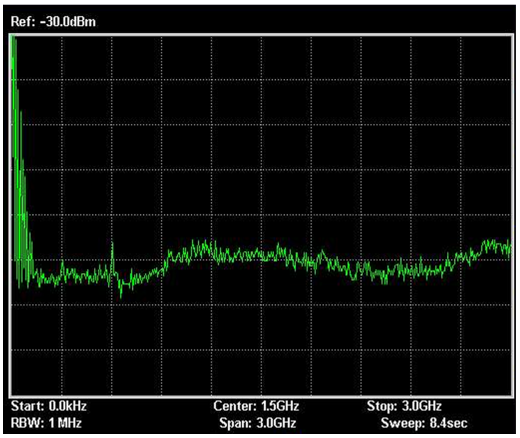

(b) Plasma with emission

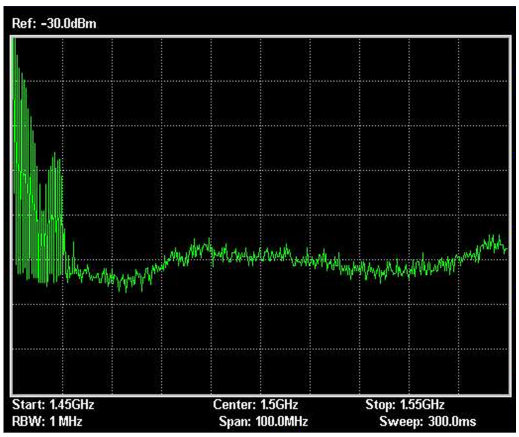

Figure B.7: Frequency spectrum obtained with (a) and without (b) electron emission.

Secondly, many configurations were tested without any signal. When the probe was optimized to give as high a emission current as possible, and the two probes were set about 0.75 cm apart, a signal was finally obtained. This is shown in Fig. B.7

The frequency spectrum showed a number of peaks in the 10-100 MHz range, with and without emission– this is the driving frequency of the plasma (13.56 MHz) and its harmonics. With electron emission from the filament, a wide "packet" of peaks appeared in the 200-300 MHz range. Geoff calculated that this corresponds to about 2×10^8 electrons per cubic centimeter, which would be in line with our expectations. However, these results were only obtained twice on the same day; the probe then burned out, Geoff's SURF program ended, and we abandoned the project.

The measured peak looked quite different from that obtained by Shirakawa & Sugai [133], as it is "spiky," an envelope of many peaks which appear to be harmonics of the 13.56 MHz driving frequency. It is also notable that the probes needed to be so close together to see any signal. Shirakawa & Sugai [133] reported that the signal peaked about 1.5 cm away, double the distance we detect a peak, and we would expect the instability to have less propagation due to our higher chamber pressure, so this is expected. However, as this distance begins to approach the Debye length, assuming that the measurement is of bulk plasma seems suspicious– this could just as easily be a sheath interaction between the two probes. I would also note that

Shirakawa & Sugai [133] makes no mention of this possibility. I would be highly skeptical of any results obtained through this method, especially in a CCP plasma such as ours.

BIBLIOGRAPHY

1. Nicolov, A., Gudipati, M. S. & Bellan, P. M. Phase and morphology of water-ice grains formed in a cryogenic laboratory plasma. *The Astrophysical Journal* **966,** 66. http://doi.org/10.3847/1538-4357/ad34b5 (2024).

2. Mastrapa, R. M. E., Grundy, W. M. & Gudipati, M. S. in *The Science of Solar System Ices* (eds Gudipati, M. S. & Castillo-Rogez, J.) 371–408 (Springer New York, New York, NY, 2013). ISBN: 978-1-4614-3076-6. https://doi.org/10.1007/978-1-4614-3076-6_11.

3. Chaubey, N. & Goree, J. Preservation of a dust crystal as it falls in an afterglow plasma. *Frontiers in physics* **10,** 879092 (2022).

4. Lockman, F. J., Benjamin, R. A., Heroux, A. & Langston, G. I. The Smith cloud: A high-velocity cloud colliding with the Milky Way. *The Astrophysical Journal* **679,** L21 (2008).

5. European Southern Observatory. *The Orion Nebula (eso0104a)* https://www.eso.org/public/images/eso0104a/. Image credit: ESO/M.McCaughrean et al. (AIP); CC BY 4.0. Jan. 2001. (2025).

6. Chuss, D. T. *et al.* HAWC+/SOFIA multiwavelength polarimetric observations of OMC-1. *The Astrophysical Journal* **872,** 187 (2019).

7. Havnes, O. *et al.* First detection of charged dust particles in the Earth's mesosphere. *Journal of Geophysical Research: Space Physics* **101,** 10839–10847 (1996).

8. Lisin, E., Tarakanov, V., Popel, S. & Petrov, O. *Lunar dusty plasma: A result of interaction of the solar wind flux and ultraviolet radiation with the lunar surface* in *Journal of Physics: Conference Series* **653** (2015), 012139.

9. Mendis, D. & Horányi, M. DUSTY PLASMA EFFECTS IN COMETS: EXPECTATIONS FOR ROSETTA. *Reviews of Geophysics* **51,** 53–75 (2013).

10. Mitchell, C. J., Horányi, M., Havnes, O. & Porco, C. C. Saturn's Spokes: Lost and Found. *Science* **311,** 1587–1589 (2006).

11. Ivlev, A. V., Padovani, M., Galli, D. & Caselli, P. Interstellar dust charging in dense molecular clouds: cosmic ray effects. *Astrophysical Journal* **812,** 135 (2015).

12. Armitage, P. J. *Astrophysics of Planet Formation* 2nd ed. (Cambridge University Press, 2020).

13. Lieberman, M. A. & Lichtenberg, A. J. *Principles of plasma discharges and materials processing* (Wiley-Interscience, 2005).

14. Sakudo, A., Yagyu, Y. & Onodera, T. Disinfection and sterilization using plasma technology Fundamentals and future perspectives for biological applications. *International journal of molecular sciences* **20,** 5216 (2019).

15. Greiner, F. *et al.* Diagnostics and characterization of nanodust and nanodusty plasmas. *The European Physical Journal D* **72,** 1–12 (2018).

16. Chen, X., Seto, T., Kortshagen, U. R. & Hogan Jr, C. J. Size and structural characterization of Si nanocrystal aggregates from a low pressure nonthermal plasma reactor. *Powder technology* **373,** 164–173 (2020).

17. Ikezi, H. Coulomb solid of small particles in plasmas. *The Physics of fluids* **29,** 1764–1766 (1986).

18. Chu, J. & I, L. Direct observation of Coulomb crystals and liquids in strongly coupled rf dusty plasmas. *Physical review letters* **72,** 4009 (1994).

19. Yu, W., Cho, J. & Burton, J. C. Extracting forces from noisy dynamics in dusty plasmas. *Physical Review E* **106,** 035303 (2022).

20. Israeli, B. Y., Bhattacharjee, A. & Qin, H. Resonant instabilities mediated by drag and electrostatic interactions in laboratory and astrophysical dusty plasmas. *Physics of Plasmas* **30** (2023).

21. Jovanović, L. *et al.* Chemical composition of Pluto aerosol analogues. *Icarus* **346,** 113774 (2020).

22. Gudipati, M. S. *et al.* Thermal behavior of astrophysical amorphous molecular ices. *Faraday Discussions* **245,** 467–487. `http://dx.doi.org/10.1039/D3FD00048F` (2023).

23. Kushwaha, R. K., Gudipati, M. S. & Henderson, B. L. Cryogenic Differential Calorimetry: Exothermicity of Amorphous-to-crystalline Phase Transitions (ACPT) in Astrophysical and Cometary Ice Analogs. *The Astrophysical Journal* **987,** 190 (2025).

24. Marshall, R. S., Chai, K.-B. & Bellan, P. M. Identification of accretion as grain growth mechanism in astrophysically relevant water–ice dusty plasma experiment. *Astrophys. J.* **837,** 56 (Mar. 2017).

25. Bartlett, J. T., van den Heuval, A. P. & Mason, B. J. The growth of ice crystals in an electric field. *Zeitschrift für angewandte Mathematik und Physik ZAMP* **14,** 599–610 (1963).

26. Bellan, P. M. Why Interstellar Ice Dust Grains Should Be Elongated. *Astrophysical Journal* **905.** Publisher: American Astronomical Society, 96. (2022) (Dec. 2020).

27. Fridman, A. *Plasma chemistry* (Cambridge university press, 2008).

28. Henderson, B. L. & Gudipati, M. S. Direct detection of complex organic products in ultraviolet (Lyα) and electron-irradiated astrophysical and cometary ice analogs using two-step laser ablation and ionization mass spectrometry. *The Astrophysical Journal* **800,** 66 (2015).

29. Shimizu, S. *et al.* Synthesis of water ice particles in a plasma chamber. *Journal of Geophysical Research* **115.** https://doi.org/10.1029/2009jd013375 (Sept. 2010).

30. Bellan, P. M. Mechanism for the Efficient Homogeneous Nucleation of Ice in a Weakly Ionized, Ultracold Plasma. *Astrophysical Journal* **936,** 52 (2022).

31. Girshick, S. L. *Nucleation of particles from the gas phase* (Cambridge University Press, 2024).

32. Havnes, O., Goertz, C. K., Morfill, G. E., Grün, E. & Ip, W. Dust charges, cloud potential, and instabilities in a dust cloud embedded in a plasma. *Journal of Geophysical Research: Space Physics* **92,** 2281–2287 (1987).

33. Havnes, O., Morfill, G. & Melandsø, F. Effects of electromagnetic and plasma drag forces on the orbit evolution of dust in planetary magnetospheres. *Icarus* **98,** 141–150 (1992).

34. Chai, K.-B. & Bellan, P. M. Spontaneous formation of nonspherical water ice grains in a plasma environment. *Geophysical Research Letters* **40,** 6258–6263 (2013).

35. Szopa, C., Cernogora, G., Boufendi, L., Correia, J. J. & Coll, P. PAMPRE: A dusty plasma experiment for Titan's tholins production and study. *Planetary and space Science* **54,** 394–404 (2006).

36. Ricketts, C. L., Contreras, C. S., Walker, R. L. & Salama, F. The coupling of a reflectron time-of-flight mass spectrometer with a cosmic simulation chamber: A powerful new tool for laboratory astrophysics. *International Journal of Mass Spectrometry* **300,** 26–30 (2011).

37. Sciamma-O'Brien, E., Upton, K. T. & Salama, F. The Titan Haze Simulation (THS) experiment on COSmIC. Part II. Ex-situ analysis of aerosols produced at low temperature. *Icarus* **289,** 214–226 (2017).

38. Abbas, M. *et al.* Laboratory experiments on rotation and alignment of the analogs of interstellar dust grains by radiation. *Astrophysical Journal* **614,** 781 (2004).

39. Nicolov, A. & Bellan, P. M. Modeling the energetic tail of a dusty plasma's electron energy distribution and its effect on dust grain charge and behavior. *Physics of Plasmas* **30.** http://doi.org/10.1063/5.0145209 (2023).

40. Shukla, P. K. & Mamun, A. A. *Introduction to dusty plasma physics* (Inst. of Physics Publ., 2002).

41. Bellan, P. M. *Fundamentals of Plasma Physics.* ISBN: 9780511807183 (Cambridge University Press, 2006).

42. Rapp, M. & Lübken, F.-J. Modelling of particle charging in the polar summer mesosphere: Part 1—General results. *Journal of Atmospheric and Solar-Terrestrial Physics* **63,** 759–770. ISSN: 1364-6826 (2001).

43. Parthasarathy, R. Mesopause dust as a sink for ionization. *Journal of Geophysical Research* **81,** 2392–2396 (1976).

44. Natanson, G. On the theory of the charging of amicroscopic aerosol particles as a result of capture of gas ions. *Sov. Phys. Tech. Phys.* **30,** 573–588 (1960).

45. Havnes, O., Morfill, G. E. & Goertz, C. K. Plasma potential and grain charges in a dust cloud embedded in a plasma. *Journal of Geophysical Research: Space Physics* **89,** 10999–11003 (1984).

46. Kopnin, S., Kosarev, I., Popel, S. & Yu, M. Localized structures of nanosize charged dust grains in Earth's middle atmosphere. *Planetary and Space Science* **52,** 1187–1194. ISSN: 0032-0633 (2004).

47. Chen, F. F. Langmuir probes in RF plasma: surprising validity of OML theory. *Plasma Sources Science and Technology* **18,** 035012 (May 2009).

48. Vasyliunas, V. M. A survey of low-energy electrons in the evening sector of the magnetosphere with OGO 1 and OGO 3. *Journal of Geophysical Research (1896-1977)* **73,** 2839–2884 (1968).

49. Stangeby, P. C. A problem in the interpretation of tokamak Langmuir probes when a fast electron component is present. *Plasma Physics and Controlled Fusion* **37.** Publisher: IOP Publishing, 1031–1037. ISSN: 0741-3335. (2022) (Sept. 1995).

50. United States Department of Energy. *Department of Energy Fundamentals Handbook: Nuclear physics and reactor theory* **2** (1993).

51. Huxley, L. Formulae for the Mean Losses of Energy in Collisions of Slow Electrons Moving in Diatomic Gases. *Australian Journal of Physics* **9,** 44–53 (1956).

52. Smith, D. & Dean, A. Electron temperature relaxation rates in flowing afterglow plasmas containing molecular nitrogen and oxygen. *Journal of Physics B: Atomic and Molecular Physics* **8,** 997 (1975).

53. Al-Joboury, M. I. & Turner, D. W. 985. Molecular photoelectron spectroscopy. Part I. The hydrogen and nitrogen molecules. *J. Chem. Soc.*, 5141–5147. `http://dx.doi.org/10.1039/JR9630005141` (0 1963).

54. Reid, G. C. Production and loss of electrons in the quiet daytime D region of the ionosphere. *Journal of Geophysical Research (1896-1977)* **75,** 2551–2562. eprint: https://agupubs.onlinelibrary.wiley.com/doi/pdf/10.1029/JA075i013p02551.https://agupubs.onlinelibrary.wiley.com/doi/abs/10.1029/JA075i013p02551 (1970).

55. Johnson, R. *et al.* Production, ionization and redistribution of O2 in Saturn's ring atmosphere. *Icarus* **180,** 393–402. https://www.sciencedirect.com/science/article/pii/S001910350500326X (2006).

56. Engvold, O., Vial, J. C. & Skumanich, A. *The Sun as a guide to Stellar Physics* (Elsevier, 2019).

57. Kimura, H. On the photoelectric quantum yield of small dust particles. *Monthly Notices of the Royal Astronomical Society* **459,** 2751–2761 (2016).

58. Walls, F. & Dunn, G. Measurement of total cross sections for electron recombination with NO+ and O2+ using ion storage techniques. *Journal of Geophysical Research* **79,** 1911–1915 (1974).

59. Bellan, P. A model for the condensation of a dusty plasma. *Physics of Plasmas* **11,** 3368–3379 (2004).

60. Zhu, X., Strobel, D. F. & Erwin, J. T. The density and thermal structure of Pluto's atmosphere and associated escape processes and rates. *Icarus* **228,** 301–314 (2014).

61. Jensen, E. J. & Thomas, G. E. Charging of mesospheric particles: Implications for electron density and particle coagulation. *Journal of Geophysical Research: Atmospheres* **96,** 18603–18615 (1991).

62. Zhang, Y. & Bellan, P. M. Neutral-charged-particle collisions as the mechanism for accretion disk angular momentum transport. *Astrophysical Journal* **930,** 167 (2022).

63. Chai, K.-B. & Bellan, P. M. Formation and alignment of elongated, fractal-like water-ice grains in extremely cold, weakly ionized plasma. *Astrophysical Journal* **802,** 112 (2015).

64. Marshall, R. S. & Bellan, P. M. Laser-induced fluorescence measurement of very slow neutral flows in a dusty plasma experiment. *Review of Scientific Instruments* **91,** 063504. https://doi.org/10.1063/5.0006684 (June 2020).

65. Chai, K.-B. & Bellan, P. M. Vortex motion of dust particles due to non-conservative ion drag force in a plasma. *Physics of Plasmas* **23** (2016).

66. Bouchoule, A. *Dusty plasmas: physics, chemistry, and technological impacts in plasma processing* (Wiley, 1999).

67. Boufendi, L., Gaudin, J., Huet, S., Viera, G. & Dudemaine, M. Detection of particles of less than 5 nm in diameter formed in an argon–silane capacitively coupled radio-frequency discharge. *Applied physics letters* **79,** 4301–4303 (2001).

68. Bohren, C. F. & Huffman, D. R. *Absorption and scattering of light by small particles* (John Wiley & Sons, 2008).

69. Marshall, R. S. *Developing Plasma Spectroscopy and Imaging Diagnostics to Understand Astrophysically-Relevant Plasma Experiments: Megameters, Femtometers, and Everything in Between* (California Institute of Technology, 2020).

70. Couedel, L., Mikikian, M., Boufendi, L. & Samarian, A. A. Residual dust charges in discharge afterglow. *Physical Review E* **74,** 026403 (2006).

71. Hecht, S., Shlaer, S. & Pirenne, M. H. Energy, quanta, and vision. *Journal of General Physiology* **25,** 819–840 (1942).

72. Chai, K.-B. & Bellan, P. M. Study on morphology and growth of water–ice grains spontaneously generated in a laboratory plasma. *Journal of Atmospheric and Solar-Terrestrial Physics* **127,** 83–91 (2015).

73. Feder, J. *Fractals* (Springer Science & Business Media, 2013).

74. Mandelbrot, B. B. *The fractal geometry of nature* (W. H. Freeman and Co., 1982).

75. Rahmani, N. H., Dabros, T. & Masliyah, J. H. Fractal structure of asphaltene aggregates. *Journal of colloid and interface science* **285,** 599–608 (2005).

76. Meakin, P., Donn, B. & Mulholland, G. W. Collisions between point masses and fractal aggregates. *Langmuir* **5,** 510–518 (1989).

77. Lee, C. & Kramer, T. A. Prediction of three-dimensional fractal dimensions using the two-dimensional properties of fractal aggregates. *Advances in colloid and Interface Science* **112,** 49–57 (2004).

78. Matthews, L. S., Land, V. & Hyde, T. W. Charging and coagulation of dust in protoplanetary plasma environments. *The Astrophysical Journal* **744,** 8 (2011).

79. Kritikos, E. M., Goddard, W. A. & Bellan, P. M. Can electrostatic stresses affect charged water structures in weakly ionized plasmas? *Physics of Plasmas* **32** (2025).

80. Wright, E. L. Fractal dust grains around R Coronae Borealis stars. *Astrophysical Journal Letters* **346,** L89–L91 (1989).

81. Draine, B. T. *Physics of the interstellar and intergalactic medium* (Princeton University Press, 2010).

82. Andersson, B., Lazarian, A. & Vaillancourt, J. E. Interstellar dust grain alignment. *Annual Review of Astronomy and Astrophysics* **53,** 501–539 (2015).

83. Chai, K.-B. Growth and Morphology of Water-, Methanol-, and Ethanol-ice Dust Grains Formed in an Astrophysically Relevant Plasma Experiment. *The Astrophysical Journal* **908,** 130 (2021).

84. Asnaz, O. H., Jung, H., Greiner, F. & Piel, A. Charging of an irregularly shaped particle in the sheath of an rf plasma. *Physics of Plasmas* **25** (2018).

85. Clapp, M., Worsnop, D. & Miller, R. Frequency-dependent optical constants of water ice obtained directly from aerosol extinction spectra. *The Journal of Physical Chemistry* **99,** 6317–6326 (1995).

86. Tazaki, R., Tanaka, H., Okuzumi, S., Kataoka, A. & Nomura, H. Light scattering by fractal dust aggregates. I. Angular dependence of scattering. *Astrophysical Journal* **823,** 70 (2016).

87. Tadsen, B., Greiner, F., Groth, S. & Piel, A. Self-excited dust-acoustic waves in an electron-depleted nanodusty plasma. *Physics of Plasmas* **22** (2015).

88. Wilson, C. T. R. XI. Condensation of water vapour in the presence of dust-free air and other gases. *Philosophical Transactions of the Royal Society of London. Series A, Containing Papers of a Mathematical or Physical Character,* 265–307 (1897).

89. Fridman, A., Boufendi, L., Hbid, T., Potapkin, B. & Bouchoule, A. Dusty plasma formation: Physics and critical phenomena. Theoretical approach. *Journal of Applied Physics* **79,** 1303–1314 (1996).

90. Eschbach, J. *Probing the electromagnetic properties of water-ice dusty plasmas* MA thesis (ETH Zurich and California Institute of Technology, 2024).

91. Vahedi, A. & Gorczyca, B. Predicting the settling velocity of flocs formed in water treatment using multiple fractal dimensions. *Water research* **46,** 4188–4194 (2012).

92. Yu, F. Modified Kelvin–Thomson equation considering ion-dipole interaction: Comparison with observed ion-clustering enthalpies and entropies. en. *The Journal of Chemical Physics* **122,** 084503. ISSN: 0021-9606, 1089-7690 (Feb. 2005).

93. Ostwald, W. Studien über die Bildung und Umwandlung fester Körper: 1. Abhandlung: Übersättigung und überkaltung. *Zeitschrift für physikalische Chemie* **22,** 289–330 (1897).

94. Ratke, L. & Voorhees, P. W. *Growth and coarsening: Ostwald ripening in material processing* (Springer Science & Business Media, 2002).

95. Dobigeon, N., Altmann, Y., Brun, N. & Moussaoui, S. in *Resolving Spectral Mixtures* (ed Ruckebusch, C.) 185–224 (Elsevier, 2016).

96. Famá, M., Loeffler, M., Raut, U. & Baragiola, R. Radiation-induced amorphization of crystalline ice. *Icarus* **207,** 314–319 (2010).

97. Berdis, J. R., Gudipati, M. S., Murphy, J. R. & Chanover, N. J. Europa's surface water ice crystallinity: Discrepancy between observations and thermophysical and particle flux modeling. *Icarus* **341,** 113660 (2020).

98. Jenniskens, P. & Blake, D. Crystallization of amorphous water ice in the solar system. *The Astrophysical Journal* **473,** 1104 (1996).

99. Nicolov, A., Kritikos, E. M. & Bellan, P. M. *How anions induce ice nucleation in a cryogenic plasma* (in preparation). 2026.

100. Libbrecht, K. G. The physics of snow crystals. *Reports on progress in physics* **68,** 855 (2005).

101. Gupta, N. D. & Ghosh, S. K. A report on the Wilson cloud chamber and its applications in physics. *Reviews of Modern Physics* **18,** 225 (1946).

102. Howling, A., Sansonnens, L., Dorier, J.-L. & Hollenstein, C. Time-resolved measurements of highly polymerized negative ions in radio frequency silane plasma deposition experiments. *Journal of applied physics* **75,** 1340–1353 (1994).

103. Tinsley, B. A. Influence of solar wind on the global electric circuit, and inferred effects on cloud microphysics, temperature, and dynamics in the troposphere. *Space Science Reviews* **94,** 231–258 (2000).

104. Gumbel, J. & Megner, L. Charged meteoric smoke as ice nuclei in the mesosphere: Part 1—A review of basic concepts. *Journal of Atmospheric and Solar-Terrestrial Physics* **71,** 1225–1235 (2009).

105. Lee, H. M., Suh, S. B., Tarakeshwar, P. & Kim, K. S. Origin of the magic numbers of water clusters with an excess electron. *The Journal of chemical physics* **122,** 044309 (2005).

106. Nachbar, M., Duft, D. & Leisner, T. The vapor pressure of liquid and solid water phases at conditions relevant to the atmosphere. *The Journal of Chemical Physics* **151** (2019).

107. Thomson, J. J. *Conduction of electricity through gases* (Watchmaker Publishing, 2005).

108. Do, H. & Besley, N. A. Structure and bonding in ionized water clusters. *The Journal of Physical Chemistry A* **117,** 5385–5391 (2013).

109. Egorov, A. V., Brodskaya, E. N. & Laaksonen, A. The effect of ions on solid–liquid phase transition in small water clusters. A molecular dynamics simulation study. *The Journal of chemical physics* **118,** 6380–6386 (2003).

110. Fridman, A. *Plasma chemistry* (Cambridge university press, 2008).

111. Nicolov, A., Pree, S. & Bellan, P. M. The dynamics of fractal ice grains in cryogenic plasma. *Physical Review Letters*. accepted. `http://doi.org/10.1103/rx5l-k7f9` (2025).

112. Ramkorun, B. *et al.* Introducing dusty plasma particle growth of nanospherical titanium dioxide. *Applied Physics Letters* **124** (2024).

113. Chai, K.-B. Observation of high phase velocity of dust acoustic waves with elongated dust grains in a cryogenic dusty plasma experiment. *Plasma Sources Science and Technology* **32,** 055010 (2023).

114. Bockwoldt, T., Arp, O., Menzel, K. O. & Piel, A. On the origin of dust vortices in complex plasmas under microgravity conditions. *Physics of Plasmas* **21** (2014).

115. Choudhary, M. A review on the vortex and coherent structures in dusty plasma medium. *Journal of Plasma Physics* **91,** E7 (2025).

116. Gopalakrishnan, R., Thajudeen, T. & Hogan, C. J. Collision limited reaction rates for arbitrarily shaped particles across the entire diffusive Knudsen number range. *The Journal of chemical physics* **135** (2011).

117. Waldmann, L. Uber die Kraft eines inhomogenen Gases auf kleine suspendierte Kugeln. *Zeitschrift fur Naturforschung A* **14,** 589–599 (1959).

118. Gallis, M., Rader, D. & Torczynski, J. Thermophoresis in rarefied gas flows. *Aerosol Science &Technology* **36,** 1099–1117 (2002).

119. Johnson, C. P., Li, X. & Logan, B. E. Settling velocities of fractal aggregates. *Environmental science &technology* **30,** 1911–1918 (1996).

120. Ma, Q., Matthews, L. S., Land, V. & Hyde, T. W. Charging of aggregate grains in astrophysical environments. *The Astrophysical Journal* **763,** 77 (2013).

121. Van Minderhout, B. *et al.* Charge of clustered microparticles measured in spatial plasma afterglows follows the smallest enclosing sphere model. *Nature Communications* **12,** 4692 (2021).

122. Ferguson, F. T., Nuth, J. A. & Paquette, J. A. Radiative Pressure on Fractal Dust Grains in Oxygen-rich AGB Stars. *The Astrophysical Journal* **975,** 211 (2024).

123. Hiltner, W. On the Presence of Polarization in the Continuous Radiation of Stars. II. *Astrophysical Journal, vol. 109, p. 471* **109,** 471 (1949).

124. Thompson, T. A., Fabian, A. C., Quataert, E. & Murray, N. Dynamics of dusty radiation-pressure-driven shells and clouds: fast outflows from galaxies, star clusters, massive stars, and AGN. *Monthly Notices of the Royal Astronomical Society* **449,** 147–161 (2015).

125. Phelps, A. V. Cross sections and swarm coefficients for nitrogen ions and neutrals in N2 and argon ions and neutrals in Ar for energies from 0.1 eV to 10 keV. *Journal of Physical and Chemical Reference Data* **20,** 557–573 (1991).

126. Lopez-Rodriguez, E. *et al.* ALMA polarimetry measures magnetically aligned dust grains in the torus of NGC 1068. *Astrophysical Journal* **893,** 33 (2020).

127. Tahani, M. Three-dimensional magnetic fields of molecular clouds. *Frontiers in Astronomy and Space Sciences* **9,** 940027 (2022).

128. Reissl, S., Seifried, D., Wolf, S., Banerjee, R. & Klessen, R. The origin of dust polarization in molecular outflows. *Astronomy & Astrophysics* **603,** A71 (2017).

129. Spitzer, L. J. The Dynamics of the Interstellar Medium. I. Local Equilibrium. *Astrophysical Journal, vol. 93, p. 369* **93,** 369 (1941).

130. Hoang, T. Rotational disruption of astrophysical dust and ice—theory and applications. *Galaxies* **8,** 52 (2020).

131. Chai, K.-B. Dynamics of nonspherical, fractal-like water-ice particles in a plasma environment. *Scientific Reports* **8,** 15405 (2018).

132. Draine, B. T. & Flatau, P. J. Discrete-dipole approximation for scattering calculations. *Josa a* **11,** 1491–1499 (1994).

133. Shirakawa, T. S. T. & Sugai, H. S. H. Plasma oscillation method for measurements of absolute electron density in plasma. *Japanese journal of applied physics* **32,** 5129 (1993).